



HAL
open science

Particle acceleration in relativistic astrophysical sources

Virginia Bresci

► **To cite this version:**

Virginia Bresci. Particle acceleration in relativistic astrophysical sources. Astrophysics [astro-ph]. Sorbonne Université, 2022. English. NNT : 2022SORUS216 . tel-03827837

HAL Id: tel-03827837

<https://theses.hal.science/tel-03827837>

Submitted on 24 Oct 2022

HAL is a multi-disciplinary open access archive for the deposit and dissemination of scientific research documents, whether they are published or not. The documents may come from teaching and research institutions in France or abroad, or from public or private research centers.

L'archive ouverte pluridisciplinaire **HAL**, est destinée au dépôt et à la diffusion de documents scientifiques de niveau recherche, publiés ou non, émanant des établissements d'enseignement et de recherche français ou étrangers, des laboratoires publics ou privés.



SORBONNE UNIVERSITÉ

ÉCOLE DOCTORALE ASTRONOMIE ET ASTROPHYSIQUE D'ÎLE-DE-FRANCE

*Institut d'Astrophysique de Paris - CNRS/Commissariat à l'Énergie Atomique et aux
Énergies Alternatives*

THÈSE DE DOCTORAT EN ASTRONOMIE ET ASTROPHYSIQUE

Accélération et dissipation dans les sources astrophysiques relativistes

Par :
Virginia BRESCI

Dirigée par :
Martin LEMOINE
Laurent GREMILLET

Présentation et soutenance prévue le

16 septembre 2022

Devant un jury composé de :

Benoît Cerutti: Rapporteur	Jacek Niemiec: Rapporteur
Elena Amato: Examinatrice	Anna Grassi: Examinatrice
Martin Lemoine: Directeur de thèse	Laurent Gremillet: Codirecteur de thèse
Frédéric Daigne: Président de jury	

September 20, 2022

Declaration of Authorship

I, Virginia BRESCI, declare that this thesis titled, “Accélération et dissipation dans les sources astrophysiques relativistes” and the work presented in it are my own. I confirm that:

- This work was done wholly or mainly while in candidature for a research degree at this University.
- Where any part of this thesis has previously been submitted for a degree or any other qualification at this University or any other institution, this has been clearly stated.
- Where I have consulted the published work of others, this is always clearly attributed.
- Where I have quoted from the work of others, the source is always given. With the exception of such quotations, this thesis is entirely my own work.
- I have acknowledged all main sources of help.
- Where the thesis is based on work done by myself jointly with others, I have made clear exactly what was done by others and what I have contributed myself.

Signed:

Date:

SORBONNE UNIVERSITÉ

Résumé

Institut d'Astrophysique de Paris - CNRS

Accélération et dissipation dans les sources astrophysiques relativistes

by Virginia BRESCI

Selon le paradigme usuel, le rayonnement non-thermique issu des sources astrophysiques de haute énergie résulte in fine de la dissipation d'un réservoir d'énergie en un gaz de particules accélérées. L'étude menée dans le cadre de ma thèse a porté sur deux mécanismes génériques : l'accélération de particules autour de fronts d'ondes de choc et l'accélération de particules dans les plasmas turbulents, dans le régime relativiste. À cette fin, nous avons conduit des simulations numériques *particle-in-cell* (PIC) à grande échelle, en parallèle de développements analytiques. Dans une première partie, nous avons déterminé le mécanisme de saturation de l'instabilité électromagnétique qui gouverne la physique des chocs relativistes, faiblement magnétisés. Dans une deuxième partie, nous avons testé à l'aide de simulations cinétiques un modèle récent d'accélération non-résonante dans une turbulence magnétisée. Enfin, dans une dernière partie, nous avons étudié l'interaction d'un choc magnétisé relativiste avec un plasma turbulent ; cela nous a notamment permis de montrer que cette interaction peut donner lieu à l'accélération de particules dans un régime de magnétisation dans lequel l'accélération autour d'ondes de choc semblait auparavant inefficace.

Abstract

Acceleration and dissipation in relativistic astrophysical sources

It is generally accepted that the observed radiation from high-energy, powerful astrophysical sources fundamentally derives from the dissipation of the energy carried by an outflow into a population of accelerated particles. The work conducted in this PhD has focused on two generic mechanisms: particle acceleration at shock fronts and particle acceleration in turbulent plasmas, in the relativistic regime. To do so, we have conducted large-scale particle-in-cell (PIC) numerical simulations, which we have combined with analytical developments. In a first part, we have determined the saturation mechanism of the electromagnetic instability that governs the physics of weakly magnetised relativistic shocks. In a second part, we have tested against kinetic simulations a recent model of non-resonant particle acceleration in magnetized turbulence. Finally, in a last part, we have studied the interaction of a relativistic magnetised shock with a turbulent flow; we demonstrate, in particular, that this interaction can revive particle acceleration in a regime of magnetization in which shock acceleration was thought to be inefficient.

Acknowledgements

The acknowledgments and the people to thank go here...

Contents

Declaration of Authorship	i
Résumé	ii
Abstract	iii
Acknowledgements	iv
1 Introduction	1
2 Particle acceleration in astrophysical environments	7
2.1 Acceleration in shock waves	8
2.1.1 Sub-relativistic shocks	10
2.1.2 Relativistic shocks	12
2.1.3 Comparison with PIC simulations	14
2.2 Acceleration in turbulence	16
2.2.1 Quasi-linear theory	20
2.2.2 PIC results: an overview	25
2.2.3 Beyond QLT	27
2.2.4 Non-resonant acceleration in turbulence	29
3 Particle-in-cell (PIC) kinetic simulations	33
3.1 PIC simulations of relativistic plasmas	37
3.1.1 The Lehe Maxwell solver	39
3.1.2 The Cole-Karkkainen Maxwell solver	40
3.1.3 Binomial filtering	40
3.1.4 The Godfrey-Vay filter	41
3.2 Turbulence driving scheme	43
3.2.1 General Scheme	43
3.2.2 Periodic turbulence	44
3.2.3 Non-periodic turbulence	46
4 Comparison of non-resonant acceleration model with PIC and MHD simulations	47
4.1 2D decaying turbulence PIC simulation	49
4.2 2D forced turbulence PIC simulation	52
4.3 3D forced turbulence PIC simulation	54
4.4 3D forced turbulence MHD simulation	58
4.5 Summary – conclusions	61
5 Weibel-mediated relativistic shocks	63
5.1 Basic features of the current filamentation instability	65
5.1.1 The Weibel frame	67
5.1.2 Linear stage of the CFI growth	68

5.1.3	Saturation of the CFI	69
	Transverse trapping	69
	Magnetization limit	70
	Particle current limit	70
5.2	Saturation of the CFI in asymmetric plasma flows	71
5.2.1	PIC simulations results	72
	Reference run	74
	Scan in parameter space	78
5.2.2	The electron–ion case	79
	Ultrarelativistic regime	80
	Mildly relativistic regime	82
5.2.3	Late–time evolution of the beam-plasma system	85
5.2.4	Conclusions	87
6	Particle Acceleration at turbulent shock fronts	89
6.1	Numerical PIC simulations	91
6.1.1	Simulation cases 1)	93
	Particle tracking	96
	Particle energy spectra	99
	Discussion	101
6.1.2	Simulation results 2)	101
	Particle tracking	103
	Particle energy spectra	106
	Comparison and additional runs	107
6.2	Discussion	108
A	Test on synthetic turbulence	116
	Bibliography	119

List of Figures

1.1	Illustration of the most common type of gamma-ray burst: on the left the core of a massive star has collapsed forming a black hole; the accretion on the central object launches jets at a relativistic velocity; collisions among shells of fast-moving gas within the jets and from the leading edge of the jet as it sweeps up and interacts with the surroundings result in radiation. Credit: NASA's Goddard Space Flight Center	2
1.2	Left panel: Sky distribution of the 2704 GRB events detected by BATSE (taken from https://gammaray.nsstc.nasa.gov/batse/grb/skymap/). Right panel: bimodal distribution of the T_{90} duration for the BATSE GRBs catalogue (taken from [114]).	2
1.3	Multi wavelength emission of the Crab Nebula. Taken from https://www.cta-observatory.org . Credits: NRAO/AUI and M. Bietenholz; NRAO/AUI and J.M. Uson, T.J. Cornwell (radio); NASA/JPL-Caltech/R. Gehrz / University of Minnesota (infrared); NASA, ESA, J. Hester and A. Loll / Arizona State University (visible); NASA/Swift/E. Hoversten, PSU (ultraviolet); NASA/CXC/SAO/F.Seward et al.(X-rays); NASA/DOE/Fermi LAT/R. Buehler (gamma rays).	3
1.4	Left: Radio (red), X-ray (blue), and optical images of the Cygnus A FR-II radio galaxy (center). Credits: X-ray, NASA/CXC/SAO; Optical, NASA/STScI; Radio, NSF/NRAO/AUI/VLA. Right: Spectral energy distribution (SED) of the source S5 0716+714 and showing the wide separation of the two peaks: the synchrotron peak is in the optical range, the IC peak at several GeV. Taken from [73].	4
2.1	Cosmic-ray energy spectrum measured by several experiments from the year 2000 on. Taken from [57].	8
2.2	Landscape of sources hosting shocks in the Universe.	9
2.3	Left: dependence of the post-shock particle spectrum on the upstream magnetization indicated in the legend, from a set of 2D simulations of electron-positron shocks with $\gamma = 15$, showing the suppression of the Fermi process in strong pre-shock fields. In the inset, maximum particle Lorentz factor evolution over time. Right: ions spectra for different magnetisation values as in the left panel for a 2D simulations of electron-ion shocks with mass ratio $m_i/m_e = 25$ and $\gamma = 15$. Taken from [149].	16
2.4	Schematic diagram of the turbulent magnetic energy spectrum E_{B_\perp} as a function of the perpendicular wavenumber k_\perp normalized to the ion gyroradius ρ_i . The reported characteristic length scales are appropriate for turbulence measured in the near-Earth solar wind. Taken from [159].	17

2.5	Current modulations aligned with the external field in a 3D-PIC simulation of forced turbulence (see Chapter 4 for more details on the turbulence characteristics).	18
2.6	Schematic illustration of stochastic particle-magnetic field interaction in the original idea by Fermi, on the left, and in its modern conception including waves, on the right.	20
2.7	PIC simulation of periodic turbulence of coherence length $\ell_c \sim 350c/\omega_p$, magnetisation $\sigma \sim 1$ and $\delta B/B_0 \sim 1$ at $t \sim 7\ell_c/c$. Current fluctuations, on the left, showing the formation of intense small scale structures where reconnection likely takes place, characterized by a null turbulent field, as visible on the right. This agrees well with the findings of [43].	26
2.8	Temporal evolution of the energy of selected test particles, on the left, showing a first kick in energy due to non-linear effects in narrow current sheets and a slower energisation at later times due to stochastic encounter with turbulent fields. These processes result in a non-thermal spectrum at $t = 2376\omega_p^{-1} \sim 7\ell_c/c$ shown in the right panel. Similar findings were reported in [43].	27
2.9	Left: Schematic representation of the shear (teal), compression (blue) and acceleration (yellow) of the field line which cause the particle acceleration in the non-resonant model. Center and right: Magnetic turbulent fluctuations and some test particles, as green circles, at two different times in a 2D-PIC driven simulation of turbulence (more details in Chapter 4). The size of each circle is proportional to the energy of the corresponding particle. The energisation that is seen between the two panels results from the aforementioned non-resonant heating processes.	29
3.1	Schematic time iterations of PIC-methods. Adapted from [6].	34
3.2	Schematic representation of the PIC simulation lattice for solving Maxwell's equations with the finite-difference time-domain method.	36
3.3	Normalised phase velocity $v_\phi = \omega/ \mathbf{k} $ of the numerical electromagnetic fields for a) Yee scheme, b) Cole-Karkkainen scheme, c) Cowan (not discussed) scheme, d) Lehe scheme. Taken from Guillaume Bouchard's lecture @Smilei Workshop - March 2022	38
3.4	Gain versus wavelength for the bilinear filter without compensation (g), with compensation ($g \cdot c_{3/2}$) and for n -pass bilinear filters with compensation ($g^n \cdot c_{\alpha_c}$), for $n = 4, 20, 50, 80$ (see the text). Taken from [169].	41
3.5	Magnetic energy density over plasma enthalpy on the left and magnetic energy density vs total energy density on the right for the 2D simulations of decaying (dark blue) and forced (orange) turbulence over the first 20 000 time steps corresponding to $t = 1980\omega_p^{-1} \sim 6\ell_c/c$ with $\ell_c \simeq 350c/\omega_p$	44
3.6	Power spectra of the magnetic fluctuations associated to a turbulent forced (right) and decaying (left) scheme.	45

- 3.7 Drifting ($\gamma = 2$) non-periodic turbulence $A_0 \sim 0.03$, $\omega_0 \sim 0$, $\Gamma_0 \sim 0.25$ and 24 wave numbers, at two different time steps and a magnetisation associated to the turbulent field $\sigma \sim 0.2$. The dashed vertical yellow line marks the position, x_f where turbulence forcing is halted. The boundary where the fluctuations start to be excited, x_i coincides with the right hand-side of the domain. Particles are “defrozen” at $x < x_{fr} = 2396c/\omega_p$ 46
- 4.1 On the left: Power spectrum of magnetic fluctuations for the 2D decaying turbulence PIC simulation at $t \simeq 1800 \omega_p^{-1} \sim 5\ell_c/c$. The fuchsia vertical dashed line marks the scale r_g^{-1} for particles with Lorentz factor $\gamma = 50$. Wavenumbers are given in units of the inverse stirring scale ℓ_c^{-1} ; units on the y -axis are arbitrary; On the right: Energy distribution of the particles in the 2D decaying turbulence PIC simulation at $t \simeq 1800 \omega_p^{-1} \sim 5\ell_c/c$. A powerlaw tail emerges at $\gamma \gtrsim 20$ up to $\gamma \sim 10^3$, with spectral index $s \simeq 2$, defining s through $dN/d\gamma \propto \gamma^{-s}$ 50
- 4.2 Histograms of correlation coefficients between the expected and observed evolution of γ' along chunks of test particle trajectories (on the left) and considering the whole trajectory (on the right) of each test particle with initial $25 < \gamma < 50$, for the 2D decaying turbulence PIC simulation. The chunks are selected at random among the whole of test particle histories, provided they fulfill the following criteria: the duration $\Delta t \simeq 1\ell_c/c$ and the energy change within that time interval verifies $|\Delta\gamma'/\gamma'| > 1$. Over the whole trajectory test particles are selected with $|\Delta\gamma'/\gamma'| > 2$. Both histogram shows that the parallel shear Θ_{\parallel} contribution, and more generally the non-resonant model as described by Eq. (2.73), match relatively well the observed variations. 52
- 4.3 Left: Power spectrum of magnetic fluctuations for the 2D forced turbulence PIC simulation at $t \simeq 1800 \omega_p^{-1} \sim 5\ell_c/c$. The fuchsia vertical dashed line marks the scale r_g^{-1} for particles with Lorentz factor $\gamma = 50$; Right: Energy distribution of the particles in the 2D forced turbulence PIC simulation at $t \simeq 1800 \omega_p^{-1} \sim 5\ell_c/c$. A powerlaw tail is clearly seen, extending from $\gamma \sim 10$ up to $\gamma \sim 10^3$, with spectral index $s \simeq 2$, defining s through $dN/d\gamma \propto \gamma^{-s}$. The test particles that we study, with $25 < \gamma < 50$, are located in the powerlaw tail. 53
- 4.4 Histogram of correlation coefficients between the expected and observed evolution of γ' along chunks of test particle trajectories (left panel) and whole trajectory (right panel) with initial $25 < \gamma < 50$, for the 2D forced turbulence PIC simulation. This histogram shows that the non-resonant model provides a satisfactory match to the observed variations, and that the parallel shear term Θ_{\parallel} provides the dominant contribution to the force terms. 54
- 4.5 Visualisation of a cube of the 3D PIC simulation, showing the magnetic energy density (in units of plasma rest-mass energy, top panel), the current density component along the mean magnetic field component (middle panel) and the mean plasma velocity (in units of c , bottom panel). 55

4.6	Left: Power spectrum of magnetic fluctuations for the 3D forced turbulence PIC simulation at $t \sim 600\omega_p^{-1} \sim \ell_c/c$. The fuchsia vertical dashed line marks the scale r_g^{-1} for particles with Lorentz factor $\gamma = 50$. The fall-off of the spectrum in the dissipative range is not as prominent as in 2D due to the data rebinning used (see main text); Right: Energy distribution of the particles in the 3D forced turbulence PIC simulation at $t \sim 600\omega_p^{-1} \sim 2\ell_c/c$. A powerlaw tail with spectral index $s \simeq 2.2$ is clearly seen, extending from $\gamma \sim 10$ up to $\gamma \sim 100$. . .	56
4.7	Histogram of correlation coefficients between the expected and observed evolution of γ' along chunks of test particle trajectories (left) and whole trajectory (right) with initial $25 < \gamma < 50$, for the 3D forced turbulence PIC simulation. This histogram shows that the combination of all force terms provides a good match to the observed variations. Among the three force terms, the parallel shear Θ_{\parallel} provides the dominant contribution.	57
4.8	Example of the time evolution of the energy for two test particles, in the 3D forced turbulence simulation. In dashed blue: the energy of the particle as measured in the simulation frame; in solid purple: the particle Lorentz factor γ'_{obs} in the \mathcal{R}_E frame; in solid red: the Lorentz factor γ'_{th} , as reconstructed using Eq. (2.73).	57
4.9	Left: magnetic power spectrum of the 3D MHD simulation, rescaled by $k^{5/3}$, vs wavenumbers in units ℓ_c^{-1} . The inverse gyroradius of the test particles is indicated by a dashed red line. It lies at the transition between the inertial and the dissipative range. Right: energy distribution of test particles propagated in the 3D MHD simulation, at a time $t \simeq 4\ell_c/c$. At the initial time $t = 0$, all particles shared a common Lorentz factor γ_0 , corresponding to a gyroradius $r_g \simeq 0.02\ell_c$. The spectrum takes a power law shape at large energies, with spectral index $s \simeq 4$, assuming $dN/d\gamma \propto \gamma^{-s}$	59
4.10	Histogram of correlation coefficients between the expected and observed evolution of γ' along blocks of the energy histories of test particles (left) and the whole history (right) that have been propagated in the 3D MHD simulation. The initial Lorentz factor for all particles is $\gamma(t = 0) = 10$ (simulation frame).	60
5.1	Spatial profiles of the Lorentz factor of the background plasma as evaluated in the downstream frame (in blue), proper temperature (in green), pressure of the suprathermal beam (in red) and energy density of the microturbulence (in grey), for a 2D3V PIC simulation of $\gamma_{\infty d} = 100$. Taken from [91].	64
5.2	Schematic representation of the Weibel instability. Taken from [109]. . .	64
5.3	2D maps of particle density (left) and magnetic field (right) in the linear stage of the current filamentation instability extracted from PIC simulations of counterstreaming asymmetric plasma along x . The parameters of the beam-plasma system are those of run a) in Tab. 5.1. . .	66

5.4	Temporal evolution of the simulated mean B -field strength (B_z , black curves) compared to various saturation criteria for reference run (a). Top panel: particle (B_p^b , green dashed-dotted curve) and trapping (B_t^b , blue dotted curve) limits as applied to the beam particles. Bottom panel: spatial magnetization (B_m^p , red dashed curve) and trapping (B_t^p , blue dotted curve) limits as applied to the plasma particles. All curves are in units of $m_e c \omega_{pp} / e$	75
5.5	Comparison of the typical filament size, as extracted from simulation (black line), with the Larmor radius of plasma particles in the simulation frame (red dashed line) and of beam particles in the instantaneous Weibel frame (orange dotted line). Both radii are computed using dynamical quantities extracted from the reference run (a) as defined in Table 5.1. Taken from [21].	76
5.6	Transverse profiles of the beam (blue curves) and plasma (yellow curves) longitudinal current densities at the time of saturation ($t \simeq 400 \omega_{pp}^{-1}$) in the reference run (a) listed, and in a limited region of the periodic y -domain. For each species, the solid and dashed curves correspond to positrons and electrons, respectively. Taken from [21].	77
5.7	Same as Fig. 5.4 for simulation run (e). Taken from [21].	79
5.8	Same as Fig. 5.4 for simulation run (f). In the top panel is also plotted the time evolution of the B -field associated with the spatial magnetization limit as applied to the beam (B_m^b , red dashed curve). Taken from [21].	80
5.9	Temporal evolution of the simulated mean B -field strength (black curves) compared to various saturation criteria for run (i1) defined in Table 5.2. Top panel: particle (green dashed-dotted curve) and trapping (blue dotted curve) limits as applied to the beam ions. Bottom panel: spatial magnetization (red dashed curve) and trapping (blue dotted curve) limits as applied to the plasma ions. All curves are in units of $m_e c \omega_{pp} / e$. Taken from [21].	81
5.10	Temporal evolution of the simulated mean B -field strength (B_z , black curves) compared to various saturation criteria for run (i2) defined in Table 5.2. Top panel: comparison of the spatial magnetization (B_m^{be} , red dashed curve), particle (B_p^{be} , green dashed-dotted curve), trapping (B_t^{be} , blue dotted curve) limits as applied to the beam electrons, plus the trapping limit applied to beam ions (B_t^{bi} , light-blue dotted curve). Also plotted is the saturated B -field from Eq. (5.34) (B_c , magenta dotted line). Bottom panel: spatial magnetization (B_m^{pe} , red dashed curve) and trapping (B_t^{pe} , blue dotted curve) limits as applied to the plasma electrons. All curves are in units of $m_e c \omega_{pp} / e$. Taken from [21].	82
5.11	Out-of-plane magnetic field (B_z) generated by the counterstreaming of mildly relativistic electron-ion flows (i2). The magnetic field is plotted at two different times: in the early ($\omega_{pp} t = 594$, top) and late ($\omega_{pp} t = 990$, bottom) phases of the CFI when cavities have started to form. Taken from [21].	83

5.12	Top left panel: magnetic field profiles along the transverse direction (y) and at successive times, as indicated, for simulation run (i2). The figure reveals the growth of the magnetic field as the cavity expands. Bottom left panel: transverse profiles of the number density of the beam and plasma components at the onset of saturation, $\omega_{pp}t \simeq 1000$. Right panel: (y, p_x) phase space of the plasma ions at the same time. Taken from [21].	84
5.13	Time evolution of various four-velocities as extracted from run (a) defined in Table 5.1. Light-green dotted curve: four-velocity of the Weibel frame. Yellow curve: four-velocity of the plasma. Blue curve: four-velocity of the beam. Magenta dashed line: four-velocity of the relaxed plasma and beam as given by Eq. (5.38). Taken from [21].	87
6.1	Plasma density in two different shock-turbulence simulations. Top panel, configuration (A): shock formation out of a non-turbulent plasma at $t \sim 0$. Bottom panel, configuration (B): the shock originates from a turbulent plasma which travelled across the whole domain.	90
6.2	Longitudinal profiles of the (transversely averaged) coherent (σ_0) and turbulent ($\sigma_{\delta B}$) magnetisations at two different times for simulation run A1). In orange the position of the shock and in lime the position of the boundary of decaying turbulence. The value of σ_0 varies, in particular slightly decreases, in time/distance as a consequence of plasma heating.	94
6.3	Same as Fig. 6.2 for simulation run B1).	94
6.4	$x - t$ evolution of the transversely averaged positron density in configurations A1), top, and B1), bottom. The compression ratio in the downstream reference frame is $R_{ d} \sim 3 - 4$ and delimits the region of shock propagation. Upstream, the turbulent drifting fluctuations are visible. See the text for a complete description.	95
6.5	Plasma velocity averaged over the transverse y - direction for simulation run A1), on the left, and B1) on the right at different time steps. The simulation frame does not correspond anymore with the instantaneous downstream frame of the shock once turbulence affects the downstream.	96
6.6	Histograms of the number of shock-crossings in simulation case A1) for different (initial) energy intervals of the tracked particles. An even number of shock crossings correspond to completed Fermi cycles around the shock front, while an odd number of shock crossings correspond to particles ending up in the downstream. The last two bins are affected by the finite time of the simulation.	97
6.7	Same as Fig. 6.6 for run B1).	98
6.8	Trajectories and Lorentz factor evolution for a few representative test particles of run A1) on the left and B1) on the right selected among those in the energy bins of injection $100 < \gamma_0 < 300$. The dashed grey line represents the shock-front trajectory.	99
6.9	Time evolution of the particle energy spectrum across the shock front of run A1) on the left and B1) on the right.	100

6.10	Particle energy distribution at $t \simeq 8000 \omega_p^{-1}$ in a simulation with ambient magnetisation $\sigma_0 \simeq 0.01$ and $\sigma_{\delta B} \simeq 0.1$. The blue and the orange lines shows the spectra computed across the shock in run A1) and B1) respectively (Fig. 6.9). The pink band represents the range of spectra measured in a same simulation without shock (D1), as extracted in various places and at various times in the interval $6000 - 10000 \omega_p^{-1}$.	101
6.11	Transversely averaged spatial profiles of the coherent and turbulent magnetisations at two different times for simulation run B2) as a function of x . In orange the position of the shock and in lime the position of the boundary of decaying turbulence.	102
6.12	$x - t$ diagram of the positron density from run B2).	102
6.13	From top to bottom: 2D maps of plasma electron density, mean Lorentz factor and magnetisation at $t \sim 12000 \omega_p^{-1}$ for simulation case B2). The lower bottom panel plots the transversely averaged magnetisation as a function of the x -position.	103
6.14	Plasma velocity averaged over the transverse y - direction for simulation run B2) which shows the evolution of the shock position in time. The simulation frame roughly corresponds to the instantaneous downstream rest-frame of the shock and the upstream medium drifts at $\beta_{u d} \sim \beta_\infty = -0.86$. In between the two medium the shock front is visible propagating at $\beta_{sh d} \sim 0.4$	104
6.15	Histograms of the number of shock-crossings in simulation case B2). Even shock crossings correspond to completed Fermi cycles around the shock front, odd shock crossings correspond to particles in the downstream.	105
6.16	Trajectories and Lorentz factor evolution for a few representative test particles of run ii) with initial energy of $30 < \gamma_0 < 100$ on the left and $100 < \gamma_0 < 300$ on the right.	105
6.17	On the left: time evolution of the particle energy spectrum across the shock front for simulation case B2); the black dotted line indicates the best-fitting powerlaw $dN/\gamma \propto \gamma^{-s}$, with $s \simeq 3.5$. On the right: time evolution of the particle energy spectrum across the shock front, setup B2)-blue lines, as compared with the spectra extracted from simulations containing either a nonturbulent shock, setup C2)-ochre line, or a drifting turbulence, setup D2)-dashed green line, as explained in the text. The red dotted line indicates the best-fitting powerlaw.	106
6.18	Time evolution of the particle energy spectrum across the shock front for the additional runs with the same parameters configuration 2) but containing only the shock (left panel, setup C2) or only the turbulence (right panel, run D2).	107
6.19	Sky maps of anisotropy in momentum distribution for suprathermal positrons of $\sqrt{p_x^2 + p_y^2 + p_z^2}/mc = p/mc = 300$ at two different times $t = 9405 \omega_p^{-1}$ on the left and $t = 12376 \omega_p^{-1}$ on the right, as a function of the longitude $\phi \in [-\pi, \pi]$ and latitude $\in [-\pi/2, \pi/2]$	109
6.20	Same as 6.19 for the electron species.	109
A.1	Power spectrum of synthetic turbulence, with locations of the inverse gyroradii indicated by dashed lines for the two experiments (A), corresponding to fast mode turbulence, and (B), for Alfvén modes.	117

- A.2 Probability density of correlation coefficients. Left: case (A), in which particle acceleration takes place through interactions with magnetic mirror modes (transit-time damping in fast mode synthetic turbulence). The model fully captures the energy gains, with a strongly dominant contribution of Θ_{\perp} , as expected. Right: case (B), in which particle acceleration now takes place through gyroresonant interactions. In that case, the model is unable to reproduce the energy gains, hence the pdf of correlation coefficients appears devoid of structure, revealing no particular preference for values close to +1. 118

List of Tables

3.1	45
5.1	Summary of simulation parameters for pair plasmas. Run (a) is the reference simulation. The parameters of the other runs differ from those of run (a) as follows: (b) $n_b \times 3$; (c) $T_b/3$; (d) $\gamma_{b d} \times 3$; (e) $\gamma_{b d}/3$, (e) $\gamma_{b d} \times 10$, $T_p \times 10$, $T_b/10$; (f) $\gamma_{b d} \times 30$, $T_p \times 30$, $T_b/30$. The table gives the simulation parameters once transformed to the Weibel frame. Temperatures are given in units of $m_e c^2/k_B$. Taken from [21].	74
5.2	Parameters of the electron-ion simulations, once transformed to the Weibel frame. Run (i1) is analogous to run (a) in which the positrons have been replaced with ions. Run (i2) treats a mildly relativistic regime. Electron and ion temperatures are given in units of $m_e c^2/k_B$ and $m_i c^2/k_B$, respectively. Taken from [21].	80
6.1	Parameters of the turbulent shock simulations: far-upstream apparent density, normalized plasma drift velocity, apparent normalized plasma temperature, normalized mean B field, spatially averaged coherent magnetisation, spatially averaged turbulent magnetisation. Each set of parameters has been run in different configurations: in A1) the shock is triggered at time $t \sim 0$ by the nonturbulent plasma hitting the left boundary; in B1 and B2) the shock originates from the turbulent plasma reflected on the mirror (lhs of the domain); D1) and D2) are "shock-free" configurations containing only a drifting periodic turbulence covering the whole domain with the same antenna parameters; C2) is a "turb-free" setup with no turbulent fluctuations.	93

Chapter 1

Introduction

The non-thermal radiative spectra observed in a wide variety of high-energy astrophysical sources are believed to result from the dissipation of a bulk energy reservoir into accelerated particles. Magnetic reconnection, acceleration at flow discontinuities and acceleration by scattering on magnetised turbulence, including in shear flows, are likely underlying the physics of acceleration in those sources. In a nutshell, magnetic reconnection is the non-linear process whereby magnetic energy is transferred into kinetic energy by rearranging the magnetic field topology; stochastic Fermi acceleration, in its original formulation, ascribes the particles energy gain through stochastic interactions with the convective electric field carried by magnetic clouds moving in the interstellar space, head-on collisions resulting in an energy gain and tail on interactions in an energy loss; shock acceleration is the way to an efficient net energy gain throughout the same process as the advection of the scattering centers towards the shock front makes all the magnetic field-particles interactions head-on as seen by the particle reference frame, hence resulting in an efficient acceleration; finally, in shear acceleration particles are energised by scattering off (small-scale) magnetic field inhomogeneities embedded in a collisionless shear flow moving with different local velocities.

As direct offsprings of the powerful outflows associated with high-energy sources, collisionless shock waves emerge as natural dissipation agents. Correspondingly, shock acceleration is one of the most studied acceleration mechanism. Yet, the current understanding of the physics of shock waves indicates that the energy gain is prohibited in most of the conditions such sources find themselves (e.g. [144]). In particular, as implied either by phenomenological modelling or by direct constraining observations, the sources we have in mind here, gamma-ray bursts (GRBs), pulsar wind nebulae (PWNe) or jets of active galactic nuclei (AGN), that will be briefly introduced in the following, are expected to host relativistic shocks, embedded in a strong magnetic field (*magnetised* hereafter).

GRBs are the most energetic electromagnetic sources in the Universe (Fig. 1.1). Their prompt gamma-ray radiation lasts between a fraction of a second to several thousands of seconds and corresponds to an energy release of 10^{51-52} erg. Given their isotropic distribution in the sky, as first observed by the BATSE instrument, these objects are of extra-Galactic origin and their temporal evolution associated to the γ -ray luminosity is extremely diverse (Fig. 1.2). The time during which 90% of the GRB energy is detected, the so-called T_{90} parameter, classifies two different populations: one of long events, with typical $T_{90} \gtrsim 2$ s, and one of short events, with $T_{90} \lesssim 2$ s. The general consensus associates long GRBs to the collapse of a massive star into a black hole with an accompanying relativistic polar outflow, powered by an equatorial accretion disk [179]. The second class of short GRBs is instead linked to the merger of compact objects, being two neutron stars or a neutron star with a black hole [114]. Supporting this evidence, GRB170817A was detected only few

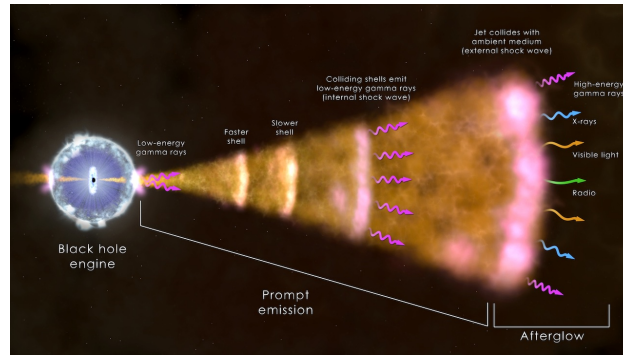


FIGURE 1.1: Illustration of the most common type of gamma-ray burst: on the left the core of a massive star has collapsed forming a black hole; the accretion on the central object launches jets at a relativistic velocity; collisions among shells of fast-moving gas within the jets and from the leading edge of the jet as it sweeps up and interacts with the surroundings result in radiation. Credit: NASA's Goddard Space Flight Center

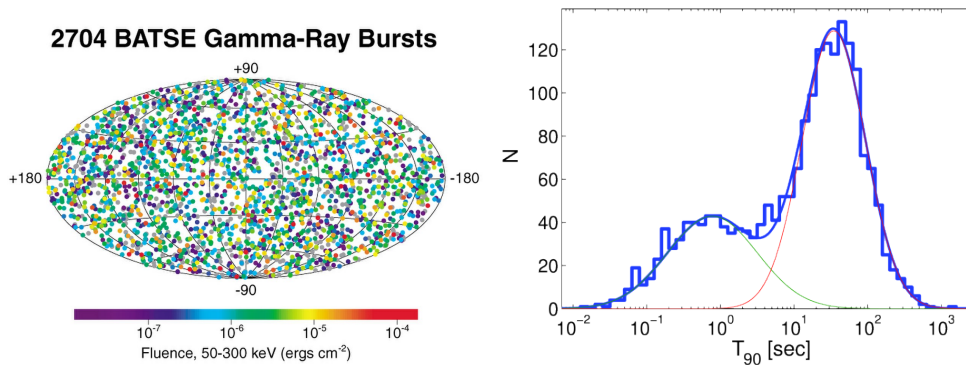


FIGURE 1.2: Left panel: Sky distribution of the 2704 GRB events detected by BATSE (taken from <https://gammaray.nsstc.nasa.gov/batse/grb/skymap/>). Right panel: bimodal distribution of the T_{90} duration for the BATSE GRBs catalogue (taken from [114]).

seconds after the gravitational wave GW170817 signal from the merger of two neutron stars [1]. For most of GRBs the prompt emission is associated to a still unclear mechanism of dissipation of the kinetic energy of ultra-relativistic particles or, possibly electromagnetic energy of a Poynting flux, into an initial flash of gamma rays from an optically thin region. Prompt radiation across the spectrum arises from hot plasma in the vicinity of the source, through collisions among shells of fast-moving plasma within the jet (internal shock waves). An afterglow emission from X-ray to optical-IR and radio through synchrotron-self Compton is then expected as the leading edge of the jet sweeps up and interacts with its surroundings (external shock, see e.g. [127, 186] for a detailed review).

PWNe constitute another bright class of relativistic sources, made of a nebula of non-thermal emission powered by the wind of a fast-spinning, highly magnetised neutron star, often detected as a pulsar when the radiation intercepts the observer line of sight. As commonly quite close objects, those represent an extremely useful laboratory for the extreme physics of relativistic "plasmas". The neutron star transfers most of its rotational energy into a relativistic outflow, made of electron-positron pairs, whose energy is mainly carried in the form of Poynting flux in the internal region of the wind and stored in the particles in the external nebula. Close to the central object, the flow is cold and radiatively inefficient. At the termination

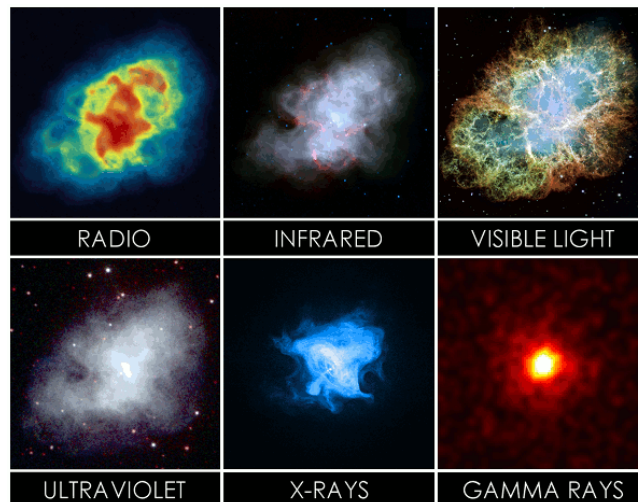


FIGURE 1.3: Multi wavelength emission of the Crab Nebula. Taken from <https://www.cta-observatory.org>. Credits: NRAO/AUI and M. Bietenholz; NRAO/AUI and J.M. Uson, T.J. Cornwell (radio); NASA/JPL-Caltech/R. Gehrz / University of Minnesota (infrared); NASA, ESA, J. Hester and A. Loll / Arizona State University (visible); NASA/Swift/E. Hoversten, PSU (ultraviolet); NASA/CXC/SAO/F.Seward et al.(X-rays); NASA/DOE/Fermi LAT/R. Buehler (gamma rays).

shock, the interaction between the relativistic wind and the non-relativistic confining medium converts the energy into particle acceleration, which eventually results in a bright nebular emission. How this energy is transferred in between this two region is still a puzzle. The Crab Nebula is one of the best studied object in our Universe, its emission covers more than 20 decades in frequency from radio to high-energy gamma rays [110] (Fig. 1.3). The main radiation mechanism is synchrotron emission up to a few hundreds of (photons) MeV where the contribution of the Compton scattering becomes important. A mean Lorentz factor of typically 10^6 , with a maximum value of 10^9 , and a rather intense magnetic field of $0.1 - 1$ mG are the parameters inferred from the modelling of the synchrotron and inverse Compton emissions. The Crab Nebula is the only source in which we find a direct evidence of particle acceleration up to petaelectronvolt (10^{15} eV, PeV) energies, but the mechanism by which such efficient particle acceleration is achieved is still mostly mysterious. It can not indeed result, a priori, from the canonical diffusive shock acceleration because the inferred shock parameters of $10^4 - 10^7$ for the wind Lorentz factor and ~ 1 for the magnetisation, witness the presence of an ultra-relativistic and highly magnetised shock, known to disfavour efficient particle acceleration. Alternative processes, as relativistic reconnection in the equatorial current sheet, have recently been proven to play a key role in particle acceleration and the emission of high-energy radiation by PIC simulations [35]. Such models, however, depends on parameters, as the pulsar inclination, viewing angles or polarization, that are not easily or only partially constrained by observations (see also [7] for a recent review on PWNe).

Another class of source candidates for particle acceleration to extreme energies are active galactic nuclei (AGN). These correspond to a class of galaxies where the mass accretion from the disk to the central supermassive black hole leads to the launch of highly relativistic, collimated jets. Famous examples are, e.g., the elliptical galaxy Messier 87 or Cygnus A (Fig. 1.4). The standard classification usually discerns among two sub-classes of sources: radio-loud and radio-quiet objects. The first class comprehends double radio sources continuously powered by jets emanating from

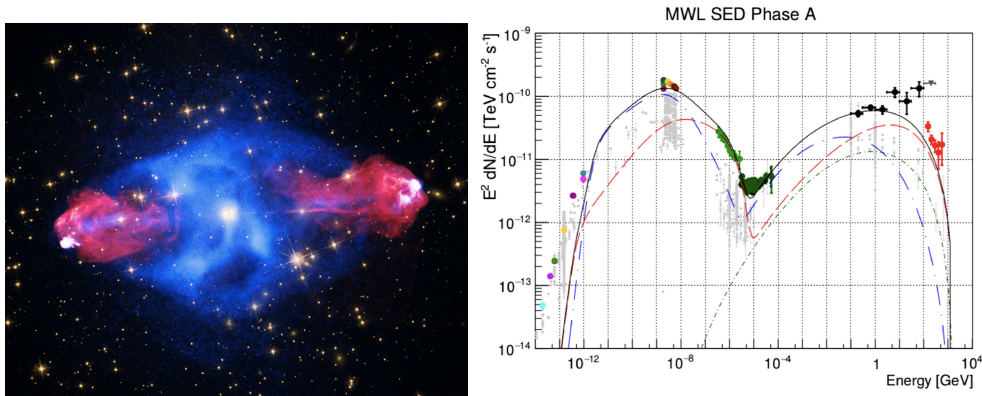


FIGURE 1.4: Left: Radio (red), X-ray (blue), and optical images of the Cygnus A FR-II radio galaxy (center). Credits: X-ray, NASA/CXC/SAO; Optical, NASA/STScI; Radio, NSF/NRAO/AUI/VLA. Right: Spectral energy distribution (SED) of the source S5 0716+714 and showing the wide separation of the two peaks: the synchrotron peak is in the optical range, the IC peak at several GeV. Taken from [73].

galactic nuclei. Their rapid radio variability is associated to a relativistic motion with typical Lorentz factor of 10 – 100 [132]. If the jet points toward the observer the radio-loud AGN is also called *blazar*. Blazar emissions are thus highly beamed and Doppler boosted, making them bright and variable at all frequencies, from radio to gamma-rays. The spectral energy distribution is characterized by a double peak, the first being commonly attributed to synchrotron radiation and the second to inverse Compton scattering on photons either provided by the synchrotron emission itself or originated from the dense radiation field generated by the direct and reprocessed accretion disk emission or molecular torus. Alternatively, hadronic mechanisms such as proton synchrotron or photon-proton pion production can account for the second peak if protons can be accelerated to sufficiently high energies (~ 10 PeV). The variability in radio and optical bands has been successfully modeled by shocks moving down the jets. According to theoretical models, the jets are launched as magnetically dominated, hence the same, long-standing, open question rises again: how and where is the jet converted from magnetically to particle dominated? Although the shock model is able to account for the optical and radio variations of blazars, at the highest energies and especially in very high energy gamma-rays the variations are often too fast to be explained by shocks. Some solutions to the problem consider jet-in-jet model where the variations are associated to mini-jets inside the jets of blazars with bulk speed of the plasma faster than the ambient jet plasma. The energy dissipation takes place in those models by means of magnetic reconnection. The reader is redirected to [18, 73], and references therein, for a complete review.

Recently, collisionless (sub-relativistic) shocks and magnetic reconnection have been explored also in laboratory experiments, thanks to the tremendous progress in the development of high-energy and high-power laser systems over the past four decades. The first theoretical investigations of laboratory collisionless shocks aimed to reproduce electrostatic and Weibel-mediated (i.e., weakly magnetised) shocks. Conducting a collisionless shock experiments requires a mean-free-path for collisions, representing the length over which the particle sees its velocity deflected by

90° , much greater than the characteristic length of shock formation. Not only, internal collisions of particles of the same flow also can be of importance if the temperature of the flow is quite low: their impact on the shock formation or on the development of the instability remains unclear. Shocks mediated by the Weibel instability, of magnetic nature, are more difficult to reproduce with respect to electrostatic ones. The main difficulty is indeed related to its growth rate: the flow densities need to be, on the one hand, sufficiently small to ensure a collisionless regime and, on the other hand, large enough for the ion Weibel instability to develop and the resulting magnetic turbulence to build up. The development of Weibel-type ion filamentation instability has yet been observed in the sub-relativistic regime [62].

Likewise, magnetic reconnection has been successfully tested in laser-plasma experiments, in different physical settings from collisional (e.g., [118, 117, 192, 61, 134]) to collisionless (e.g., [53]) non-relativistic flows and in the collisionless regime of relativistic reconnection (i.e., magnetic field energy greater than the electron rest mass [131]), showing a general agreement with supporting PIC simulations.

Experimental campaigns strongly rely on numerical simulation, either fluid or particle-in-cell (PIC) kinetic methods. Numerical simulations constitute indeed, by themselves, a powerful tool to probe the extreme plasma physics of the sources and the dissipation mechanisms, helping in the deep understanding of the complex mechanism at play in such environments, not always accessible by observations. Besides, if any, direct measurements probe length and time scales order of magnitude beyond the scales relevant to particle acceleration and injection. Particle-in-cell simulations had a determinant role in, e.g., highlighting the non-linear connection between turbulence and particles in the vicinity of the shock or the development of a non-thermal power-law tail of accelerated particles in magnetised turbulence.

A comprehensive understanding of the microphysics behind the acceleration processes that results in observable radiation from non-thermal particles become more and more urgent especially nowadays in the emerging era of multi-messenger astrophysics.

Outline

This thesis focuses on the dissipation of energy and the acceleration of particle in relativistic astrophysical objects. **Chapter 2** presents an overview of the acceleration mechanisms in the high-energy sources this work dealt with. The first section reviews the physics of particle acceleration at shock waves, in the sub-relativistic and relativistic regime, putting some emphasis on the latter as the regime we are interested in. The following section treats particle acceleration in turbulence. The detailed mechanism that governs particle acceleration being still subject to debate, it is first presented in the common framework of quasilinear theory and lately in an alternative, non-resonant picture. An overview of the latest results from PIC simulations in the field closes both sections. This chapter sets the stage for the original contributions presented in § 4-5-6.

Chapter 3 describes standard techniques of state-of-the-art numerical simulations (in particular particle-in-cell kinetic simulations) included in the numerical code we made use of. The last section of the Chapter provides the additional implemented modification specific to the study conducted in § 4.

Chapter 4 reports on the test of the non-resonant model for particle acceleration in strongly magnetised turbulence presented in the last section of Chapter 2. The model predictions, in particular the predicted time histories of particle momenta, are compared with the observed ones in 2D-PIC, 3D-PIC and 3D-MHD simulations. The predicted history is reconstructed by extracting from the simulations, at each point along the particle trajectory, the three force terms that control acceleration. Overall, the finding of a clear correlation between the model predictions and the numerical experiments, indicates that this non-resonant model can successfully account for the bulk of particle energisation through Fermi-type processes in strongly magnetised turbulence.

Chapter 5 presents the numerical investigation of the saturation of the current filamentation instability (CFI) in (asymmetric) conditions relevant for astrophysical sources, and in particular to the precursor of relativistic collisionless shock waves in the weakly magnetized regime. Understanding this saturation level is of prime importance as this instability controls the growth of the microturbulence, hence the overall magnetisation of the blast. We first recall the properties of the instability, and the saturation criteria known in literature. The magnetic fields extracted from large-scale 2D particle-in-cell simulations of counterstreaming electron-positron pair and electron-ion plasmas are compared with the theoretical limits. The results of this study allowed us to identify the criterion among all relevant for saturation, as well as the species which governs the halt of the magnetic field growth and the properties of the instability, such as the growth rate and the maximum wave number. Our results can be directly applied to the physics of relativistic, weakly magnetised shock waves, but they can also be generalized to other cases of study.

The purpose of **Chapter 6** is to revisit the problem of the acceleration efficiency of relativistic magnetised shocks by performing the first PIC simulations of a relativistic shock propagating in a turbulent plasma. We first present the numerical scheme of turbulence adapted to the generation of the shock in the simulation domain: the random magnetic fluctuations are set in motion to eventually reflect at one side of the simulation domain to trigger the shock. Those fluctuations are nonetheless excited isotropically in their rest frame. We then present the simulations we carried out in different magnetisation regimes and our analysis on the particle spectra and on test particles trajectories. Overall, our results indicate that the external, well-developed turbulence can unlock Fermi cycles and promote shock acceleration in superluminal magnetised configurations in which it cannot operate otherwise. In addition, we demonstrate that the acceleration becomes dominated by the turbulence upstream of the plasma if the turbulent magnetisation is sufficiently high.

Chapter 2

Particle acceleration in astrophysical environments

Particle acceleration is ubiquitous in astrophysical plasmas and it results in the non-thermal radiation that constitutes the vast majority of the observables at our disposal. Some sources emit photons up to multi-TeV energies, a signature of the presence, within them, of particles with extreme energies, much higher than those achievable with the largest accelerators on Earth. Even more compelling evidence of the acceleration efficiency of astrophysical sources comes from the study of cosmic rays, namely, charged relativistic particles that reach the Earth. Indeed, their spectrum extends over at least 11-12 decades in energy showing an almost perfect power law behaviour broken at the *knee*, $\sim 3 - 4$ PeV and at the *ankle*, $\sim 3 - 4 \times 10^3$ PeV (see Fig. 2.1). Sources capable of accelerating particles up to these energies are still unknown.

Generally speaking, charged particles are accelerated by electric fields but they are able to attain the highest energy because their residence time in the acceleration zone is increased at the hands of magnetic fields. Particle acceleration can be divided into three main categories: acceleration at flow discontinuities, diffusive acceleration and acceleration by direct electric fields. The combination of the former two makes up the Fermi processes responsible for particle acceleration at shocks, while the mixture of the latter two is at play in turbulent environments.

The original idea proposed by Fermi in 1949 for cosmic-ray acceleration was based on the fact that the interstellar medium (ISM) is filled with magnetic clouds in motion with respect to the Galactic frame. As such, even if the ISM has globally no mean electric field and is an almost perfectly conductor, transient electric fields can be found as a result of locally varying magnetic fields according to the Maxwell-Faraday equation $\nabla \times \mathbf{E} = -\partial \mathbf{B} / \partial t$. Said otherwise, as implied by Lorentz transformations, a pure magnetic field \mathbf{B}' in a given reference frame is seen as a magnetic field \mathbf{B} plus an electric field \mathbf{E} in another reference frame moving relative to it.

Let us consider, as in its original formulation by Fermi [60], a magnetic cloud moving at normalized velocity to the speed of light c , $\beta_v \ll 1$, and a particle bouncing on it at speed β . Assuming specular reflection, meaning an equal angle between the cloud and the direction of incidence and of reflection, the double change of reference frame, Galactic frame \rightarrow cloud frame \rightarrow Galactic frame, gives

$$\frac{E_{\text{out}}}{E_{\text{in}}} = \gamma_v^2 [1 + \beta_v^2 - 2\beta_v \beta \mu_{\text{in}}], \quad (2.1)$$

with $\mu_{\text{in}} \equiv \cos \theta_{\text{in}}$ pitch-angle of incidence in the Galactic frame [60]. The second-order term $\propto \beta_v^2$ in Eq. (2.1), corresponds to the "Fermi II" mechanism of acceleration. Note that the magnetic field carried by the cloud only mediates the reflection but

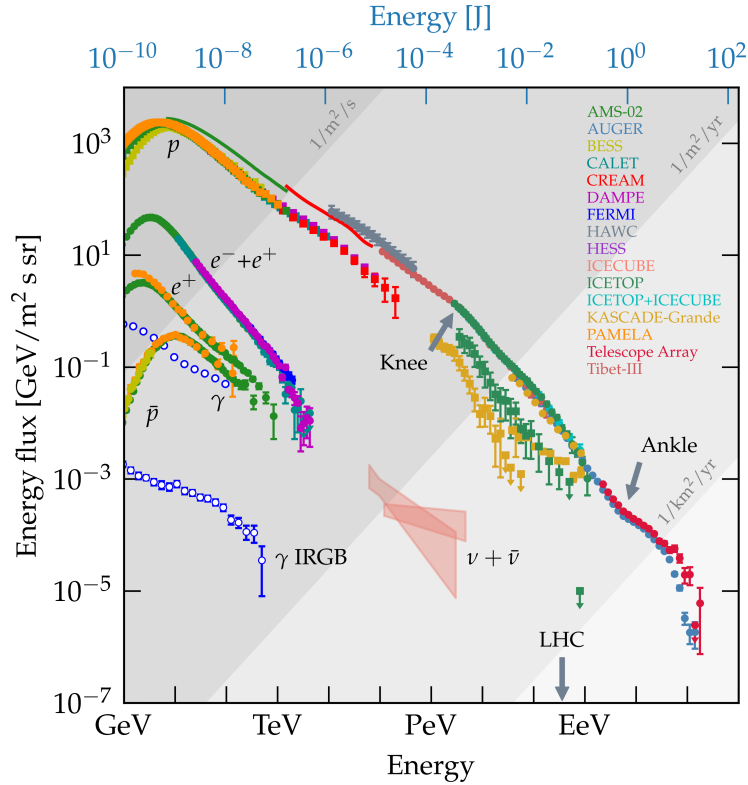


FIGURE 2.1: Cosmic-ray energy spectrum measured by several experiments from the year 2000 on. Taken from [57].

does not appear explicitly. Moreover, Eq. (2.1) corresponds to a net energy gain only for head-on collisions $\mu_{in} < 0$, if $\beta_v \ll 1$.

The details of Fermi acceleration in different regimes will be addressed in the following and in particular in the context of shocks in §2.1 and in §2.2 for scattering off magnetic turbulent fluctuations.

2.1 Acceleration in shock waves

Astrophysical shock waves, mediated by wave-particle interactions rather than Coulomb collisions, constitute good environments for efficient Fermi processes because they can provide head-on collisions between the carried magnetic field and the particles. Shocks are found in a wide variety of settings in the universe. Major examples are supernova remnants (SNRs), galaxy clusters (GCs), active galactic nuclei or gamma-ray bursts. The shock waves arising in the two former systems propagate at sub-relativistic speed in the background medium while they can move close to the speed of light in the latter two. Figure 2.2 shows the landscape of astrophysical sources that host shocks according to the propagation 4-velocity of the shock $u_{sh} = \gamma_{sh}\beta_{sh}$ (β_{sh} shock velocity normalised to the speed of light) and the shock *magnetisation*, σ , i.e. the ratio between the intensity of the magnetic fluctuations and the kinetic energy of the flow, as it will be made explicit further on. As will be clear in the following, in spite of the fact that the shock geometry favours head-on interactions between particles and magnetic fluctuations, the efficiency of acceleration is significantly different according to the values of u_{sh} and σ .

In general, a shock forms from outflows propagating with velocities larger than the local speed of sound. The background medium is unable to smoothly adjust

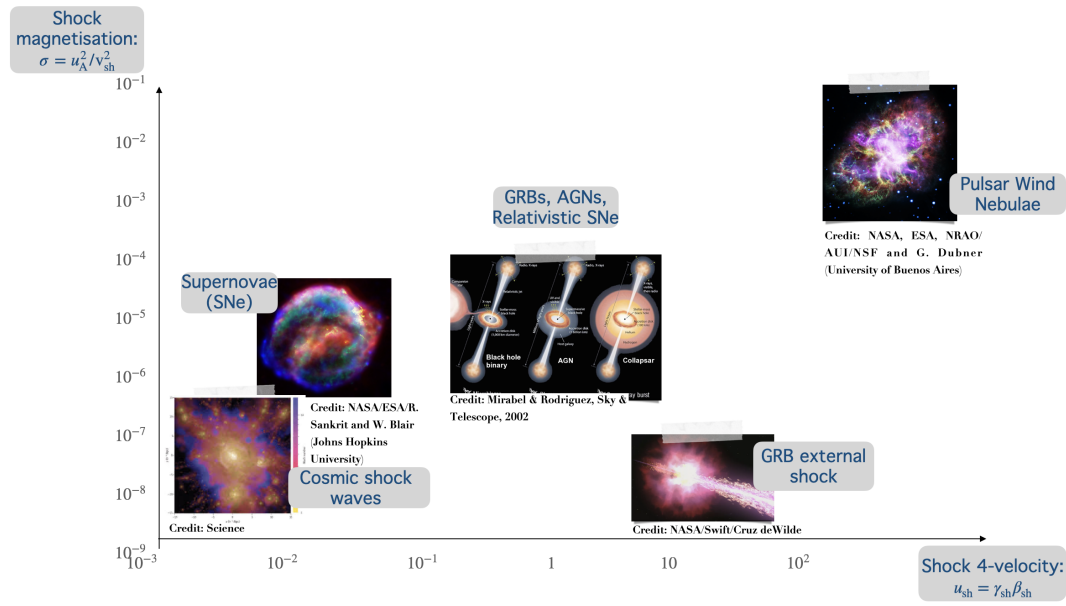


FIGURE 2.2: Landscape of sources hosting shocks in the Universe.

to such perturbations, hence jumps in magneto-hydrodynamical quantities arise in between the shocked and unshocked plasmas, also known as downstream and upstream regions respectively. The Rankine-Hugoniot conservation conditions connect quantities across these two regions. The location where the jump appears is identified as the shock front.

The shocks that develop in astrophysical environments do have their own characteristics, notably they are *collisionless*. This means that the dissipation process that mediates the shock transition occurs via wave-particle interactions instead of particle-particle interactions (referred to as binary Coulomb collisions). A common feature is the generation of non-thermal radiation in the form of high-energy power-law spectra, attributed to synchrotron or inverse Compton emission by the shock-accelerated electrons. Yet, the processes by which the radiating electrons can reach the extreme energies associated with the observed gamma-ray spectra is a lingering puzzle, as is the origin of the strong magnetic fields, generated or amplified, required to explain observations.

Depending also on the plasma beta (ratio of the plasma pressure to the magnetic pressure), composition (e.g. electron-positron or electron-ion plasmas), shock Mach number (ratio of flow velocity to the local speed of sound) and upstream magnetic field orientation with respect to the direction of shock propagation, different types of electromagnetic turbulence-driving instabilities can arise in the upstream region of the shock and shape its structure. Non-relativistic, weakly magnetised ($\sigma \lesssim 10^{-3}$) and low-Mach number shocks are believed to be mediated by electrostatic streaming (electron two-stream or electron-ion Buneman) instabilities (e.g., [19]). With increasing Mach number or going to relativistic velocities of shock propagation, the Weibel-type current filamentation instability have been shown to mediate weakly magnetised shock (e.g., [154]). By contrast, strongly magnetised shocks are typically mediated by coherent magnetic reflection of particles on the shock barrier, under which condition the shock front extends over a distance of the order of the particles gyroradius. Most importantly, first-principles numerical simulations, based on the

particle-in-cell technique (further detailed below), highlighted the non-linear connection between turbulence and particles: accelerated particles trigger the microinstabilities that amplify or even self-generate the magnetic field in the shock precursor, i.e. the region upstream populated by the most energetic particles. In turn, the turbulence regulates the scattering of particles, hence the acceleration process (e.g. [16, 144]). The acceleration process is then connected to the observable (or observable in the near future) radiation, its investigation is thus of crucial importance.

In the following, we will briefly address first the sub-relativistic regime to focus then on relativistic shocks, as the main topic of this thesis.

2.1.1 Sub-relativistic shocks

Non-relativistic shocks are the most commonly studied in the literature. The most representative example is that of the external shocks in supernova remnants. In such settings, when particles are efficiently reflected on the front, several instabilities can develop in the precursor region (e.g., Buneman, firehose, whistler, Weibel, gyroresonant, Bell), depending on the Mach number, magnetic field strength and obliquity. Hence, the phenomenology is more complex than in ultra-relativistic shocks, where the most likely configuration is characterized by a near-perpendicular mean magnetic field as it will be shown in the next section, but particle acceleration is more efficient. For example, non-relativistic quasi-parallel configurations, where the shock waves propagate along a mean magnetic field, are common and lead to efficient magnetic field amplification through resonant and Bell instability in the shock precursor (see [105] and references therein).

Let us now present the basics of Fermi-type particle acceleration in a shock propagating at sub-relativistic speed. If we concentrate only on the velocity discontinuity, an observer at rest in the upstream frame (hereafter denoted as $|_u$) will see the shock and the shocked medium behind the shock (the downstream) approaching with velocity $v_1 = v_{sh}$ and $\Delta v = v_1 - v_2 = v_{sh}(r - 1)/r$ respectively, where r is the compression ratio of the shock. By contrast, an observer at rest with respect to the downstream ($|_d$ hereafter), sees the shock going away with a velocity v_2 and the upstream medium approaching at the same relative velocity (in absolute value) as before: $v_1 = v_{sh}$ and $\Delta v = v_1 - v_2 = v_{sh}(r - 1)/r$. Since the undisturbed interstellar medium is magnetised, a particle coming from the upstream medium and passing through the shock would see the downstream medium as a magnetic cloud facing it and vice-versa. In this configuration then, all the collisions will be head-on.

If we relax the assumption of specular reflection, in a cycle upstream \rightarrow downstream \rightarrow upstream across the shock, the ratio of the final, $E_{f|u}$, and initial, $E_{i|u}$, energies of the particle in the upstream frame is

$$\frac{E_{f|u}}{E_{i|u}} = \gamma_{sh|u}^2 (1 - \beta_{sh|u} \mu_{u \rightarrow d|u}) (1 + \beta_{sh|u} \mu_{d \rightarrow u|d}), \quad (2.2)$$

where $\beta_{sh|u} \ll 1$ is the non-relativistic shock front velocity of propagation in the upstream medium, $\gamma_{sh} = 1/\sqrt{1 - \beta_{sh|u}^2}$ the related Lorentz factor, $\mu_{u \rightarrow d|u}$ and $\mu_{d \rightarrow u|d}$ the cosine of the angle of the particle momentum with respect to the shock front normal as it crosses the front from upstream to downstream and viceversa in the upstream and downstream frame respectively. To obtain the mean energy gain we need to consider the probability a particle has to cross the shock with an angle between θ and $\theta + d\theta$. Assuming a particle density n_0 , the number of particles crossing the shock with an angle between θ and $\theta + d\theta$ through a surface dS in the infinitesimal

time dt is

$$\frac{n_0}{4\pi} v \cos \theta d\Omega dS dt = \frac{n_0}{2} v \cos \theta \sin \theta d\theta dS dt. \quad (2.3)$$

The probability is then $\propto \cos \theta \sin \theta d\theta$ and

$$\langle \cos \theta \rangle = \frac{\int_{\theta_{\min}}^{\theta_{\max}} \cos^2 \theta \sin \theta d\theta}{\int_{\theta_{\min}}^{\theta_{\max}} \cos \theta \sin \theta d\theta}. \quad (2.4)$$

To cross the shock from downstream (upstream), a particle needs to have $\mu \equiv \cos(\theta) \geq (\leq) \beta_{\text{sh|u}}$ which gives $\theta_{\min} = 0 (\pi/2) + \mathcal{O}(\beta_{\text{sh|u}})$ and $\theta_{\max} = \pi/2 (\pi) + \mathcal{O}(\beta_{\text{sh|u}})$. This trivially gives

$$\langle \mu_{\text{d} \rightarrow \text{u} | \text{d}} \rangle = 2/3, \quad (2.5)$$

$$\langle \mu_{\text{u} \rightarrow \text{d} | \text{u}} \rangle = -2/3. \quad (2.6)$$

Finally,

$$\frac{\Delta E}{E} = \frac{4}{3} \beta_{\text{sh|u}} \left(\frac{r-1}{r} \right) + \mathcal{O}(\beta_{\text{sh|u}}^2) \quad (2.7)$$

which is, as anticipated, an always positive gain of energy. The described process is known as diffusive shock acceleration (DSA) or first-order mechanism.

The linear theory of diffusive particle acceleration for a sub-relativistic shocks yields a power-law distribution for the accelerated particles of momenta p :

$$f(p) \propto \frac{1}{p^2} \frac{dN}{dp} \propto p^{-s_p}, \quad (2.8)$$

with $s_p = s + 2 = 3\beta_{\text{u|sh}} / (\beta_{\text{u|sh}} - \beta_{\text{d|sh}})$, $\beta_{\text{d|sh}}$ being the fluid velocity of the downstream medium in the frame of the shock (see e.g. [54, 77, 104], for comprehensive reviews). For strong shocks in an ideal gas with adiabatic index $\Gamma = 5/3$, this implies $s_p = 4$. The strength of DSA theory is to produce a power-law distribution as a function of energy which is similar to the CR spectrum as observed from Earth $N_{\text{obs}}(E)dE \propto E^{-2.7}dE$. Such particle spectrum is believed to arise from an (isotropic) acceleration mechanism at the source able to return $N_{\text{source}}(E)dE = 4\pi p^2 f(p) dp \propto E^{-s}dE$ with $2.1 \lesssim s \lesssim 2.4$, which is then modulated by the diffusive transport in the Galaxy.

It should be noted that even in the absence of fluctuations which scatter particles, a shock front is able to energize particles through the convective electric field $E_c = -\mathbf{v}_{\text{sh|u}}/c \times \mathbf{B}$ upstream of the shock front, due to the motion of the flow at a speed $v_{\text{sh|u}}$. The particle guiding-center can undergo a drift motion along E_c due to the effect of the electric field and to the gradient of the magnetic field close to the shock front. *Shock drift acceleration* (SDA) takes place when an upstream field line intersects the shock as the particle guiding center drifts along the shock; the particle can either be transmitted or reflected at the shock front where the magnetic field is compressed (e.g. [50, 32]). *Shock surfing acceleration* (SSA) is produced when a particle is trapped between the shock electrostatic potential, which appears in the shock vicinity, and the upstream Lorentz force along the shock normal, which carries the particle back to the front (e.g. [138, 86]).

2.1.2 Relativistic shocks

The study of particle acceleration in relativistic shocks is relevant to many astrophysical systems such as gamma ray bursts [173, 63], jets in active galactic nuclei [133], X-ray binaries [59], pulsar wind nebulae [82, 125, 146] and might be relevant for the production of ultrahigh energy cosmic rays. The investigation of Fermi-type particle acceleration is more complicated when it comes to relativistic shocks, mainly because the distribution function of particles near the shock front becomes highly anisotropic and one must simultaneously determine the spectrum and the angular distribution of the particles [65]. As a consequence, the diffusion approximation for spatial transport does not apply and particle acceleration near relativistic shocks departs from the DSA type because the propagation of accelerated particles near the shock, and in particular ahead of the shock, cannot be described as spatial diffusion.

The relativistic shock jump conditions can be obtained from the conservation of the four-current $J^\nu = (\gamma n, n\mathbf{u})$ and energy-momentum tensor $T^{\mu\nu} = wu^\mu u^\nu + p\eta^{\mu\nu}$, where $w = p + e$ represents the fluid enthalpy, e , p and n the fluid energy density, pressure and proper density, and $u^\mu = (\gamma, \mathbf{u})$ the fluid four-velocity in natural units. Integration of the conservation equations across the shock front gives the shock-crossing conditions, that we derive here following [96], in the downstream rest frame. Clearly, the shock frame and the downstream/upstream frames are related by Lorentz transformations, e.g. $\beta_{u|sh} = (\beta_{u|d} - \beta_{sh|d}) / (1 - \beta_{sh|d}\beta_{u|d})$. In the downstream frame, if the velocity (in units of c) of the shock is $\beta_{sh|d}$, the four-vector normal to the shock surface is given by $l_\nu = (\gamma_{sh|d}\beta_{sh|d}, \gamma_{sh|d}, 0, 0)$. The shock crossing conditions hence read

$$[nu^\nu]l_\nu = 0 \quad (2.9)$$

$$[T^{\mu\nu}]l_\nu = 0 \quad (2.10)$$

that break down in the unmagnetised case in

$$\gamma_{u|d}n_u(\beta_{u|d} - \beta_{sh|d}) = -n_d\beta_{sh|d}, \quad (2.11)$$

$$\gamma_{u|d}^2 w_u(\beta_{u|d} - \beta_{sh|d}) + \beta_{sh|d}p_u = -\beta_{sh|d}(w_d - p_d), \quad (2.12)$$

$$\gamma_{u|d}^2 \beta_{u|d} w_u(\beta_{u|d} - \beta_{sh|d}) + p_u = p_d. \quad (2.13)$$

In the case of a strong shock, for which $p_u \ll w_u$, the shock jump conditions reduce to [168]

$$\frac{n_d}{n_u} = \gamma_{u|d} \left(1 - \frac{\beta_{u|d}}{\beta_{sh|d}} \right) \quad (2.14)$$

$$\frac{p_d}{n_u m} = \gamma_{u|d}^2 \beta_{u|d} (\beta_{u|d} - \beta_{sh|d}), \quad (2.15)$$

$$\frac{T_d}{m} = -\gamma_{u|d} \beta_{sh|d} \beta_{u|d}. \quad (2.16)$$

For an ultra-relativistic shock propagating along $+x$, $\beta_{u|d} \sim -1$, and assuming a 3D relativistically hot plasma downstream (i.e. polytropic index $\hat{\Gamma}_d = 4/3$), one has $\beta_{sh|d} \sim +1/3$ corresponding to $\gamma_{sh|d} \sim 3/(2\sqrt{2})$. The compression ratio, defined as the ratio of apparent densities in the shock frame, directly derives from current conservation $\gamma_{sh|d}n_d\beta_{sh|d} = \gamma_{u|sh}n_u\beta_{u|sh}$, from which $\gamma_{sh|d}n_d/(\gamma_{u|sh}n_u) = 3$. More often, PIC simulations are restricted to 2D spatial geometries to save computational

resources. In these case the most appropriate adiabatic index is that of a 2D relativistic gas, $\hat{\Gamma}_d = 3/2$, and consequently one has $\beta_{sh|d} \sim +1/2$, $\gamma_{s|d} n_d / (\gamma_{u|sh} n_u) = 2$ [168]. However, given that a 3D configuration is usually retained in momentum, one usually expects values in between those aforementioned.

The relative energy gain as the particle completes a shock-crossing cycle (e.g. up-down-upstream), $\Delta E/E \equiv (E_{f|u} - E_{i|u})/E_{i|u}$, can be derived from Eq. (2.2), as it only contains a double Lorentz transformation on relativistic particles without any assumption on the shock velocity. The mean energy gain is obtained by averaging over the crossing angles of the particles from upstream to downstream and downstream to upstream with respect to the direction of the boost. As shown in [65, 4, 94], an accelerated particle only experiences an energy gain $\propto \gamma_{sh|u}^2$ during the very first cycle, in correspondence of which the initial distribution function in the upstream medium is isotropic. The ultra-relativistic equivalent of the Fermi acceleration at a shock is affected, with respect to its non-relativistic counterpart, by the occurrence of large anisotropies in the distribution of the accelerated particles near the shock in subsequent cycles. Those anisotropies are due to the fact that, particles re-crossing the shock into the upstream region are only those with $\mu_{d \rightarrow u|u} > \beta_{sh|u}$, hence with $\theta_{d \rightarrow u|u} < \theta_c \sim 1/\Gamma_{sh|u}^2$. Upstream deflection or scattering must change the upstream flight angle to a value $\theta > \theta_c$ before a new crossing cycle can begin. If we consider a complete cycle from upstream to downstream and back, in the upstream frame the angle must hence satisfy the two constraints given above: $\theta_{d \rightarrow u|u} < 1/\Gamma_{sh|u} < \theta_{u \rightarrow d|u}$. Using the small angle approximation, the expression for the energy gain in subsequent cycles gives

$$\frac{E_{f|u}}{E_{i|u}} \approx \frac{2 + \Gamma_{sh|u}^2 \theta_{u \rightarrow d|u}^2}{2 + \Gamma_{sh|u}^2 \theta_{d \rightarrow u|u}^2}. \quad (2.17)$$

Because of the constraints on the flight angle, the above average is always larger than unity but only of the order of two on average, as demonstrated in [4], leading to $\Delta E/E \sim \mathcal{O}(1)$ in the relativistic regime.

Concerning the particle energy spectrum, the formation of a power-law is the result of the competition between the energy gain per shock-crossing cycle and the chance of escaping the acceleration mechanism while downstream. A generalized formulation in terms of shock speed gives an energy spectral index [80]:

$$s = \frac{\beta_{u|sh} - 2\beta_{u|sh}\beta_{d|sh}^2 + \beta_{d|sh}^3 + 2\beta_{d|sh}}{\beta_{u|sh} - \beta_{d|sh}}, \quad (2.18)$$

which converges to $s = 4.222\dots$ in the relativistic limit, where $|\beta_{u|sh}| \rightarrow 1$ and $|\beta_{d|sh}| \rightarrow 1/3$, in good agreement with numerical simulations (e.g. [12, 81, 4, 94]). This spectrum is not properly universal as it depends on the geometry of the turbulence and has been derived in the assumption of isotropic scattering in the downstream region [97].

Another limitation on the efficiency of Fermi acceleration at magnetised relativistic shocks derives from the fact that relativistic shocks are generally *superluminal* [49, 14]. In effect, for strongly magnetised shocks, the particle gyro-centers are constrained to slide along the field lines, which are advected downstream from the shock. There exists then a critical magnetic obliquity above which particles sliding along the magnetic field should be moving faster than the speed of light in order to return upstream. This critical angle of intersection between the upstream magnetic

field and the shock direction of propagation divides the shock into two categories: subluminal, if it is smaller than the critical magnetic obliquity, and superluminal otherwise.

In a relativistic shock, the mean magnetic field can be considered as almost perpendicular in the shock front frame as its transverse component is amplified by a factor $\sim \gamma_{\text{sh}}$ relative to the longitudinal component (i.e. along the shock normal) with respect to the upstream frame. As a result of this Lorentz transformation to the frame of the relativistic shock, the most generic configuration is hence quasi-perpendicular and superluminal.

It can be shown that in this superluminal configuration, if the background turbulence around the shock is absent or if its coherent length is larger than the particle gyroradius [95], before being advected downstream the particle cannot undergo more than one cycle and a half while returning to the shock from downstream to upstream. There are then two necessary conditions for both efficient scattering and acceleration at relativistic shock fronts: the turbulence which develops around the shock has to be 1) strong enough, $\delta B/B \gg 1$, to unlock the particles off the field lines which would otherwise drive them away from the shock front, and 2) characterized by spatial scales smaller than the particle gyroradius in the total magnetic field [123].

2.1.3 Comparison with PIC simulations

Until the late 2000s, most progress on the underlying physics of particle acceleration at relativistic shocks relied on Monte-Carlo (MC) techniques [11, 119, 13, 12]. In a nutshell, this method integrates numerically the trajectory of test particles injected upstream from the thermal plasma, which then develop a power-law suprathermal tail as they undergo pitch-angle scattering on a prescribed micro-turbulence, according to a Monte Carlo method. Momentum diffusion is neglected and only pitch-angle scattering is considered. Another approach consists in 1) integrating exactly the particles trajectory both upstream and downstream; 2) constructing by means of Monte Carlo iteration the laws of probability of return to the shock both from upstream and downstream as a function of ingress and egress pitch-angle; 3) finally combining these probability laws with the energy gain formula and simulate the acceleration process [94].

The non-linear back reaction of the supra-thermal particles on the shock can be incorporated in a phenomenological way in Monte Carlo simulations. If the pressure exerted by the accelerated particles is strong enough to slow down the flow, a subshock forms (see e.g. [55] for the relativistic case and [172, 8] for the sub-relativistic regime). As a result, only the most energetic particles which penetrate far across the shock, are able to experience the high velocity gradient of the original shock, while the low energy ones only probe the smaller compression ratio associated to the subshock. However, this is expected to play a critical role only in the sub-relativistic regime, where it leads to a softening of the spectrum. In the relativistic case ($\gamma_{\text{sh|u}} \gtrsim 3$) the typical size of the subshock is short compared to the particle mean free path and non-linear processes do not deeply affect the shape of the spectra, at least in the parallel configuration [55]. Non-linear MC techniques have hence been mainly developed for non-relativistic shocks.

At odds, kinetic particle-in-cell (PIC) simulations are better suited to tackle the problem: they can capture the full non-linear relationship between particles and fields; they have the considerable advantage of self-generating the magnetic micro-turbulence, which plays a major role in the relativistic regime (e.g. [123, 129]) and

of treating particles self-consistently. Kinetic methods advance in fact a collection of particles through a grid where electric and magnetic fields are discretised; the detailed technique will be presented further on. However they are more costly and not adequate for studying large-scale processes due to their computational cost and their limited spatiotemporal extent. Fully PIC simulations have though enabled much progress on the microphysical side, in particular on the understanding of the interplay of turbulence generation, background plasma deceleration and suprathermal beam transport, notably confirming major and recent analytical studies, e.g. [138, 26, 154, 136], as well as demonstrating the dominant role of small plasma instabilities in forming and mediating collisionless shocks.

The ultra-relativistic regime was the first regime to be investigated by means of PIC simulations because the higher energy gain ($\Delta E/E \sim 1$ instead of $\Delta E/E \sim \beta_{\text{sh}}$ of the sub-relativistic regime) and the short scattering time needed for particles to be accelerated at the shock build, in principle, non-thermal power-laws faster than in the non-relativistic case. Spitkovsky [151] first demonstrated in 2008 self-consistent first-order Fermi acceleration in shocks for a 2D configuration of an unmagnetised pair plasma with an upstream Lorentz factor of $\gamma_0 = 15$. The electromagnetic micro-turbulence generated by the Weibel-type current filamentation instability near the shock, promotes particles from the thermal pool to the shock acceleration process, with an energy gain consistent with the theoretical expectation of $\Delta E/E \simeq 1$. The analytical work of [95] anticipated this finding that Fermi acceleration can operate in the ultrarelativistic shock waves only in association with the development of a micro-turbulence, which amplifies the magnetic field on small scales, as it is the case of the Weibel instability. In [152] the first study of electron-ion relativistic shock was presented for an unmagnetised shock and different ion-to-electron mass ratios. The most important result of this study is that electrons reach near equipartition (same amount of energy fraction in the system) with ions in the precursor, with the electron temperature reaching $\sim 50\%$ of the ion temperature, while no non-thermal tail was observed in particle distributions for the limited duration of the simulation. The observation of a power-law tail in the ion distribution was made only one year later by Martins et al. in 2009 [107].

An analysis on the efficiency of particle acceleration in relativistic shocks as a function of the magnetisation and the shock geometry was first conducted in [148] for a pair plasma and in [147] for an electron-ion plasma, using 2D and 3D PIC simulations. In particular, it has been shown that in strongly magnetised ($\sigma = 0.1$) parallel shocks (hence subluminal) the relativistic version of the Bell instability is triggered and able to promote efficient first-order Fermi acceleration. In oblique but still subluminal shocks, the shock drift acceleration mechanism competes with the former and the power spectra index varies as a consequence between 2.2 and 2.8. In superluminal shocks acceleration has been found to be completely inhibited, as anticipated in [93]: at high magnetisation, the length of the shock precursor is too short for the micro-instabilities to develop, and in the absence of micro-turbulence which amplifies the small-scale magnetic power the acceleration is not possible. In [149] it was shown that the critical magnetisation above which relativistic perpendicular shocks are not accelerating particles is $\sigma_{\text{cr}} \approx 3 \times 10^{-3}$ for electron-positron composition and $\sigma_{\text{cr}} \approx 3 \times 10^{-5}$ for electron-ion composition (see Fig. 2.3). Weakly magnetised shock with $\sigma \lesssim \sigma_{\text{cr}}$ were found to be mediated by the Weibel-filamentation instability that generates strong small-scale magnetic fields in the vicinity of the shock front and an efficient acceleration. A more extended study was recently provided by

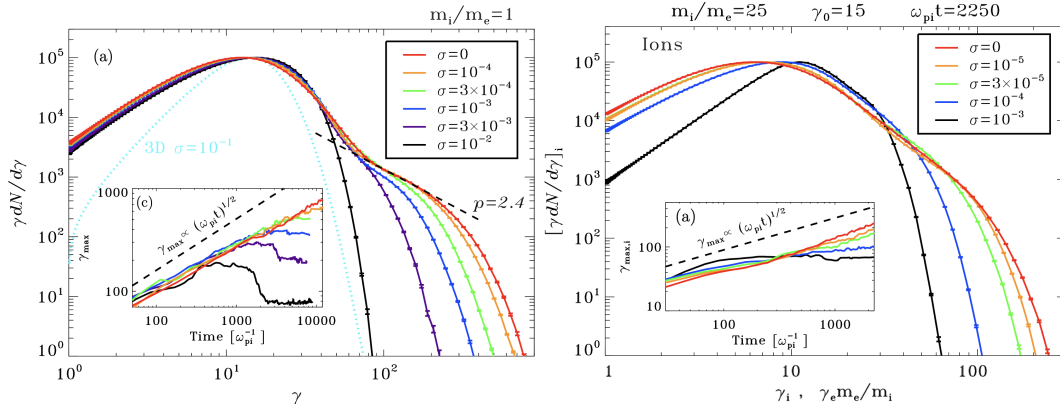


FIGURE 2.3: Left: dependence of the post-shock particle spectrum on the upstream magnetization indicated in the legend, from a set of 2D simulations of electron–positron shocks with $\gamma = 15$, showing the suppression of the Fermi process in strong pre-shock fields. In the inset, maximum particle Lorentz factor evolution over time. Right: ions spectra for different magnetisation values as in the left panel for a 2D simulations of electron–ion shocks with mass ratio $m_i/m_e = 25$ and $\gamma = 15$. Taken from [149].

Plotnikov et al. in 2018 [128]. The authors captured the transition from Weibel mediated shocks ($\sigma < 10^{-3}$) where particle acceleration is efficient to magnetic reflection-shaped shocks ($\sigma > 10^{-2}$) where particle acceleration is inhibited confirming previous findings. Moreover, the diffusion coefficient in momentum space was directly extracted from the particle trajectories, yielding the scaling $D_\gamma \propto E^2$ in the weakly magnetised regime.

The case of mildly relativistic shocks with $\gamma_{\text{sh}}\beta_{\text{sh}} \geq 1$ where the energy gain per Fermi cycle is large and the shock is easily subluminal has been little studied. A recent work by Crumley et al. (2019) [45] found that the shock physics in quasi-parallel configurations is similar to that of nonrelativistic shocks.

Anyhow, it is worth stressing that, as powerful as they are, current fully PIC simulations remain unable to probe the large astrophysical temporal or spatial scales: they are of limited extent (typically a thousand of ion skin depth c/ω_{pi} , where $\omega_{\text{pi}} = (4\pi ne^2/m_i)^{1/2}$ is the ion plasma frequency) and duration (the long simulations of [148, 147] ran for $\sim 10^3 \omega_{\text{pi}}^{-1}$, i.e. a fraction of a second for a typical interstellar environment) compared to astrophysical sources hosting high-energy phenomena (e.g. the comoving dynamical time scale of a gamma-ray burst external shock wave is $R/(\gamma_{\text{sh}}c) \sim 10^4$ s, given the shock radius of the afterglow $R \sim 10^{17}$ cm and the shock Lorentz factor $\gamma_{\text{sh}} \sim 300$ in the upstream medium). The fate of the micro turbulence and, more generally, the long-term evolution of weakly magnetised shocks remain major unanswered questions in relativistic (but also in non-relativistic) shock physics. For a comprehensive review on the weakly magnetised limit see Vanthieghem et al. [168].

2.2 Acceleration in turbulence

High-energy astrophysical plasmas are often characterised by very low densities, relativistically high temperatures, negligible collisionality and large-scale motions driven by a variety of mechanisms (e.g. shear flows, shocks). Under most circumstances, turbulence is inevitable given the high magnetic Reynolds number found in such environments, defined as $R_m = uL/\eta$ at a typical scale L and for a fluid

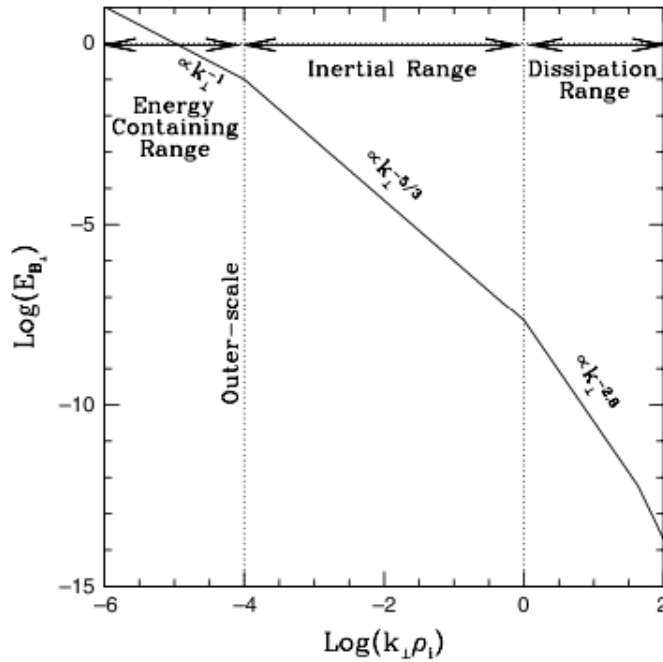


FIGURE 2.4: Schematic diagram of the turbulent magnetic energy spectrum E_{B_\perp} as a function of the perpendicular wavenumber k_\perp normalized to the ion gyroradius ρ_i . The reported characteristic length scales are appropriate for turbulence measured in the near-Earth solar wind. Taken from [159].

of velocity u and magnetic diffusivity η . As an example, the Reynolds number in the solar wind varies in the range $10^5 - 10^6$ at a distance of 1 – 10 AU from the sun (e.g. [121]). As proven by high-resolution multi-wavelength images, systems as the Crab nebula and the Messier 87 jet are manifestly turbulent [72, 150]. Magnetised turbulence, as a source of scattering agent, also plays a central role in the process of diffusive acceleration and its interaction with particles is modelled to explain the non-thermal radiation of gamma-ray sources as GRBs, AGN and jets (e.g. [30, 85]), PWNe (e.g. [180]) and blazars (e.g. [10]).

The basic properties of turbulence in astrophysical environments remain poorly constrained by both theory and observations. Collisionless turbulence is commonly described as a transfer of energy (*cascade*) by non linear processes from a large scale, where energy resides, to small scales where dissipation mechanisms of kinetic origin limit the transfer, dissipate the fluid motions and deposit heat (Fig. 2.4). If it is assumed that in the intermediate range (the *inertial range*) between these two scales the statistical properties of the turbulence do not depend on the macrophysics of injection or on the microphysics of dissipation, that those are spatially homogeneous and isotropic and that the energy transfer is local in scale space, the flux of kinetic energy through any inertial-range scale is scale-independent. By simple dimensional considerations, the cascade time can only be associated to the typical size of the fluctuations and one readily obtains the well-known *Kolmogorov* spectrum of kinetic energy fluctuations $\propto k^{-5/3}$, where k represents a wavenumber.

Yet, astrophysical plasmas are highly conducting and support magnetic fields whose energy is generally comparable to the kinetic energy of the motions. In the inertial range, turbulence is well described in the frame of magneto-hydro-dynamic (MHD; e.g. [139]). As a fluid model which couples Maxwell's equations with hydrodynamics, MHD is indeed appropriate to describe the macroscopic behavior of the

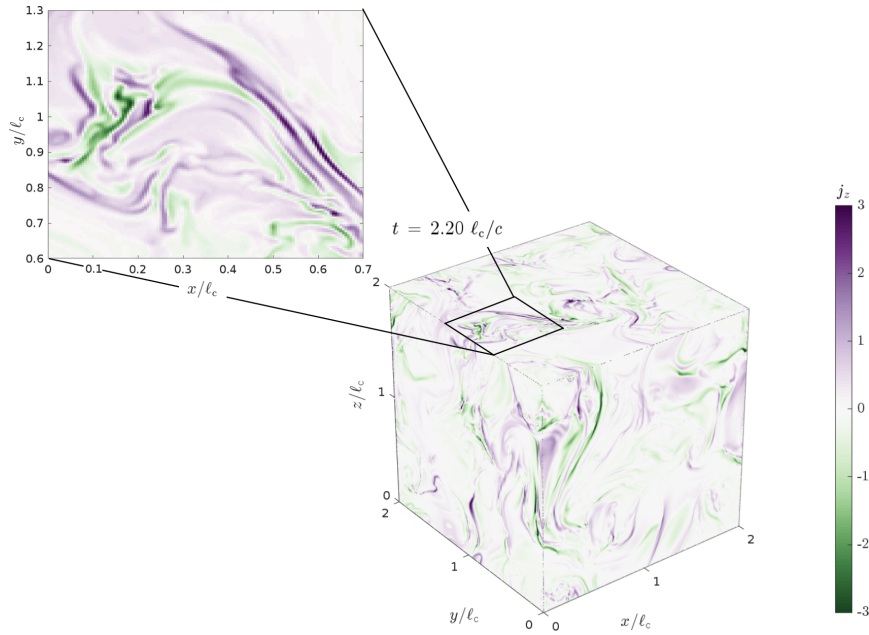


FIGURE 2.5: Current modulations aligned with the external field in a 3D-PIC simulation of forced turbulence (see Chapter 4 for more details on the turbulence characteristics).

plasma on (large) scales greater than the electron/ion gyroradii and on timescales longer than the inverse of the plasma frequency and the electron/ion cyclotron frequencies. The presence of the magnetic field also introduces an additional length scale and preferred direction, i.e. the typical scale of the fluctuation along the magnetic field line, besides that associated to the size of the fluctuation (hence, in the transverse plane). The first theories of MHD turbulence assumed an isotropic, meaning that the fluctuations size were associated to their scale along the field lines, cascade of weakly interacting Alfvén wave-packets and obtained a $k^{-3/2}$ spectrum [75, 83]. Not confirmed by observations, the isotropy assumption has soon been discarded in favour of anisotropic MHD theories.

The modern phenomenology of strong (turbulent fluctuations greater than the background magnetic field) incompressible MHD turbulence in the non-relativistic regime is based on the theory of Goldreich and Sridhar [69]. This theory essentially relies on the assumptions that: 1) the cascade of turbulent fluctuations in the magnetic field and fluid velocity from large scale to small scales is caused by interactions between counterpropagating Alfvén wave packets travelling along the background magnetic field; 2) the turbulence becomes anisotropic due to the presence of the large-scale magnetic field: the wavevector is then decomposed in components parallel and perpendicular to the background field direction, and those are related one to the other through $k_{\parallel} \sim k_{\perp}^{2/3} L^{-1/3}$, with L the scale at which the so-called critical balance steps in (see below); the energy spectrum in the inertial range is predicted to scale as $E(k_{\perp}) \sim k_{\perp}^{-5/3}$, and $E(k_{\parallel}) \sim k_{\parallel}^{-2}$; 3) the interactions between the Alfvén-wave packets are strong and at sufficiently small scales L the turbulence always arranges itself in such a way that the Alfvén timescale and the perpendicular nonlinear interaction timescale are comparable to each other (*critical balance* assumption). Figure 2.5 is an example of how turbulent fluctuations become increasingly anisotropic on, e.g., small-scale current sheets, as revealed by the current component parallel to the external field.

In spite of the fact that the theory of relativistic turbulence is substantially less developed, numerical investigations on the relativistic regime showed similarities with the non-relativistic case for the energy spectra and the statistical properties of the turbulence (e.g. [194, 193, 156, 157]). The Goldreich and Sridhar theory was extended to the limit of ultra-relativistic strong MHD turbulence by Thompson and Blaes [162], and more recently by TenBarge et al. [160]. The authors considered an highly magnetised plasma $\sigma \gg 1$, or equivalently $v_A \equiv \delta B / \sqrt{4\pi mn} = \sqrt{\sigma/(\sigma+1)} c \sim c$. In this case the inertia of the plasma can be neglected and the system can be treated in the force-free MHD framework. The nonlinear interaction is described for long-wavelength, low frequency perturbations, corresponding to Alfvén, slow and fast modes, and it leads, in the assumption of critical balance, to the production of a magnetic energy spectrum identical to the non-relativistic regime.

The MHD Alfvénic cascade is believed to further continue developing through the kinetic range, which begins as soon as k_\perp becomes of the order of the ion gyro-radius [139]. On small scales, non-ideal effects might appear: sharp gradients of the magnetic field can give rise to non-linear parallel electric field to the magnetic field component (as in reconnection layers). Then, a large current and a finite resistivity that enables the plasma to move across the field lines break the Alfvén theorem, milestone of the ideal MHD assumption, according to which the plasma is frozen along the field lines. More importantly, the kinetic range extends to scales far below the ion mean free path, deep into the collisionless regime where the density and magnetic perturbations can be damped. This regime is hence more properly described by kinetic theory rather than fluid equations. Here, the Alfvénic cascade can continue as a kinetic Alfvénic cascade or as an entropy cascade, i.e. a nonlinear phase mixing process whereby the collisionless damping occurring at the ion and electron gyroscales is made irreversible and particles are heated. In the first case the magnetic energy spectrum is predicted to scale as $E(k_\perp) \sim k_\perp^{-7/3}$ and in the second case as $E(k_\perp) \sim k_\perp^{-16/3}$.

The MHD turbulence phenomenology of the non-relativistic Goldreich-Sridhar framework and the statistical properties of the turbulence are supported by recent PIC simulations by Zhdankin et al. [191]. Their results also suggest that ultra-relativistic plasma temperatures and near-relativistic turbulence motions do not substantially alter the nature of the turbulent cascade. In the kinetic regime, those authors measured a slightly shallower spectra for magnetic fluctuations $\propto k_\perp^{-4.5}$ with respect to the predictions from a steeper entropy cascade, but at small scales PIC simulations suffer of particle noise and the kinetic scales were only minimally resolved as of the order of the cell size.

At the dissipation scale energy is converted to plasma energy, and subsequently to radiation, as attributed to synchrotron or inverse Compton scattering in turbulent astrophysical environments. The main feature of turbulence we are interested in here, is its capability of accelerating particles up to the formation of supra-thermal power law energy distributions. In its original formulation, the interaction of particles with a moving magnetic center at β_m results in second order Fermi-acceleration on timescales, in the sub-relativistic regime, $t_{\text{acc}} \sim t_{\text{scatt}} / \beta_m^2$, with t_{scatt} the scattering time, roughly the time needed for a particle to change by one its pitch-angle. In modern theories, the acceleration is more related to stochastic wave-particles interactions (see Fig. 2.6 for a schematic illustration). How particles gain energy in a turbulent environment can be addressed analytically using quasi-linear theory (QLT) under

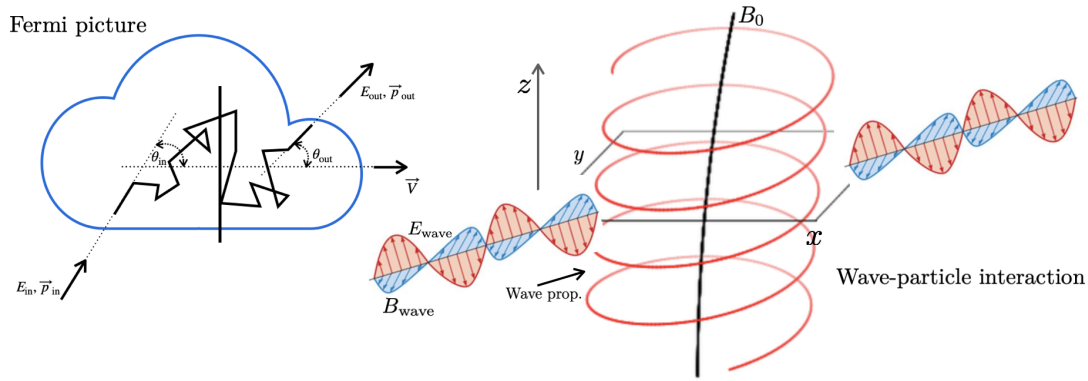


FIGURE 2.6: Schematic illustration of stochastic particle-magnetic field interaction in the original idea by Fermi, on the left, and in its modern conception including waves, on the right.

simplified assumptions. QLT provides the basics of the modeling and the interpretation of particle transport and energisation due to interactions with the electromagnetic fluctuations. The classic derivation allows one to describe the particle dynamics and to derive the diffusion coefficients that account for the effect of the resonant wave-particle interactions as a function of the particle dynamical quantities and the electromagnetic wave spectral properties.

This will be addressed up to a certain level in the upcoming section (see e.g. [140] for a complete and detailed derivation), to next give the way to an overview of recent results obtained with PIC simulations and to an extended theory in the last part.

2.2.1 Quasi-linear theory

QLT provides an analytical estimates of the various diffusion tensor components to first order in the spectrum of electromagnetic fluctuations which are commonly described as a sum of linear eigenmodes of the plasma. In the ideal MHD approximation those are the incompressible Alfvén modes, the fast and the slow magnetosonic modes. Since in astrophysical objects Alfvén waves propagating parallel or antiparallel to the ordered magnetic field have the shortest growth times [155] they have been investigated at length. The quasilinear approximation is comparable to a first-order perturbation theory in magnetic perturbations. The electromagnetic fields are expressed as a sum of the coherent component and the turbulent fluctuations, in the hypothesis (i) that the latter have small amplitudes so as to retain only first order terms in the turbulent perturbation. Also the distribution function is divided into an average value and a fluctuating part, on the assumption that (ii), as to discard second order perturbative terms, once applying the propagator to follow its evolution, the temporal variation on the fluctuating part induced by the electromagnetic turbulent perturbations remains much smaller than the variation induced on the average. Moreover, within the quasilinear approximation, the particle velocity and the position of the particle are replaced by the unperturbed trajectory (iii), instead of considering the true particle orbit. Because of the permanent interaction with the turbulent fields, the deviation between the unperturbed orbit and the true motion becomes larger during time. Therefore, for late times, the quasilinear approximation becomes less and less valid, meaning that QLT is correct only if later times are unimportant.

In more detail, the starting point is the Vlasov equation, which describes the evolution of the distribution function of a plasma (here expressed in the non-relativistic

limit),

$$\frac{\partial f}{\partial t} + \mathbf{v} \cdot \frac{\partial f}{\partial \mathbf{x}} + \dot{\mathbf{p}} \cdot \frac{\partial f}{\partial \mathbf{p}} = \mathcal{S}, \quad (2.19)$$

with the equations of motion:

$$\dot{\mathbf{p}} = q \left[\mathbf{E}(\mathbf{x}, t) + \frac{\mathbf{v}}{c} \times \mathbf{B}(\mathbf{x}, t) \right], \quad (2.20)$$

$$\dot{\mathbf{x}} = \mathbf{v} = \frac{\mathbf{p}}{\gamma}, \quad (2.21)$$

\mathcal{S} denotes sources and sinks of particles; the magnetic field is expressed as sum of an ordered component and plasma turbulence, (i) $\mathbf{B} = \mathbf{B}_0 + \delta\mathbf{B}$; the electric field only contains the turbulent part, $\mathbf{E} = \delta\mathbf{E}$ given the high conductivity of cosmic plasmas. The fluctuations consist of transverse left- and right-hand polarized waves propagating parallel or antiparallel to the homogeneous magnetic field:

$$\delta B_{L,R} \equiv \frac{1}{\sqrt{2}}(\delta B_x \pm i\delta B_y), \quad \delta B_{\parallel} = \delta B_z, \quad (2.22)$$

$$\delta E_{L,R} \equiv \frac{1}{\sqrt{2}}(\delta E_x \pm i\delta E_y), \quad \delta E_{\parallel} = \delta E_z. \quad (2.23)$$

Because of the gyration of the particles in the homogeneous background field the actual position of the particles is replaced by the coordinate of the guiding center (iii) $\mathbf{R} = (X, Y, Z)$ of their orbit, given by (e.g. [140]):

$$\mathbf{R} = \mathbf{r} + \frac{\mathbf{v} \times \mathbf{e}_z}{\epsilon\Omega}, \quad \begin{cases} X = x + \frac{v\sqrt{1-\mu^2}}{\epsilon\Omega} \sin\phi \\ Y = y - \frac{v\sqrt{1-\mu^2}}{\epsilon\Omega} \cos\phi \\ Z = z \end{cases} \quad (2.24)$$

with $\epsilon = q/|q|$ and $\Omega = |q|B_0/\gamma mc$, and having used spherical coordinates in momentum space (p, μ, ϕ) defined by

$$p_x = p \cos\phi \sqrt{1-\mu^2}, \quad p_y = p \sin\phi \sqrt{1-\mu^2}, \quad p_z = p\mu. \quad (2.25)$$

In the new set of coordinates $x_\sigma = (p, \mu, \phi, X, Y, Z)$ Eq. (2.19) reads

$$\frac{\partial f}{\partial t} + v\mu \frac{\partial f}{\partial Z} - \epsilon\Omega \frac{\partial f}{\partial \phi} + \frac{1}{p^2} \frac{\partial}{\partial x_\sigma} (p^2 g_{x_\sigma} f) = \mathcal{S}(\mathbf{x}, \mathbf{p}, t), \quad (2.26)$$

with the components of the fluctuating force term g_{x_σ} given by

$$g_p = \dot{p} = \frac{mc\gamma\epsilon\Omega}{pB_0} \mathbf{p} \cdot \delta\mathbf{E} = \frac{\epsilon\Omega pc}{vB_0} \left[\mu\delta E_{\parallel} + \sqrt{\frac{1-\mu^2}{2}} (\delta E_L e^{-i\phi} + \delta E_R e^{i\phi}) \right], \quad (2.27)$$

$$g_\mu = \dot{\mu} = \frac{\epsilon\Omega\sqrt{1-\mu^2}}{B_0} \left[\frac{c}{v} \sqrt{1-\mu^2} \delta E_{\parallel} + \frac{i}{\sqrt{2}} \left[e^{i\phi} \left(\delta B_R + i\mu \frac{c}{v} \delta E_R \right) \right. \right. \quad (2.28)$$

$$\left. \left. - e^{-i\phi} \left(\delta B_L - i\mu \frac{c}{v} \delta E_L \right) \right] \right], \quad (2.29)$$

$$g_\phi = -\epsilon\Omega \frac{\delta B_{\parallel}}{B_0} + \frac{\Omega}{\sqrt{2(1-\mu^2)}B_0} \left[e^{i\phi} \left(\mu\delta B_R + i\frac{c}{v}\delta E_R \right) + e^{-i\phi} \left(\mu\delta B_L - i\frac{c}{v}\delta E_L \right) \right], \quad (2.30)$$

$$g_X = -v\sqrt{1-\mu^2} \cos\phi \frac{\delta B_{\parallel}}{B_0} + \frac{ic}{\sqrt{2}B_0} \left[\delta E_R - \delta E_L - \frac{i\mu v}{c} (\delta B_L + \delta B_R) \right], \quad (2.31)$$

$$g_Y = -v\sqrt{1-\mu^2} \sin\phi \frac{\delta B_{\parallel}}{B_0} - \frac{c}{\sqrt{2}B_0} \left[\delta E_R + \delta E_L + \frac{i\mu v}{c} (\delta B_L - \delta B_R) \right], \quad (2.32)$$

$$g_Z = 0. \quad (2.33)$$

Since the knowledge about the fluctuations given in Eq. (2.23) is usually limited, quasilinear theory considers an ensemble of possible fluctuating fields. The fluctuations are assumed to be stationary homogeneous Gaussian random fields, fully characterized by their power spectrum, i.e. $\langle \delta\mathbf{B} \rangle = \langle \delta\mathbf{E} \rangle = 0$, implying $\langle \mathbf{B} \rangle = B_0$, $\langle \mathbf{E} \rangle = 0$, where the brackets denote the ensemble averaging. From the homogeneity follows that there are space-independent correlation functions:

$$R_{PQ}(\xi, t) = \langle P(z + \xi, t + \tau) Q(z, t)^* \rangle, \quad (2.34)$$

with P, Q standing for either δB_x , δB_y , δB_R or δB_L . Different wave types are not assumed to be correlated.

In order to find the evolution of the particle distribution function in the phase space under the influence of such fluctuating perturbations to the electromagnetic fields, it is convenient to consider also an ensemble of the distribution functions, all equal at some initial time t_0 , such that the appropriate ensemble-averaging gives $f(\mathbf{x}, \mathbf{p}, t) = F(\mathbf{x}, \mathbf{p}, t) + \delta f(\mathbf{x}, \mathbf{p}, t)$.

Using the above definitions in Eq. (2.26) and subtracting the resulting equation from the original form, it is possible to obtain an equation for the fluctuations $\delta f(\mathbf{x}, \mathbf{p}, t)$. The latter further reduces to:

$$\frac{\partial \delta f}{\partial t} + v\mu \frac{\partial \delta f}{\partial Z} - \epsilon\Omega \frac{\partial \delta f}{\partial \phi} \simeq -g_{x_\sigma} \frac{\partial F}{\partial x_\sigma}, \quad (2.35)$$

in the assumption (ii) of small amplitude fluctuations for which there exists a timescale smaller than the timescale on which g_{x_σ} affects the evolution of the distribution function (see e.g. [140] for a complete derivation).

Solving by the method of characteristics one obtains

$$\delta f(t) = \delta f(t_0) - \int_{t_0}^t ds g_{x_\sigma}(X'_\mu, s) \frac{\partial F}{\partial X'_\sigma}(X'_\mu, s), \quad (2.36)$$

where the characteristics, i.e. an unperturbed particle orbit in the homogeneous magnetic field, is given by the system of Eqs. (2.24) with the changing

$$\begin{aligned} Z' &= z_0 + v\mu(s - t) \\ \phi' &= \phi_0 - \epsilon\Omega(s - t) \end{aligned} \quad (2.37)$$

In order to get an useful equation for F after having inserted Eq. (2.36) into Eq. (2.26), one needs to find a way to evaluate the integral.

Three more basic assumptions are made: 1) at the initial time t_0 the particle's space density is completely uncorrelated to the turbulent field so that $\langle \delta f(t_0) g_{x_\sigma} \rangle = 0$; 2) there exists a correlation time τ_c such that the correlation function $R_{p,Q}(\xi, \tau)$, as defined in Eq. (2.34), becomes negligible if $\tau > \tau_c$, which implies that the important (finite) contribution to the integral comes from the interval $t - \tau_c \rightarrow t$; 3) during this time interval the variation of $\partial F(X'_\mu, s) / \partial X'_\sigma$ is so small that the value is nearly equal to that at $s = t$.

With these rearrangements one finally obtains a diffusion equation, involving only second-order correlation functions of the fluctuating field g_{x_σ} integrated along the unperturbed orbit, referred to as the **Fokker-Planck equation**:

$$\frac{\partial F}{\partial t} + v\mu \frac{\partial F}{\partial Z} - \epsilon\Omega \frac{\partial F}{\partial \phi} = \mathcal{S}(x, p, t) + \frac{1}{p^2} \frac{\partial}{\partial x_\sigma} (p^2 D_{\sigma\nu} \frac{\partial F}{\partial x_\nu}), \quad (2.38)$$

with the **Fokker-Planck coefficients**

$$D_{\sigma\nu} = \int_0^t ds \langle \bar{g}_{x_\sigma}(t) \bar{g}_{x_\nu}(s) \rangle. \quad (2.39)$$

The bar notation indicates that the force fields have to be calculated along the unperturbed orbit of the particles, given by combining Eqs. (2.37) with Eqs. (2.24),

$$\begin{aligned} \bar{x} &= x_0 - \frac{v\sqrt{1-\mu^2}}{\epsilon\Omega} \sin \phi' \\ \bar{y} &= y_0 + \frac{v\sqrt{1-\mu^2}}{\epsilon\Omega} \cos \phi' \\ \bar{z} &\equiv z' = z_0 + v\mu(s - t) \\ \bar{p} &\equiv p' = p \\ \bar{\mu} &\equiv \mu' = \mu \\ \bar{\phi} &\equiv \phi' = \phi_0 - \epsilon\Omega(s - t). \end{aligned} \quad (2.40)$$

To further proceed on the computation of the Fokker-Planck coefficients one needs to first determine the fluctuations on the unperturbed orbits. This is usually done using the Fourier representation of the fluctuating electromagnetic fields and approximating the true orbit x with the unperturbed one \bar{x}

$$\delta \mathbf{E}(x, t) \simeq \int d^3k \mathbf{E}(k, t) e^{ik \cdot \bar{x}(t)}, \quad (2.41)$$

$$\delta \mathbf{B}(x, t) \simeq \int d^3k \mathbf{B}(k, t) e^{ik \cdot \bar{x}(t)}. \quad (2.42)$$

Additional reductions require some assumptions on the properties of the plasma turbulence. In the test-wave approach the Fourier transforms are represented as superpositions of N individual plasma modes of frequencies $\omega = \omega_j(\mathbf{k}) = \Re\omega_j -$

$i\Gamma_j$, with Γ_j the damping of the wave, so that

$$\mathbf{B}(\mathbf{k}, t) = \sum_{j=1}^N \mathbf{B}^j(\mathbf{k}) e^{-i\omega_j t}, \quad (2.43)$$

$$\mathbf{E}(\mathbf{k}, t) = \sum_{j=1}^N \mathbf{E}^j(\mathbf{k}) e^{-i\omega_j t}; \quad (2.44)$$

the two coefficients being related by Maxwell's induction law:

$$\mathbf{B}^j(\mathbf{k}) = \frac{c}{\omega_j} \mathbf{k} \times \mathbf{E}^j(\mathbf{k}). \quad (2.45)$$

As a consequence of this representation the magnetic correlation tensor becomes

$$P_{\alpha\beta}(\mathbf{k}, \xi) = \sum_{j=1}^N P_{\alpha\beta}^j(\mathbf{k}) e^{i\omega_j \xi}, \quad P_{\alpha\beta}^j(\mathbf{k}) = \langle \mathbf{B}_\alpha^j(\mathbf{k}) \mathbf{B}_\beta^{j*}(\mathbf{k}_s) \rangle \delta(\mathbf{k} - \mathbf{k}_s), \quad (2.46)$$

where B_α^j denotes the Cartesian components of the fluctuating magnetic field $\delta\mathbf{B}$ of the j -th wave, and the magnetic energy density in wave component j is given by the trace

$$(\delta B^j)^2 = \int d^3k \left(P_{11}^j(\mathbf{k}) + P_{22}^j(\mathbf{k}) + P_{33}^j(\mathbf{k}) \right) \quad (2.47)$$

of the coefficients of the magnetic correlation tensor. Similar relations hold for the correlation tensor involving the electric field and the mixed correlation tensors involving the electric and the magnetic field. These equations contain the coupling of the cosmic rays particles with the background plasma: the properties of the possible plasma modes of the electromagnetic turbulence affect the cosmic rays through the Fokker-Planck equation. Using Eq. (2.46) and making the assumption that the Fourier components of the different plasma modes are uncorrelated one can compute the Fokker-Planck coefficients. The calculation of the Fokker-Planck coefficients then is straightforward but lengthy. From the time integrated Fourier transform of the correlation function (Eq. (2.39)) that connects the position of the particle at different times in the turbulent bath, one obtains the resonance function

$$\mathcal{R}_j(\mathbf{k}, \omega_j) = \frac{1}{2\pi} \int_{-\infty}^{+\infty} d\tau e^{i(k_{\parallel} v \mu - \Re\omega_j + n\Omega)\tau}, \quad (2.48)$$

with $\mu = v_{\parallel}/v$, and \parallel indicates the uniform magnetic field direction, as before. In standard quasi linear theory this resonance becomes a Dirac-function

$$\mathcal{R}_j(\mathbf{k}, \omega_j) \propto \delta(k_{\parallel} v \mu - \Re\omega_j + n\Omega). \quad (2.49)$$

For $n \neq 0$ Eq. (2.49) describes gyroresonances, i.e. the **resonant** interaction of wave and particle. Usually harmonics $n = (-1, 1)$ dominate the interaction and are associated with wave polarization (left- and right-handed respectively). For $n = 0$ Eq. (2.49) describes the Landau resonance, also called transit-time damping (TTD) resonance, which results from the interaction of the particle magnetic momentum with the magnetic gradient parallel to the background magnetic field.

To progress further, the plasma wave spectrum needs to be specified and some

assumptions made on the magnetic fluctuation tensor, possibly relying on observations. In-situ observations in the interplanetary medium suggests a Kolmogorov-type power law dependence [9, 39] of the power spectrum

$$P_{\alpha\beta}^j(\mathbf{k}) \propto k^{-q} \quad (2.50)$$

with $1 \leq q \leq 2$ in a finite wavevector range $k_1 \leq k \leq k_2$.

Low-frequency Alfvén waves and magnetosonic waves are of most interest due to their short growth times in cosmic plasmas. In the simplified assumption that the particle distribution function is only slowly varying in space (“diffusion approximation”) and that the scattering time is shorter than any other relevant time-scale of the system, the distribution function can be assumed to be spatially isotropic and uniform in momentum space, namely $F(x, \mathbf{p}, t) = F(p, t)$. In these conditions and in the absence of any source or sink, the Fokker-Planck equation 2.38 reduces to the most common momentum diffusion equation

$$\frac{\partial F(p, t)}{\partial t} = \frac{1}{p^2} \frac{\partial}{\partial p} \left[p^2 D_{pp} \frac{\partial F(p, t)}{\partial p} \right]. \quad (2.51)$$

The momentum diffusion coefficient can be then evaluated, for e.g. isotropic Alfvén turbulence characterised by a magnetic correlation tensor of the form 2.50, as

$$D_{pp} \approx \left(\frac{\delta B}{B_0} \right)^2 \frac{\beta_A^2 p^2 c}{r_g^{2-q} \lambda_{\max}^{q-1}} \propto p^q, \quad (2.52)$$

where $r_g = pc/|q|B_0$, $\lambda_{\max} = 2\pi/k_1$ and $\beta_A = B_0/\sqrt{4\pi mnc^2}$ the normalised Alfvén velocity [153]. This result is valid for particles with gyroradii smaller than the correlation length of the field, while the diffusion coefficient of particles with larger r_g is basically independent of their momentum because they interact with the entire spectrum (see [120] and references therein for further details). This finally allows one to find the characteristic timescale of the acceleration process due to stochastic wave-particle interactions

$$t_{\text{acc}} \equiv \frac{p^2}{D_{pp}} \propto \frac{p^{2-q}}{\beta_A^2}. \quad (2.53)$$

Similarly, analogous formulae can be derived in the case of magnetosonic modes.

2.2.2 PIC results: an overview

Numerically, the physics of transport and acceleration in turbulence has long been investigated by following test particles in a synthetic turbulence generated from a sum of plane waves (e.g. [111, 102]) or following test particles in full MHD simulations (e.g. [181, 46, 41]). More recently, kinetic particle-in-cell simulations addressed similar studies (e.g. [191, 189, 190, 42, 188, 43, 178]). While MHD simulations provide a useful representation of the largest length scales with a potentially large dynamic range, PIC simulations offer a description from plasma length scales upward, thus allowing, in particular, a self-consistent treatment of the early injection and acceleration stages.

To the best of our knowledge, Zhdarkin *et al.* [189] conducted the first PIC simulation of driven turbulence in magnetised, collisionless, relativistically hot electron-positron plasmas. The authors reported on the agreement of statistical properties

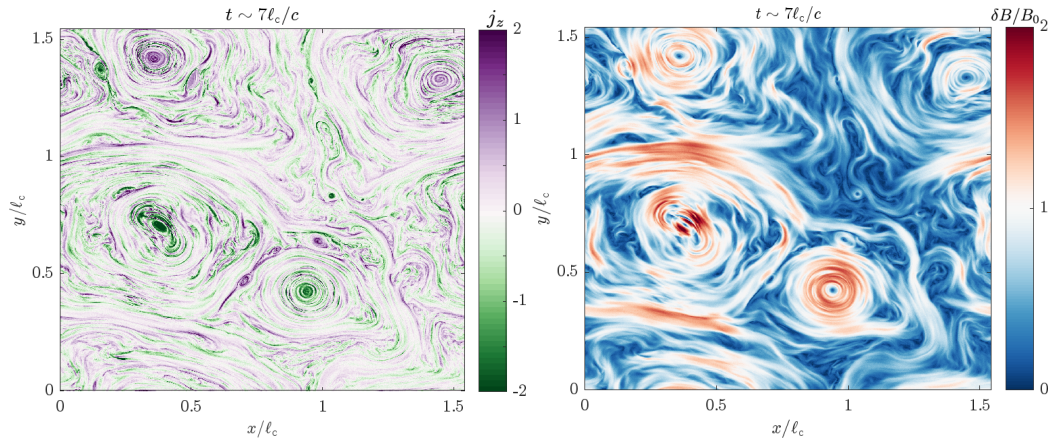


FIGURE 2.7: PIC simulation of periodic turbulence of coherence length $\ell_c \sim 350c/\omega_p$, magnetisation $\sigma \sim 1$ and $\delta B/B_0 \sim 1$ at $t \sim 7\ell_c/c$. Current fluctuations, on the left, showing the formation of intense small scale structures where reconnection likely takes place, characterized by a null turbulent field, as visible on the right. This agrees well with the findings of [43].

of turbulence between the 3D PIC simulations and the classical MHD phenomenology. In a subsequent study [190] they analysed the acceleration process and showed that the efficiency of non-thermal particle acceleration at the hands of turbulence depends on turbulent fluctuating field strength. However, the power-law tail was found to vary with the system size, with disappointing implications for large-scale astrophysical systems. This study was extended to the electron-ion case confirming that non-thermal particle acceleration is efficient for both species in the fully relativistic regime but revealing a lower efficiency for electron acceleration when the initial temperature is decreased to the semirelativistic regime. To produce a hard non-thermal electron radiative signatures, either a high magnetisation or ions with near-relativistic temperature is demanded [188]. An additional word of caution was raised by the authors themselves: the driving of turbulence applying a fluctuating external current density in the form of an oscillating Langevin antenna [159] steadily inputs energy in the system at each time step, hence increasing the fluid internal energy linearly in time. In the absence of energy sinks, energy might pile up and give rise to artificial heating and non-thermal particle acceleration. However, the generation of a power-law particle energy spectrum as a by-product of relativistic turbulence was also observed in a decaying turbulence setting by Comisso and Sironi [42]. The decaying turbulent setup injects energy in the form of magnetic fluctuations, perturbing the initial equilibrium, only at the beginning of the simulation; turbulence starts from these strong magnetic field fluctuations and gradually decays. The simulation domain of [42] was large enough to capture both the MHD cascade at large scales and the kinetic cascade at small scales, and in astrophysically relevant settings it has proven the spectral slope to attain an asymptotic value, independently on the size of the system. It has also been shown that the slope of the energy spectrum gets harder for larger magnetisations and stronger turbulence fluctuations. A detailed analysis of the acceleration process was presented by Comisso and Sironi [43]. The results of our simulation nicely agree with their findings: 1) the presence of small-scale strong fluctuations organised in structures, identified with reconnection plasmoids, within narrow current sheets hosting nonlinear processes (Fig. 2.7); 2) a two-stage acceleration process, first mediated by plasmoid-driven reconnection, which is very efficient in accelerating particles, extracting them from the

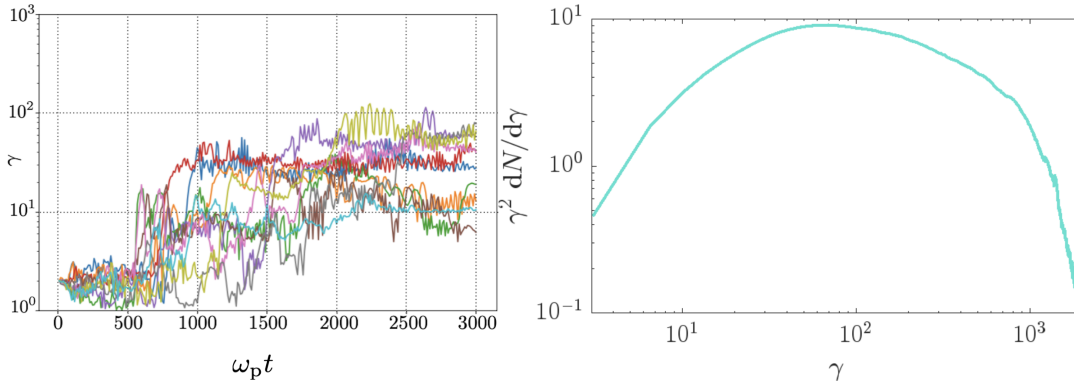


FIGURE 2.8: Temporal evolution of the energy of selected test particles, on the left, showing a first kick in energy due to non-linear effects in narrow current sheets and a slower energisation at later times due to stochastic encounter with turbulent fields. These processes result in a non-thermal spectrum at $t = 2376\omega_p^{-1} \sim 7\ell_c/c$ shown in the right panel. Similar findings were reported in [43].

thermal pool, and further sustained by stochastic acceleration scattering off turbulent fluctuations (Fig. 2.8).

The diffusive nature of non-thermal particle acceleration was first tested by Wong *et al.* [178] (and later in [43]) by measuring the Fokker-Planck diffusion and advection coefficients as a function of the particle energy.

Further investigations to characterize stochastic non-thermal particle acceleration are certainly needed, nevertheless it can be firmly stated that turbulence can contribute to particle acceleration with important applications to astrophysical systems such as PWN, AGN accretion flows, AGN jets and gamma-ray bursts.

2.2.3 Beyond QLT

An important outcome of quasi-linear calculations is the existence of resonant particle-wave interactions which provides possibly fast scattering rates, hence short acceleration timescales. At odds, modern MHD turbulence theories show that Alfvén modes reveal a scale-dependent Goldreich-Sridhar anisotropy [40], and that these intrinsic anisotropies make the pitch-angle scattering due to particle-wave resonances inefficient [141, 182].

The idealized resonance of Eqs. (2.48)-(2.49) derives from the assumption of no damping and uncorrelated plasma waves. It has long been appreciated, however, that there is an actual broadening to some degree due to 1) finite lifetime of turbulent modes (i.e. damping $\Gamma_j \neq 0$) and 2) partial randomization of the pitch angle of the particle. If these two effects are taken into account, the resonance function which characterizes the interaction between the particles and the waves is not anymore the Dirac peak in the infinite discrete set of resonances of the standard quasilinear theory.

Concerning 1), if a finite lifetime is assigned to the linear eigenmodes with $\Gamma_j > 0$, the resonance function takes the Breit-Wigner form

$$\mathcal{R}_j = \frac{1}{\pi} \frac{\Gamma_j}{(k_{\parallel} v \mu - \Re \omega_j + n\Omega)^2 + \Gamma_j^2} \quad (2.54)$$

whose finite width is determined by Γ_j . The resonance broadening associated with the finite lifetime of the modes is particularly important for an anisotropic cascade of

Alfvén waves. Indeed, as shown in [51], this effect increase the scattering efficiency of the Alfvénic cascade at low $r_g k_{\min}$.

Regarding 2), the randomization of the pitch-angle cosine allows one to make the expansion

$$\langle e^{i(k_{\parallel}\mu - \Re\omega_j + n\Omega)\Delta t} \rangle \simeq e^{i(k_{\parallel}\langle\mu\rangle - \Re\omega_j + n\Omega)\Delta t - \frac{1}{2}k_{\parallel}^2\langle\Delta\mu^2\rangle\Delta t^2}, \quad (2.55)$$

and the resonance function becomes

$$\mathcal{R}_j = \frac{e^{-\frac{(k_{\parallel}\langle\mu\rangle - \Re\omega_j + n\Omega)^2}{2k_{\parallel}^2\langle\Delta\mu^2\rangle}}}{(2\pi k_{\parallel}^2\langle\Delta\mu^2\rangle)^{1/2}} \quad (2.56)$$

The effect of the resonance broadening that results from the partial randomization of the pitch angle depends on the type of waves considered: it is quite narrow for Alfvén waves, as they are not characterised by a magnetic perturbation parallel to the mean magnetic field; it prevails on gyroresonances for an anisotropic cascade of slow waves; fast modes generally preserve resonant interactions, the resonance broadening effect associated to the pitch angle only prevails for small longitudinal phase velocity of the wave for an isotropic cascade, and it becomes comparable to gyroresonances only for particles with $r_g k_{\min} \ll 1$ (see [51] for a detailed discussion).

When resonant broadening is taken into account, it can be shown that all scales above the gyroradius equally contribute to the diffusion coefficient, hence restoring the momentum diffusion dependency $D_{pp} \propto p^2$ up to logarithmic corrections [51], in line with the numerical work of [178].

In general, whether collisionless turbulence can be realistically described as a sum of waves is a long-standing debate [74]. MHD seems to be better represented by a collection of structures rather than linear uncorrelated waves, as revealed by in-situ measurements of the solar wind and numerical simulations. In addition, if one is interested in the large-amplitude turbulent regime, in which the turbulent fluctuations become as strong as the coherent field as it is the case for astrophysical turbulent environments, the waves can no longer be considered as uncorrelated and non-interacting [106]. Essentially, a strong turbulent environment acts on the particles' propagation more as velocity and magnetic fluctuations than as waves contributing to (non-resonant) wave-particle interactions. Yet, a definite theoretical model that connects the particle acceleration with the characteristic of a turbulent bath as observed in numerical experiments is still lacking. Some progress has recently been made on particle acceleration in strong turbulence considering non-resonant interaction with velocity structures in [89, 90]. Both approaches rely on a formalism that connects the source of energy gain and losses to the non-inertial nature of the frame where the electric field vanishes. The first explored the isotropic interaction between a particle and a random flow characterised by a single length scale, which can be representative of a turbulent scenario where the particles gyroradius is comparable or greater than the coherence scale of the turbulence. The second [90] focused on a regime $r_g \ll \ell_c$ of the turbulence bath, where ℓ_c denotes the coherence scale of the turbulent power spectrum, i.e. the length scale on which most of the turbulent power lies. This way, particles experience the anisotropy imposed by the magnetic field fluctuations and are influenced by all modes at scales larger than r_g . This so-called non-resonant wave-particle interaction will be detailed in the following.

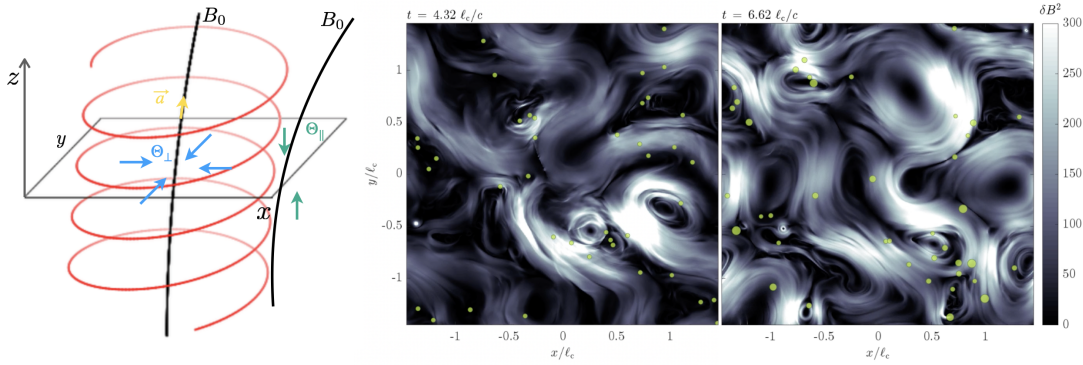


FIGURE 2.9: Left: Schematic representation of the shear (teal), compression (blue) and acceleration (yellow) of the field line which cause the particle acceleration in the non-resonant model. Center and right: Magnetic turbulent fluctuations and some test particles, as green circles, at two different times in a 2D-PIC driven simulation of turbulence (more details in Chapter 4). The size of each circle is proportional to the energy of the corresponding particle. The energisation that is seen between the two panels results from the aforementioned non-resonant heating processes.

2.2.4 Non-resonant acceleration in turbulence

Since a sum of linear plasma eigenmodes may not provide a faithful description of the strong turbulence and gyroresonant wave-particle interactions may be removed by anisotropy effects, non-resonant processes have been recently investigated as an alternative, possibly more efficient, source of energy gain. On a general level the problem at hand is that of the interaction of a charged particle with the fluctuating electric fields associated with the plasma velocity fluctuations through the ideal Ohm's law. The particles can then gain energy as they experience the compression, the shear, the vorticity and the acceleration of the medium (see Fig. 2.9). In the local rest frame where the electric field vanishes, the particle spatially diffuses by pitch-angle scattering at hands of the Lorentz force, but its energy gain is determined by the inertial force associated to the change of velocity of the fluid which determines its local frame. Because of the nonuniform velocity field, there is not a global reference frame in which the electric field vanishes everywhere, a property which ensures the particle energisation. The original idea of [89] is hence to track the particle momentum in a sequence of comoving non inertial frames \mathcal{R}_E , defined along the particle trajectories, in which the electric field is exactly zero. In general relativistic kinetics, space variables and momenta are commonly described in two different frames [174, 175]. The motion of the particle in physical space is hence tracked in the lab-frame, while its evolution in momentum space is described in the \mathcal{R}_E frame. The two frames are related by the tetrad which connects lab-frame quantities to quantities evaluated in \mathcal{R}_E , which hence provides the instantaneous Lorentz transform between the twos. The choice of this tetrad is not unique. In the application of the model to relativistic turbulence, two directions essentially capture the physics of particle acceleration: the direction of the magnetic field which scatter particles, and the four-velocity of the non-inertial frame \mathcal{R}_E in the lab frame, whose change in time results in the acceleration of particles. It is thus useful to expand the tetrad along the two aforementioned directions plus their orthogonal plane. Once decomposing the equation of motion for the particle in the frame \mathcal{R}_E on this tetrad, since by construction the temporal part of the Maxwell field strength tensor vanishes (null electric-field), the variation in the particle Lorentz factor is possible only

if there is a variation in the velocity of the \mathcal{R}_E -frame. Note that, i) assuming that ideal MHD is a good approximation, the local plasma rest frame coincides with the frame where the electric field vanishes. The second assumption made at this point is that ii), since the influence of turbulent fluctuations on scales smaller than r_g on the particles trajectories can be neglected, as they carry a small fraction of the magnetic power, particle energisation is associated to interactions with moving magnetised structures on scales larger than their gyroradius. Formally this means that the velocity of the frame \mathcal{R}_E , i.e. $\beta_E = (\mathbf{E}_l \times \mathbf{B}_l) / B_l^2$, where E_l, B_l contain the coherent fields and the turbulent-field perturbations on scales $l > r_g$, differs from the effective one by $\mathcal{O}(\delta B_l^2 / B^2)$. The model hence do not capture the effects of higher order in r_g / ℓ_c or nonideal contributions to Ohm's law. Finally, in order to simplify the calculations and directly identify the processes which govern the momentum history of the particle, the last assumption considers that iii) particles undergo local gyromotion around the perturbed field lines. Hence, averaging over a gyroperiod, the gradients in the plane orthogonal to \mathbf{u}_E and \mathbf{B}_l do not change significantly.

We report now the salient features of the calculations outlined above, while the reader is redirected to [89, 90] for a detailed analysis.

In the comoving \mathcal{R}_E frame,

$$\mathbf{B}' = \gamma_E \mathbf{B} - \mathbf{u}_E \times \mathbf{E}, \quad \mathbf{B} = \gamma_E \mathbf{B}' \quad (2.57)$$

$$\mathbf{E}' = 0, \quad \mathbf{E} = -\mathbf{u}_E \times \mathbf{B}' \quad (2.58)$$

with $\gamma_E = B / B' = B / \sqrt{B^2 - E^2}$ and $\mathbf{u}_E = \gamma_E \beta_E$ the Lorentz factor of the frame in \mathcal{R}_E and the four-velocity in the lab frame in units of c . This tacitly assumed that the frame \mathcal{R}_E exists (i), meaning that the Lorentz invariant quantity $B^2 - E^2$ is always positive, which is satisfied in the MHD approximation. Primed (unprimed) quantities are then computed in the $|_E$ frame (laboratory frame) where latin (a, b, \dots) (greek (α, β, \dots)) indices are used. The four-velocity of the particle in the locally inertial frame \mathcal{R}_E , u'^a evolves, in terms of proper time $d\tau = dt' / \gamma'$, as

$$\frac{1}{c} \frac{du'^a}{d\tau} = \frac{q}{m} F_b^a u'^b - \hat{\Gamma}_{bc}^a u'^b u'^c, \quad (2.59)$$

with F^{ab} the Maxwell field strength tensor in \mathcal{R}_E which is hence purely magnetic ($F_b^0 = 0$). The connection between the two frames is expressed by

$$\hat{\Gamma}_{bc}^a = -\varepsilon_b^\beta \varepsilon_c^\gamma \frac{\partial}{\partial x^\gamma} \varepsilon_\beta^a \quad (2.60)$$

where we choose the tetrad

$$\varepsilon_a^\mu = \{u_E^\mu, b^\mu, e_2^\mu, e_3^\mu\} \quad (2.61)$$

$$\varepsilon_\mu^a = \{u_{E\mu}, b_\mu, e_{2\mu}, e_{3\mu}\}, \quad (2.62)$$

with $e_{2,3}^\mu$ in the plane orthogonal to both u_E^μ and b_μ . This choice is such that the magnetic four-vector in \mathcal{R}_E is $B^a = \varepsilon_\mu^a B^\mu = \{0, B', 0, 0\}$ and the four-velocity of the particle is $u^a = \varepsilon_\mu^a u^\mu = \{\gamma', u'_\parallel, u'_2, u'_3\}$. The space-like four vector b^μ is defined as

$$b^\mu = \frac{B^\mu}{\sqrt{B^\alpha B_\alpha}}, \quad \text{with } B^\mu = -{}^*F_\nu^\mu u_E^\nu = \{0, \mathbf{B}'\}. \quad (2.63)$$

The dual strength tensor is defined as ${}^*F^{\mu\nu} = \frac{1}{2} \varepsilon^{\mu\nu\alpha\beta} F_{\alpha\beta}$, with $\varepsilon^{0123} = -1$.

The Lorentz-force in the comoving frame is purely magnetic and thus it does not contribute to the evolution of γ' , where only the derivative of the velocity field u_E enters. The latter can be decomposed as:

$$\partial_\beta u_E^\alpha = \sigma_{E\beta}^\alpha + \omega_{E\beta}^\alpha + \frac{1}{3}\Theta_E h_{E\beta}^\alpha + a_{E\beta}^\alpha, \quad (2.64)$$

in terms of the shear tensor $\sigma_{E\beta}^\alpha$, the vorticity tensor $\omega_{E\beta}^\alpha$, the expansion scalar Θ_E and the acceleration tensor $a_{E\beta}^\alpha$, defined by

$$h_E^{\alpha\beta} = \eta^{\alpha\beta} + u_E^\alpha u_E^\beta, \quad (2.65)$$

$$\sigma_{E\beta}^\alpha = \frac{1}{2}h_E^{\alpha\mu} h_E^{\beta\nu} (\partial_\nu u_{E\mu} + \partial_\mu u_{E\nu}) - \frac{1}{3}\Theta_E h_E^{\alpha\beta}, \quad (2.66)$$

$$\omega_{E\beta}^\alpha = \frac{1}{2}h_E^{\alpha\mu} h_E^{\beta\nu} (\partial_\nu u_{E\mu} - \partial_\mu u_{E\nu}), \quad (2.67)$$

$$\Theta_{\parallel} = b^\alpha b^\beta \partial_\alpha u_{E\beta}, \quad (2.68)$$

$$\Theta_{\perp} = (\eta^{\alpha\beta} - b^\alpha b^\beta) \partial_\alpha u_{E\beta}, \quad (2.69)$$

$$\Theta_E \equiv \partial_\alpha u_E^\alpha = \Theta_{\parallel} + \Theta_{\perp}, \quad (2.70)$$

$$a_{E\beta}^\alpha = -u_E^\beta u_E^\mu \partial_\mu u_E^\alpha. \quad (2.71)$$

The evolution of γ' is given by Eq. (2.59)

$$\frac{1}{c} \frac{d\gamma'}{d\tau} = -\gamma' u'_{\parallel} b^\beta u_E^\gamma \partial_\gamma u_{E\beta} - u'_{\parallel}{}^2 b^\beta b^\gamma \partial_\gamma u_{E\beta} - u_2'^2 e_2^\beta e_2^\gamma \partial_\gamma u_{E\beta} - u_3'^2 e_3^\beta e_3^\gamma \partial_\gamma u_{E\beta}, \quad (2.72)$$

where crossed terms including only one power of u_2' and u_3' have been neglected. That is because turbulent modes of wavelengths much smaller than the gyroradius of the particles weakly contribute to particle energisation. Hence, retaining only the contributions of modes of scales $l \gtrsim r_g$ (ii), the gradients can be approximated to their average over the gyroperiod of the particles and we assume that on such short timescales $\langle u_2' \rangle = \langle u_3' \rangle = 0$ but $\langle u_2'^2 \rangle = \langle u_3'^2 \rangle = u_{\perp}^2/2$ (iii). In this approximation, Eq. (2.72) can be eventually recast into [90]

$$\frac{1}{c} \frac{d\gamma'}{d\tau} = -\gamma' u'_{\parallel} \mathbf{a}_E \cdot \mathbf{b} - u'_{\parallel}{}^2 \Theta_{\parallel} - \frac{1}{2} u_{\perp}^2 \Theta_{\perp}, \quad (2.73)$$

and the mean field direction \mathbf{b} has to be interpreted now as the direction of the magnetic field composed of the coherent field, \mathbf{B}_0 , and of all modes on scales larger than the gyroradius making up the turbulent-field perturbations $\delta\mathbf{B}_{l>r_g}$.

The components of the shear of the field line four-velocity parallel and perpendicular to the magnetic field line are represented by Θ_{\parallel} and Θ_{\perp} . The first term in Eq. (2.73), proportional to \mathbf{a}_E , describes the effective gravity the particle suffers in the direction of the magnetic field line as the field line accelerates or decelerates. The second term, proportional to Θ_{\parallel} , can be related to the projection on \mathbf{E} of the drift velocity, due to the curvature of the field line. It can be described as a form of shear acceleration along the magnetic field line and formally corresponds to the curvature drift contribution, or as a Fermi type-B interaction in the original Fermi formulation. The third, proportional to Θ_{\perp} , derives from the shear of the field line velocity field in the plane transverse to the magnetic field line. It is related to the compression or expansion in the plane transverse to the field line, it thus characterizes the mirror force, or a Fermi type-A interaction, corresponding to the grad-B drift

term.

In contrast to the original Fermi scenario, particles gain or lose energy in a non-stochastic manner in every region where the gradients Θ_{\parallel} and Θ_{\perp} are different from zero. Energy gain or losses are related to the sign of the terms instead of to the head-on or tail-on angles of collisions. The force term associated to the curvature of the field lines leads to an energy gain if negative and viceversa. For a transverse compression, the mirror force results in an energy gain for the particle tied to the magnetic field through its orbit, while a transverse expansion draws energy from the particle.

It is possible to show (see [90] for further details) that the two gradients responsible for acceleration are related to the temporal evolution of the magnetic energy density, meaning that the net energy gain can be related to the net heating of the plasma through large-scale motions; the particles that populate the non-thermal power law are those that have had the chance to encounter more zones of heating than the rest of the population. Yet, these sites have been proven numerically to be sparsely localised and highly intermittent, so that the filling fraction of these regions in the overall turbulent volume plays an important role.

Chapter 3

Particle-in-cell (PIC) kinetic simulations

Particle-in-cell methods refer to a specific technique used to solve a certain class of partial differential equations. PIC techniques were first used as early as 1955 and gained popularity in the late '50s-early '60s as applied to plasma simulations by Buneman [27] and Dawson [48]. The PIC method consists of coupling a Lagrangian description of individual charged particles in continuous phase space with an Eulerian description of the moments of the distribution and of the electromagnetic fields the particles are subjected to. At each iteration time the charge and current density are projected on the grid nodes starting from the particle position. This allows the electromagnetic fields to be computed from the Maxwell's equations. The fields are then interpolated again on the particle position in order to advance them through the equation of motion (Fig. 3.1).

The (collisionless) Vlasov-Maxwell equation for the plasma species, s ,

$$\partial_t f_s + \frac{\mathbf{p}}{m_s \gamma} \cdot \nabla f_s + q_s \left(\mathbf{E} + \frac{\mathbf{p}}{m_s \gamma} \times \mathbf{B} \right) \cdot \nabla_{\mathbf{p}} f_s = 0 \quad (3.1)$$

where f_s , m_s , q_s , γ , \mathbf{p} , \mathbf{E} , \mathbf{B} , denote the particle distribution function, mass, charge, Lorentz factor, momentum, electric and magnetic field, is hence coupled with Maxwell's equations

$$\nabla \cdot \mathbf{E} = 4\pi\rho \quad (3.2)$$

$$\nabla \cdot \mathbf{B} = 0 \quad (3.3)$$

$$\nabla \times \mathbf{B} = 4\pi\mathbf{J} + \partial_t \mathbf{E} \quad (3.4)$$

$$\nabla \times \mathbf{E} = -\partial_t \mathbf{B} \quad (3.5)$$

being $\rho(t, \mathbf{x}) = \sum_s \int d\mathbf{p} f_s(\mathbf{x}, \mathbf{p}, t)$ and $\mathbf{J}(t, \mathbf{x}) = \sum_s q_s \int d\mathbf{p} \frac{\mathbf{p}}{m_s \gamma} f_s(\mathbf{x}, \mathbf{p}, t)$. Everything is written in CGS Gaussian units with $c = 1$.

Note that the collisionless Vlasov-Maxwell description of the plasma provides a set of natural units for length-scales (c/ω_p), timescales (ω_p^{-1}) and electromagnetic fields ($m_s c \omega_p / q_s$), based on the plasma frequency $\omega_p = \sqrt{4\pi n e^2 / m}$, introduced before. Direct integration of the Vlasov equation 3.1, as a partial differential equation in $N_x \otimes N_p$ phase space, if N_x and N_p are the position and momentum degrees of freedom, has tremendous computational cost.

The PIC ansatz consists in representing the distribution function as an ensemble of "macro-particles", s , for each specie α , each characterised by a position, impulse,

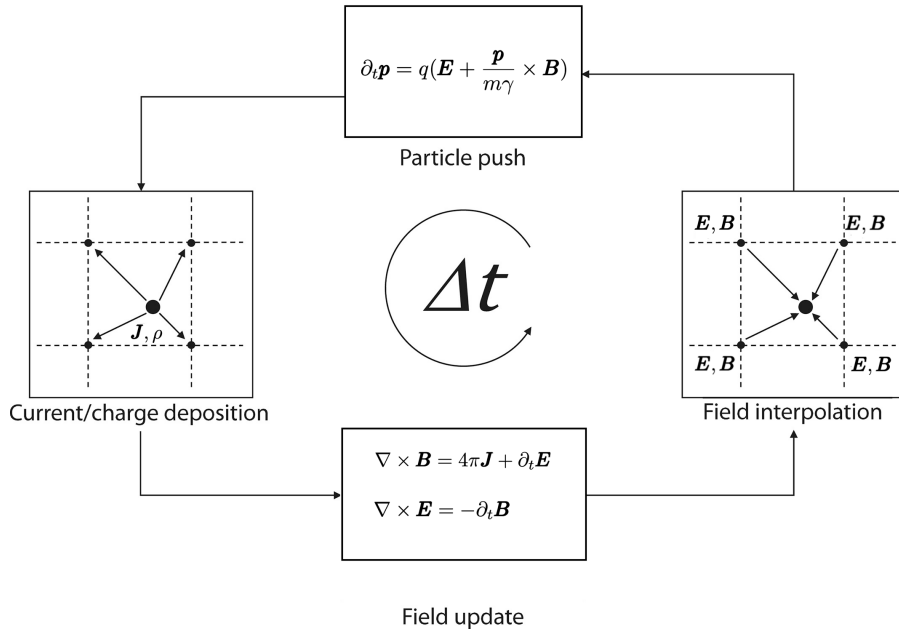


FIGURE 3.1: Schematic time iterations of PIC-methods. Adapted from [6].

and statistical weight w_α :

$$f_s(\mathbf{x}, \mathbf{p}, t) = \sum_{\alpha=1}^{N_s} w_\alpha \mathcal{S}(\mathbf{x} - \mathbf{x}_\alpha(t)) \delta(\mathbf{p} - \mathbf{p}_\alpha(t)) \quad (3.6)$$

The shape function $\mathcal{S}(\mathbf{x} - \mathbf{x}_\alpha(t))$ is symmetric and satisfies $\int \mathcal{S}(\mathbf{x} - \mathbf{x}_\alpha(t)) d\mathbf{x} = 1$, with \mathbf{x} the coordinates of the grid and \mathbf{x}_α the location of the macro-particle. The most commonly adopted shapes are spline functions of order $n \leq 4$. Note that the shape functions should extend on a sufficient number of grid points to minimize the numerical noise and avoid numerical heating, but not too many not to be too computationally costly. The Vlasov equation is then integrated by solving the trajectories of these so-called macro-particles, which reduces to solve for all α

$$\frac{d\mathbf{p}_\alpha}{dt} = q_\alpha \left(\mathbf{E}_\alpha + \frac{\mathbf{p}_\alpha}{m_\alpha \gamma} \times \mathbf{B}_\alpha \right), \quad (3.7)$$

$$\frac{d\mathbf{x}_\alpha}{dt} = \frac{\mathbf{p}_\alpha}{\gamma} \quad (3.8)$$

with the e.m. fields interpolated on the particle positions

$$\mathbf{E}_\alpha = \int d\mathbf{x} \mathbf{E}(\mathbf{x}) \mathcal{S}(\mathbf{x} - \mathbf{x}_\alpha(t)), \quad (3.9)$$

and similarly for \mathbf{B}_α . Particles are advanced solving the equation of motion 3.8. The most common method is the **Boris leap-frog pusher** [20]:

$$\frac{\mathbf{x}^{n+1} - \mathbf{x}^n}{\Delta t} = \frac{\mathbf{p}^{n+1/2}}{m_\alpha \gamma^{n+1/2}} \quad (3.10)$$

$$\frac{\mathbf{p}^{n+1/2} - \mathbf{p}^{n-1/2}}{\Delta t} = q_\alpha \left[\mathbf{E}^n + \frac{\mathbf{p}^{n+1/2} + \mathbf{p}^{n-1/2}}{2m_\alpha \gamma^n} \times \frac{\mathbf{B}^{n+1/2} + \mathbf{B}^{n-1/2}}{2} \right], \quad (3.11)$$

where the subscript $n + 1$ refers to updated quantities computed at time step $t_{n+1} = t_n + \Delta t$.

If the charge is conserved (i.e $\partial_t \rho + \nabla \cdot \mathbf{J} = 0$), and if at time $t = 0$ Poisson's and Gauss' equations are satisfied, only Maxwell-Ampère's and Maxwell-Faraday's equations need to be solved. The most common adopted charge-conserving current scheme is **Esirkepov's scheme** [56]:

$$(J_{x,\alpha})_{i+1/2,j,k}^{n+1/2} = (J_{x,p})_{i-1/2,j,k}^{n+1/2} + q_\alpha w_\alpha \frac{\Delta x}{\Delta t} (W_x)_{i+1/2,j,k}^{n+1/2} \quad (3.12)$$

$$(J_{y,\alpha})_{i,j+1/2,k}^{n+1/2} = (J_{y,p})_{i,j-1/2,k}^{n+1/2} + q_\alpha w_\alpha \frac{\Delta y}{\Delta t} (W_y)_{i,j+1/2,k}^{n+1/2} \quad (3.13)$$

$$(J_{z,\alpha})_{i,j,k+1/2}^{n+1/2} = (J_{z,p})_{i,j,k-1/2}^{n+1/2} + q_\alpha w_\alpha \frac{\Delta z}{\Delta t} (W_z)_{i,j,k+1/2}^{n+1/2} \quad (3.14)$$

where the vector W_α is related to the charge density at two consecutive time steps,

$$(W_x)_{i,j,k} + (W_y)_{i,j,k} + (W_z)_{i,j,k} = \frac{\rho_{i,j,k}^{n+1} - \rho_{i,j,k}^n}{\sum_\alpha q_\alpha} \quad (3.15)$$

$$= \mathcal{S}_{i,j,k}(x + dx, y + dy, z + dz) - \mathcal{S}_{i,j,k}(x, y, z), \quad (3.16)$$

with $(x + dx, y + dy, z + dz)$ the shift of the particle due to the motion at time $n + 1$. This vector can be written in a compact form [166] as

$$\mathbf{W} = \sum_{r=1}^8 c^r \mathcal{S}_r, \quad (3.17)$$

with the \mathcal{S}_j functions defined as

$$\mathcal{S}_1 = \mathcal{S}(x, y, z), \mathcal{S}_8 = \mathcal{S}(x + dx, y + dy, z + dz) \quad (3.18)$$

$$\mathcal{S}_2 = \mathcal{S}(x + dx, y, z), \mathcal{S}_3 = \mathcal{S}(x, y + dy, z), \mathcal{S}_4 = \mathcal{S}(x, y, z + dz) \quad (3.19)$$

$$\mathcal{S}_5 = \mathcal{S}(x, y + dy, z + dz), \mathcal{S}_6 = \mathcal{S}(x + dx, y, z + dz), \mathcal{S}_7 = \mathcal{S}(x + dx, y + dy, z) \quad (3.20)$$

and

$$c^r = \begin{pmatrix} -1/3 \\ -1/3 \\ -1/3 \end{pmatrix}, \begin{pmatrix} 1/3 \\ -1/6 \\ -1/6 \end{pmatrix}, \begin{pmatrix} -1/6 \\ 1/3 \\ -1/6 \end{pmatrix}, \begin{pmatrix} -1/6 \\ -1/6 \\ 1/3 \end{pmatrix}, \begin{pmatrix} -1/3 \\ 1/6 \\ 1/6 \end{pmatrix}, \begin{pmatrix} 1/6 \\ -1/3 \\ 1/6 \end{pmatrix}, \begin{pmatrix} 1/6 \\ 1/6 \\ -1/3 \end{pmatrix}, \begin{pmatrix} 1/3 \\ 1/3 \\ 1/3 \end{pmatrix}.$$

The knowledge of the current (Eqs. (3.12)-(3.14)) is necessary to compute the electric field in Maxwell-Ampère's equation. That is solved commonly through a finite difference time domain integration (FDTD)(see Fig. 3.2 for a schematic representation). The most popular FDTD scheme is the Yee scheme [184]. As an example, let us restrict to a two dimensional plasma in the $x - y$ plane and to transverse magnetic

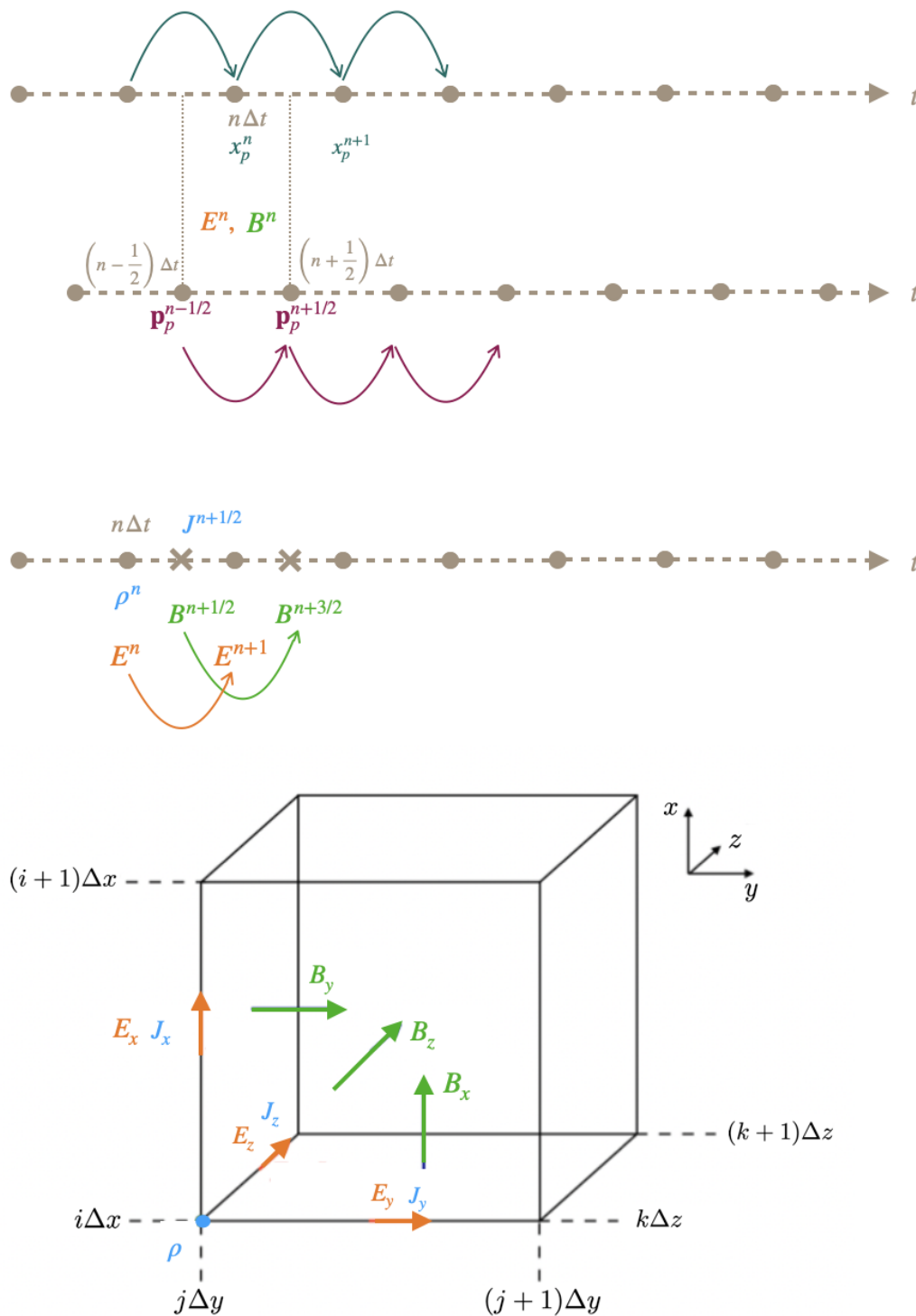


FIGURE 3.2: Schematic representation of the PIC simulation lattice for solving Maxwell's equations with the finite-difference time-domain method.

modes which consist of (E_x, E_y, B_z) . Maxwell's equations are then solved as:

$$\frac{(B_z)_{i,j}^{n+1/2} - (B_z)_{i,j}^{n-1/2}}{\Delta t} = -\frac{(E_y)_{i+1/2,j}^n - (E_y)_{i-1/2,j}^n}{\Delta x} + \frac{(E_x)_{i,j+1/2}^n - (E_x)_{i,j-1/2}^n}{\Delta y}, \quad (3.21)$$

$$\frac{(E_x)_{i,j+1/2}^{n+1} - (E_x)_{i,j+1/2}^n}{\Delta t} = \frac{(B_z)_{i,j+1}^{n+1/2} - (B_z)_{i,j}^{n+1/2}}{\Delta y} - (J_x)_{i,j+1/2}^{n+1/2}, \quad (3.22)$$

$$\frac{(E_y)_{i+1/2,j}^{n+1} - (E_y)_{i+1/2,j}^n}{\Delta t} = \frac{(B_z)_{i+1,j}^{n+1/2} - (B_z)_{i,j}^{n+1/2}}{\Delta x} - (J_y)_{i+1/2,j}^{n+1/2}. \quad (3.23)$$

Due to the centered space-time differencing and the correlation between temporal and spatial numerical derivatives, the electric and magnetic fields do not share the same grid as the particles but are computed instead on a grid staggered by one-half. Using this scheme the Courant-Friedrichs-Levy (CFL) condition for numerical stability reads

$$\frac{1}{c^2 \Delta t^2} > \sum_j \frac{1}{\Delta x_j^2}, \quad (3.24)$$

meaning that light is not able to cross more than one cell in one time step (in one dimension) which ensures that the scheme is able to access all the information required to form the solution. Another constraint on the integration time step over space steps comes from the need of resolving the plasma frequency of the system: $\Delta t \lesssim 1.5\omega_p^{-1}$ [17]. Moreover, to avoid numerical instabilities the simulation grid should also resolve the Debye length of the plasma: $\Delta x \lesssim \lambda_{D_e} = \sqrt{k_B T / 4\pi n q^2}$.

In general PIC codes exhibit numerical artifacts due to their mixing of a Lagrangian framework associated to the particles and the Eulerian description employed for the fields. All the more so if the plasma is drifting at relativistic speeds. Since we have been interested in relativistic plasma, we present in the following sections a few prescriptions that allow to get rid of, or reduce, some numerical spurious modes which arise in this regime.

3.1 PIC simulations of relativistic plasmas

The FDTD solver is subject to numerical dispersion as the numerical light wave velocity is found to depend on its wavenumber orientation. In particular the light wave velocity is smaller than c with increasing wavenumbers, as shown in the top left panel of Fig. 3.3, which displays the normalised phase velocity of the electromagnetic fields for different methods. A small cell size would then be required to keep minimum the error for the large wavenumber range. In contrast, such precaution is not needed for the Cole-Karkkainen method (presented in the following) which is dispersion free along the grid axis enabling numerical simulations with larger cell size than the Yee solver. However, this scheme presents an error on the phase velocity for wave propagating along the diagonal axis. So, for laser studies for instance, according if the laser pulse propagates along the longitudinal or the oblique axis, a different Maxwell solver should be chosen, and more in general the scheme should always be adequate to the problem under study.

The direct consequence of an inexact numerical dispersion relation, is the possible resonance of fast particles with light waves of matching phase velocity. This produces a severe numerical instability known as *numerical Cherenkov instability* [67].

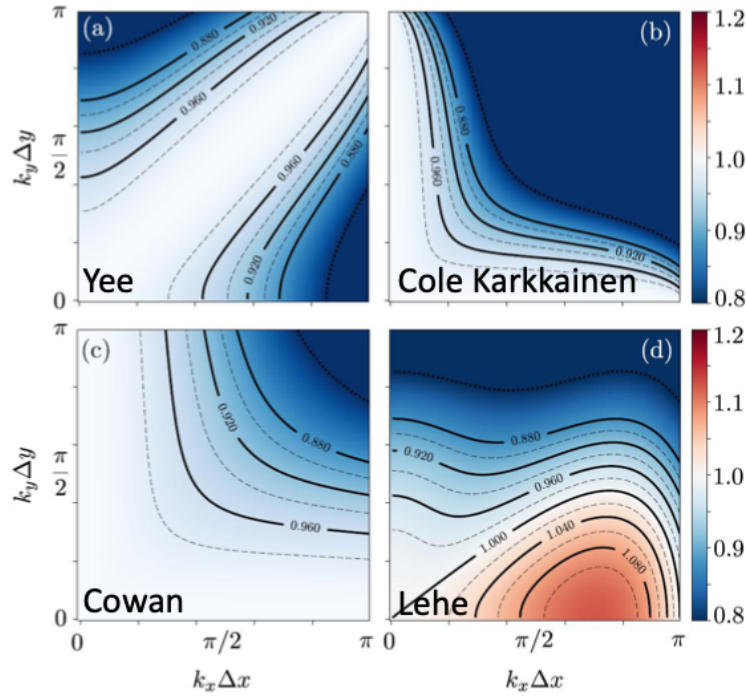


FIGURE 3.3: Normalised phase velocity $v_\phi = \omega/|\mathbf{k}|$ of the numerical electromagnetic fields for a) Yee scheme, b) Cole-Karkkainen scheme, c) Cowan (not discussed) scheme, d) Lehe scheme. Taken from Guillaume Bouchard's lecture @Smilei Workshop - March 2022

Due to spatial and temporal discretisation in the Yee scheme, the actual numerical dispersion relation of electromagnetic waves reads

$$\frac{1}{c^2 \Delta t^2} \sin^2 \left(\frac{\omega \Delta t}{2} \right) = \frac{1}{\Delta x^2} \sin^2 \left(\frac{k_x \Delta x}{2} \right) + \frac{1}{\Delta y^2} \sin^2 \left(\frac{k_y \Delta y}{2} \right) + \frac{1}{\Delta z^2} \sin^2 \left(\frac{k_z \Delta z}{2} \right). \quad (3.25)$$

If we now consider a charged particle traveling e.g. along the x axis with velocity βc , it may resonate and excite modes if its velocity equals the phase velocity of the modes along the x -axis. The modes excited are then those with dispersion relation

$$\frac{1}{c^2 \Delta t^2} \sin^2 \left(\frac{ck_x \Delta t}{2} \right) = \frac{1}{\Delta x^2} \sin^2 \left(\frac{k_x \Delta x}{2} \right) + \frac{1}{\Delta y^2} \sin^2 \left(\frac{k_y \Delta y}{2} \right) + \frac{1}{\Delta z^2} \sin^2 \left(\frac{k_z \Delta z}{2} \right). \quad (3.26)$$

A number of solutions have been proposed to avoid numerical Cherenkov instability: some of them consist in using digital filtering to damp high-energy radiation [70, 71, 169], others modify the discretisation of Maxwell equations [130, 84]. The first class can not be used if the physics at study involves frequencies close to the filtered ones. It is not adapted for instance in laser-wakefield acceleration studies, which involve high-frequency lasers that would be damped along with the Cherenkov radiation. The second set of solutions modify the discretisation of the Maxwell equations to allow an exact dispersion relation for modes aligned with the particles drift, i.e. $c \Delta t = \Delta x$. Yet, it has been shown that this solution triggers other spurious oscillations at the Nyquist frequency $ck = \pi c / \Delta x$ [169]. Consequently, the used prescription has to be accurately chosen accordingly to the problem under study and we present in the following two possibilities we made use of, well-suited for the simulations we have run.

3.1.1 The Lehe Maxwell solver

In the Lehe solver scheme high-frequency radiation is damped using digital filtering [88], and it has been developed in particular for anisotropic grids.

The electric and magnetic fields are defined on the same lattices as in the Yee scheme. For a field $F_{i,j,k}^n$ defined on the nodes of the computational lattice, the discretized leap-frog operators as in the Yee scheme,

$$D_t F_{i,j,k}^{n+1/2} = \frac{F_{i,j,k}^{n+1} - F_{i,j,k}^n}{\Delta t}, \quad (3.27)$$

$$\nabla_x F_{i+1/2,j,k}^n = \frac{F_{i+1,j,k}^n - F_{i,j,k}^n}{\Delta x}, \quad (3.28)$$

(and similarly for ∇_y and ∇_z) enters Maxwell-Ampère equation $D_t \mathbf{E} = \nabla \times \mathbf{B} - 4\pi \mathbf{J}$. Maxwell-Faraday equation is instead modified as $D_t \mathbf{B} = \nabla^* \times \mathbf{E}$, where the modified operator is:

$$\nabla_x^* F_{i+1/2,j,k}^n = \alpha_x \frac{F_{i+1,j,k}^n - F_{i,j,k}^n}{\Delta x} \quad (3.29)$$

$$+ \beta_{x,y} \frac{F_{i+1,j+1,k}^n - F_{i,j+1,k}^n}{\Delta x} \quad (3.30)$$

$$+ \beta_{x,y} \frac{F_{i+1,j-1,k}^n - F_{i,j-1,k}^n}{\Delta x} \quad (3.31)$$

$$+ \beta_{x,z} \frac{F_{i+1,j,k+1}^n - F_{i,j,k+1}^n}{\Delta x} \quad (3.32)$$

$$+ \beta_{x,z} \frac{F_{i+1,j,k-1}^n - F_{i,j,k-1}^n}{\Delta x} \quad (3.33)$$

$$+ \delta_x \frac{F_{i+2,j,k}^n - F_{i-1,j,k}^n}{\Delta x}, \quad (3.34)$$

$$\beta_{y,x} = \beta_{z,x} = 1/8; \beta_{z,y} = \beta_{y,z} = 0; \quad (3.35)$$

$$\beta_{x,y} = \Delta x^2 / (8\Delta y^2); \beta_{x,z} = \Delta x^2 / (8\Delta z^2); \quad (3.36)$$

$$\delta_x = \frac{1}{4} \left(1 - \frac{\Delta x^2}{c^2 \Delta t^2} \sin^2 \left(\frac{c\pi \Delta t}{2\Delta x} \right) \right); \delta_y = \delta_z = 0. \quad (3.37)$$

As long as $c\Delta t \leq \Delta x$, this scheme is CFL-stable. This scheme comes along with the Friedman filtering which replaces the electric field by

$$\mathbf{E}_f^n = \left(1 + \frac{\theta}{2} \right) \mathbf{E}^n - \theta \left(1 - \frac{\theta}{2} \right) \mathbf{E}^{n-1} + \frac{1}{2} (1 - \theta)^2 \bar{\mathbf{E}}^{n-2}, \quad (3.38)$$

with

$$\bar{\mathbf{E}}^{n-2} = \mathbf{E}^{n-2} + \theta \bar{\mathbf{E}}^{n-3}, \quad (3.39)$$

and $0 \leq \theta < 1$ is the chosen damping parameter of the filter. If the Friedman filter is employed, the condition on the maximum time step is somewhat problematic to derive. We hence redirect to [71], and references therein, for further details.

3.1.2 The Cole-Karkkainen Maxwell solver

The Lehe scheme is by construction superluminal because Cherenkov radiation is suppressed imposing that the modes aligned with the plasma propagate faster than the light. It turns out that this scheme is not appropriate to the description of astrophysical relativistic shocks because it leads to the development of a nonphysical electromagnetic precursor upstream. Moreover, Friedman filtering excessively cools down and compresses the downstream plasma [166].

The Cole-Karkkainen scheme [84] is similar to the Lehe scheme but it better preserves the physics of relativistic shock systems. Similarly, a modified operator, based on the usual leap-frog one defined in Eq. (3.28), is introduced in Maxwell-Faraday equation and in the divergence-free constraint on the magnetic field. This reads

$$\nabla_x^* = (\alpha + \beta S_x^1 + \gamma S_x^2) \nabla_x, \quad (3.40)$$

with

$$S_x^1 F_{i+1/2,j,k}^n = F_{i+1/2,j+1/2,k}^n + F_{i+1/2,j-1/2,k}^n + F_{i+1/2,j,k+1/2}^n + F_{i+1/2,j,k-1/2}^n \quad (3.41)$$

$$S_x^2 F_{i+1/2,j,k}^n = F_{i+1/2,j+1/2,k+1/2}^n + F_{i+1/2,j-1/2,k+1/2}^n \quad (3.42)$$

$$+ F_{i+1/2,j+1/2,k-1/2}^n + F_{i+1/2,j-1/2,k-1/2}^n. \quad (3.43)$$

The numerical stability of the solver is ensured if [169]

$$c\Delta t_c = \min \left[\Delta x, \Delta y, \Delta z, 1 / \sqrt{(\alpha - 4\gamma) \max \left[\frac{1}{\Delta x^2} + \frac{1}{\Delta y^2}, \frac{1}{\Delta x^2} + \frac{1}{\Delta z^2}, \frac{1}{\Delta y^2} + \frac{1}{\Delta z^2} \right]}, \right. \quad (3.44)$$

$$\left. 1 / \sqrt{(\alpha - 4\beta + 4\gamma) \frac{1}{\Delta x^2} + \frac{1}{\Delta y^2} + \frac{1}{\Delta z^2}} \right]. \quad (3.45)$$

In the other directions the operators are obtained by cyclic permutation of the index. The coefficients are bounded by the relation $\alpha + 4\beta + \gamma = 1$, and if $\alpha = 1$, $\beta = \gamma = 0$ the original Yee solver is retrieved. The Cole-Karkkainen solver adopts, in its original formulation, $\alpha = 7/12$, $\beta = 1/12$, $\gamma = 1/48$, with cubic cells $\Delta x = \Delta y = \Delta z$.

3.1.3 Binomial filtering

The filtering method reduces the impact of high wavenumber resonances. A wide-band low-pass filtering is applied to the current densities [17, 169]. We make use of a three-point digital filtering on the current,

$$\phi_j^J = \alpha \phi_j^J + \beta (\phi_{j-1}^J + \phi_{j+1}^J), \quad (3.46)$$

where ϕ_j^J is the filtered quantity. The filter is called binomial if $\alpha = 0.5$ and $\beta = (1 - \alpha)/2$. Given $\phi = \exp(ikx)$, this transforms under filtering as $\phi^J = g_{\alpha\beta}(k) \exp(ikx)$, where the *gain* (g), using Eq. (3.46), is given by

$$g_{\alpha\beta}(k) = \alpha + 2\beta \cos(k\Delta x) \simeq 1 - \beta(k\Delta x)^2 + \mathcal{O}(k^4), \quad (3.47)$$

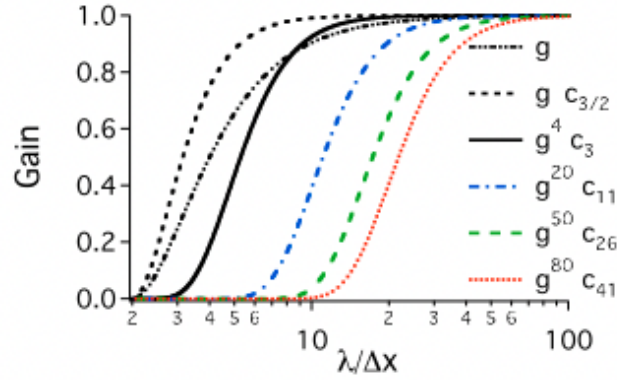


FIGURE 3.4: Gain versus wavelength for the bilinear filter without compensation (g), with compensation ($g \cdot c_{3/2}$) and for n -pass bilinear filters with compensation ($g^n \cdot c_{\alpha_c}$), for $n = 4, 20, 50, 80$ (see the text). Taken from [169].

For n successive applications of filters of coefficients $\alpha_1, \dots, \alpha_n, \beta_1, \dots, \beta_n$, the total attenuation G is given by

$$G = \prod_{j=1}^n g_{\alpha_j \beta_j}(k) \simeq 1 - \sum_{j=1}^n \beta(k \Delta x)^2 + \mathcal{O}(k^4). \quad (3.48)$$

A sharper cutoff in k space is obtained by using an additional step, called *compensation* [17]. Following n application of the bilinear factors, α_n, β_n the compensation factor is

$$\alpha_{n+1} = \alpha_c = \frac{n}{2} + 1 \quad (3.49)$$

$$\beta_{n+1} = \beta_c = -\frac{n}{4} \quad (3.50)$$

with associated gain

$$g_{\alpha_1, \dots, \alpha_n, \beta_1, \dots, \beta_n} = g_{\alpha \beta}^n(k) \cdot g_{\alpha_c \beta_c}(k) \simeq +\mathcal{O}(k^4). \quad (3.51)$$

The gain is plotted in Fig. 3.4 for the bilinear filter without compensation ($G \equiv g = g_{1/2, 1/4}(k)$), with compensation ($G \equiv g \cdot c_{3/2} = g_{1/2, 1/4}(k) \cdot g_{3/2, -1/4}(k)$) and for n -pass bilinear filters with compensation ($G \equiv g^n \cdot c_{\alpha_c} = g_{1/2, 1/4}^n(k) \cdot g_{n/2+1, -n/4}(k)$) for $n = 4, 20, 50, 80$ [169]. The bilinear filter provides complete suppression of the signal at the grid Nyquist wavelength, i.e. twice the grid cell size $\lambda = 2\Delta x$ [169].

3.1.4 The Godfrey-Vay filter

A straightforward approach for greatly reducing the numerical Cherenkov instability growth rates in FDTD-Esirkepov PIC simulations of relativistic beams and streaming plasma was present in 2014 by B.B. Godfrey and J.L. Vay [68]. It can be shown that employing the Esirkepov current-conserving algorithm (Eqs. (3.12)-(3.17)) [56] in the Maxwell-Ampère equation gives the dispersion relation [76],

$$C_0 + n \sum_{m_x} C_1 \csc \left[(\omega - k'_x \beta_x) \frac{\Delta t}{2} \right] + C_1 \csc^2 \left[(\omega - k'_x \beta_x) \frac{\Delta t}{2} \right] = 0, \quad (3.52)$$

where n is the proper density of the beam, m_x are the beam resonances, $k'_x = k_x + m_x 2\pi / \Delta x$ and we restricted to the 2D case of a beam propagating along x for tractability. The coefficients C_0, C_1, C_2 depend on (k'_x, k'_y, ω) . The first one represents the vacuum dispersion relation

$$C_0 = [\omega]^2 - \mathcal{D}_x^*[k_y]^2 - \mathcal{D}_y^*[k_x]^2, \quad (3.53)$$

where brackets indicate their finite difference representation in Fourier space: $[k]_i = k_i \text{sinc}(k_i \Delta t / 2)$. Using the Cole-Karkkainen scheme described above, the differential operator \mathcal{D}_j^* reads

$$\mathcal{D}_j^* = 1 - \frac{1}{2} \sin^2 \left(k_j \frac{\Delta x_j}{2} \right). \quad (3.54)$$

In the limit of infinitely small mesh sizes and time steps Eq. (3.52) reduces to $C_0 + n = 0$, as expected. All the beam modes in Eq. (3.52) are numerical artifacts, even the $m_x = 0$ mode. Coupling between these modes and electromagnetic modes roots of $C_0 = 0$ gives rise to the resonances referred as the numerical Cherenkov instability at large wave numbers. The binomial filter presented above can be implemented to quench them. At lower wavenumbers, unphysical growing modes appear due to the mismatch in the coefficient C_2 between transverse electric and magnetic fields, resulting in

$$\frac{\mathcal{S}^{E_y}}{[\omega]} \Big|_{\omega=k_x} \neq \frac{\mathcal{S}^{B_z}}{[k_x]}, \quad (3.55)$$

where \mathcal{S} denotes the Fourier-transformed field interpolation functions. This non-resonant instability can be suppressed by multiplying the interpolation functions \mathcal{S}^{E_y} and \mathcal{S}^{B_z} by $\mathcal{S}^{B_z} / [k_x]$ and $\mathcal{S}^{E_y} / [\omega]$ respectively [68].

For our simulations we made use of a 4th-order interpolation function for the shape function, the Esirkepov current-conserving algorithm combined with the Godfrey-Vay filter, a modified Cole-Karkkainen solver, originally proposed in [130] with all zero coefficients except $\beta = 1/8$, for Maxwell's equations and up to 30 binomial filtering passes per time step depending on the problem under study.

3.2 Turbulence driving scheme

3.2.1 General Scheme

As in typical turbulent plasmas there are typically many orders of magnitude between the outer scales and the dissipation range (see Fig. 2.4), it is not possible to capture in a single simulation both the large-scale process driving the turbulence and the energy dissipation at the kinetic (small-scale) level. A promising strategy is to focus on a sub-range of the complete turbulent cascade. As such, the *oscillating Langevin antenna* models the magnetic fluctuations at the domain scale as if they were generated by the transfer of energy caused by nonlinear interactions between counterpropagating Alfvén waves at scales larger than the simulation domain [159]. The *antenna* typically drives an external current parallel to the external magnetic field and it is expressed as a sum of plane waves whose temporal profile satisfies a Langevin equation in which the source is white noise.

To enter the details, let us restrict to a 2D plane $x - y$ (i.e. $\partial_z = 0$) and consider an out-of-plane external magnetic field $\mathbf{B} = B_0 \hat{z}$. Maxwell's equations require $\nabla \cdot \mathbf{B} = 0$ which translates into $\mathbf{k}_\perp \cdot \delta \mathbf{B}_\perp = 0$, where \perp refers to the orientation of B_0 . This is true in general since the eigenfunction for the Alfvén wave has no magnetic fluctuation aligned with the equilibrium magnetic field. In its original formulation, the scheme imposes, on the plasma, an external current parallel to the initial magnetic field $\mathbf{J}_{\text{ext}} = J_z \hat{z}$. This current can be re-expressed in terms of a vector potential through the curl of the magnetic field $\mathbf{J}_{\text{ext}} = c/(4\pi) \nabla \times \delta \mathbf{B} = -(c/4\pi) \nabla^2 A_z$, with $\delta \mathbf{B} = \nabla \times \mathbf{A}_{\text{ext}}$ [159]. Yet, this neglects the current displacements and it is hence not appropriate to the relativistic regime. As such, for our purposes, instead of making use of the vector potential A_z^{ext} in the external current to excite the perturbations, we directly employed it to excite external magnetic fluctuations δB_x and δB_y . The vector potential A_z^{ext} has the form [159]

$$A_z^{\text{ext}}(k_x, k_y, t) = a_n(t) e^{i\mathbf{k} \cdot \mathbf{r}}, \quad (3.56)$$

where the discrete complex value of the driving coefficient at time step n is $a_n \equiv a(t_n)$. The driving coefficient is initialised as $a_0 = A_0 \exp i\phi$, with ϕ an arbitrary phase, and it is evolved in time as

$$a_{n+1} = a_n e^{-i\omega_a \Delta t} + F_a \Delta t, \quad (3.57)$$

with $F_a = A_0 \sqrt{12|\Gamma_0|/\Delta t} \xi_n$; ξ_n a delta-correlated uniform complex random number with $1/2 \leq \Re(\xi_n) \leq 1/2$ and $1/2 \leq \Im(\xi_n) \leq 1/2$; $\omega_a = \omega_0 + i\Gamma_0$, ω_0 real frequency and $\Gamma_0 < 0$ decorrelation rate. In the continuous limit the temporal part of the antenna satisfy the equation of a stochastically driven and damped harmonic oscillator,

$$\frac{da}{dt} = -i\omega_0 a + \Gamma_0 a + F_a, \quad (3.58)$$

which reduces to the standard Langevin equation describing Brownian motion in the absence of the oscillating term, hence the name.

In particular, in conjunction with Martin Lemoine, we modified the PIC CALDER code [87, 166] to include a module of turbulence excitation with the characteristic outlined above. The set of parameters, $(\mathbf{k}, A_0, \omega_0, \Gamma_0)$ determines the characteristic length scales of the driving mode, the level of turbulence and its evolution in time. The turbulence can be excited as periodic or not in the box.

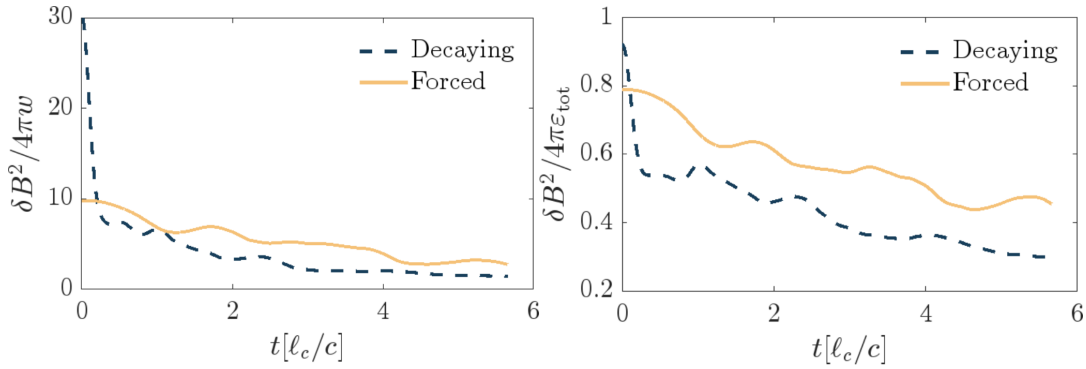


FIGURE 3.5: Magnetic energy density over plasma enthalpy on the left and magnetic energy density vs total energy density on the right for the 2D simulations of decaying (dark blue) and forced (orange) turbulence over the first 20 000 time steps corresponding to $t = 1980\omega_p^{-1} \sim 6\ell_c/c$ with $\ell_c \simeq 350c/\omega_p$.

3.2.2 Periodic turbulence

When turbulence is studied in a periodic box, we excite magnetic fluctuations in a finite time interval, starting at t_i . Before an intermediate time t_{fr} (with $t_{fr} > t_i$) particles remain “frozen”, meaning they neither experience nor contribute to the electromagnetic fields in the time interval $t_i < t < t_{fr}$. Resorting to this trick has proven necessary to avoid the sudden and premature energisation of the particles by the antenna’s electric fields, before the magnetic fluctuations could attain the desired level. By construction, for $t_i < t < t_{fr}$, the electric and magnetic fields are associated with the antenna only, while at later times they are made up by the coupled contributions of the external antenna and the plasma. The magnetic field of the antenna is computed at each time step as the (numerical) curl of the external vector potential of Eqs. (3.56)-(3.57). The electric field follows from Maxwell’s equations. The time at which the fluctuations start to be excited, t_i , usually coincides with the starting time of the simulation and particles are typically unfrozen after a few inverse plasma frequencies, $(t_{fr} - t_i) \sim 1 - 10\omega_p^{-1}$. The value of the parameter t_f determines the forced or decaying nature of the simulated turbulent scenario: if that parameter is set so as to cover the duration of the whole simulation, the turbulence is forced in the sense that the antenna keeps driving magnetic fluctuations throughout the simulation, i.e. its temporal part is evolved at each time step until the end. Otherwise, the antenna ceases to excite fluctuations for $t > t_f$, the temporal coefficients are not advanced in time anymore and the energy injection in the turbulence is halted.

Figure 3.5 compares the time evolution of the fluctuating magnetic energy in forced (dashed dark blue lines) and decaying (solid orange lines) 2D turbulent simulations. The pair plasma, of initial temperature $T = 1$ MeV, is immersed in a mean B field along z , $B_0/\sqrt{m_e c \omega_p/e} = 5$, and turbulence is driven, in this case, with the parameters $A_0 \sim 0.1 c/\omega_p \sqrt{m_e c \omega_p/e}$, $\omega_0 \sim 0$, $\Gamma_0 \sim 0.2\omega_p$. In the left panel, the turbulent magnetic energy is normalized to the plasma enthalpy w , which at the beginning of the simulation is $w_0 \sim 8nmc^2$ while it is normalized to the total, plasma + field, energy in the right panel. In the decaying turbulence, the magnetic energy density keep on decreasing, albeit with a time scale that gets longer and longer as the decay proceeds, because the cascade/dissipation-time scales with ℓ_c/v_A , and the Alfvén velocity related to the turbulent field decreases as δB does.

The two configurations give rise to similar power magnetic spectra, with a general Kolmogorov-like scaling in the inertial range and a steepening at kinetic scales

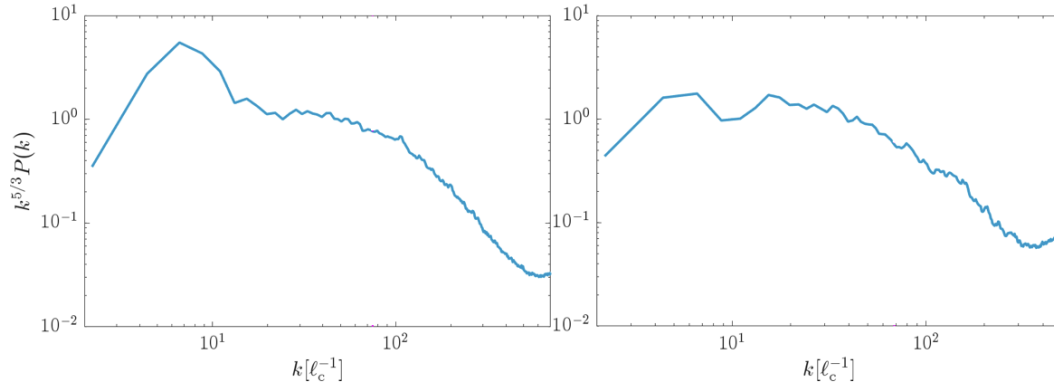


FIGURE 3.6: Power spectra of the magnetic fluctuations associated to a turbulent forced (right) and decaying (left) scheme.

($k \gtrsim 100/\ell_c$, Fig. 3.6). The main difference is the amplitude of the spectrum at the stirring scale ℓ_c , defined in the simulations as the box size in the transverse direction divided by the mean wavenumber. This is not completely unexpected as in the forced turbulence the energy is continuously injected at the stirring scale while the spectrum moves in time to larger wavenumbers in a decaying scenario. Besides, according to test runs, we adopted in our simulations a real frequency $\omega_0 \approx 0$ to avoid excessive heating of the plasma at early times caused by the rapid generation of non ideal electric fields on large scales. For the same reason the condition $\nabla \cdot A_{\text{ext}} = 0$ is imposed. The choice of A_0 is instead characteristic of each study. For the 2D and 3D simulations we used $N = 24$ wavenumbers $k = 2\pi n/L_{\text{max}}$, with $L_{\text{max}} = L_y$ the box extent along y , so that the typical scale of a turbulent eddie is not affected by the relativistic motion in the case of moving turbulence. The coefficients n are reported in Tab. 3.1. The potential vectors excites fluctuations in the plane transverse to the external coherent field, i.e. δB_x and δB_y for the 2D configuration, and along all the three dimension in the 3D case.

2D			3D		
n_x	n_y	n_z	n_x	n_y	n_z
+1	+1	0	+1	+2	0	+1	+1	0	+1	+1	+1
+1	-1	0	+1	-2	0	+1	-1	0	-1	+1	+1
+1	+2	0	+2	+1	0	+2	+1	0	+1	-1	+1
+1	-2	0	+2	-1	0	+2	-1	0	+1	+1	-1
+1	+3	0	+1	0	+2	+3	+1	0	+1	-1	-1
+1	-3	0	+1	0	-2	+3	-1	0	-1	+1	-1
+1	+4	0	+2	0	+1	+4	+1	0	-1	-1	+1
+1	-4	0	+2	0	-1	+4	-1	0	-1	-1	-1
+2	+2	0	+0	+1	+2	+2	+2	0	+1	+1	+1
+2	-2	0	+0	+1	-2	+2	-2	0	-1	+1	+1
+2	+3	0	+0	+2	+1	+3	+2	0	+1	-1	+1
+2	-3	0	+0	+2	-1	+3	-2	0	+1	+1	-1
...

TABLE 3.1

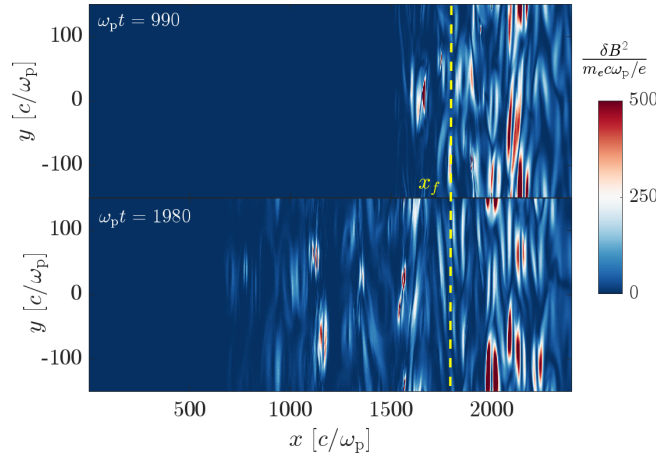


FIGURE 3.7: Drifting ($\gamma = 2$) non-periodic turbulence $A_0 \sim 0.03$, $\omega_0 \sim 0$, $\Gamma_0 \sim 0.25$ and 24 wave numbers, at two different time steps and a magnetisation associated to the turbulent field $\sigma \sim 0.2$. The dashed vertical yellow line marks the position, x_f where turbulence forcing is halted. The boundary where the fluctuations start to be excited, x_i coincides with the right hand-side of the domain. Particles are “defrozen” at $x < x_{fr} = 2396c/\omega_p$.

3.2.3 Non-periodic turbulence

Joint simulations of turbulence and shock (more details of this particular case will be given in Chapter 6) contain non-periodic turbulence. Indeed, turbulence is set in motion (see Fig 3.7) and the left boundary condition of the domain, which triggers the shock, is turned into reflective. In this case, the parameters that determine where the antenna is turned on depend on space rather than time. Namely, we specify an initial, x_i , and final, x_f , coordinate which identify the region where fluctuations, as they propagate, are excited, and an intermediate coordinate, x_{fr} with $x_f < x_{fr} < x_i$, at which point the particles become unfrozen. The boundary where the fluctuations start to be excited, x_i , usually coincides with the right hand-side of the domain where fresh plasma is continuously injected. A forced scheme is reproduced if the parameter x_f is set equal to the left hand-side of the domain $x = 0$. Contrarily, if the parameter is set as to only cover a finite spatial domain, in the region $x < x_f$ the turbulence decays freely in a decaying scenario. Fig 3.7 shows an example of the magnetic fluctuations extracted from a non-periodic turbulent simulation at two different time steps. The plasma drifts at $\gamma = 2$ from the right to the left of the simulation domain in a mean out-of-plane magnetic field $B_0/\sqrt{m_e c \omega_p/e} = 0.38$. In the region $1800 < x[c/\omega_p] < 2400$, the driving of the turbulence is sustained by an antenna made of 24 wavenumbers, amplitude $A_0 \sim 0.03 c/\omega_p \sqrt{m_e c \omega_p/e}$, $\omega_0 \sim 0$, $\Gamma_0 \sim 0.25 \omega_p$.

Chapter 4

Comparison of non-resonant acceleration model with PIC and MHD simulations

The goal of the following study is to test, using two different (PIC and MHD) simulation frameworks, the recent model of non-resonant particle acceleration in strongly magnetized turbulence depicted in 2.2.4, which ascribes the energisation of particles to their continuous interaction with the random velocity flow of the turbulence. Building on the fact that if the flow velocity is not uniform there does not exist a global unique frame in which the electric field vanishes, Fermi acceleration is described as a continuous journey of the particle momentum through the instantaneous rest frames where the electric field is locally zero (if ideal MHD conditions apply) [89]. At each point, the particle energy evolves due to the inertial forces that result from the space-time dependence of the continuous inertial frames (see Eq. (2.73)). At a given time t , the particle Lorentz factor can be expressed as

$$\gamma'_{\text{th}}(t) = \gamma'_{\text{obs}}(t_0) + \int_{\tau(t_0)}^{\tau(t)} d\tau \left. \frac{d\gamma'}{d\tau} \right|_{\text{th}}, \quad (4.1)$$

where t_0 represents some initial time, and $(d\gamma'/d\tau)|_{\text{th}}$ is given by Eq. (2.73). In order to benchmark the model against numerical (PIC or MHD) experiments, a large number of particles have been tracked in the simulations and the temporal evolution of their energy $\gamma'_{\text{obs}}(t)$ has been compared to the above prediction $\gamma'_{\text{th}}(t)$. The theoretical histories, and in particular, $(d\gamma'/d\tau)|_{\text{th}}$, are reconstructed by extracting from the numerical simulations at each point of the trajectory the various quantities that enter the equation, namely u_E^β and its gradients $\partial_\alpha u_E^\beta$. This allows the quantities $\mathbf{a}_E \cdot \mathbf{b}$, Θ_{\parallel} and Θ_{\perp} to be computed and to eventually predict, at each time step of the trajectory, how $\gamma'_{\text{th}}(t)$ evolves by integrating Eq. 4.1.

Before digging into the numerical details, it is important to stress the several effects that affect the reconstruction of the trajectories and the underlying approximations. For one, the above model is an approximation obtained in the limit $r_g \ll \ell_c$, where ℓ_c denotes the coherence scale of the turbulent power spectrum, *i.e.* the length scale on which most of the turbulent power lies. That is supported by the fact that the particles are expected to be weakly affected on their trajectory by fluctuations on scales smaller than their gyroradii as those fluctuations carry a small fraction of the magnetic power and their effect averages out over a gyro-orbit. Though, some effects of order r_g/ℓ_c might alter the model predictions. Because numerical simulations are restricted in their dynamic range (an effective rigidity $\rho = 2\pi r_g/\ell_c \sim 0.03 - 0.1$ is close to what can be currently achieved at best), such effects can be significant, especially where r_g can then take large values relative to its average at

a given energy, e.g. in regions of low magnetic field strength. Likewise, particles can experience substantial acceleration over a period of time, which also leads to an increase in r_g , and hence to a loss of accuracy of the model predictions.

Furthermore, for the same reason, the model assumes that the fields \mathbf{u}_E , \mathbf{E} , \mathbf{B} and their gradients are coarse-grained quantities, meaning that sub-Larmor scales have been filtered out (see section 2.2.4). Such a procedure would be overly expensive to implement in PIC simulations, as the Larmor scale changes from particle to particle, and even from time step to time step, since the energy of a particle itself varies in time. We thus use the actual fields and gradients, as measured in the simulation on the scale of the numerical grid, and discard any filtering. This introduces high-frequency noise in the reconstruction of γ'_{th} , associated with small-scale effects. To test how this may affect our comparison, we have also performed a reconstruction of the trajectories including time filtering, in order to smoothen the temporal profile of $\gamma'_{\text{obs}}(t)$ over time scales $\simeq r_g/c$. More explicitly, we smooth the fields \mathbf{u}_E , \mathbf{B}' and their gradients that each particle encounters on its trajectory before performing the reconstruction. While the reconstructed trajectory differs from that obtained in the absence of this time filtering, the overall result remains similar.

Finally, the comparison with the model is made further complicated by non-ideal MHD effects. Kinetic simulations have indeed demonstrated that particles of the thermal pool initially gain energy through non-ideal parallel electric field components in reconnection layers, then start to probe the large-scale turbulence once their gyroradius exceeds the typical scale of those layers [42, 43]. The contribution of non-ideal parallel electric fields is observed to decrease as the energy of the particle increases, in general agreement with the idea that on large scales, the physics tends toward the ideal MHD regime, as assumed by the non-resonant acceleration model. However, on the simulation scales, those non-ideal electric fields can affect the energy gain process, and thus perturb the comparison. For this reason, we also compare our model to a three-dimensional MHD simulation, in which we propagate particles and follow their interaction with electric fields that are calculated using ideal MHD Ohm's law.

From the above considerations, we do not expect an exact match between γ'_{obs} and γ'_{th} . To test the model, we thus calculate, for each particle i , a Pearson correlation coefficient r_i ,

$$r_i \equiv \frac{\text{cov} [\gamma'_{\text{obs}}(i); \gamma'_{\text{th}}(i)]}{\text{cov} [\gamma'_{\text{obs}}(i); \gamma'_{\text{obs}}(i)]^{1/2} \text{cov} [\gamma'_{\text{th}}(i); \gamma'_{\text{th}}(i)]^{1/2}}, \quad (4.2)$$

where $\text{cov} [A(i); B(i)]$ represents the covariance of the histories of the quantities A and B over the trajectory of particle i . The correlation coefficients have been computed for the whole sample of tracked particles and represented together in the form of histograms. A correlation coefficient in the vicinity of $+1$, denotes perfect correlation, hence perfect reconstruction. At odds, a coefficient value of -1 stands for anti-correlation; 0 for no correlation and a poor reliability of the model.

As will be detailed in the following, sub-Larmor effects related to non-ideal electric fields on small length scales can lead to a sharp departure in the history of γ'_{obs} , and to a different departure in γ'_{th} . The acceleration due to non-linear events, as reconnecting current sheets, is associated to short timescales, hence the deviation between the predicted and observed particle Lorentz factors can be very sharp, yet a strong correlation between the two histories can still be found before and after this sudden event even if the global trajectory shows a lesser degree of correlation. To avoid running into such small-scale effects, we compared both the whole time

histories and chunks of trajectories at intermediate timescales. The duration of the interval over which we follow the trajectories is written Δt . Additionally, among all tracked particles, in order to test Eq. (2.73), we follow only those particles undergoing a large enough variation in energy, treating on an equal footing energy gains and losses. We hence adopted arbitrarily a threshold g_{\min} and consider those trajectories, or chunks of trajectories, that satisfy $\Delta\gamma'/\gamma' \geq g_{\min}$ with $\Delta\gamma' = \max(\gamma') - \min(\gamma')$ over the interval of duration Δt .

In the following Section, I describe the numerical simulations and the results of the reconstruction, including some details specific to each. The model was tested against 2D and 3D PIC simulations, as well as 3D (incompressible) magnetohydrodynamic (MHD) simulations, of particle acceleration in turbulence. In addition, Appendix A reports the results on simulations that follow test particles in a synthetic turbulence, meaning a turbulence that is constructed from a sum of non-interacting linear eigenmodes (Alfvén, fast or slow magnetosonic modes) of the plasma, following the study of Ref. [51]. The interest of this numerical experiment is that the physics of particle acceleration in such turbulence is relatively well understood, as it follows the predictions of quasilinear theory, and that part of it (transit-time damping acceleration related to magnetic mirroring effects) can be captured by the above model. It can therefore be used to gauge the amount of information contained in the probability density of correlation coefficients that we reconstruct and the reliability of the method.

In particular, the comparison between the histories predicted by the model and those observed in several numerical experiments has been tested in: (i) a 2D decaying turbulence PIC simulation; (ii) a 2D forced turbulence PIC simulation; (iii) a 3D forced turbulence PIC simulation; and (iv) a 3D forced turbulence MHD simulation. All PIC simulations assume a pair plasma composition and have been run in fully periodic (2D or 3D) geometry. They have been conducted using the finite-difference time-domain, relativistic PIC CALDER code [87], in which the turbulence stirring module described in section 3.2.1, has been implemented. The MHD simulation is that made available for public use on the Johns Hopkins Turbulence database¹ [99, 58].

For the sake of clarity, I remark here that my role in this study has been to take care of the analysis and comparison of PIC simulations.

4.1 2D decaying turbulence PIC simulation

We first analyse a 2D decaying turbulence PIC simulation with the following characteristics: domain size $N_x \times N_y = 10\,000^2$ cells, corresponding to physical size $L_x \times L_y = 1\,000^2 c^2 / \omega_p^2$, integrated over a time $T = 5\,000 \omega_p^{-1}$. Here, $\omega_p = (4\pi n_{\pm} e^2 / m)^{1/2}$, with n_{\pm} the initial (uniform) proper density of positrons/electrons and e the elementary charge, represents the non-relativistic plasma frequency of one species, so $1/\sqrt{2}$ of the total plasma frequency. The cell size is $\Delta x = \Delta y = 0.1 c / \omega_p$, and the time step $\Delta t = 0.099 \omega_p^{-1}$. The plasma is initialized with temperature $T_0 = 1$ MeV, with 10 particles per species per cell.

The initial magnetization (associated with the mean-field component) is $\sigma_0 = 1.6$, and $\delta B / B_0 = 2.8$, corresponding to an initial magnetization of the turbulent component $\sigma_{\delta B} \simeq 13$. We define the magnetization parameters with respect to the

¹available from:

http://turbulence.pha.jhu.edu/Forced_MHD_turbulence.aspx.

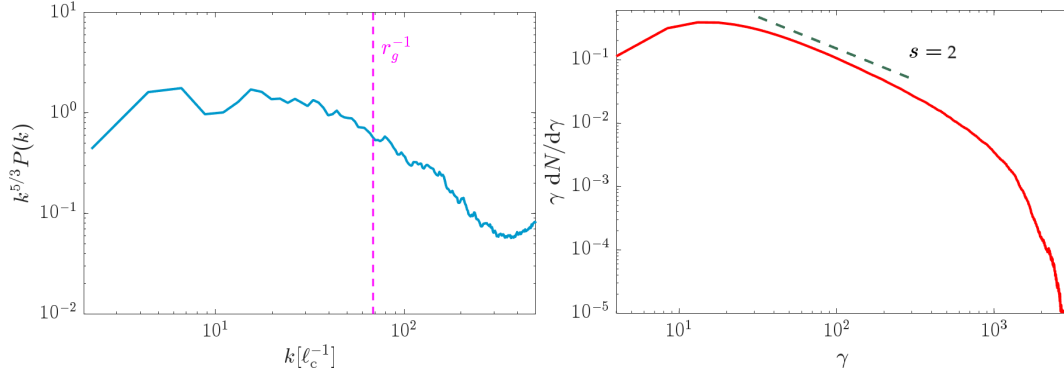


FIGURE 4.1: On the left: Power spectrum of magnetic fluctuations for the 2D decaying turbulence PIC simulation at $t \simeq 1800 \omega_p^{-1} \sim 5 \ell_c / c$. The fuchsia vertical dashed line marks the scale r_g^{-1} for particles with Lorentz factor $\gamma = 50$. Wavenumbers are given in units of the inverse stirring scale ℓ_c^{-1} ; units on the y -axis are arbitrary; On the right: Energy distribution of the particles in the 2D decaying turbulence PIC simulation at $t \simeq 1800 \omega_p^{-1} \sim 5 \ell_c / c$. A powerlaw tail emerges at $\gamma \gtrsim 20$ up to $\gamma \sim 10^3$, with spectral index $s \simeq 2$, defining s through $dN/d\gamma \propto \gamma^{-s}$

total enthalpy density of the plasma, *i.e.*

$$\sigma = \frac{B^2}{4\pi w}, \quad (4.3)$$

with w the enthalpy density and $n = n_+ + n_-$. The enthalpy density can be expressed as $w \simeq 8nmc^2$ for an electron-positron pair plasma at a temperature of 1 MeV. For the present 2D simulations, we excite external current fluctuations along the mean magnetic field (z -axis) only, with wavemodes oriented in the (x, y) plane. We use 24 modes, with mean wavenumber $\langle k \rangle = (2\pi/L_x) \times 2.9$ and coefficient reported in Tab. 3.1, corresponding to a stirring scale $\ell_c \simeq L_x/2.9 \simeq 350 c/\omega_p$. The square root of the average of the squared wavenumbers give a similar estimate, $\langle k^2 \rangle^{1/2} = (2\pi/L_x) \times 3.0$. Here, we will not distinguish the stirring scale from the coherence (or integral) scale; various definitions exist for the latter, which give values differing by a factor of order unity of ℓ_c . Those external currents generate δB_x and δB_y . We then tune the amplitude of the antenna to reproduce the chosen initial turbulent magnetization. The Langevin antenna is also characterized by a real frequency ω_0 and a damping term Γ_0 , as detailed in Section 3.2.1. We found it useful to set the real frequency to low values, in practice $\omega_0 \approx 0$, in order to avoid excessive heating of the plasma at early times, caused by the rapid generation of non-MHD electric fields on large scales. Regarding the damping term, we tune it in order to ensure that the auto-correlation time of the turbulent magnetic field matches roughly ℓ_c/c ; in practice, we set $\Gamma_0 \simeq -0.6\langle k \rangle c$. The modes initialized at time 0 excite δB_x and δB_y fluctuations which are left to evolve freely with the plasma at time $t > 0$, as described in Sec. 3.2.2 and similarly to Refs. [42, 43, 44], *i.e.* we simulate a decaying turbulence.

The left panel of Fig. 4.1 shows the power spectrum of magnetic fluctuations as measured in this 2D decaying turbulence PIC simulation. It reveals a general scaling close to $k^{-5/3}$ at large scales, *i.e.* the Kolmogorov scaling, followed by a steeper spectrum characteristic of the dissipation range. This shape generally matches that observed in previous PIC simulations of decaying turbulence [42, 43, 44].

In that figure, the dashed line indicates the scale corresponding to the inverse gyroradius of particles with initial – meaning, at the time $t = 1500 \omega_p^{-1} \sim 4\ell_c/c$ at which we initiate the test – Lorentz factor $\gamma \sim 50$, which we follow in order to compare the model to the data using the method described earlier². We recall that this model assumes $r_g \ll \ell_c$, hence r_g cannot be made arbitrarily larger. However, it cannot be made arbitrarily small either, otherwise the particle gyroradius will lie out of the range of the inertial (non-dissipative) spectrum. Furthermore, on small spatial scales, corresponding to gyroradii of particles with energies in the thermal part of the spectrum – $\gamma \sim 10$ – particle energisation is mostly controlled by parallel electric fields, as recalled above [42, 43]. We thus conclude that Lorentz factors in the range $\sim 20 - 60$ provide a reasonable compromise to test the theoretical model of non-resonant acceleration. In the present case, the effective rigidity $2\pi r_g/\ell_c$ of particles with Lorentz factor $\gamma \sim 50$ is of the order of 0.1, in the range anticipated earlier. The right panel of Fig. 4.1 plots the energy spectrum of particles, $dN/d\gamma$, in this 2D decaying turbulence simulation, at time $t \simeq 5\ell_c/c$. A powerlaw tail, $dN/d\gamma \propto \gamma^{-s}$ with index $s \simeq 2$, has developed from Lorentz factors $\gamma \sim 20$ up to $\gamma \sim 10^3$, at which point the gyroradius of particles becomes comparable to the maximal scale of the turbulent cascade, implying less efficient acceleration at larger energies.

I now turn to the comparison between the model predictions and the PIC simulation. The trajectories of a sample/subset of particles are recorded from $t = 1500 \omega_p^{-1} \sim 4\ell_c/c$ up to $5000 \omega_p^{-1} \sim 14\ell_c/c$. The initial time ensures that the turbulence has had time to cascade down to small scales by the time the test starts. In the PIC simulations, both time and space derivatives are calculated using simple first-order differences, *i.e.* from one cell to the next (or one step to the next for time). The time derivatives are smoothed through 16 repeated applications of binomial filtering (Sec. 3.1.3). The spatial derivatives are computed from fields that also underwent 16 successive applications of binomial filtering. This helps eliminate shot noise on the scale of the mesh (here, $\sim 0.1 c/\omega_p$) that would otherwise pollute the reconstruction of derivatives which, as discussed before, are meant to be calculated on scales significantly larger than the grid size.

The test has been carried out for two typical durations: $\Delta t \simeq 1\ell_c/c$, see left panel of Fig. 4.2 and $\Delta t \simeq 10\ell_c/c$, see right panel of Fig. 4.2. Those figures present the probability density function (p.d.f.) of the correlation coefficients r_i , as defined in Eq. (4.2). To construct the histogram shown on the left of Fig. 4.2, we have selected at random, for each test particle, chunks of trajectories in which the energy of the particle changes by an amount at least equal to unity, *i.e.* $\Delta\gamma'/\gamma' \geq 1$ with $\Delta\gamma' = \max(\gamma') - \min(\gamma')$. We typically use 10^4 test particles to construct such a histogram; each test particle history, extending over $\simeq 10\ell_c$, is sampled at most 10 times to obtain a chunk of extent $1\ell_c/c$. In the right plot of Fig. 4.2, the integration is performed over the full particle trajectories, provided $|\Delta\gamma'/\gamma'| \geq 2$.

The left histogram in Figure 4.2 indicates a genuinely positive degree of correlation for the contribution of the Θ_{\parallel} force terms, and similarly when all contributions (labeled as “All”) are summed together as in Eq. (2.73). More specifically, to plot the probability density of the correlation coefficients for one force contribution, we use Eq. (2.73) but set the contributions of the other two terms to zero. This figure suggests that neither the force term Θ_{\perp} nor $\mathbf{a}_E \cdot \mathbf{b}$ appear to contribute strongly to the evolution of the particle energy. The dominance of Θ_{\parallel} is a common trait to our PIC simulations, which will also hold in 3D as discussed further on.

²We select here a range in γ , not γ' , but this does not significantly influence our results, as we have explicitly checked for the 2D PIC driven turbulence and the MHD simulations discussed further below.

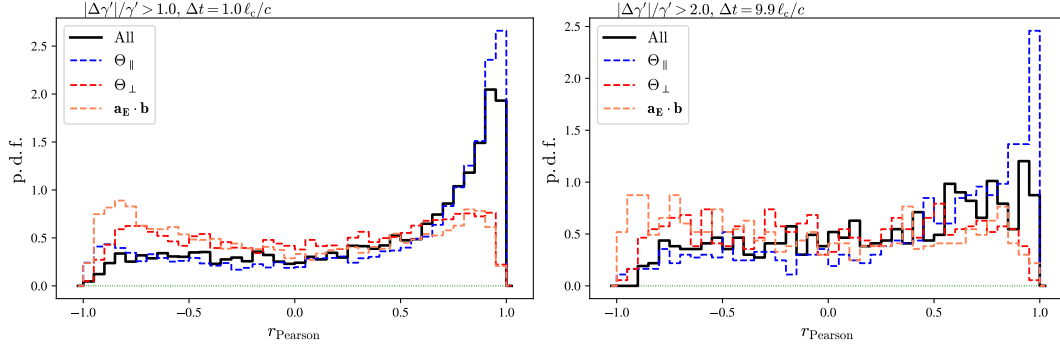


FIGURE 4.2: Histograms of correlation coefficients between the expected and observed evolution of γ' along chunks of test particle trajectories (on the left) and considering the whole trajectory (on the right) of each test particle with initial $25 < \gamma < 50$, for the 2D decaying turbulence PIC simulation. The chunks are selected at random among the whole of test particle histories, provided they fulfill the following criteria: the duration $\Delta t \simeq 1 \ell_c/c$ and the energy change within that time interval verifies $|\Delta\gamma'/\gamma'| > 1$. Over the whole trajectory test particles are selected with $|\Delta\gamma'/\gamma'| > 2$. Both histogram shows that the parallel shear $\Theta_{||}$ contribution, and more generally the non-resonant model as described by Eq. (2.73), match relatively well the observed variations.

The trend observed in the right panel of Fig. 4.2 is similar. The level of noise is larger in that figure, because we can select only one trajectory for each tracked particle instead of a number of distinct time intervals, and because our stronger constraint on the amount of energy variation within the interval limits further the number of test particles that are selected for the test.

We note that the above figures and results are relatively insensitive to the choice of the threshold of energy variation $|\Delta\gamma'/\gamma'|$, as we have verified. It is also somewhat insensitive to the duration of the interval that we consider. The latter must be large enough, obviously, to accommodate a large number of gyroperiods, since the model considers only contributions from scales larger than r_g .

4.2 2D forced turbulence PIC simulation

We now analyze a 2D driven turbulence PIC simulation with characteristics similar to that for the decaying turbulence scenario: domain size $N_x \times N_y = 10\,000^2$ cells, corresponding to physical size $L_x \times L_y = 1\,000^2 c^2/\omega_p^2$, integrated over time $T = 5\,000 \omega_p^{-1}$; the cell and step size are, as before, $\Delta x = \Delta y = 0.1 c/\omega_p$ and $\Delta t = 0.099 \omega_p^{-1}$. The initial magnetisations are the same as for the decaying turbulence scenario, $\sigma_0 \simeq 1.6$ and $\sigma_{\delta B} \simeq 13$.

Turbulence is excited using a Langevin antenna scheme [159] in a forced configuration, as described in sec. 3.2.1, similar to the implementation of Refs. [191, 190, 188, 178] and with the same antenna parameters of the previous section. Here, we use as well 24 wavenumbers, with mean wavenumber $\langle k \rangle = (2\pi/L_x) \times 2.9$ (and similar $\langle k^2 \rangle^{1/2}$), implying $\ell_c \simeq 350 c/\omega_p$, as before. The mean field lies in the out-of-plane direction (along z).

The power spectrum of magnetic fluctuations, shown in the left panel of Fig. 4.3, reveals a shape similar to that seen in the decaying turbulence case, with a (roughly) $k^{-5/3}$ generic scaling over the inertial domain, followed by the steeper dissipative range at kinetic scales. The spectrum amplitude is more pronounced at the stirring

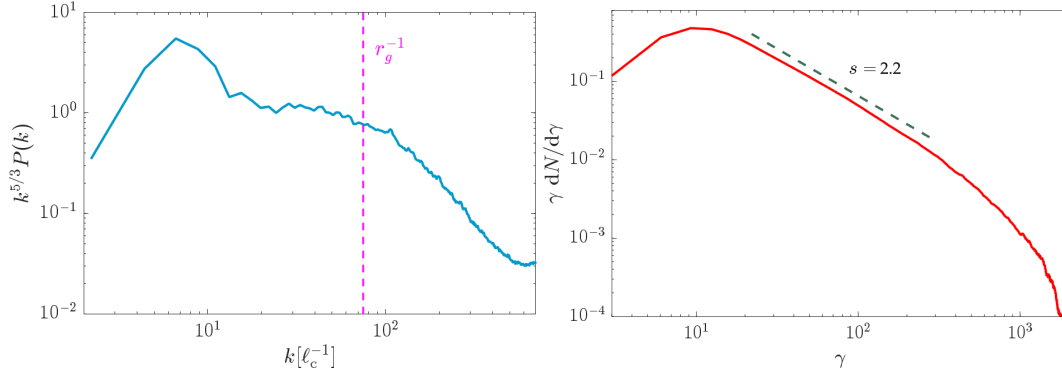


FIGURE 4.3: Left: Power spectrum of magnetic fluctuations for the 2D forced turbulence PIC simulation at $t \simeq 1800 \omega_p^{-1} \sim 5 \ell_c/c$. The fuchsia vertical dashed line marks the scale r_g^{-1} for particles with Lorentz factor $\gamma = 50$; Right: Energy distribution of the particles in the 2D forced turbulence PIC simulation at $t \simeq 1800 \omega_p^{-1} \sim 5 \ell_c/c$. A powerlaw tail is clearly seen, extending from $\gamma \sim 10$ up to $\gamma \sim 10^3$, with spectral index $s \simeq 2$, defining s through $dN/d\gamma \propto \gamma^{-s}$. The test particles that we study, with $25 < \gamma < 50$, are located in the powerlaw tail.

scale, a characteristic trend of forced turbulence PIC simulations (compare Refs. [43] and [189]). This is expected insofar turbulence is continuously injected at the stirring scale in forced turbulence, while the spectrum moves in time to larger k in decaying turbulence.

As in the decaying turbulence scenario, the dashed line represents the inverse gyroradius of particles with Lorentz factor $\gamma \sim 50$. Again, their effective rigidity is of the order of 0.1, which falls in the right range to test the non-resonant acceleration model.

The right panel of Fig. 4.3 plots the particle energy distribution, which reveals a powerlaw tail extending from $\gamma \sim 10$ up to $\gamma \sim 10^3$, as for the decaying turbulence scenario. The best-fitting spectral index, $s \simeq 2.2$, is also close to that found previously. We note that in forced turbulence simulations, the spectrum evolves slowly in time, as the energy that is continuously injected in the simulation maintains $\delta B/B$ (and, to a lesser degree, the overall magnetization) at values not far from its initial state, thereby guaranteeing that acceleration can proceed at all times. In decaying turbulence simulations, the drop in magnetization associated with magnetic dissipation within $\sim 5 - 10 \ell_c/c$ implies that acceleration becomes much slower, so that the particle spectrum essentially freezes on those timescales [42, 43, 44].

To reconstruct the probability density distributions of the correlation coefficients between observed and reconstructed histories, we follow test particles from $t = 1500 \omega_p^{-1} \sim 4 \ell_c/c$ up to $5000 \omega_p^{-1} \sim 14 \ell_c/c$, as for decaying turbulence. Those probability densities are presented in Fig. 4.4. The parameters (duration, amount of variation of the energy) are the same as in the decaying turbulence scenario. We observe a similar trend, namely, the non-resonant captures fairly well the observed energy histories, and Θ_{\parallel} provides the dominant contribution among the three force terms. The perpendicular contribution Θ_{\perp} and the inertial term do not show such significant degrees of correlation, although that of Θ_{\perp} is skewed towards positive values, at least for short $\Delta t \simeq 1 \ell_c/c$ timescales.

Generally speaking, the degree of agreement between model and simulations appears more satisfactory for the present forced turbulence scenario than for the decaying one. In that respect, we note that the shape of the spectrum can impact

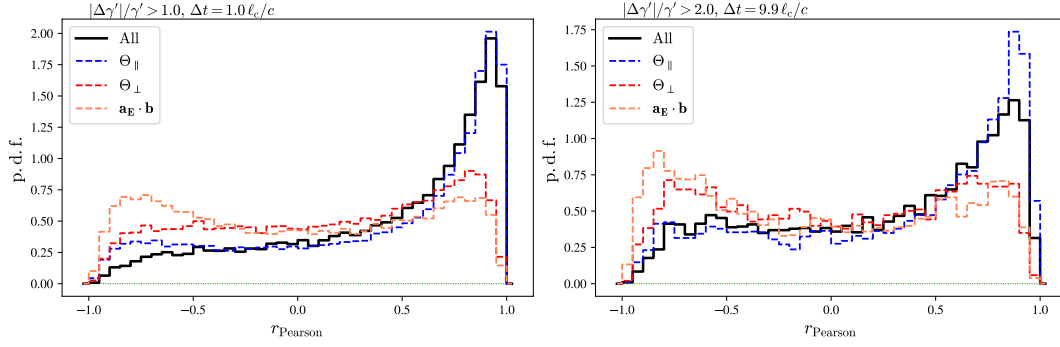


FIGURE 4.4: Histogram of correlation coefficients between the expected and observed evolution of γ' along chunks of test particle trajectories (left panel) and whole trajectory (right panel) with initial $25 < \gamma < 50$, for the 2D forced turbulence PIC simulation. This histogram shows that the non-resonant model provides a satisfactory match to the observed variations, and that the parallel shear term $\Theta_{||}$ provides the dominant contribution to the force terms.

this comparison in the following way. The power spectrum of the forced simulation shows a larger amplitude on the smallest k -modes, meaning on the largest length scales, than the decaying turbulence one, all things being considered equal. This difference can be read off left panels in Fig. 4.1 and 4.3, but it is actually more pronounced at later times, since the power spectrum of the decaying turbulence shifts to larger k as time progresses. This implies that, on the whole, particles experience a turbulence on larger scales in the forced turbulence case than in the decaying turbulence one, as measured relatively to their gyroradius. Since the model works to order r_g/ℓ_c , this larger degree of agreement is therefore not unexpected, at least at a qualitative level.

4.3 3D forced turbulence PIC simulation

I will now discuss the results of 3D simulations. We have first performed a 3D forced turbulence PIC simulation with domain size $N_x \times N_y \times N_z = 1080^3$ cells, corresponding to physical size $L_x \times L_y \times L_z = 540^3 c^3/\omega_p^3$, integrated over 5000 time steps, corresponding to a time $t \simeq 1500 \omega_p^{-1}$; the mesh size is now $\Delta x = \Delta y = \Delta z = 0.5 c/\omega_p$, $\Delta t = 0.495 \omega_p^{-1}$ and we use 15 particles per species per cell. This choice of parameters is motivated by the need to optimize the execution time, while avoiding excessive shot noise associated with too few macro-particles per skin depth volume. When measured in terms of the total relativistic plasma frequency, $\Omega_p = [4\pi(n_+ + n_-)e^2/(w/n)]^{1/2}$, the mesh size reads $\delta x \simeq 0.25 c/\Omega_p$; given that the plasma further heats with time in the turbulence, this provides a relatively fair sampling of the skin depth volume. Figure 4.5 offers a general view on the simulation at time $t \simeq 600 \omega_p^{-1}$: magnetic energy density (top panel), current density component along the mean field direction (middle panel) and plasma bulk velocity (bottom panel).

The initial mean field magnetization is $\sigma_0 = 1.6$ as before, while $\sigma_{\delta B} \simeq 8$. The forced turbulence is excited using the same Langevin antenna scheme as in 2D, with the following parameters: in 3D, we generate 24 modes of external current density fluctuations along x , along y and along z separately, with mean wavenumbers $\langle k \rangle = 2\pi/L_{\max} \times 2$. (the coefficients are listed in Tab. 3.1); for reference, $\langle k^2 \rangle^{1/2} \simeq$

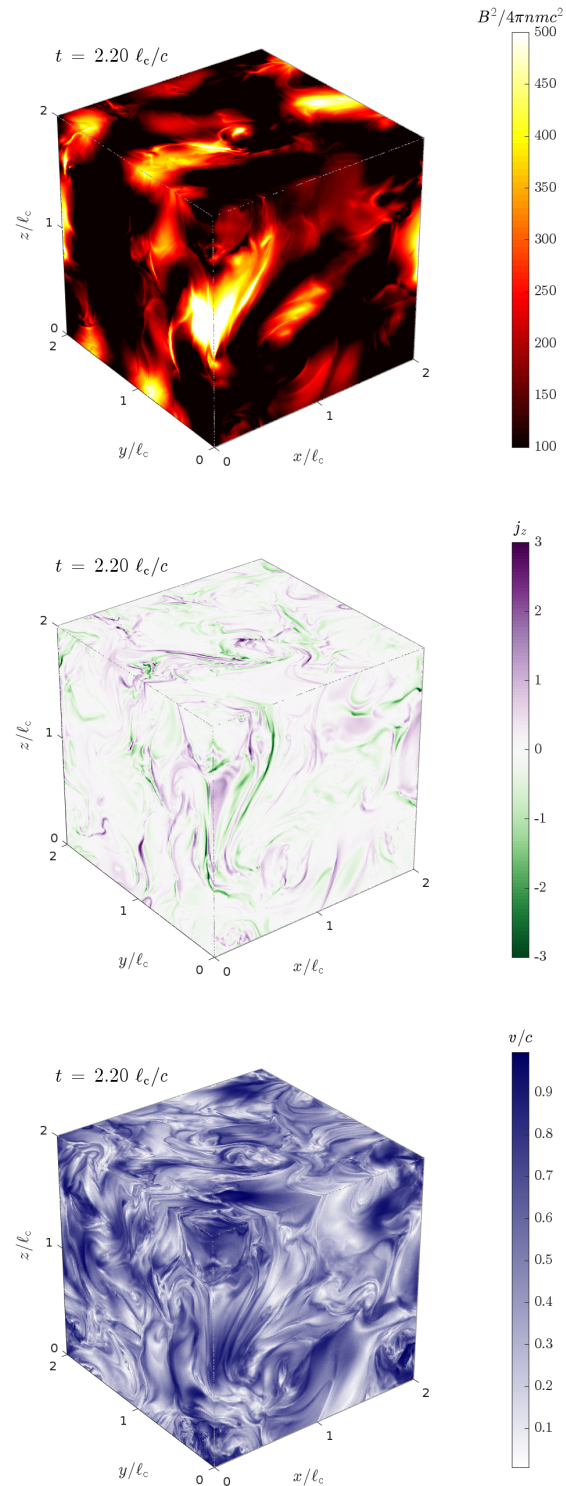


FIGURE 4.5: Visualisation of a cube of the 3D PIC simulation, showing the magnetic energy density (in units of plasma rest-mass energy, top panel), the current density component along the mean magnetic field component (middle panel) and the mean plasma velocity (in units of c , bottom panel).

$2\pi/L_{\max} \times 2$, as well, guaranteeing a stirring scale $\ell_c \simeq L_{\max}/2 \simeq 270 c/\omega_p$. We use a real frequency $\omega_0 = 0$ to avoid the generation of external electric fields in the

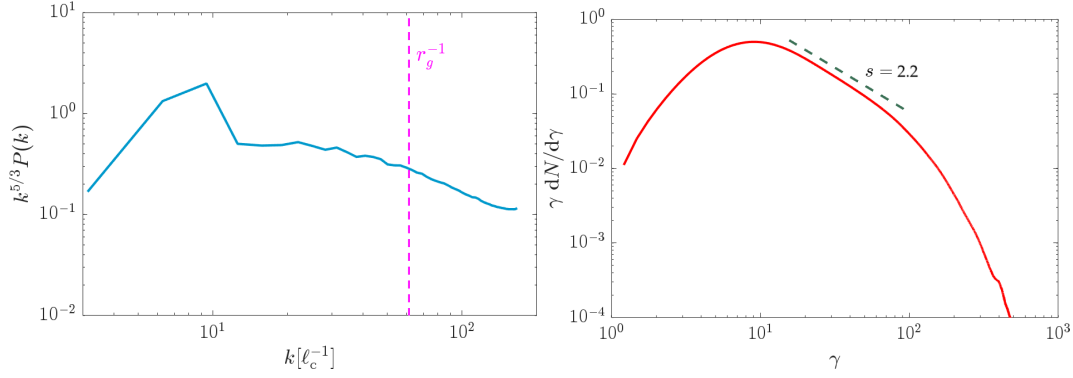


FIGURE 4.6: Left: Power spectrum of magnetic fluctuations for the 3D forced turbulence PIC simulation at $t \sim 600\omega_p^{-1} \sim \ell_c/c$. The fuchsia vertical dashed line marks the scale r_g^{-1} for particles with Lorentz factor $\gamma = 50$. The fall-off of the spectrum in the dissipative range is not as prominent as in 2D due to the data rebinning used (see main text); Right: Energy distribution of the particles in the 3D forced turbulence PIC simulation at $t \sim 600\omega_p^{-1} \sim 2\ell_c/c$. A powerlaw tail with spectral index $s \simeq 2.2$ is clearly seen, extending from $\gamma \sim 10$ up to $\gamma \sim 100$

forcing scheme, and a damping term $\Gamma_0 = -0.4\langle k \rangle c$.

As before, Fig. 4.6 shows the power spectrum of magnetic fluctuations on the left and the particle energy distribution at $t \simeq 600\omega_p^{-1} \sim 2.2\ell_c/c$, on the right. To compute the 3D power spectrum (and preserve memory usage), the field values have been rebinned by ten, so that the minimum length scale plotted is $10\delta_x = 5c/\omega_p$. Consequently, the power spectrum shown in Fig. 4.6 lacks data at large wavenumbers (in the dissipative range); it covers about two decades, even though the grid size contains 1 080 cells along each its axis.

That timescale $t \sim 2.2\ell_c/c$ is shorter than that used in 2D PIC simulations for plotting purposes, because of the shorter duration of that 3D simulation. Consequently, the peak amplitude associated with the externally injected energy appears more prominent in the 3D simulation, and the powerlaw tail of the energy distribution has not yet reached the maximum energy fixed by the coherence length, of the order of several hundreds here.

To compute the probability density function of the correlation coefficients r_i plotted in Fig. 4.7, we have followed the test particle trajectories from $t \simeq 500\omega_p^{-1} \sim 2\ell_c/c$ up to $1500\omega_p^{-1} \sim 6\ell_c/c$, the final simulation time. As anticipated, the p.d.f. is sharply peaked around +1 for this 3D simulation, indicating a nice match between the energy variations predicted by the model and those observed in the simulation. The parallel compression term Θ_{\parallel} provides as before the leading contribution; the p.d.f. of the perpendicular force term is slightly biased toward positive values, as for the 2D forced turbulence simulation, while the inertial term does not show any clear signature, as in 2D. Interestingly, the correlation appears slightly enhanced when all force terms are taken together as in Eq. (2.73), compared to when they are taken one by one, at least for the case in which intervals of duration $1\ell_c/c$ are examined.

In Fig. 4.8, I present the temporal evolution of the energy of two test particles, which are fair representatives of their parent population. The dotted blue line shows the evolution of $\gamma(t)$, *i.e.*, the Lorentz factor of the particle as measured in the simulation frame. It displays characteristic oscillations associated with the gyromotion of the particle around magnetic field lines that move at velocity v_E : depending on the phase of that gyromotion, the particle motion is aligned or anti-aligned with

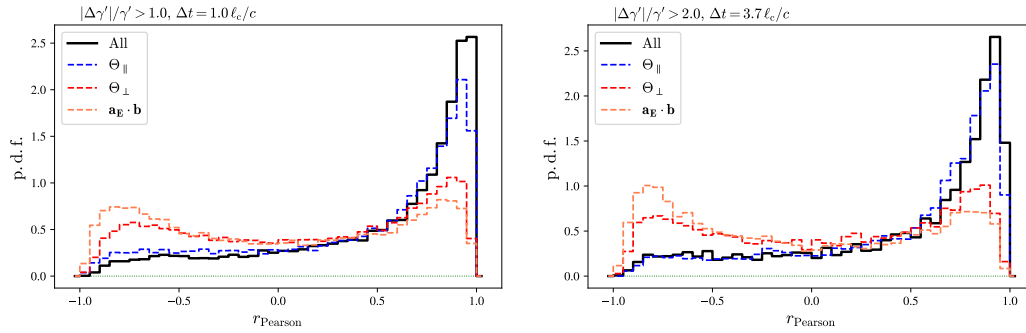


FIGURE 4.7: Histogram of correlation coefficients between the expected and observed evolution of γ' along chunks of test particle trajectories (left) and whole trajectory (right) with initial $25 < \gamma < 50$, for the 3D forced turbulence PIC simulation. This histogram shows that the combination of all force terms provides a good match to the observed variations. Among the three force terms, the parallel shear $\Theta_{||}$ provides the dominant contribution.

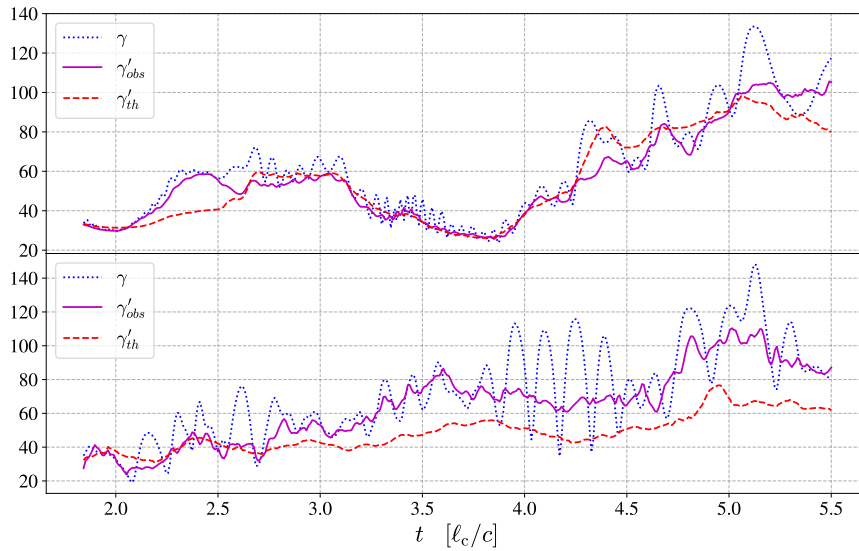


FIGURE 4.8: Example of the time evolution of the energy for two test particles, in the 3D forced turbulence simulation. In dashed blue: the energy of the particle as measured in the simulation frame; in solid purple: the particle Lorentz factor γ'_{obs} in the \mathcal{R}_E frame; in solid red: the Lorentz factor γ'_{th} as reconstructed using Eq. (2.73).

v_E , leading to a larger or smaller apparent energy in the simulation frame, see also Refs. [178, 51]. The period of those oscillations thus provides an estimate of $2\pi r_g/c$, which takes different values at different times, depending on the strength of the magnetic field and of the particle energy. The solid purple line shows the evolution of $\gamma'_{\text{obs}}(t)$, in the frame \mathcal{R}_E in which the motional electric field vanishes. The oscillations have disappeared and $\gamma'_{\text{obs}}(t)$ evolves as the particle gains or loses energy through Fermi processes. Finally, the dashed red line shows the reconstructed particle history $\gamma'_{\text{th}}(t)$, using Eq. (2.73) with initial condition $\gamma'_{\text{th}}(t_0) = \gamma'_{\text{obs}}(t_0)$ at the initial time $t_0 = 1.8 \ell_c/c$.

In the upper panel, we observe that the match between the reconstructed and the observed trajectories is rather tight in regions where the frequency of the oscillations increases, e.g. $3 \ell_c/c \lesssim t \lesssim 4 \ell_c/c$. This is not unexpected, insofar as an increase in the frequency of oscillations corresponds to a decrease in the particle gyroradius, and the model works to order r_g/ℓ_c . On the contrary, at later times $t \gtrsim 5 \ell_c/c$, the particle has achieved a larger energy, and it seemingly propagates in a region of lower-than-average magnetic strength, hence the ratio r_g/ℓ_c is no longer small compared to unity, as evidenced by the time scale of the oscillations. Deviations from the observed trajectory can thus be expected at that stage, although they remain rather mild.

In the lower panel, the energy history is well reconstructed at early times $t \lesssim 3 \ell_c/c$. We observe an offset in the vertical direction between the predicted and observed trajectories at later times, although those two histories maintain a rather strong degree of correlation. Had we chosen as initial time $t_0 \simeq 3 - 3.5 \ell_c/c$, we would thus have obtained a nice match to the observed history at late times. In effect, the departure between the model and the simulation is limited to the interval $\sim 2.7 - 3.3 \ell_c/c$, and likely related to some small scale effect. As mentioned before, this observation has motivated our choice to adopt two timescales for the comparison of the model to the simulations: one reduced timescale of the order of $1 \ell_c/c$, and one integrating over the whole history.

4.4 3D forced turbulence MHD simulation

Finally, we compare the model to trajectories of test particles that were tracked in the 3D forced MHD simulation of the JHU turbulence database [99, 58]. This 3D direct numerical simulation solves the incompressible MHD equations on a 1024^3 periodic grid with a time resolution $\Delta t \simeq 0.04 \Delta x$. The database output provides 1024 time snapshots, with sampling interval $10 \Delta t$. The simulation is visco-resistive, with magnetic Prandtl number unity, and magnetic Reynolds number $R_\lambda \sim 140$ at the Taylor scale $\lambda \sim 1.05 \times 10^{-2} L$; here, L represents the size of one side of the simulation cube and the Taylor scale is defined as $\lambda = (5 \int dk S_k / \int dk k^2 S_k)^{1/2}$, where S_k denotes the one-dimensional power spectrum of magnetic fluctuations. The Alfvén velocity is $v_A = 0.41c$ and the rms velocity $\langle \delta u^2 \rangle^{1/2} \simeq 0.4c$. The turbulence is excited through an external force acting on the velocity field at a stirring wavenumber $k_f \simeq 12.6 L^{-1}$. At the reference time $t = 0$, the simulation, as made available on the database, has already achieved a steady state.

The integral scale of the turbulence, as defined in the database, is $L_w \sim 0.1$ in units of the cube size. The simulation volume thus comprises many coherence cells of the turbulence, hence the effective dynamic range is restricted to $L_w/\delta x \sim 100$. The power spectrum of magnetic fluctuations is shown in Fig. 4.9, on the left. It

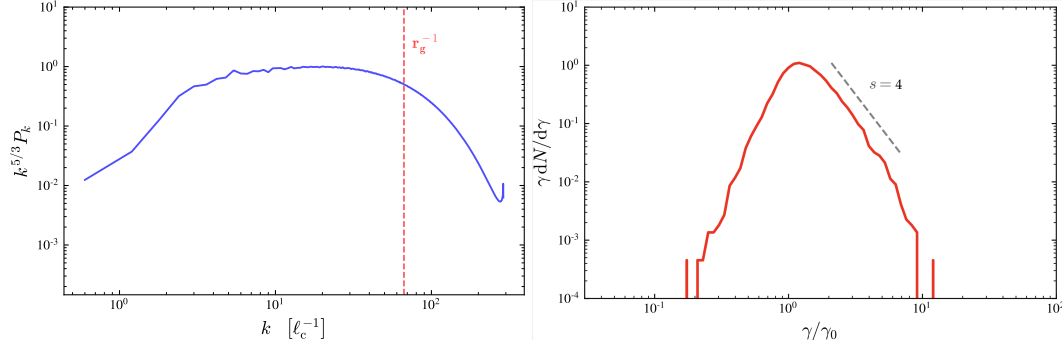


FIGURE 4.9: Left: magnetic power spectrum of the 3D MHD simulation, rescaled by $k^{5/3}$, vs wavenumbers in units ℓ_c^{-1} . The inverse gyroradius of the test particles is indicated by a dashed red line. It lies at the transition between the inertial and the dissipative range. Right: energy distribution of test particles propagated in the 3D MHD simulation, at a time $t \simeq 4 \ell_c/c$. At the initial time $t = 0$, all particles shared a common Lorentz factor γ_0 , corresponding to a gyroradius $r_g \simeq 0.02 \ell_c$. The spectrum takes a power law shape at large energies, with spectral index $s \simeq 4$, assuming $dN/d\gamma \propto \gamma^{-s}$.

correspondingly reveals a lack of power at wavenumbers $k \lesssim 3 \ell_c^{-1}$ followed by the $k^{-5/3}$ scaling in the inertial range. We adopt here $\ell_c = 0.1 L$.

We follow test particles with a gyroradius $r_g \simeq 2\Delta x$, in order to maintain r_g/ℓ_c as small as possible while preserving a reasonable reconstruction of the particle trajectory. As can be seen from Fig. 4.9, the inverse gyroscale r_g^{-1} lies at the transition between the inertial and the dissipative range. The effective rigidity is $2\pi r_g/\ell_c \sim 0.1$. Experiments conducted with a gyroradius twice as large provide similar results. We propagate 24 000 particles over $4.2 \ell_c/c \sim 200 r_g$; those particles were initialized with a common Lorentz factor (in the simulation frame), corresponding to the desired gyroradius, at random positions and velocity orientations. For each test particle, we integrate its trajectory over the duration of the simulation, using a numerical Monte Carlo code which, at each time step, queries the database to retrieve the values of the magnetic and velocity field at the particle location. The field values are determined at the particle spatial location using high-order (4th or 6th) Lagrangian interpolation. Although we sample the particle trajectory with a time step of $0.1 r_g/c$, we do not seek to interpolate the field values at the corresponding intermediate times, and rather use the values calculated from the nearest snapshot. Given that the typical velocity on the grid size is of the order of $(\Delta x/\ell_c)^{1/3} \langle \delta u^2 \rangle^{1/2} \sim 0.050 c$ – assuming a standard Kolmogorov scaling – this represents a reasonable approximation. This also allows us to maintain the computational time within reasonable limits, since computational time is here dominated by the queries to the database, which are performed online.

The code computes the electric field at the particle location using the ideal Ohm’s law, then advances the particle using a Boris pusher. All along the trajectories, we record the time and space derivatives of the magnetic and electric fields; the latter is computed from the magnetic and velocity derivatives. Those derivatives, provided by the database as 4th-order centered finite differencing, are used to calculate the quantities that enter the force terms in Eq. (2.73), as for the PIC simulation. The database does not directly provide time derivatives; those are thus calculated using first-order finite differencing from values obtained at consecutive times. We note that the force terms that enter Eq. (2.73) are dominated by the spatial derivatives in the sub- or mildly relativistic conditions of the present MHD simulation.

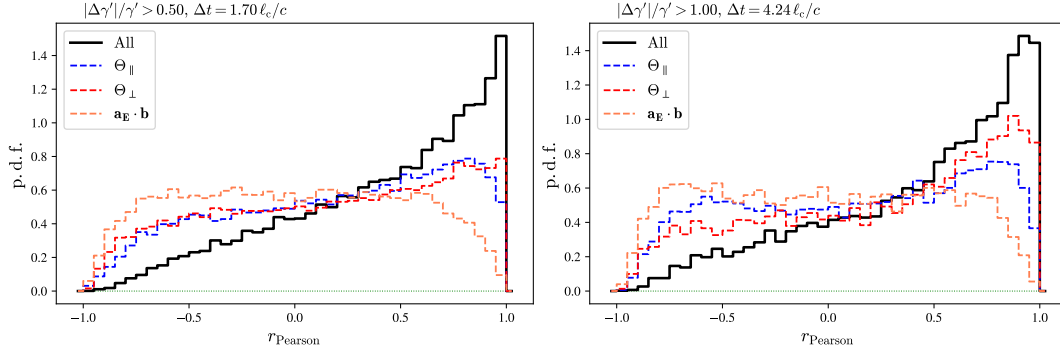


FIGURE 4.10: Histogram of correlation coefficients between the expected and observed evolution of γ' along blocks of the energy histories of test particles (left) and the whole history (right) that have been propagated in the 3D MHD simulation. The initial Lorentz factor for all particles is $\gamma(t=0) = 10$ (simulation frame).

In the right panel of Fig. 4.9, we plot the resulting energy distribution after a time $t \simeq 4 \ell_c/c$. It reveals a powerlaw tail at large momenta, as in the PIC simulation. To our knowledge, such a behavior had not been observed in time-evolving MHD simulations before. The spectral index $s \simeq -4$ is somewhat larger (in absolute value) than that observed in the PIC simulation, as expected for particle acceleration in a turbulence of smaller magnetization level [42, 90].

Fig. 4.10, contains the histograms of the correlation coefficients. As duration of integration and threshold of energy variation, we have adopted $\Delta t \simeq 1.7 \ell_c/c$ and $|\Delta\gamma'|/\gamma' > 0.5$ in a first case (Fig. 4.10 on the left), $\Delta t \simeq 4.2 \ell_c$ and $|\Delta\gamma'|/\gamma' > 1$ in a second one (Fig. 4.10 on the right). The lower threshold in energy variation and longer duration of the interval, comparatively to the PIC simulations, are meant to compensate for slower acceleration in the present simulation.

We recover here a high degree of correlation, as observed in the 3D PIC simulation. Interestingly, that degree of correlation is, in the present case, substantially higher when all force terms are combined together using Eq. (2.73) to reconstruct $\gamma'_{\text{th}}(t)$, than when they are taken individually. We also note that both Θ_{\parallel} and Θ_{\perp} seem to provide contributions with a net positive degree of correlation, when taken individually, while the influence of $a_E \cdot b$ is not visible here. Interestingly, the degrees of correlation of Θ_{\perp} and Θ_{\parallel} appear to be of the same or order of magnitude, while the PIC simulations showed a clear dominance of Θ_{\parallel} . We cannot identify here the exact reason why that is so, but we speculate that this difference may indicate that their relative contribution depends on how the turbulence is driven: incompressible turbulence driven by external velocity fluctuations in the MHD case *vs* compressible turbulence driven by magnetic perturbations in the kinetic regime. Recent PIC simulations have similarly demonstrated that the efficiency of acceleration depends on the stirring procedure [187]. This difference may also be affected by the different velocity regimes (sub-relativistic for MHD, relativistic for PIC).

As regards the test of our model, we stress here the significance of observing such a significant degree of correlation for both 3D PIC and MHD simulations, up to the above difference in individual contributions: on the “large” length scales that we are interested in (comparatively to the kinetic scales), both should in principle reproduce the same physics of acceleration; however, both rely on different schemes of approximations. In particular, the MHD case neglects all kinetic effects and all deviations of Ohm’s law that are inherently included in PIC simulations.

4.5 Summary – conclusions

We have carried out a comprehensive benchmark of a recent model of non-resonant particle acceleration in magnetized turbulence against PIC, both in 2D and 3D geometry, simulations and a 3D (incompressible) MHD simulation, subject of the publication [22] in Physical Review D. This model describes energisation as the continuous interaction of the particle with the random velocity flow of the turbulence, in the frame of ideal MHD; it can thus be regarded as the direct generalization to a continuous turbulent flow of the original Fermi picture of discrete, point-like interactions [89, 90]. It does so by following the evolution of the particle momentum in the frame \mathcal{R}_E that moves with the magnetic field lines at velocity $\mathbf{v}_E = \mathbf{E} \times \mathbf{B}/B^2$, and where the electric field vanishes. This allows the sources of energy gains and losses to be related to the gradients of the velocity field \mathbf{v}_E , and more particularly to three main contributions: an inertial term $\mathbf{a}_E \cdot \mathbf{b}$, a longitudinal shear term Θ_{\parallel} and a perpendicular compressive mode Θ_{\perp} , the notions of longitudinal/perpendicular being defined relative to the mean magnetic field direction at that location. To lowest order in the ratio of particle gyroradius to coherence scale of the turbulence, r_g/ℓ_c , the evolution of the particle energy is captured by Eq. (2.73).

To test this theoretical model, we have conducted PIC simulations of 2D decaying turbulence, of 2D and 3D driven turbulence in the relativistic regime $v_A \sim c$, and we have made use of the 3D forced MHD simulation of the JHU-database. We have then followed the time histories of the energy for a large sample of particles and compared the observed time histories to those reconstructed by the model. For what regards the MHD simulation, we have propagated test particles through the simulation, properly taking into account the time evolution of the fields. In all simulations, we have selected particles whose inverse gyroradius corresponds to wavenumbers at or below the transition between the inertial and the dissipative range of the turbulence, in order to test the model in conditions in which it applies, namely a ratio r_g/ℓ_c as small as possible and near-MHD conditions. To obtain the reconstructed particle histories, we have extracted from the simulations the quantities $\mathbf{a}_E \cdot \mathbf{b}$, Θ_{\parallel} and Θ_{\perp} then used Eq. (2.73) at each point along the particle trajectory to integrate in time the particle energy using Eq. (2.73). As detailed in Section 2.2.4, those terms correspond to, respectively, the acceleration of the non-inertial frame where the electric field vanishes projected on the magnetic field direction, shear acceleration along the direction of the magnetic field line due to the curvature of the field, shear acceleration of the field line velocity field in the plane transverse to the magnetic field. We have then computed for each particle trajectory a Pearson correlation test between the two histories (observed vs reconstructed), then derived from the sample of particles a probability density of the correlation coefficients r . A perfect adequation of the model to the data would translate in a probability density sharply peaked around +1, while an complete inadequacy would rather yield a featureless, roughly uniform histogram over the interval $[-1, +1]$. We have verified the adequacy of this procedure using Monte Carlo simulations of test-particle transport in a synthetic turbulence composed of a sum of linear eigenmodes of the plasma, see App. A.

Our main result is that we observe a clear-cut correlation between the model predictions and the numerical experiments, with histograms of the Pearson correlation coefficients distinctly peaked around +1, for all numerical simulations. This indicates that the non-resonant model can successfully account for the bulk of particle energisation through stochastic Fermi processes. Let us recall here that particle acceleration in a magnetized turbulence appears to proceed in two distinct stages: an

injection into the non-thermal population through non-ideal electric fields, then acceleration à la Fermi up to much higher energies [42, 43]. The model and the tests we have performed thus apply to the second stage, where the influence of non-ideal electric fields can be neglected.

In our PIC numerical simulations, we observe that the longitudinal shear term Θ_{\parallel} appears to provide the dominant contribution to particle energisation, because the correlation histogram when neglecting the other two force terms in the theoretical reconstruction of the energy histories lies close to that obtained when considering all force terms. This longitudinal shear term can be depicted as a form of slingshot acceleration in a moving, curved magnetic field, as in the Fermi type-B interaction of the original Fermi model [60]. Contrariwise, the MHD simulation reveals about similar degrees of correlation of Θ_{\perp} and Θ_{\parallel} , with a slight preference for the former, which characterizes magnetic mirroring effects, or type-A Fermi interactions. This MHD simulation also shows a significantly higher degree of correlation when all contributions are summed together as in the model Eq. (2.73) than when only one force term is considered individually, and the other two discarded.

This difference in contributions between the MHD and the PIC simulations suggests that the physics of acceleration, in particular the dominant energisation process, depends on the stirring process, on the nature of the turbulence and/or the velocity regime: while the (sub-relativistic) turbulence of the MHD simulation is by construction incompressible and forced through solenoidal velocity motions, the (relativistic) turbulence in the PIC simulations is compressible and driven through external magnetic perturbations. A dependence of the energy distribution of accelerated particles on the stirring process (solenoidal vs compressible) has been noted before in Ref. [187].

Chapter 5

Weibel-mediated relativistic shocks

We described in chapter 2 how particles are accelerated at shock fronts and how the efficiency of acceleration varies with the magnetisation and the Lorentz factor of the shock. For relativistic shocks, the accelerated particles moving upstream at some angle with the shock front normal will be rapidly overtaken by the shock and sent downstream [4]. The shock precursor is hence quite limited in extension and the development of plasma instabilities is possible only if their growth rate is large enough [95]. In the relativistic regime of weakly magnetised ($\sigma \ll 10^{-4}$ for the ambient medium) collisionless shocks, the dominant instability in the upstream precursor is the current filamentation instability (CFI), e.g. [25, 23, 93, 92]. In weakly magnetised shock simulations, the magnetic energy density is generally observed to reach a few percent of the available kinetic energy density, see Fig. 5.1 [91]. This suggests that some form of saturation has been attained, and that the physics probed in such precursors through PIC simulations could in principle be extrapolated over arbitrarily long length scales, i.e. astrophysical scales. Yet, the saturation mechanisms are still debated and their understanding is crucial as saturation controls the production of high-energy particles and radiation in such environments. However, saturation mechanisms have mostly been studied in symmetric configurations (characterized by counterstreaming flows of equal densities, temperatures and Lorentz factors) that are irrelevant to relativistic shock precursors, where (as seen in the shock's rest frame) a dilute beam of relativistically hot, suprathermal particles interacts with a colder and denser, inflowing background plasma.

In 1959 Weibel realized that within a plasma at rest characterised by a distribution function with anisotropic thermal velocities, purely transverse waves can grow exponentially along the lower-temperature axis [176]. The same year, Fried showed that counterstreaming cold plasma beams are also subjected to modulations growing normal to the flow distribution function [64]. An analogy then exists between an anisotropic Weibel-unstable hot plasma and a cold filamentation-unstable two-stream system, so that filamentation and "Weibel" instabilities are used almost interchangeably in the literature. To understand how the instability generally develops let us consider for simplicity two cold electron flows initially moving along the $+x$ and $-x$ directions in the presence of an oscillating seed magnetic field polarized along the z -axis. The Lorentz force deflects the electron trajectories as shown by the dashed lines in Fig. 5.2. As a result, the electrons moving to the right and those moving to the left will concentrate in neighbouring magnetic nodes. Current sheaths thus form and the magnetic field they induce add up onto the seed fluctuations.

In the context of astrophysical shocks, the CFI is triggered by the suprathermal particles reflected at the shock counterstreaming against the background plasma in the shock precursor. For a pair plasma, the electrons of one population (either the beam of the suprathermal reflected component or the inflowing background plasma) are pinched together with positrons of the other, making up alternating-sign current

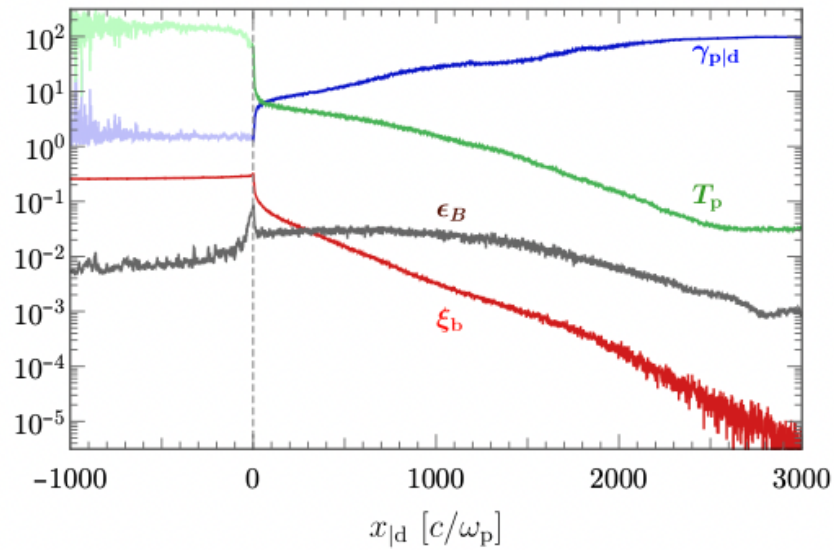


FIGURE 5.1: Spatial profiles of the Lorentz factor of the background plasma as evaluated in the downstream frame (in blue), proper temperature (in green), pressure of the suprathermal beam (in red) and energy density of the microturbulence (in grey), for a 2D3V PIC simulation of $\gamma_{\infty|d} = 100$. Taken from [91].

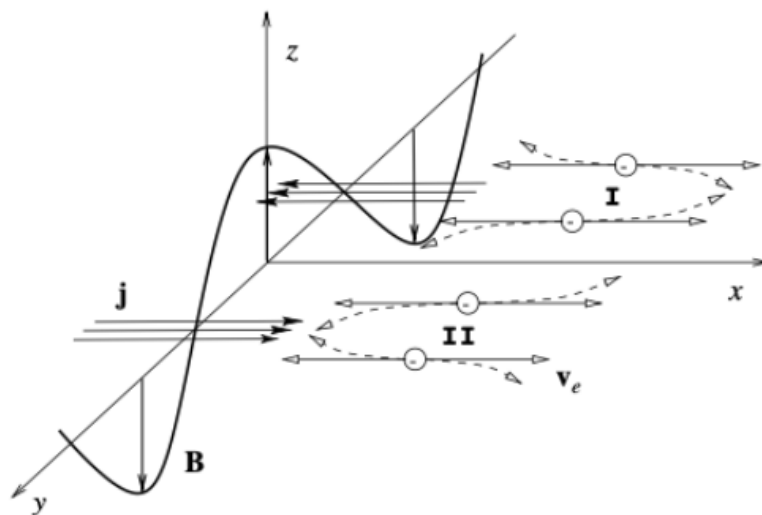


FIGURE 5.2: Schematic representation of the Weibel instability. Taken from [109].

density filaments which exert a positive feedback on the initial magnetic perturbation, sustaining the development of the instability. The aim of the study conducted in this Chapter has been to identify the relevant criterion of saturation in asymmetric configurations, at present poorly investigated, where there is a further ambiguity on which specie, the plasma or the background plasma, determines the end of the magnetic field growth.

5.1 Basic features of the current filamentation instability

If we assume initial charge and current neutrality in the system, and we express every quantity ξ , be it a vector or a scalar, as the sum of the equilibrium value ξ_0 and a perturbation $\xi_1 \ll \xi_0$:

$$\xi = \xi_0 + \xi_1 \exp(i\mathbf{k} \cdot \mathbf{r} - i\omega t), \quad (5.1)$$

the combination of Maxwell-Faraday's and Maxwell-Ampère's equations gives

$$\mathbf{k} \times (\mathbf{k} \times \mathbf{E}_1) + \frac{\omega^2}{c^2} \left(\mathbf{E}_1 + \frac{4i\pi}{\omega} \mathbf{J}_1 \right) = 0. \quad (5.2)$$

Perturbations of the form (5.1) spontaneously arise in a plasma possibly turning unstable. Further linearising the distribution function, whose evolution is described by the Vlasov equation (3.1), one can finally obtain the expression

$$\left(\frac{\omega^2}{c^2} \epsilon(\mathbf{k}, \omega) + \mathbf{k} \otimes \mathbf{k} - k^2 \mathbf{I} \right) \cdot \mathbf{E}_1 \equiv \mathbf{D}(\mathbf{k}, \omega) \cdot \mathbf{E}_1 = 0, \quad (5.3)$$

where \mathbf{I} is the unity tensor and $\mathbf{k} \otimes \mathbf{k}$ the tensorial product $k_i k_j$. The dielectric tensor $\epsilon_{ij}(\mathbf{k}, \omega)$ elements read

$$\epsilon_{ij}(\mathbf{k}, \omega) = \delta_{ij} + \sum_{\alpha} \frac{\omega_{p\alpha}^2}{\omega^2} \int \int \int d^3 p \frac{p_i}{\gamma(\mathbf{p})} \frac{\partial f_{\alpha}^{(0)}}{\partial p^j} \quad (5.4)$$

$$+ \sum_{\alpha} \frac{\omega_{p\alpha}^2}{\omega^2} \int \int \int d^3 p \frac{p_i p_j}{\gamma^2(\mathbf{p})} \frac{\mathbf{k} \cdot \partial f_{\alpha}^{(0)} / \partial \mathbf{p}}{m_{\alpha} \omega - \mathbf{k} \cdot \mathbf{p} / \gamma(\mathbf{p})}, \quad (5.5)$$

where the (non-relativistic) plasma frequency of the species $\alpha \in (\mathbf{b}, \mathbf{p})$ is defined as $\omega_{p\alpha} = (4\pi n_{\alpha} e^2 / m_{\alpha})^{1/2}$, with n_{α} denoting the proper density. The dispersion relation follows from Eq. (5.3) and is given by solving

$$\det \mathbf{D}(\mathbf{k}, \omega) = 0. \quad (5.6)$$

If ω_k are the complex roots of this equation, for a given real wave vector \mathbf{k} the related modes have their electric field lying in the linear subspace defined by $\mathbf{D}(\mathbf{k}, \omega_k) \cdot \mathbf{E}_1 = 0$. Purely electromagnetic modes verify $\mathbf{k} \cdot \mathbf{E}_1 = 0$ and purely electrostatic modes are characterised by $\mathbf{k} \times \mathbf{E}_1 = 0$.

Let us now consider a 2D3V (2D in space, 3D in momentum) problem where the beam (subscript b) and the plasma (subscript p) flow along the $+x$ and $-x$ directions, respectively. The momentum distribution functions of both populations will be assumed even along the p_y and p_z directions. Without loss of generality, the wave vector will be defined as $\mathbf{k} = (k_x, k_y) \equiv (k_{\parallel}, k_{\perp})$. For such a wavevector, the solutions of Eq. (5.6) belong to two branches [25]. The first one, fully electromagnetic in

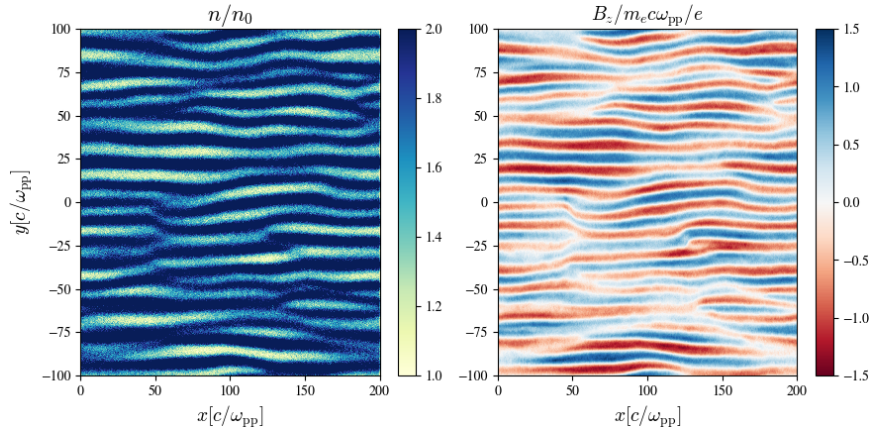


FIGURE 5.3: 2D maps of particle density (left) and magnetic field (right) in the linear stage of the current filamentation instability extracted from PIC simulations of counterstreaming asymmetric plasma along x . The parameters of the beam-plasma system are those of run a) in Tab. 5.1.

nature, fulfills the dispersion relation,

$$\omega^2 \epsilon_{zz} - c^2 k^2 = 0, \quad (5.7)$$

and is characterized by $\mathbf{E}_1 \parallel \mathbf{z}$. The second one, of mixed electromagnetic/electrostatic nature, obeys the dispersion relation

$$(\omega^2 \epsilon_{yy} - c^2 k_x^2)(\omega^2 \epsilon_{xx} - c^2 k_y^2) - (\omega^2 \epsilon_{xy} - c^2 k_x k_y)^2 = 0, \quad (5.8)$$

and is characterized by \mathbf{E}_1 in the $x - y$ plane with $\mathbf{k} \cdot \mathbf{E}_1 \neq 0$. We will concentrate on this branch in the following.

In the relativistic regime, the dominant unstable modes pertain to two main classes [24, 25]: (i) the quasi-electrostatic, propagating oblique two-stream instability (OTSI) with $k_\perp \gtrsim k_\parallel \simeq \omega_{pp}/c$ and $\Re\omega \simeq \omega_{pp}$; (ii) the quasi-magnetic, non-propagating, current filamentation instability (CFI) with $k_\parallel \ll k_\perp$ and $\Re\omega \simeq 0$. Taking $k_\parallel \equiv k_x = 0$, the dispersion relation of the CFI reads:

$$\epsilon_{yy}(\epsilon_{xx} - c^2 k_\perp^2 / \omega^2) = \epsilon_{xy}. \quad (5.9)$$

The CFI is associated with an inductive E_\parallel field component (along the beam flow) and an electrostatic E_\perp component (along the wave vector). Under conditions relevant to relativistic shock precursors the inductive component can be neglected because its magnitude is of the order of $|\Im\omega/k_\perp c| \ll 1$ relative to the magnetic field component. The density and field modulations generated in a beam-plasma system governed by the CFI are illustrated by the PIC simulation results shown in Fig. 5.3: the instability develops through the pinching of the counterstreaming plasmas into filamentary structures oriented along \hat{x} , each endowed with a net current. These structures are surrounded by perpendicular (along z) magnetic fields $\delta\mathbf{B}_\perp$ and perpendicular (along y) electric fields $\delta\mathbf{E}_\perp$. The dominance of the magnetic component means $\delta B_\perp^2 - \delta E_\perp^2 > 0$ for each unstable wavenumber \mathbf{k}_\perp , and hence that there exists a frame, moving at velocity (in units of c)

$$\beta_w = \frac{\delta\mathbf{E}_\perp \times \delta\mathbf{B}_\perp}{\delta B_\perp^2}, \quad (5.10)$$

in which the transverse electric field component vanishes. In this frame, which is called the “Weibel frame”, the CFI can be regarded as purely magnetic, up to the weak inductive component which cannot be erased by a Lorentz boost. This frame is discussed in detail in Ref. [122], and we will recap in the following its most salient features.

In the precursor of relativistic shocks, this frame gains special importance because the interaction between the beam of accelerated particles and the background plasma is so asymmetric that, as seen by the beam reference frame, $\beta_w \simeq 1$, meaning $\delta E_\perp \simeq \delta B_\perp$. It is crucial to properly characterize this frame, as it is where particles undergo elastic interactions in the course of their acceleration and it controls the heating and slowdown of the background plasma [91]. Hence, the Weibel frame is connected to acceleration processes and has direct phenomenological consequences. In the limit of a symmetric configuration, the frame must coincide with the lab frame.

5.1.1 The Weibel frame

Let us now consider a set of initial beam $\{n_b, T_b, u_{b|r}\}$ and plasma $\{n_p, T_p, u_{p|r}\}$ parameters, where $u_{\alpha|r} \equiv \gamma_{\alpha|r}\beta_{\alpha|r}$ denotes the x -component of the four-velocity of species α , and $\beta_{\alpha|r}$ and $\gamma_{\alpha|r}$ are the associated normalized three-velocity (in units of c) and Lorentz factor, all defined in some reference frame (subscript $|r$). We use proper densities, n_α , and proper temperatures, T_α unless explicitly specified otherwise. By convention, the beam corresponds to the population with the lower relativistic plasma frequency. The latter is defined as (cgs-Gauss units are used throughout, with $c \neq 1$)

$$\Omega_{p\alpha} = \left(\frac{4\pi n_\alpha e^2}{\tilde{w}_\alpha / c^2} \right)^{1/2}, \quad (5.11)$$

where e is the elementary charge and \tilde{w}_α the enthalpy per particle of charged species $\alpha \in \{b+, b-, p+, p-\}$ in its initial state. Note that, in our notations, n_α refers to a single charged species; it thus represents half of the initial total number density of the corresponding component (beam or plasma). Introducing the corresponding particle mass m_α , adiabatic index $\hat{\Gamma}_\alpha$ and proper temperature T_α , one has $\tilde{w}_\alpha = m_\alpha c^2 + \hat{\Gamma}_\alpha k_B T_\alpha / (\hat{\Gamma}_\alpha - 1)$. This implies $\tilde{w}_\alpha \simeq m_\alpha c^2$ for a plasma of subrelativistic temperature, $k_B T_\alpha / m_\alpha c^2 \ll 1$, and $\tilde{w}_\alpha \simeq \hat{\Gamma}_\alpha k_B T_\alpha / (\hat{\Gamma}_\alpha - 1)$ for a relativistically hot plasma, $k_B T_\alpha / m_\alpha c^2 \gg 1$. Given the inverse normalized temperature of species α , $\mu_\alpha \equiv m_\alpha c^2 / (k_B T_\alpha)$, one has $\tilde{w}_\alpha \simeq m_\alpha c^2$ and $\Omega_{p\alpha} \simeq \omega_{p\alpha}$ for a plasma of nonrelativistic temperature ($\mu_\alpha \gg 1$), but $\tilde{w}_\alpha \simeq \hat{\Gamma}_\alpha k_B T_\alpha / (\hat{\Gamma}_\alpha - 1)$, and hence $\Omega_{p\alpha} \simeq \omega_{p\alpha} \sqrt{\mu_\alpha} / 2$ (taking $\hat{\Gamma}_\alpha = 4/3$) for a relativistically hot plasma ($\mu_\alpha \ll 1$).

The corresponding Weibel frame velocity can be determined in the following two ways.

In the linear phase of the CFI, one can define the Weibel frame as that in which the electrostatic component of the dispersion relation vanishes. This has been done in Ref. [136] in the subrelativistic regime, and in Refs. [122, 91] in the relativistic regime. This is not a trivial step, as the dielectric tensor itself depends on the solution to the dispersion relation, see Ref. [122] for a discussion of the procedure.

Alternatively, one can describe the nonlinear phase of the instability as a quasistatic equilibrium between particles and fields, ordered along the transverse y -direction in a periodic sequence of current filaments. In a four-fluid (isothermal) description, the density of each component at equilibrium can be written as a function of the electromagnetic potentials, see Ref. [167] for details. Setting the electrostatic contribution to zero imposes a relationship between the physical characteristics of

the fluid, in the form

$$\frac{n_b \gamma_{b|w}^2 \beta_{b|w}}{T_b} + \frac{n_p \gamma_{p|w}^2 \beta_{p|w}}{T_p} = 0, \quad (5.12)$$

where the normalized x -velocities $\beta_{\alpha|w}$ and Lorentz factors $\gamma_{\alpha|w}$ are here measured in the Weibel frame. The above equation can be solved to obtain the velocity of the Weibel frame in the reference frame. As it turns out, both linear and nonlinear approaches give similar expressions for this velocity under conditions relevant to the precursor of relativistic shocks. Here, we rely on the latter method and make the result explicit, as follows.

Writing $\beta_{\alpha|w}$ and $\gamma_{\alpha|w}$ in terms of $\beta_{\alpha|r}$ and $\gamma_{\alpha|r}$ through standard Lorentz transforms, one finds that the Weibel frame velocity, relative to the reference frame, can be expressed as

$$\beta_{w|r} = \frac{Q_w - \sqrt{Q_w^2 - 4}}{2}, \quad (5.13)$$

where

$$Q_w = \frac{n_b \gamma_{b|r}^2 (1 + \beta_{b|r}^2) / T_b + n_p \gamma_{p|r}^2 (1 + \beta_{p|r}^2) / T_p}{n_b \gamma_{b|r}^2 \beta_{b|r} / T_b + n_p \gamma_{p|r}^2 \beta_{p|r} / T_p}. \quad (5.14)$$

The minus sign in Eq. (5.13) reflects the fact that $\beta_{w|r} \simeq \beta_{p|r}$ if the beam component becomes negligible: the turbulence is then mostly magnetic in the rest frame of the background plasma. Once $\beta_{w|r}$ is known, the velocity of each species in a given reference frame can be Lorentz transformed to the Weibel frame.

In the remaining of this Chapter, all velocities or Lorentz factors that do not carry a subscript $|r$ are understood to be defined in the Weibel frame.

5.1.2 Linear stage of the CFI growth

In the early linear stage of the instability, oppositely charged particles from each component of the system (beam or plasma), deflected by magnetic field fluctuations with a polarity perpendicular to their initial drift velocity, focus in different regions, forming “current filaments”. Particles of opposite charges concentrate in the same filaments, their currents add up and the initial magnetic field perturbation is amplified, developing the instability. Each mode grows as

$$\delta B_z(k_{\perp}) = \delta B_0(k_{\perp}) e^{\Gamma_w(k_{\perp}) t}, \quad (5.15)$$

where $\delta B_0(k_{\perp})$ is the seed magnetic field fluctuation and Γ_w the k -dependent growth rate. Assuming that the magnetic spectrum ends up being dominated by modes of similar growth rate and seeded by comparable fluctuations, one can infer the instantaneous growth rate through

$$\Gamma_w = \frac{1}{2} \frac{d}{dt} \ln \left[\frac{\langle \delta B_z(t)^2 \rangle}{\langle \delta B_z(0)^2 \rangle} \right]. \quad (5.16)$$

The quantity in the rhs can be easily extracted from numerical simulations and directly compared with analytic estimations of Γ_w . The latter involve rather heavy calculations of the dielectric tensor (5.5) contained in the kinetic dispersion relation of which we will summarize here only the general key points.

As shown in Ref. [122], approximate growth rates of the CFI can be obtained in two asymptotic limits that depend on the value of the parameter $\chi_{\alpha} = \gamma_{\alpha} |\zeta| / \sqrt{1 - \zeta^2}$,

where $\zeta = \omega/k_{\perp}c$ and $\omega = i\Gamma_w$. For each plasma species, we define the *hydrodynamic* limit in which the thermal velocity spread of the distribution function is, broadly speaking, smaller than the (imaginary) “phase velocity” of the waves, and the opposite *kinetic* limit. More precisely, the hydrodynamic (resp. kinetic) limit for the cold plasma component corresponds to $\tilde{\chi}_p \equiv \chi_p \sqrt{\mu_p/2} \gg 1$ (resp. $\ll 1$). For the relativistically hot beam component, the hydrodynamic (resp. kinetic) limit is rather defined as $\chi_b \gg 1$ (resp. $\ll 1$), see [122] for details.

We can thus derive two useful approximations of the maximum growth rate and associated wave number in terms of the nonrelativistic plasma frequencies of the plasma species, one in the fully kinetic regime – meaning the kinetic approximation for both species – and one in the combined hydrodynamical (beam) and kinetic (plasma) regimes, respectively,

$$\begin{aligned}\Gamma_{w,k-k} &\simeq \frac{(\omega_{pb}^2 \mu_b)^{3/2} \gamma_{b|p}^3 \beta_{b|p}^3}{\sqrt{2\pi\mu_p \omega_{pp}^2 + \frac{3\pi}{2}\omega_{pb}^2 \mu_b \gamma_{b|p}^3}}, \\ k_{\perp,w,k-k} &\simeq \sqrt{\frac{2}{3}\mu_b \gamma_{b|p} \omega_{pb}},\end{aligned}\quad (5.17)$$

and

$$\begin{aligned}\Gamma_{w,k-h} &\simeq \sqrt{\omega_{pb}^2 \mu_b}, \\ k_{\perp,k-h} &\simeq (2\pi\omega_{pb}^2 \mu_p \mu_b)^{1/6} \omega_{pp}^{2/3}.\end{aligned}\quad (5.18)$$

The quantities $\beta_{b|p}$ and $\gamma_{b|p}$ represent the normalized three-velocity of the beam relative to the plasma and its corresponding Lorentz factor. It is important to stress that the above formulae have been derived solving the dispersion relation of the CFI instability, Eq. (5.9), assuming a cold plasma ($k_B T_p \ll m_{\alpha} c^2$) and a relativistically hot beam ($k_B T_b \gg m_{\alpha} c^2$) in the dielectric tensor. Furthermore, those approximations assume that the plasma moves at subrelativistic velocities with respect to the Weibel frame; consequently, it neglects terms of order $\mathcal{O}(\beta_{p|w})$. Those formulas encompass the majority of the situations addressed by means of PIC simulations in the following; if not, this will be made explicit.

5.1.3 Saturation of the CFI

The linear stage of the CFI corresponds to particle trajectories remaining ballistic to leading order, an approximation which holds provided the growing fields remain weak enough. When this is no longer true, the particle trajectories can be strongly modified by the fields and saturation mechanisms take place, slowing or halting the instability development. Ultimately, the CFI enters a strongly nonlinear stage, in which secondary instabilities, such as the merging of filaments of equal polarity, or the kink of current filaments, can arise, see Ref. [167] for a detailed discussion. The transition between these two phases, i.e., saturation and the strongly nonlinear stage, is fraught with ambiguities, as filaments can coalesce while the current filaments keep building up through the CFI. The mechanisms that lead to the saturation of the CFI are still debated and they will be presented in the following.

Transverse trapping

The widely used trapping-based saturation criterion, first proposed by Davidson in the nonrelativistic regime [47], and later generalized to the relativistic regime [183,

[103, 5, 78], expresses the fact that, in the weakly nonlinear phase of the CFI, particles quiver transversely around the center of the filament (i.e., around a magnetic field node) in which they are focused. Assuming a harmonic B -field profile of amplitude B and wavenumber k_{\perp} , a particle of Lorentz factor γ and mass m oscillates at the bounce frequency

$$\omega_B = \left(\frac{ek_{\perp}\beta_{\parallel}B}{\gamma m} \right)^{1/2}. \quad (5.19)$$

The onset of saturation can be viewed as when the assumption of zero-order ballistic particle motion no longer holds. This occurs when ω_B becomes comparable with the instability growth rate, Γ_w . Introducing $\langle\gamma\rangle$ the typical Lorentz factor of the considered species, the corresponding saturation magnetic field can thus be expressed as

$$B_t = \frac{\Gamma_w^2 \langle\gamma\rangle m}{k_{\perp} \beta_{\parallel} e}. \quad (5.20)$$

Magnetization limit

In the nonlinear phase of the CFI, the plasma can be modelled as an ensemble of cylindrical filaments of radius $r \simeq \lambda_{\perp}/4 \simeq \pi/2k_{\perp}$, carrying a current density j . As the B -field grows in amplitude, the Larmor radius of the particles, $r_L = \gamma\beta mc^2/eB$, shrinks, possibly up to the point where it becomes smaller than the filament radius. Particles then become *spatially trapped* within the filaments in both the longitudinal and transverse directions, while orbiting around the B -field extrema. In the literature, this limit is often referred to as the ‘‘Alfvén limit’’ [79]. Similarly, particles gyrating at a Larmor frequency $\omega_L = eB/m\gamma$ higher than the instability growth rate can be regarded as *temporally magnetized*. In either case, the linear approximation, which assumes rectilinear motion across the filaments, breaks down. The maximum value of the magnetic field set by this condition is then given by

$$B_m = \max(B_{m,r_L}, B_{m,\omega_L}), \quad (5.21)$$

where

$$B_{m,r_L} = \frac{2}{\pi} k_{\perp} \langle\gamma\beta\rangle \frac{mc^2}{e} \quad (5.22)$$

satisfies the spatial constraint and

$$B_{m,\omega_L} = \Gamma_w \langle\gamma\rangle \frac{mc}{e} \quad (5.23)$$

the temporal one. Since the CFI is characterized by $\Gamma_w \ll k_{\perp}c$ in relativistic shock precursors [122], it follows that usually $B_m \equiv B_{m,r_L}$ if $\beta \sim 1$. Similar saturation criteria were considered in [113, 109, 103, 26].

Particle current limit

The magnetic field is also bounded by above by the maximum current density that can sustain it [79]. This maximum current density corresponds to the current carried by one of the two oppositely charged species making up the component (i.e., beam or plasma) under study. This limit thus tacitly assumes that, at maximum magnetic field, all the particles of a given component within a transverse length $\lambda_{\perp}/2$ have undergone complete spatial separation in two adjacent filaments. Assuming these have a uniform current density, the B -field created by a charged species of initial

apparent density γn (with γ characterizing here the drift motion) has a maximum strength

$$B_p \simeq 2\pi^2 \frac{e\gamma n}{k_\perp} \langle \beta_\parallel \rangle. \quad (5.24)$$

In the case of complete spatial separation, the contributions of counterstreaming species of opposite charge should add up within a filament. In an asymmetric configuration, only the particle limit associated with the component that carries most, if not all of the particle current density, matters.

Most studies on the saturation of the CFI, and, to our knowledge, all those related to relativistic astrophysical systems, have considered symmetric configurations in which the interpenetrating plasmas share similar characteristics (i.e., identical temperatures, densities and drift velocities).

The hierarchy among the above saturation criteria depends on the characteristic wave number of the instability and the growth rate, given that

$$\frac{B_t}{B_p} \sim \left(\frac{\Gamma_w}{\omega_p} \right)^2, \quad (5.25)$$

$$\frac{B_m}{B_p} \sim \left(\frac{k_\perp c}{\omega_p} \right)^2, \quad (5.26)$$

where ω_p represents here the nonrelativistic plasma frequency of the component to which the saturation criterion is applied, and k_\perp denotes the dominant transverse wavenumber. Considering first a cold symmetric counterstreaming configuration, one has $\Gamma_w \sim \omega_{pp}$ and $k_\perp \gg \omega_{pp}/c$ to leading order, e.g. [177, 24]. As a consequence, $B_t \simeq B_p \ll B_m$, implying that the trapping and particle limits are equivalent and determine saturation. For symmetric counterstreaming hot plasmas, Γ_w is reduced to values below ω_{pp} , because it scales with the relativistic plasma frequency $\Omega_p = \omega_p \sqrt{\mu}/2$ and $\mu \ll 1$. Consequently, the trapping criterion is expected to become more stringent than the other two. In addition, a relativistic temperature likely prevents the oppositely charged species of a given component from fully segregating from each other within a filament, further weakening the particle limit in this regime.

5.2 Saturation of the CFI in asymmetric plasma flows

The goal of our study, published in Physical Review E [21], is to determine which saturation criterion for the CFI holds under asymmetric conditions typical of relativistic shock precursors, and whether this criterion applies to the beam or to the background plasma. Indeed, a key difference with symmetric counterstreaming plasmas, which are more commonly envisaged, is the ambiguity, arising in the asymmetric configuration, of which component (beam or plasma) is eventually responsible for the saturation, and through which mechanism.

In an asymmetric configuration, one has to identify distinct saturation limits for the beam and the plasma, the respective superscripts ^b and ^p will be used in the following. As a general trait of such configurations, we observe that the beam moves at relativistic velocities in the Weibel frame, while the drift of the background plasma is most often sub- or mildly relativistic. This can be read off Eq. (5.12), which relates the quantities $n_b/T_b \propto \Omega_{pb}^2$ and $n_p/T_p \propto \omega_{pp}^2 \mu_p$. The beam is usually defined as the component with the smaller plasma frequency of the two, hence $\Omega_{pb} \ll \omega_{pp}$ suggests that $\gamma_{b|w}^2 |\beta_{b|w}| \gg \gamma_{p|w}^2 |\beta_{p|w}|$. Therefore, one must expect $B_t^b \gg B_t^p$.

We anticipate that, for what concerns saturation through trapping, only the larger of the two values B_t^b and B_t^p matters, and this trend will be confirmed by the simulations.

We also expect, for the same reasons as above, that $B_t^b < B_p^b$ and $B_t^b \ll B_m^b$, because of the large temperature of the beam. Consequently, we may anticipate that the overall criterion for saturation will be set by the trapping limit of beam particles.

The saturation is defined as the point at which the growth of the magnetic energy density is halted, or at least significantly reduced. The temporal evolution of the magnetic field as extracted from fully periodic particle-in-cell simulations of initially unmagnetized, collisionless plasmas, is compared to the different criteria of saturation presented above. For most of the study, we considered plasmas composed of equal mass species, interpenetrating each other at a relativistic velocity. This configuration is typical of the precursor of a relativistic shock propagating in a pair plasma, but it is also relevant for the study of the CFI in asymmetric electron-electron or ion-ion flows. The study has also been extended to the case of electron-ion plasmas, in the ultrarelativistic and mildly relativistic regimes.

The simulations are initialised in the Weibel frame associated with the initial configuration of the plasma-beam system. As the beam-plasma parameters evolve in time during the run, the simulation frame departs from the Weibel frame at time $t = 0$. In any case, this frame still provides the most convenient choice to study the development of the instability: in that frame, the CFI mode is essentially magnetic in nature, meaning that the magnetic fluctuations overwhelm the electric ones, $\delta B_\perp \gg \delta E_\perp$. This provides a clear way to identify the CFI as the leading mode, and to define the saturation point where δB halts or slows its growth. Furthermore, the saturation criteria introduced above are all defined under the assumption that $\delta B_\perp \gg \delta E_\perp$. It is easy to show that the center of mass (cm-) frame $|_{\text{cm}}$ (such that $\gamma_{b|\text{cm}}^2 \beta_{b|\text{cm}}^2 w_b = \gamma_{p|\text{cm}}^2 \beta_{p|\text{cm}}^2 w_p$), generically moves at relativistic speeds with respect to the Weibel frame. Therefore $\delta B_\perp \sim \delta E_\perp$ in that frame, making the identification of the CFI and the notion of saturation less obvious. Finally in the cm-frame, the growth timescale of the instability is enlarged by time dilation, requiring longer simulations.

5.2.1 PIC simulations results

I have performed a number of 2D3V (2D in space, 3D in momentum) PIC simulations of counterstreaming electron-positron pair plasmas, which initially obey Maxwell-Jüttner distribution functions, using the massively parallel CALDER code [87]. These simulations resolve the direction parallel to the plasma flows and one transverse direction, and use periodic boundary conditions in both directions. Such “in-plane” 2D configurations have been shown to reproduce more accurately the results of 3D simulations than “out-of-plane” 2D simulations restricted to the transverse plane [143, 158]. Good agreement between “in-plane” 2D and 3D geometries was also found in relativistic shock simulations, with plasma injection at one boundary of the domain [149]. Moreover, because they capture both CFI and OTSI modes, “in-plane” 2D simulations allow one to check the dominance of the CFI over electrostatic modes, in which case their results on the dynamics of the CFI have a broader range of validity than those of purely transverse simulations.

To resolve properly the initial CFI instability, the cell size is set to $\Delta x = \Delta y = 0.1 c/\omega_{\text{pp}}$ and the simulations are run over 2×10^4 time steps of $\Delta t = 0.099 \omega_{\text{pp}}^{-1}$ on a 2D (x, y) grid of 2000×2000 cells. Henceforth, ω_{pp} represents the nonrelativistic plasma frequency of each of the two charged species of the plasma component

in its initial state, i.e., $\omega_{pp} = (4\pi n_p e^2 / m_e)^{1/2}$ (m_e is the electron mass). Each cell contains initially 100 macro-particles per species, yielding a total number of about 10^9 macro-particles. Time and length are normalized to the inverse nonrelativistic plasma frequency ω_{pp}^{-1} and the plasma inertial length c/ω_{pp} . In order to suppress the numerical Čerenkov instability (see Chapter 3), which affects simulations of relativistic drifting plasmas, we used the Godfrey-Vay filtering scheme combined with the Cole-Karkkainen finite difference field solver [68] and multiple passes of binomial filtering [17, 169] in order to quench non-resonant and resonant modes, respectively. Our code has been extensively and successfully tested against Čerenkov heating, up to large values of drift Lorentz factors, e.g. [167, 91].

As previously mentioned, we aim to investigate the saturation of the CFI in an asymmetric interaction between a hot dilute beam and a cold, dense, inflowing plasma as it happens in the precursor of astrophysical collisionless shock waves in pair plasmas. For this reason, we initiate our study making use of parameters borrowed from a large-scale shock simulation corresponding to a relative upstream to downstream Lorentz factor of 10, as described in [91]. The parameters of the beam and plasma populations, as measured in the downstream shock frame, are as follows: $\gamma_{b|d} = 1.38$, $\gamma_{p|d} = 9.67$, $T_b = 45m_e c^2 / k_B$, $T_p = 0.2m_e c^2 / k_B$, and $n_b / n_p = 0.1$. Those values are extracted from a region deep inside the precursor of the shock, where the background plasma has been slightly slowed down and heated to mildly relativistic temperatures. As announced, we then transform those initial parameters from the downstream shock frame to the Weibel frame. This change of frame gives the set of parameters indicated by (a) in Table 5.1, hereafter referred to as the reference run. Note that the plasma moves at subrelativistic velocities in this Weibel frame, while the beam is now ultrarelativistic. This difference demonstrates the importance of the Weibel frame regarding the development of the instability, and more importantly, regarding its saturation, since the saturation criteria depend on the inertia of the particles, which in turn depend on the reference frame. The parameters of subsequent runs have been varied accordingly to fall in the region of the parameter space dominated by the CFI over electrostatic and oblique modes. In particular, we investigate a case where the initial beam proper density is tripled with respect to the reference case [run (b)], one in which the initial beam proper temperature is reduced by a factor of 1/3 [run (c)], one with an initial beam Lorentz factor reduced by a factor of 1/3 [run (d)]. Finally, we examine two more extreme configurations by reducing the initial temperature of the beam while increasing its initial Lorentz factor and the initial plasma temperature by a factor of 10 each [run (e)] or 30 each [run (f)]. The latter runs are of particular interest for the present study, because their parameters are such that the roles of background plasma and beam are interchanged with respect to other runs.

What we refer to as the *beam* is set in motion in the positive x -direction and represents the hot cloud reflected by the shock, which encounters the cold incoming *plasma* streaming along the negative direction. Correspondingly, the transverse CFI generates an out-of-plane magnetic field component, B_z , aligned with the \hat{z} direction, and its associated electrostatic component E_y , along \hat{y} . Since the simulation frame initially coincides with the Weibel frame, E_y remains much smaller than B_z during the initial development of the instability. A stronger E_y then emerges gradually, and as time progresses, the physical conditions of the plasma and/or the beam change, and so does the instantaneous Weibel frame. In particular, the filamentary structures start to move along \hat{x} at an approximately coherent velocity corresponding to the time-dependent value of β_w . To discriminate between the various saturation criteria,

Run	γ_b	γ_p	T_b/γ_b	T_p/γ_p	$\gamma_b n_b/\gamma_p n_p$
(a)	18.9	1.01	2.4	0.2	1.9
(b)	16.7	1.05	2.9	0.2	4.6
(c)	16.7	1.05	0.95	0.2	1.5
(d)	40.8	1.2	1.09	0.2	3.5
(e)	25.	5.3	0.2	0.4	0.5
(f)	25.	15.4	0.06	0.4	0.2

TABLE 5.1: Summary of simulation parameters for pair plasmas. Run (a) is the reference simulation. The parameters of the other runs differ from those of run (a) as follows: (b) $n_b \times 3$; (c) $T_b/3$; (d) $\gamma_{b|d} \times 3$; (e) $\gamma_{b|d}/3$, (e) $\gamma_{b|d} \times 10$, $T_p \times 10$, $T_b/10$; (f) $\gamma_{b|d} \times 30$, $T_p \times 30$, $T_b/30$. The table gives the simulation parameters once transformed to the Weibel frame. Temperatures are given in units of $m_e c^2/k_B$. Taken from [21].

the magnetic field is directly extracted from PIC simulations and compared with the theoretical estimates of the saturated B -field given in Sec. 5.1.3.

In what follows, I discuss the linear and saturation phases of the instability, while the late-time evolution is left aside and treated in Sec. 5.2.3.

Reference run

The growth of the magnetic field during the linear and saturation phases of the reference case (a) can be clearly seen in Fig. 5.4 (thick black line). In this figure, and subsequent similar ones, the mean B -field strength is expressed in dimensionless units, $\bar{B}_z = eB_z/m_e c \omega_{pp} = B_z/\sqrt{4\pi n_p m_e c^2}$. This value is directly computed from the total magnetic energy contained in the system, output of the simulation. The expected maximum growth rate is $\Gamma_w \simeq 0.02 \omega_{pp}$ at $k_\perp \simeq 0.6 \omega_{pp}/c$, as obtained by solving numerically the dispersion relation of the CFI [23]. This computation also yields $\tilde{\chi}_p \simeq 0.006$ and $\chi_b \simeq 0.07$, thus showing that the kinetic limit does apply for both components. For reference, the approximations of Eq. (5.17) give $\Gamma_{w,k-k} \simeq 0.01 \omega_{pp}$ and $k_\perp \simeq 0.7 \omega_{pp}/c$ in that regime. These predictions fairly match the simulations results: the growth rate evaluated using Eq. (5.16) between $t = 200 \omega_{pp}^{-1}$ and $t = 450 \omega_{pp}^{-1}$ is $\Gamma_w^{\text{PIC}} \simeq 8 \times 10^{-3} \omega_{pp}$, while the dominant k_\perp in the Fourier spectrum of B_z at saturation ($t \simeq 500 \omega_{pp}^{-1}$) is measured to be $k_\perp^{\text{PIC}} \simeq 0.8 \omega_{pp}/c$. Considering that the spectrum of the instability is rather broad and variable with time, the factor of ~ 2 discrepancy between the theoretical and simulation results is not very significant.

The measured value of \bar{B}_z is compared to the saturation limits B_t^b and B_p^b in the upper panel of Fig. 5.4, and to B_t^p and B_m^p in the lower panel. As explained earlier, the plot only contains the maximum of the two ‘‘particle limit’’ criteria corresponding to either component, since the lower one is not relevant for determining saturation. In the present case, the current density carried by the beam largely dominates that of the plasma because $|\beta_p| \ll 1$. B_m^b lies far above B_t^b , as expected from the discussion of Sec. 5.1.3, and it is therefore not plotted. Recalling that the limits given in Eqs. (5.20), (5.21) and (5.24) are upper bounds, saturation is expected to occur once the measured B value exceeds one of the corresponding curves in Fig. 5.4. All limits shown in the figures are computed from the instantaneous quantities measured in the simulation, which explains their evolution in time. A word of caution thus appears necessary regarding B_t : as it scales with Γ_w^2 , which is computed through Eq. (5.16), this limit becomes meaningless outside the phase of linear growth of the CFI. In particular,

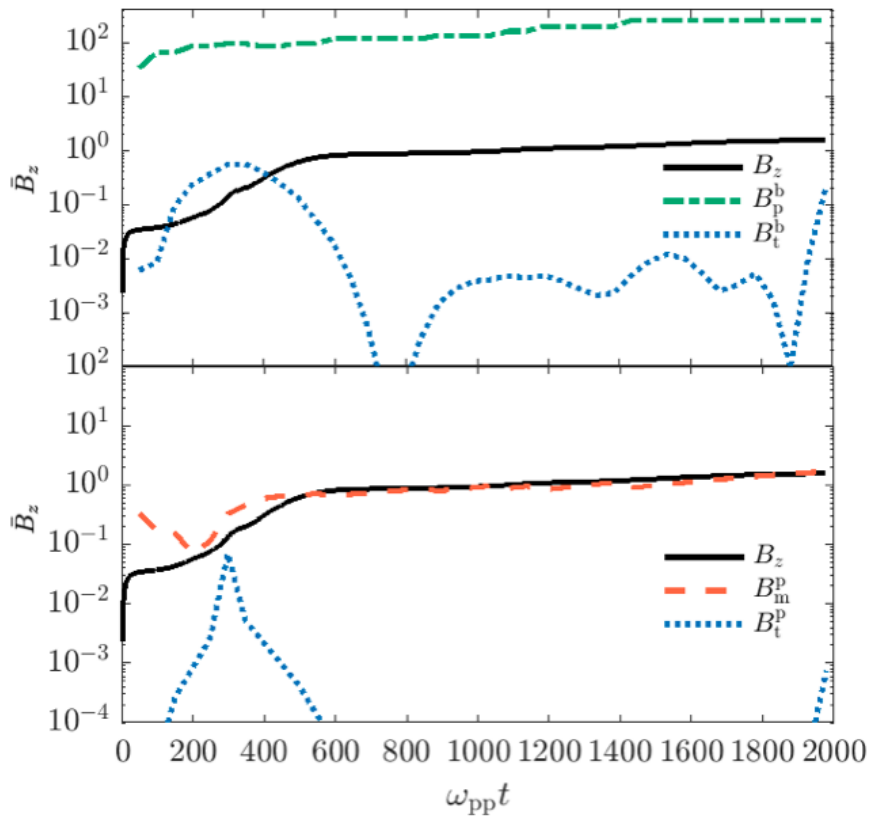


FIGURE 5.4: Temporal evolution of the simulated mean B -field strength (B_z , black curves) compared to various saturation criteria for reference run (a). Top panel: particle (B_p^b , green dashed-dotted curve) and trapping (B_t^b , blue dotted curve) limits as applied to the beam particles. Bottom panel: spatial magnetization (B_m^p , red dashed curve) and trapping (B_t^p , blue dotted curve) limits as applied to the plasma particles. All curves are in units of $m_e c \omega_{pp} / e$.

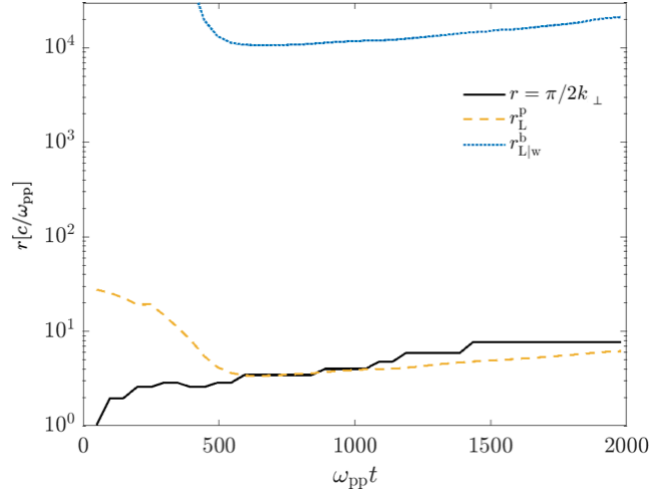


FIGURE 5.5: Comparison of the typical filament size, as extracted from simulation (black line), with the Larmor radius of plasma particles in the simulation frame (red dashed line) and of beam particles in the instantaneous Weibel frame (orange dotted line). Both radii are computed using dynamical quantities extracted from the reference run (a) as defined in Table 5.1. Taken from [21].

the fact that $\bar{B}_t^b < \bar{B}_z$ at early times ($t \lesssim 100 \omega_{pp}^{-1}$), does not mean that saturation has occurred. On the other hand, the fact that \bar{B}_t^b and \bar{B} cross each other at $t \simeq 400 \omega_{pp}^{-1}$ is indicative of saturation through trapping.

Around $t \simeq 400 \omega_{pp}^{-1}$ the magnetic field indeed becomes so strong that the quiver frequency of the beam particles exceeds the growth rate of the instability. Beam particles can then be regarded as transversely *trapped* around the B -field nodes (Fig. 5.4 top panel). To quantify this, we consider the characteristic momentum and Lorentz factor averaged over the Maxwell-Jüttner distribution as $\langle \gamma_b \beta_{b\parallel} \rangle \simeq \langle \gamma_b \rangle \simeq 4\gamma_b / \mu_b$. Combining those values with the theoretical estimates of Γ_w, k_\perp , and the parameters of Table 5.1, we derive the trapping limit as $\bar{B}_t^b \simeq (\Gamma_w / \omega_{pp})^2 (\omega_{pp} / k_\perp c) \langle \gamma_b \rangle / \beta_{b\parallel} \simeq 0.5$, which matches well the observed saturation value $\bar{B}_z \simeq 1$. \bar{B}_t^b is also close to the estimate from the measured values of $\Gamma_w, k_\perp, \langle \gamma_b \rangle$ and $\beta_{b\parallel}$, that is, $\bar{B}_t^{b,PIC} \simeq 0.3$. As expected, the particle limit for the beam lies above those values,

$\bar{B}_p^b \simeq (\pi/2)(n_b/n_p)(\omega_{pp}/k_\perp c) \langle \gamma_b \beta_{b\parallel} \rangle \simeq 50$, and the magnetization limit lies well above, $\bar{B}_{m,r_L}^b \simeq (2/\pi)(k_\perp c / \omega_{pp}) \langle \gamma_b \beta_{b\parallel} \rangle \simeq 1.6 \times 10^3$. As anticipated in Sec. 5.1.3, the trapping limit for the beam thus appears to provide the relevant criterion for saturation. Interestingly, $\bar{B}_t^p \ll \bar{B}_z$ at all times, even during linear growth, indicating that the strong quiver motion of the plasma component does not prevent the CFI from growing, neither does it matter from the point of view of saturation.

The large value of \bar{B}_m^b confirms that magnetic trapping does not act longitudinally, meaning that the Larmor radius of the beam particles remains much larger than the characteristic radius of a filament; see in particular Fig. 5.5 which carries out such a comparison. As already pointed out in Sec. 5.1.3, if the drift velocity is relativistic, as is the case for the beam particles, the magnetization limit is determined by the spatial constraint $r_L \lesssim r$. We recall that the notion of Larmor radius implies a constant B -field along with a null electric field, and hence has to be computed in the instantaneous Weibel frame, which departs, given the development of the instability, from the simulation frame. This change of frame is relevant for the

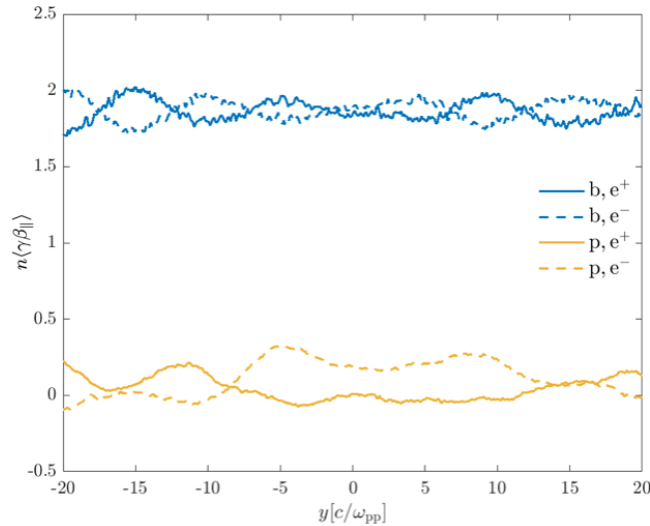


FIGURE 5.6: Transverse profiles of the beam (blue curves) and plasma (yellow curves) longitudinal current densities at the time of saturation ($t \simeq 400 \omega_{pp}^{-1}$) in the reference run (a) listed, and in a limited region of the periodic y -domain. For each species, the solid and dashed curves correspond to positrons and electrons, respectively. Taken from [21].

beam, which moves relativistically in the simulation frame at $u_b \simeq 19 \simeq \text{const}$, while it can be neglected for the background plasma, given that its velocity and the Weibel frame velocity remain sub-relativistic in the simulation frame ($|\beta_{p|w}| \ll 1$).

To better understand why the particle limit does not provide the relevant saturation criterion here, we quantify the contribution of the beam to the total current to this effect. Figure 5.6 shows the particle current density ($n\langle\gamma\beta_{\parallel}\rangle$) of each species in a limited region of the periodic y -domain. One can see that the contributions of the beam and the plasma to the electric current density fluctuations are comparable in scale, although the beam dominates the total particle current density, which enters Eq. (5.24). Importantly, charge separation is not complete and the filaments are rather diluted than spatially split. For this reason, the magnetic field associated with the maximum particle limit among the components remains always greater than the simulated value (compare the green and black curves in Fig. 5.4), and therefore does not account for saturation.

Concerning the background plasma, it remains sub-relativistic and relativistically cold in the Weibel frame, hence $\langle\gamma_p\rangle \sim \gamma_p$ and $\langle u_p\rangle \sim \gamma_p\beta_p$. As previously mentioned, the B -field associated with particle trapping inside the filaments is nearly everywhere much smaller than measured in the simulation,

$\bar{B}_t^p \simeq (\Gamma_w/\omega_{pp})^2(\omega_{pp}/k_{\perp}c)\langle\gamma_p\rangle/\beta_{p\parallel} \simeq 0.001$, as can be verified using the above theoretical estimates for Γ_{\max} and k_{\perp} . As a matter of fact, the bottom panel of Fig. 5.4 shows that the background plasma particles are rapidly trapped inside the filaments, both transversely and longitudinally, since $\bar{B}_{m,rL}^p \simeq (2/\pi)(k_{\perp}c/\omega_{pp})\gamma_p\beta_p \simeq 0.1 < \bar{B}_z$. Actually, $\bar{B}_{m,rL}^p$ rapidly approaches \bar{B}_z (at $\omega_{pp}t \simeq 200$) and stays remarkably close to it at later times. We do not interpret this as a cause for saturation of the CFI, but rather as a relaxation of the low-inertia background plasma into the strong magnetic fields driven by the large-inertia beam particles. In runs (b), (c) and (d), $\bar{B}_{m,rL}^p$ gets even smaller than \bar{B}_z during linear growth, indicating that plasma particles become magnetically trapped inside the filaments without inhibiting the CFI growth.

Well beyond saturation, the characteristic filament radius r increases, roughly

linearly in time (see Fig. 5.5), as a consequence of filament coalescence. However, the B -field strength as measured in the Weibel frame, that is, $(B_z^2 - E_y^2)^{1/2}$, remains approximately constant. The slow evolution of \bar{B} in the simulation frame results from the slow evolution of the Weibel frame velocity; it is therefore of kinematic origin. Interestingly, Fig. 5.5 shows that the typical Larmor radius of background plasma particles adjusts at all times to the filament radius, $r_{L,p} \sim r$, which increases from $r \sim 3c/\omega_{pp}$ at saturation to $r \sim 10c/\omega_{pp}$ at the final time. This growth implies that background plasma particles gain energy inside the filaments. Qualitatively, this process can be related to the chaotic dynamics of particles trapped in an effective potential characterized by the potential four-vector $A_x \sim rB_z$, which tends to bring equipartition between kinetic $\langle p \rangle$ and potential eA_x/c energies, under the approximate conservation of the canonical momentum $\Pi_x = p_x + eA_x/c$. Such equipartition indeed corresponds to $r_{L,p} \sim r$.

We note that simulations were precisely stopped once the transverse direction could not accommodate more than several filaments. Furthermore, saturation as we define it occurs well before that stage, making the transverse size of the simulation domain sufficient for our purposes.

Scan in parameter space

The parameters of the reference run (a) are such that the beam carries most of the energy density of the system, and its relativistic plasma frequency is the lower among the two. The smaller inertia of the background plasma particles, which remain sub- or mildly relativistic in the Weibel frame, explains why they relax rapidly in the magnetized filamentary structures while the rigid beam current keeps driving the instability. For this reference run, we thus find that the transverse trapping of beam particles provides the relevant criterion for determining the saturation of the CFI. This general picture proves robust (*i.e.*, it applies from runs (a) to (e) in Table 5.1) even if the initial parameters are pushed to extreme values, though always in the CFI-dominated regime.

For instance, Fig. 5.7 compares the saturation criteria for run (e), in which the initial γ_b and T_p have been multiplied by 10 and T_b divided by 10. The instability grows fast, with a measured growth rate $\Gamma_w^{\text{PIC}} \simeq 0.3 \omega_{pp}$, $k_\perp^{\text{PIC}} \simeq 0.9 \omega_{pp}/c$, saturating at $t \simeq 30 \omega_{pp}^{-1}$. Here as well, transverse magnetic trapping of beam particles appears to control the saturation level, while the Larmor radius of background plasma particles still adapts to the filaments size. The parameters of this simulation, though, are such that Eq. (5.17) cannot be applied because the plasma is hot, and because it moves at relativistic velocities in the Weibel frame. Solving numerically the dispersion relation of the CFI, we obtain $\Gamma_w \simeq 0.3 \omega_{pp}$ at $k_\perp \simeq 1.2 \omega_{pp}/c$, which nicely agrees with the PIC values. We then obtain $\bar{B}_t^b \simeq 37$, a factor of a few above the simulated value $\bar{B}_z \simeq 10$, and slightly below the theoretical particle limit $\bar{B}_p^b \simeq 44$. The time evolution of these limits, computed with the instantaneous measured values and plotted in the top panel of Fig. 5.7, confirms that saturation results from transverse trapping of the beam particles. Moreover, the closeness of the PIC field value and plasma magnetization limit (compare \bar{B}_z and \bar{B}_m^b in the bottom panel of Fig. 5.7) indicates that the plasma particles are fully trapped in the filaments, as before.

Case (f) of Table 5.1, where T_b is reduced by a factor of 30 while γ_b and T_p are increased by the same amount, provides an exception to that general picture. In this particular configuration, both the beam and the plasma become relativistically hot, leading to comparable initial relativistic plasma frequencies, namely, $\Omega_{pb} \simeq 0.14 \omega_{pp}$

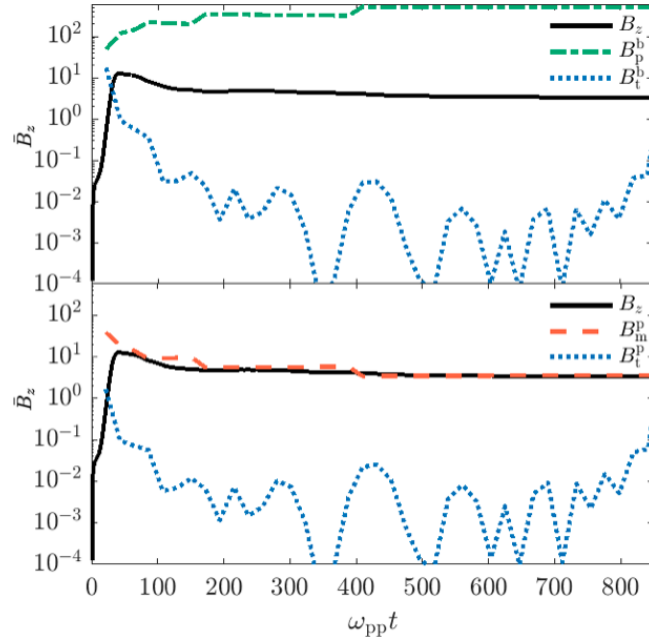


FIGURE 5.7: Same as Fig. 5.4 for simulation run (e). Taken from [21].

and $\Omega_{pp} \simeq 0.2 \omega_{pp}$. One can then hardly discern which plays the role of the beam and which plays the role of the background plasma. What matters for the (transverse or longitudinal) trapping limits, however, is the inertia of the particles. Here, $\langle u_b \rangle \simeq 40$ and $\langle u_p \rangle \simeq 100$ initially, so that the background plasma particles will be trapped later than the beam particles.

In detail, we measure $\Gamma_w^{\text{PIC}} \simeq 0.3 \omega_{pp}$ and $k_{\perp}^{\text{PIC}} \simeq 3 \omega_{pp}/c$, in fair agreement with the numerical solution to the CFI dispersion relation ($\Gamma_w \simeq 0.4 \omega_{pp}$ at $k_{\perp} \simeq 1.6 \omega_{pp}/c$) and which translates into a plasma trapping limit, $\bar{B}_t^p \simeq 38$, exceeding the beam trapping limit, $\bar{B}_t^b \simeq 15$. Moreover, since the plasma now carries a larger current density than the beam, it gives a greater particle limit: $\bar{B}_p^p \simeq 180$ vs. $\bar{B}_p^b \simeq 38$. Those limits have been evaluated using the simulation parameters; they qualitatively match (yet overestimate by a factor of a few) the values obtained using the instantaneous simulation parameters (as plotted in Fig. 5.8). We therefore expect saturation to be determined by transverse plasma trapping as confirmed by Fig. 5.8.

In summary, we observe that the CFI growth rate is set by the species with the lower (relativistic) plasma frequency, while the saturation level is determined by that component with the larger inertia per particle, according to the transverse trapping criterion. The expected overall B -field amplitude at saturation can thus be approximated as

$$\frac{B_{\text{sat.}}}{\sqrt{4\pi n_p m c^2}} \simeq \left(\frac{\Gamma_w}{\omega_{pp}} \right)^2 \frac{\omega_{pp}}{k_{\perp} c} \max(\langle \gamma_b \rangle, \langle \gamma_p \rangle). \quad (5.27)$$

In the forthcoming section, we extend this analysis to electron-ion compositions.

5.2.2 The electron–ion case

The presence of ions introduces a new scale in the problem, associated with the hierarchy m_i/m_e (m_i ion mass). If both ions and electrons are cold, the ratio of ion to electron plasma frequencies scales in proportion to $\sqrt{m_e/m_i}$. If the electrons are

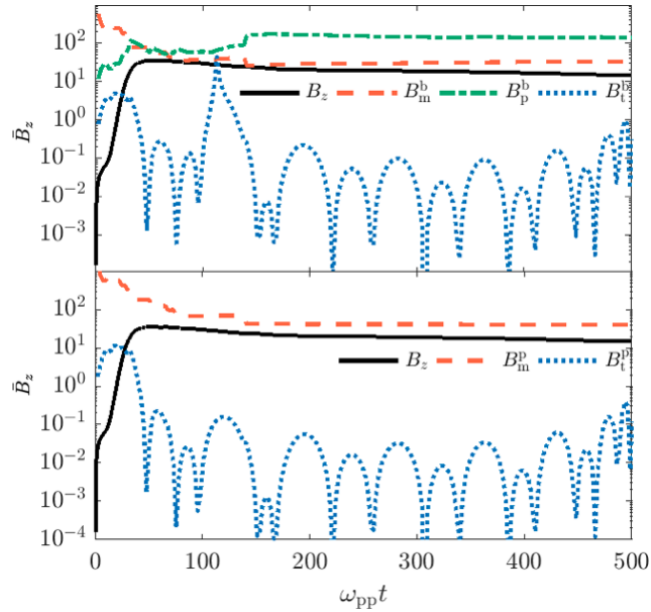


FIGURE 5.8: Same as Fig. 5.4 for simulation run (f). In the top panel is also plotted the time evolution of the B -field associated with the spatial magnetization limit as applied to the beam (B_m^b , red dashed curve). Taken from [21].

Run	γ_b	γ_p	$\frac{T_{be}}{\gamma_b}$	$\frac{T_{bi}}{\gamma_b}$	$\frac{T_{pe}}{\gamma_p}$	$\frac{T_{pi}}{\gamma_p}$	$\frac{\gamma_b n_b}{\gamma_p n_p}$
(i1)	18.9	1.011	2.4	0.024	0.20	0.0020	1.9
(i2)	6.7	1.00075	4.5	0.15	0.2	0.002	1.3

TABLE 5.2: Parameters of the electron-ion simulations, once transformed to the Weibel frame. Run (i1) is analogous to run (a) in which the positrons have been replaced with ions. Run (i2) treats a mildly relativistic regime. Electron and ion temperatures are given in units of $m_e c^2 / k_B$ and $m_i c^2 / k_B$, respectively. Taken from [21].

heated to such a degree that their effective inertia becomes similar to that of the ion species, then the above hierarchy disappears: both species share a similar relativistic plasma frequency, and hence the electron-ion component effectively behaves as a pair plasma. Thus, one may expect to obtain results similar to those for the pair systems examined in the previous section.

In the particular context of relativistic shock physics, it is known that electrons are efficiently heated up to near equipartition in ultrarelativistic, weakly magnetized conditions (see e.g. [144, 168] and references therein). By contrast, in the mildly relativistic and magnetized regime, electron heating appears to be weak, implying that some hierarchy between the response of electrons and ions remains preserved. Both situations will be addressed in the following. In order to be able to capture the physics of the instability for both electron and ion species, with a sufficient number of macro-particles per cell and spatial extent, we will adopt an ion-to-electron mass ratio $m_i / m_e = 100$.

Ultrarelativistic regime

Let us first examine the saturation criteria for case (i1) described in Table 5.2. The parameters of this run are obtained from run (a) by replacing the positrons with ions of

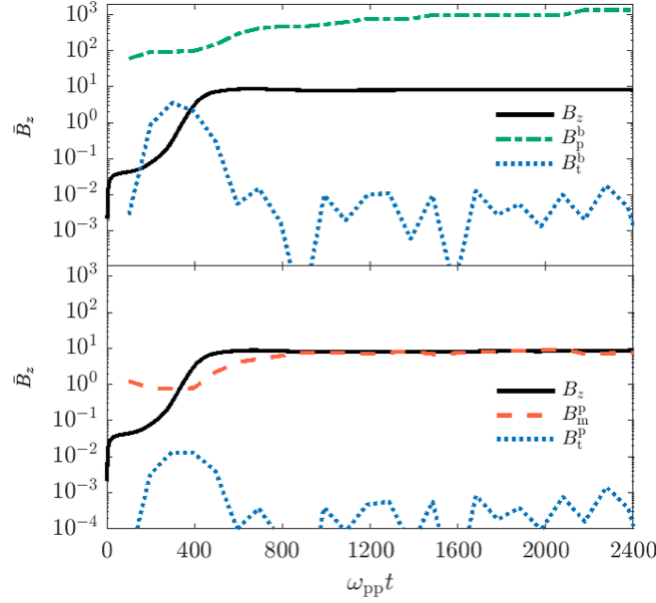


FIGURE 5.9: Temporal evolution of the simulated mean B -field strength (black curves) compared to various saturation criteria for run (i1) defined in Table 5.2. Top panel: particle (green dashed-dotted curve) and trapping (blue dotted curve) limits as applied to the beam ions. Bottom panel: spatial magnetization (red dashed curve) and trapping (blue dotted curve) limits as applied to the plasma ions. All curves are in units of $m_e c \omega_{pp} / e$. Taken from [21].

charge $+e$ and mass $m_i = 100 m_e$. The beam electrons and ions then have a comparable inertia: $\langle p_{be} \rangle / m_e c \simeq 4\gamma_b T_{be} \simeq 3430$ and $\langle p_{bi} \rangle / m_e c \simeq \gamma_b \beta_b (m_i / m_e) K_3(\mu_{bi}) / K_2(\mu_{bi}) \simeq 4520$ (K_n is the modified Bessel function of the n th kind). Note that the beam ions have a proper temperature $T_{bi} / m_i c^2 \simeq 0.45$, so that they cannot be considered as fully relativistic.

Accounting for the ion mass modifies the trapping and magnetization limits as

$$B_t^i = \frac{\Gamma_w^2 \langle \gamma \rangle m_i}{k_{\perp} \beta_{\parallel} e} \quad (5.28)$$

and

$$B_{m,rL}^i = \frac{2}{\pi} k_{\perp} \langle \gamma \beta \rangle \frac{m_i c^2}{e}. \quad (5.29)$$

The time evolution of the simulated mean B -field is plotted in Fig. 5.9. Unlike previous studies (e.g. [137]), the system does not experience an early phase governed by electrons, in which the CFI grows faster, before moving to a regime ruled by the slower ion-driven CFI. We ascribe this behavior to the similar inertia of the beam ions and electrons. Solving the CFI dispersion relation in the presence of ions yields a maximum growth rate $\Gamma_w \simeq 0.025 \omega_{pp}$ for a wavenumber $k_{\perp} \simeq 0.5 \omega_{pp} / c$ (as before, ω_{pp} denotes the *electron* plasma frequency of the background plasma). These values are very close to the simulation values, namely, $\Gamma_w^{\text{PIC}} \simeq 0.024 \omega_{pp}$ (as obtained by exponentially fitting $B_z(t)$ over $300 < \omega_{pp} t < 500$) and $k_{\perp}^{\text{PIC}} \simeq 0.4 \omega_{pp} / c$ (as measured from the spatial Fourier spectrum of B_z).

As in run (a), the CFI saturates through transverse trapping of the beam particles (electrons and ions). This is consistent with the fact that the theoretical trapping

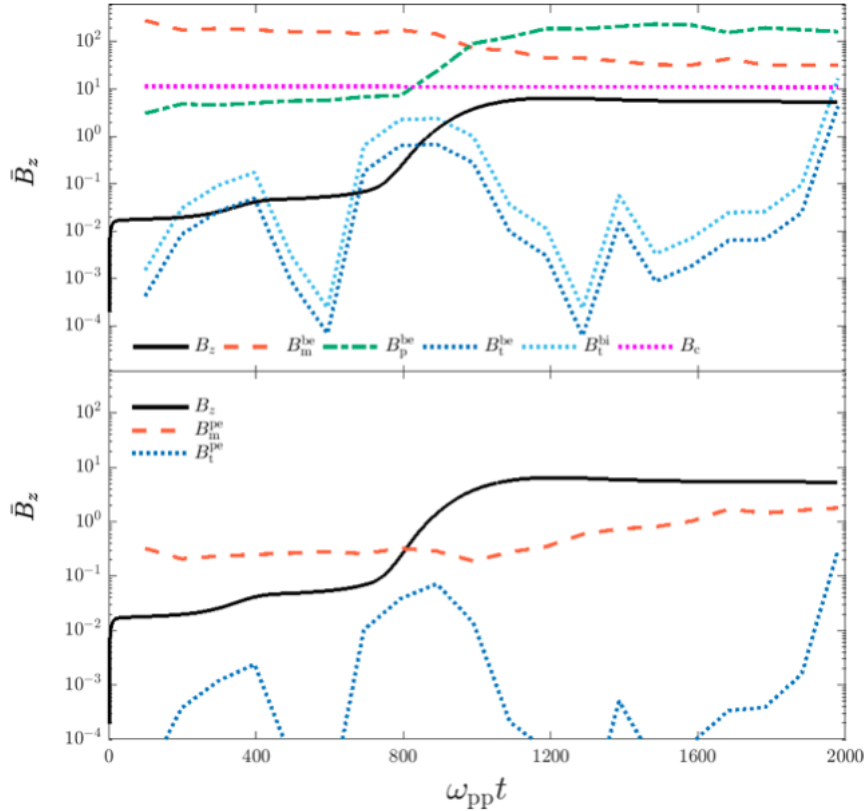


FIGURE 5.10: Temporal evolution of the simulated mean B -field strength (B_z , black curves) compared to various saturation criteria for run (i2) defined in Table 5.2. Top panel: comparison of the spatial magnetization (B_m^{be} , red dashed curve), particle (B_p^{be} , green dashed-dotted curve), trapping (B_t^{be} , blue dotted curve) limits as applied to the beam electrons, plus the trapping limit applied to beam ions (B_t^{bi} , light-blue dotted curve). Also plotted is the saturated B -field from Eq. (5.34) (B_c , magenta dotted line). Bottom panel: spatial magnetization (B_m^{pe} , red dashed curve) and trapping (B_t^{pe} , blue dotted curve) limits as applied to the plasma electrons. All curves are in units of $m_e c \omega_{\text{pp}} / e$.

Taken from [21].

limit, $\bar{B}_t^{\text{b}} \simeq 6$, is much smaller than the particle limit, $\bar{B}_p^{\text{b}} \simeq 75$, both limits being computed for the beam ions and using the initial simulation parameters. This estimate of \bar{B}_t^{b} matches well that evaluated at saturation time ($t \simeq 400 \omega_{\text{pp}}^{-1}$) instantaneous simulation parameters (see top panel of Fig. 5.9). At later times, again similarly to run (a), the background plasma particles turn fully magnetized, with their typical Larmor radius adjusting to the mean filament size (bottom panel of Fig. 5.9). A notable difference with run (a), however, is that the mean B -field strength here remains quasi-constant following saturation (up to the final simulation time, $t = 2400 \omega_{\text{pp}}^{-1}$), rather than slowly increasing as in Fig. 5.4.

In short, in this asymmetric, relativistic electron-ion simulation, in which both species share a similar inertia, we recover the general picture of the previous section. Accordingly, the CFI saturation is determined by the trapping limit as applied to the species with the largest inertia.

Mildly relativistic regime

We now address the case of two electron-ion plasmas counterstreaming with a moderate Lorentz factor (~ 3) in a reference frame. These two plasma flows mainly differ

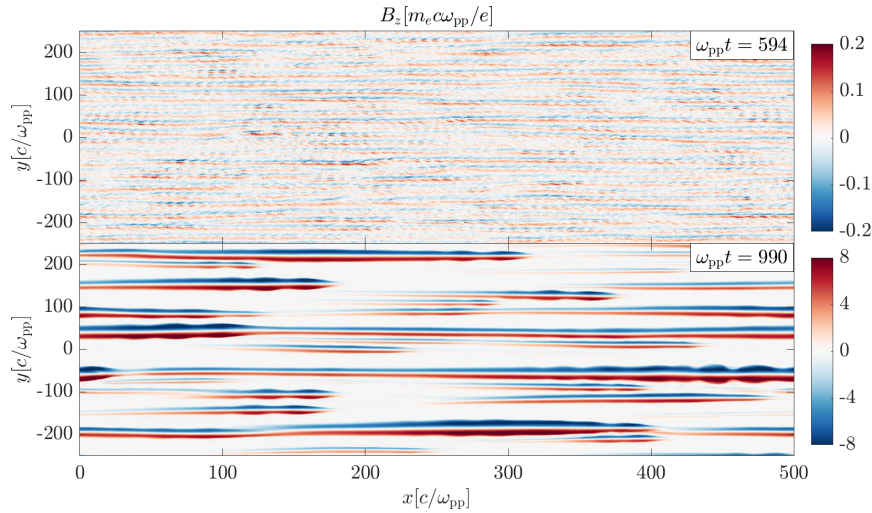


FIGURE 5.11: Out-of-plane magnetic field (B_z) generated by the counter-streaming of mildly relativistic electron-ion flows (i2). The magnetic field is plotted at two different times: in the early ($\omega_{pp}t = 594$, top) and late ($\omega_{pp}t = 990$, bottom) phases of the CFI when cavities have started to form. Taken from [21].

in their temperatures: the beam's electron and ion populations are much hotter than their plasma counterparts, and for each (beam or plasma) component, the electrons are also much hotter than the ions. In particular, the difference in temperature between the beam ions and electrons is justified by the fact that, according to kinetic simulations, the shock-reflected ions have a temperature at least three times larger than their electronic counterpart in the downstream frame (see [31, 45, 100, 101] and references therein). The initial parameters for this run (i2), as expressed in the corresponding Weibel frame, are summarized in Table 5.2.

In this configuration, one has $\langle p_{be} \rangle \simeq 800 m_e c$, while $\langle p_{bi} \rangle \simeq 3000 m_e c$. A hierarchy therefore persists between the beam electrons and ions, leading to a somewhat different picture for the evolution of the instability and its saturation level.

Figure 5.10 shows that after a transient early phase ruled by oblique modes, the CFI sets in at $t \simeq 300 \omega_{pp}^{-1}$ and rapidly saturates at $t \simeq 400 \omega_{pp}^{-1}$ with a measured growth rate $\Gamma_w^{\text{PIC}} \simeq 5 \times 10^{-3} \omega_{pp}$ and a dominant wave number $k_{\perp}^{\text{PIC}} \simeq 0.35 \omega_{pp}/c$. During this short period, the B -field grows only by a factor of a few, likely because the transverse trapping limit for beam electrons is already partially fulfilled, see top panel of Fig. 5.10. This figure also suggests that the trapping of beam ions contributes to the instability saturation, as would be expected from their larger inertia.

At later times ($t \gtrsim 700 \omega_{pp}^{-1}$), a secondary instability develops, leading the mean B -field strength to rise by almost two orders of magnitude. As shown in Fig. 5.11, this instability generates isolated, large-scale magnetic filamentary structures, which are essentially filled with beam electrons and plasma ions, and devoid of beam ions and plasma electrons.

Those structures, or “cavities”, have been observed in previous electron-ion simulations [135, 115] and studied recently in greater detail in Ref. [124]. Although the latter paper considered a simpler setting consisting of an electron beam-plasma system embedded in an ion background, the picture that it sketches can be readily extended to the present problem. Specifically, the cavities are driven by the beam electrons, which are initially overdense relative to the plasma ($\gamma_{be} m_{be} /$

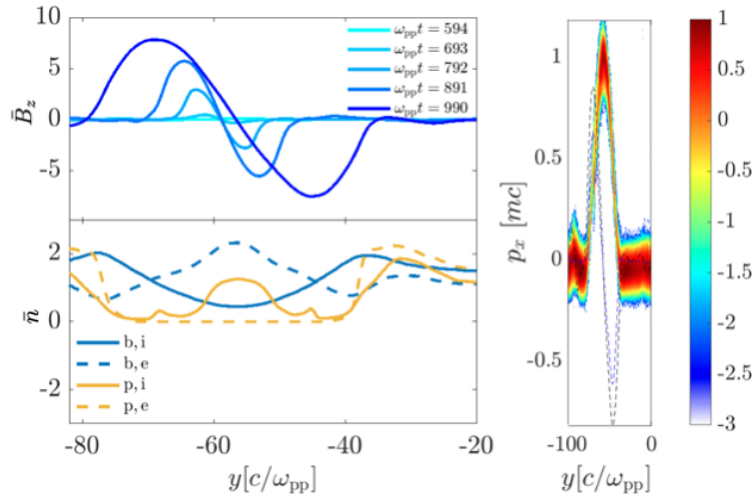


FIGURE 5.12: Top left panel: magnetic field profiles along the transverse direction (y) and at successive times, as indicated, for simulation run (i2). The figure reveals the growth of the magnetic field as the cavity expands. Bottom left panel: transverse profiles of the number density of the beam and plasma components at the onset of saturation, $\omega_{pp}t \simeq 1000$. Right panel: (y, p_x) phase space of the plasma ions at the same time. Taken from [21].

($\gamma_{pe}n_{pe}$) $\simeq 1.3$ at $t = 0$). As a cavity expands due to the magnetic pressure exerted by the beam electron current, more beam electrons join and add their contribution to the current inside the cavity, thus feeding back positively on the magnetic field. Meanwhile, the beam ions are expelled from the cavity by the growing field, just as the plasma electrons. The background ions accumulate in the cavity, mainly (initially) as a result of the confining force exerted by the E_y electric field component. This scenario is illustrated in Fig. 5.12, in the case of the cavity formed at $(x, y) \simeq (450, -60) c/\omega_{pp}$ in the bottom panel of Fig. 5.11. The top left panel depicts the time evolution of the B -field profile across the cavity, while the bottom left panel plots the density profiles of the various populations of the system.

Interestingly, this secondary instability is essentially driven by one species, here the beam electrons, and it leads to a sharp contrast between the beam electron density inside and outside the cavity. Thus, it is not surprising that the particle limit, as evaluated for the beam electrons, nicely follows the evolution of the magnetic field during this nonlinear phase¹, yet this does not cause the instability to saturate.

We also note that a key factor for this secondary instability is a clear hierarchy between the beam ions and the beam electrons. Were they of equal inertia, these two species would react similarly in adjacent filaments, leading to the growth of all filaments as in the standard CFI. A comparison of this simulation with the previous one (i1) suggests that in order for the instability to develop, the beam electrons and ions should differ in their inertia by at least a factor of a few.

This instability causes the magnetic field to grow rapidly, until saturation is reached at $t \simeq 1100 \omega_{pp}^{-1}$. While in [124], the magnetic pressure pushes a “wall” composed of background ions initially at rest, in the present case it evacuates the beam ions, which are relativistic. We can thus adapt the calculation of the instability

¹In Fig. 5.10 there is an offset of about an order of magnitude between the measured value B_z (black solid curve) and the theoretical limit given by Eq. (5.24) (green dashed-dotted curve). This offset is related to the overall geometry, in particular the fact that the structures are not space-filling while the averages are taken over the simulation box. It is clear, however, that inside a cavity, the magnetic field is mostly carried by the beam electrons.

growth rate made in that study to our conditions by taking into account the inertia of the beam ions, as follows.

Assuming that the B -field inside the cavity is mainly generated by the beam electrons, the magnetic pressure acting on this wall can be expressed as

$$\frac{B_z^2}{8\pi} = \frac{(4\pi en_{be}\gamma_{be}\beta_{be}r_c)^2}{8\pi}. \quad (5.30)$$

The momentum per unit area of the wall is mainly carried by the expelled beam ions, and so can be estimated as $\gamma_{bi}n_{bi}\langle p_{bi} \rangle r_c(t)$, where $r_c(t)$ is the instantaneous cavity radius. Momentum balance in the transverse (y) direction then leads to

$$\frac{d}{dt} \left(\gamma_{bi}n_{bi}\langle p_{bi} \rangle r_c \frac{dr_c}{dt} \right) = 2\pi(en_{be}\gamma_{be}\beta_{be}r_c)^2, \quad (5.31)$$

The solution to this equation grows as $r_c \propto e^{\Gamma_c t}$, where the growth rate is given by

$$\Gamma_c = \frac{\Omega_{pbi}}{2}. \quad (5.32)$$

In the present case, $\Omega_{pbi} \simeq 0.02 \omega_{pp}$ and therefore, $\Gamma_c \simeq 0.01 \omega_{pp}$, which is in fair agreement with the growth rate $\Gamma^{\text{PIC}} \simeq 0.015 \omega_{pp}$ measured in the simulation over the interval $750 \lesssim \omega_{pp} t \lesssim 960$.

According to [124], saturation is reached once the background plasma ions are accelerated by the inductive electric field (E_x) to a point where they become relativistic ($p_{i,x} \simeq m_i c$) and neutralize the electron beam current. The right panel of Fig. 5.12, which displays the (y, p_x) phase space of the plasma ions at the onset of saturation ($\omega_{pp} t = 990$), confirms that they have indeed attained relativistic momenta by that time inside the cavity. Adapting again the calculations in Ref. [124], the radius of the cavity at saturation can be expressed as

$$r_{c,\text{sat}} = \frac{c}{\gamma_b^{1/2} \omega_{pbi}} = \frac{c}{\langle \gamma_{bi} \rangle^{1/2} \Omega_{pbi}}, \quad (5.33)$$

recalling that $\omega_{pbi} = \sqrt{4\pi n_{bi} e^2 / m_i}$. This gives $r_{c,\text{sat}} \simeq 10 c / \omega_{pp}$, which agrees relatively well with the size of the structures seen in Figs. 5.11 and 5.12.

The corresponding saturated value of the magnetic field is given by

$$\bar{B}_c \simeq \gamma_{be}^{1/2} \left(\frac{m_i}{m_e} \right)^{1/2} \frac{\omega_{pbe}}{\omega_{pp}} \quad (5.34)$$

in normalized units. One obtains $\bar{B}_c \simeq 11$ in correct agreement with the observed value $\bar{B}_z \simeq 6$ (see top panel of Fig. 5.10). Note that in Ref. [124] an extra factor of 1/2 was added in the estimation of the saturated field, which is not included here.

5.2.3 Late-time evolution of the beam-plasma system

We conclude by investigating briefly the late-time evolution of the beam-plasma system after the saturation of the magnetic field growth. It is worth noting that in this final stage, both the beam and plasma components are expected to relax to isotropy in the turbulence frame. This can be seen as a transition from the two-stream collisionless system to a long-term hydrodynamical system in which everything has been effectively mixed. In this respect, if we assume that the beam and plasma have

relaxed to the same final velocity but with different temperatures, the conservation of energy and momentum implies:

$$\gamma_{\text{bi}}^2 w_{\text{bi}} - p_{\text{bi}} + \gamma_{\text{pi}}^2 w_{\text{pi}} - p_{\text{pi}} = \gamma_{\text{f}}^2 (w_{\text{bf}} + w_{\text{pf}}) - p_{\text{bf}} - p_{\text{pf}}, \quad (5.35)$$

$$\gamma_{\text{bi}}^2 \beta_{\text{bi}} w_{\text{bi}} + \gamma_{\text{pi}}^2 \beta_{\text{pi}} w_{\text{pi}} = \gamma_{\text{f}}^2 \beta_{\text{f}} (w_{\text{bf}} + w_{\text{pf}}), \quad (5.36)$$

where the subscripts i and f here refer, respectively, to the initial and final states of the beam (b) and plasma (p) components. As before, w denotes the enthalpy density and p the pressure. Note that we have neglected the contribution of magnetic turbulence in the final state, as it is expected to be subdominant.

In the case where the final states of the beam and plasma are relativistically hot, and therefore share the same adiabatic index, $\hat{\Gamma}_{\text{f}} = w_{\text{f}} / (w_{\text{f}} - p_{\text{f}})$ (w_{f} and p_{f} are the total final enthalpy density and pressure), the final velocity β_{f} satisfies

$$\frac{\gamma_{\text{bi}}^2 w_{\text{bi}} - p_{\text{bi}} + \gamma_{\text{pi}}^2 w_{\text{pi}} - p_{\text{pi}}}{\gamma_{\text{bi}}^2 \beta_{\text{bi}} w_{\text{bi}} + \gamma_{\text{pi}}^2 \beta_{\text{pi}} w_{\text{pi}}} = \frac{\kappa_{\text{f}} - 1 + \beta_{\text{f}}^2}{\kappa_{\text{f}} \beta_{\text{f}}}, \quad (5.37)$$

where $\kappa_{\text{f}} \equiv \hat{\Gamma}_{\text{f}} / (\hat{\Gamma}_{\text{f}} - 1)$.

Consider for instance the case, exemplified by run (a) of Table 5.1, of an initially sub-relativistic ($\beta_{\text{p,i}} \sim 0$) and cold ($p_{\text{p,i}} \sim 0$) plasma interacting with a relativistically hot beam which carries most of the energy (*i.e.* $\gamma_{\text{b,i}}^2 p_{\text{b,i}} \gg w_{\text{p,i}}$). We then have $\kappa_{\text{f}} \simeq 4$ (as in the initial state), so that

$$\begin{aligned} \beta_{\text{f}} &\simeq \beta_{\text{b}} \left(1 - \frac{1}{2} \frac{w_{\text{pi}}}{\gamma_{\text{bi}}^2 p_{\text{bi}}} \right), \\ \gamma_{\text{f}} &\simeq \gamma_{\text{b}} \left(1 - \frac{w_{\text{pi}}}{p_{\text{bi}}} \right). \end{aligned} \quad (5.38)$$

The second equation further assumes $w_{\text{pi}} \ll p_{\text{bi}}$. The Lorentz factors are evaluated in the simulation frame of the two-stream system.

The above indicates that the asymptotic velocity of the relaxed components should be close to the initial beam velocity. This behavior is illustrated in Fig. 5.13, which plots the time evolution of various four-velocities as extracted from our reference run (a). The beam four-velocity decreases steadily with time, slowly approaching from above the predicted asymptotic four-velocity, $u_{\text{f}} = \beta_{\text{f}} \gamma_{\text{f}}$ (magenta dashed line). For detailed analyses of the late-time momentum and energy transfers in (nonrelativistic) unstable beam-plasma systems, see Ref. [142]. Conversely, the plasma four-velocity, u_{p} , is seen to increase steadily toward u_{f} . Also overlaid is the instantaneous four-velocity of the Weibel frame (green dotted line), computed from the simulation data as $u_{\text{w}} = \gamma_{\text{w}} \beta_{\text{w}}$ with $\beta_{\text{w}} = (\langle E_y^2 \rangle / \langle B_z^2 \rangle)^{1/2}$ (the average is taken over the simulation domain). Note that this quantity is not defined at early times because of the dominance of oblique modes characterized by $\langle E_y^2 \rangle / \langle B_z^2 \rangle > 1$. The four-velocity of the Weibel frame tracks that of the background plasma quite well. We note that the convergence to the hydrodynamical regime is not attained over the time scale of the simulation. As a matter of fact, we expect the convergence to proceed at an increasingly slower rate as time passes. This is because relaxation takes place in the Weibel frame, hence time dilation effects associated with the relativistic velocity of the Weibel frame relative to the simulation frame will decrease the apparent relaxation rate.

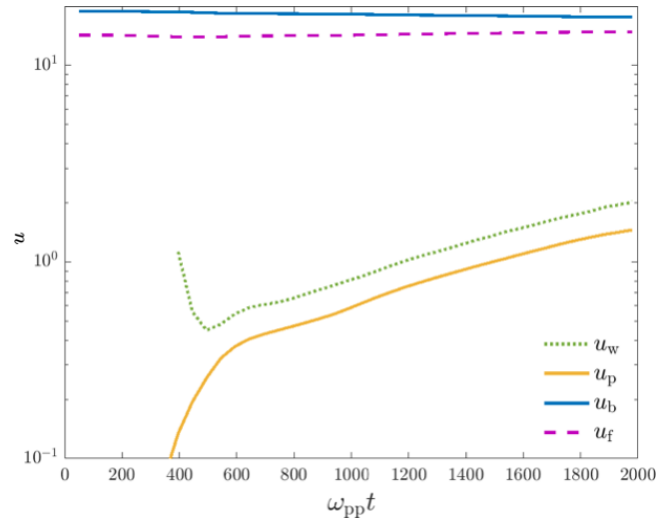


FIGURE 5.13: Time evolution of various four-velocities as extracted from run (a) defined in Table 5.1. Light-green dotted curve: four-velocity of the Weibel frame. Yellow curve: four-velocity of the plasma. Blue curve: four-velocity of the beam. Magenta dashed line: four-velocity of the relaxed plasma and beam as given by Eq. (5.38). Taken from [21].

5.2.4 Conclusions

We have investigated the saturation mechanism of the current filamentation instability, or Weibel instability, in an asymmetric configuration, meaning in the case in which the counterstreaming plasmas differ in terms of velocity, temperature and density. This configuration is notably representative of the precursor region of electron-positron or electron-ion shocks, although the implications of our results are not restricted to such systems. Our study relies on large-scale periodic PIC simulations of counterstreaming flows composed of a hot dilute population representing the beam (e.g. the particles reflected at the shock front) and a relatively cold plasma (e.g. the background plasma that is incoming toward the shock). The parameters of our fiducial run have been directly borrowed from a large-scale relativistic shock simulation at a position deep in the precursor; the parameters of subsequent runs have then been varied in an *ad hoc* manner to explore different possible settings. We have discussed several theoretically motivated criteria for saturation and compared them to the simulation results.

The asymmetric counterstreaming configuration departs from its symmetric counterpart in two important ways: (1) there exists an ambiguity as to whether a given criterion should be applied to the beam, or to the plasma component; (2) there exists a preferred reference frame, dubbed here the “Weibel frame” [122], in which the instability is purely magnetic; this reference frame does not *a priori* coincide with that in which the total momentum flux vanishes, as happens for the symmetric configuration. Here, we pay particular attention to that latter point. We have set up our simulations such that for each set of parameters characterizing the plasma flows, the simulation frame initially coincides with the Weibel frame.

We have then compared different mechanisms as possible sources of saturation of the magnetic field associated with the instability: magnetic trapping, particle limit, Alfvén limit. Our general conclusion is that, for pair plasmas, the saturation level is determined by the criterion of magnetic trapping as applied to the (beam or plasma) component that carries the larger inertia of the two: the growth rate is found to diminish strongly once the quiver frequency of that component becomes

comparable with, or larger than the instability growth rate. For all studied cases, our theoretical estimates of the instability properties, such as the maximum growth rate and associated wave number, are consistent with those extracted from the simulations. Consequently, it is possible to obtain reasonable analytical approximations for the strength of the magnetic field at saturation. Furthermore, we find that the particle limit is never fulfilled, all the more so when the component of larger inertia is relativistically hot, as its temperature then prevents its charged species from being fully segregated in separate filaments. We have observed that the component of smaller inertia becomes rapidly trapped inside the filaments, in some cases even during the linear phase of the CFI. At late times, the Larmor radius of those particles closely follows the characteristic filament radius and thus grows in time through coalescence. Asymptotically, the system tends to a final state where the two fluids are effectively mixed, drifting at the same mean velocity. However, due to relativistic time dilation effects, this ultimate regime could not be accessed from our simulations.

We have also investigated the case of asymmetric electron-ion systems with a mass ratio $m_i/m_e = 100$. As long as there is not a clear hierarchy in inertia between the electron and ions species of a given (beam or plasma) component at the beginning of the simulation, the development of the instability and the saturation proceed much as in the case of a pair plasma. The picture and saturation criterion discussed above thus remain applicable. However, if the electron and ion inertia differ by a factor of a few or more, a different instability eventually supersedes the CFI. It leads to the formation of cavities in which the beam electrons and background plasma ions accumulate and drive magnetic field growth, while the beam ions are pushed outwards along with the plasma electrons. This mechanism comes to an end when the plasma ions inside the cavities, accelerated by the inductive electric field, become capable of neutralizing the electron beam current, as discussed recently in Ref. [124]. This study has been published in [21].

Chapter 6

Particle Acceleration at turbulent shock fronts

As discussed in Sec. 2.1.2, in relativistic and substantially magnetised configurations, acceleration appears to be strongly inhibited by the generic superluminal configuration of the shock front [14, 95, 93, 149]. As the magnetisation parameter σ takes values above 10^{-4} , the extent of the powerlaw tail of nonthermal particles becomes more and more restricted, until it vanishes at $\sigma \sim 10^{-2}$ [149, 144, 128]. Yet, such a substantial magnetisation is expected in a wide class of high-energy astrophysical jets, as encountered in gamma-ray bursts, pulsar wind nebulae or active galactic nuclei, this hence raises the question of the relevance and the role of shocks as dissipation and acceleration agents [145].

One limitation of previous studies is to systematically consider laminar flow conditions, i.e. a nonturbulent, homogeneous background with uniform magnetisation, in stark contrast with the generic turbulent conditions of astrophysical plasmas with large Reynolds number. The presence of an intense turbulence upstream of a fast shock front may have several consequences. Turbulence may pre-accelerate the plasma particles via a stochastic Fermi process [178]; it may corrugate the shock front and modify locally the superluminal or subluminal nature of the magnetic configuration [98]. In turn, the corrugation will reprocess the turbulence between upstream and downstream, meaning that turbulence will not be trivially transformed through the shock, see e.g. [185, 28, 112, 163] in connection with the solar wind, or [96] for a theoretical discussion of the relativistic magnetized regime. In the context of PWNe, the work of [36] investigated the presence of a strong plasma turbulence in the downstream flow of the wind termination shock, as induced by current-driven instabilities in sharp velocity shear between strongly and weakly magnetized regions. In this picture, current sheets in the equatorial plane and at the poles would mix and lead to efficient nonthermal particle acceleration through magnetic reconnection.

Eventually, turbulence may in general well affect the dissipative properties, and therefore the acceleration efficiency, of relativistic, magnetized shocks.

In this Chapter we will mainly investigate, through self-consistent PIC simulations, the interaction between a relativistic shock and a turbulent magnetised plasma. Particular emphasis will be put on analysing the acceleration efficiency of the shock+turbulence system, notably by tracking a large number of particles in the simulations. Given the central role of the turbulence in several astrophysical sources, such simulations are the object of growing interest.

In our numerical setup, the shock is triggered by the interpenetration of two plasmas: the one continuously injected from the right-hand (rhs) side of the simulation domain, which propagates toward the left, and the plasma that, injected on the right boundary, has travelled the whole domain to be reflected on the left-hand

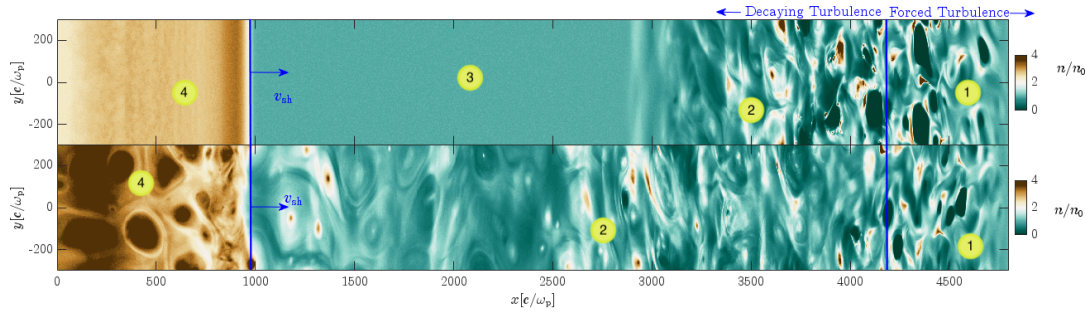


FIGURE 6.1: Plasma density in two different shock-turbulence simulations. Top panel, configuration (A): shock formation out of a non-turbulent plasma at $t \sim 0$. Bottom panel, configuration (B): the shock originates from a turbulent plasma which travelled across the whole domain.

side (lhs), which plays the role of a contact discontinuity, and propagates towards the right. The latter method is widely used in shock simulations [152]: it allows one to save computational time as it only produces one shock wave instead of a double system of forward and reverse shocks. The magnetic turbulence is driven using the Langevin antenna technique described in the dedicated Sec. 3.2.3. Although, there is an important difference to consider: the reference frame of the simulation coincides with the downstream of the shock while the turbulence is excited isotropically in its proper rest frame. Given that the plasma is drifting at a relativistic speed, the two frames do not coincide. As a consequence, the antenna has to be excited in the frame where it is at rest and hence differently in different points of the numerical grid connected to the rest frame of the turbulence by a Lorentz transform. This will be detailed in the following.

We explored two different main configurations: one, referred to as configuration (A) hereafter, where the shock suddenly originates from the injected plasma at $t \sim 0$ everywhere in the simulation box (top panel of Fig. 6.1); the other, configuration (B), where the shock originates only once the plasma, which had the time to couple with the turbulence travelling over the whole domain, reaches the left reflective boundary of the simulation box (bottom panel of Fig. 6.1). As already mentioned in Sec. 3.2.1, we recall that the simulation domain is divided into three main regions: one region, extending over a few cells, where the turbulence is initialised and sets the magnetic and electric fields but the particles do not feel the fields nor act on them; an adjacent zone where the turbulent is forced (rightmost part of the domain, numbered as “1”); next to it, the decaying turbulent part, where turbulence decays and evolve freely (“2” in Fig. 6.1). These three regions make up the upstream of the shock in configuration (A), along with the non-turbulent plasma populating the box at the beginning of the simulation and drifting with a negative velocity (“3” in Fig. 6.1). On the leftmost part, numbered as “4”, the either unperturbed (top panel for configuration (A)) or turbulent (bottom panel for configuration (B)) shock downstream. All the boundaries of these regions drift along with the plasma at a relativistic speed.

We aimed initially to study high plasma magnetisation levels ($\sigma > 1$) and ultra-relativistic shocks. Unfortunately, this turned out to be unfeasible because the magnetic energy density decays away rapidly, even if on timescales which get longer and longer because the dissipation-time is proportional to the Alfvén velocity and hence to the turbulent field which decreases along with the turbulent fluctuations δB . It is thus hard to keep a high magnetisation level of $\sigma \gtrsim 1$ throughout the simulation, and in particular by the time the turbulent plasma interacts with

the shock. Such magnetisation cannot even be attained in simulations of forced turbulence because of the rapid plasma heating (unless efficient cooling mechanisms are considered [191]). We hence performed simulations with magnetisation level $\sigma \sim 10^{-2} - 10^{-1}$ and $\delta B/B \sim 3 - 10$. Moreover, to save computational resources, we restricted ourselves to mildly relativistic shocks, adopting a shock Lorentz factor of $2 - 3$. Indeed, relativistic time dilation implies that, in the simulation frame, the characteristic length over which the turbulence evolves non-linearly scales with the drift Lorentz factor.

6.1 Numerical PIC simulations

In order to perform the simulation in the downstream frame of the shock, turbulence is set in motion along with the injected plasma while maintaining its excitation in its proper frame. In the following, primed quantities denote those evaluated in the plasma/turbulence rest frame and unprimed quantities those evaluated in the simulation (downstream) frame.

In the rest frame of the drifting plasma, which propagates at a normalized velocity β_∞ and Lorentz factor γ_∞ in the simulation (downstream) frame, turbulence is excited isotropically as a sum of $N_w = 24$ plane waves, with mean wavenumber $\langle k' \rangle \simeq 2.9 \times 2\pi/L'_{\max}$ (the wavenumbers coefficients used for the 2D geometry are reported in Tab. 3.1), where $L'_{\max} = L_y$, represents the extent of the simulation domain in the transverse (y) direction, the coherence length is defined as $\ell'_c = 2\pi/\langle k' \rangle$. The turbulence is driven through external δB_x and δB_y magnetic perturbations, which are seeded by the external vector potential $A_z = \sum_{i=1}^{N_w} a_i(t') e^{ik'_i \cdot \mathbf{r}'}$ via a Langevin antenna schema [159], as described in Section 3.2.1. Numerically, the excitation scheme is implemented so as to have it evolved in the simulation grid, while the antenna external vector potential is evaluated on refined grids

$$t' = \gamma_\infty [t - \beta_\infty (x - x_L)], \quad (6.1)$$

$$x' = \gamma_\infty [-\beta_\infty t + (x - x_L)], \quad (6.2)$$

with x_L the boundary of turbulence injection. Fluctuations decorrelate on timescales ℓ'_c/v_A in their proper frame and hence on timescales $\gamma_\infty \ell'_c/v_A$ in the simulation frame. Practically, the excitation scheme is numerically modified, for simulations containing a shock, with the following adjustments:

1. As the time index in the simulation frame increases to j with timestep Δt , in the rest frame of the plasma/turbulence the time step is given by $\Delta t' = \Delta t/\gamma_\infty$. Accordingly, we build a finer grid in proper time that spans the range of values covered by the simulation grid. The time coordinate t' also depends on the position on the grid: the left-hand boundary of the turbulence zone is associated with time coordinate $t' = t/\gamma_\infty$ (by using Eq.(6.2) with $x' \equiv 0$ into Eq.(6.2)), while the right-hand boundary has $t' = \gamma_\infty t$ (by using Eq.(6.2) with $x' \equiv x_L$ into Eq.(6.2)). As a result, the finer sub-grid in time, with index n_j , should span over Δn_j values with $\Delta n_j = \text{int}(\gamma_\infty^2) + 1$. The temporal part of the antenna, $a_i(t')$, is then advanced in *proper* time steps as

$$a_{i,n_j+1} = a_{i,n_j} \exp(-i\omega_0 \Delta t' + \gamma_0 \Delta t') + A_0 \sqrt{12|\gamma_0| \Delta t'} \xi_{n_j},$$

with $n_j \in [1, \Delta n_j]$.

2. The temporal coefficients are further smoothed to get rid of high-frequency noise which would translate in strong temporal gradients for the magnetic field, hence in strong electric fields, hence in plasma heating. We are indeed only interested in the frequencies such that the auto-correlation time of the fluctuations is nearly ℓ_c/v_A . We can thus discard higher frequencies smoothing the temporal coefficients over more than a few coherence time scales.
3. At a given position in the space-time grid of the simulation, using Eq. (6.1), we calculate the corresponding proper time in the turbulence rest frame on which we interpolate the temporal coefficients of the antenna from the new finer temporal array mentioned before.
4. All values of k'_i and ω'_i remain defined in the proper frame of the turbulence, A_z is expressed in terms of proper quantities of Eqs. (6.1)-(6.2) as $A_z = \sum_{i=1}^{N_w} a_i(t') e^{ik'_i \cdot \mathbf{r}'}$.

This procedure allows an isotropic turbulence to be excited in the rest frame of the leftward-moving, background plasma. Through nonlinear coupling with the plasma, a fully turbulent flow propagates towards the left side of the box, either to trigger a shock or to interact with a previously formed, nonturbulent shock, the properties of which will then be modified.

Such simulations are computationally expensive; the choice of box size and integration time has to accommodate both the following requirements and the computational cost. An extended domain is needed so that 1) the region where turbulence is driven covers at least one stirring scale for an effective coupling with the plasma, 2) the evolution of the interaction between the turbulence and the triggered turbulent shock can be followed in a sufficiently large part of the domain, before the shock attains the boundary of sustained turbulence. As a consequence of turbulence injection in its proper frame, if the shock is relativistic, time dilation also requires a longitudinal box size large enough that the moving turbulence has the time to evolve nonlinearly over $\Delta x > \gamma_\infty \ell'_c c/v_A$. These two latter reasons put some constraints on the shock Lorentz factor, hence our choice to restrict to a mildly relativistic γ_∞ of 2. The transverse dimension must be large enough to accommodate $\gtrsim 1 - 2 \ell'_c$, and ℓ'_c itself must be large enough compared to the kinetic scale c/ω_p . Last, if the shock is triggered by the turbulent plasma, the first part of the simulation is devoted to the building up of the turbulent flow and to its propagation all the way through the simulation box to eventually reflect on the left hand side and create the shock.

The simulations of the interaction of a turbulent plasma and a relativistic shock were performed in 2D3V geometry (2D in space, 3D in momentum) using the massively parallel, fully electromagnetic and relativistic CALDER code [87]. In each simulation, described below, we adopted a box of $48\,000 \times 6\,000$ grid cells of size $\Delta x = \Delta y = 0.1 c/\omega_p$, $\omega_p = (4\pi n e^2/m_e)^{1/2}$ representing the nonrelativistic plasma frequency of each species (i.e. $1/\sqrt{2}$ of the total plasma frequency). All simulations ran over the order of $1.2 \cdot 10^5$ time steps $\Delta t = 0.099 \omega_p^{-1}$, hence corresponding to an integration time of the order of $t \simeq 1.2 \cdot 10^4 \omega_p^{-1}$. In the downstream frame, the pair plasma initially follows a Maxwell-Jüttner distribution function, drifting at a velocity $v_x = -0.87$ (Lorentz factor $\gamma_\infty = 2$) from the rhs of the domain with a (apparent) temperature $T = 2m_e c^2/k_B$. Ten particles populate each cell and a uniform magnetic guide field B_0 is initialized along the out-of-plane z direction. Particles are frozen over a few grid cells ($x_{fr} = 4796c/\omega_p$) to avoid the sudden growth of the electric field and the consequent sudden dissipation of energy before the turbulent cascade can develop, as already discussed. With these box parameters, the coherence length of the turbulence is $\ell_c = 2\pi/\langle k' \rangle = L_y/2.9 \simeq 200c/\omega_p$ in its rest frame (we drop

Setup	$n'\gamma_\infty$	β_∞	$k_B T' / \gamma_\infty m_e c^2$	B_0	$\langle \sigma_0 \rangle$	$\langle \sigma_{\delta B} \rangle$
*1)	1	-0.87	2	0.38	$\sim 2 \cdot 10^{-3}$	$\sim 10^{-1}$
*2)	1	-0.87	2	0.19	$\sim 7 \cdot 10^{-4}$	$\sim 2 \cdot 10^{-2}$

TABLE 6.1: Parameters of the turbulent shock simulations: far-upstream apparent density, normalized plasma drift velocity, apparent normalized plasma temperature, normalized mean B field, spatially averaged coherent magnetisation, spatially averaged turbulent magnetisation. Each set of parameters has been run in different configurations: in A1) the shock is triggered at time $t \sim 0$ by the nonturbulent plasma hitting the left boundary; in B1 and B2) the shock originates from the turbulent plasma reflected on the mirror (lhs of the domain); D1) and D2) are “shock-free” configurations containing only a drifting periodic turbulence covering the whole domain with the same antenna parameters; C2) is a “turb-free” setup with no turbulent fluctuations.

hereafter the primed notation for simplicity). In order for the turbulent fluctuations to have the time to decorrelate and evolve non linearly, the forcing of the turbulent is applied in the region $x_f < x < x_{fr}$, with $x_f = 4200c/\omega_p$. Elsewhere, i.e. $x < x_f$, the injection of energy in the system is halted and the turbulence decays freely initiating the cascade.

To investigate the nature of acceleration, we performed different additional simulations with the same geometry but considering, respectively, the shock propagating in the external coherent field only (i.e. without turbulent fluctuations), referred to as case (C), and a drifting periodic turbulence covering the whole domain (i.e. without triggering any shock), referred to as case (D). We also considered two different levels of magnetisation associated with the turbulent component to test its impact on the efficiency of the combined acceleration process. We essentially used two set of parameters, 1) and 2), summarized in Tab. 6.1, the results of each will be presented in the following.

6.1.1 Simulation cases 1)

These simulations ran over 105 000 time steps, corresponding to an integration time $t \simeq 10\,400\omega_p^{-1}$. The value of the turbulent magnetisation, as attained close to the end of the simulation, is $\sigma_{\delta B} \sim 10^{-1}$ and $\delta B/B_0 \sim 5$. This is shown in Figs. 6.2-6.3: the first represents configuration (A), where the shock is almost instantaneously triggered by reflection of the non-turbulent plasma injected everywhere in the box at the beginning of the simulation, it is present in the domain since the very beginning ($x_{sh} \sim 270c/\omega_p$ at $\omega_p t = 594$); the second figure corresponds to configuration (B) where the shock is triggered by reflection of a turbulent plasma ($x_{sh} \sim 1200c/\omega_p$ at $\omega_p t = 9306$) and it has hence appeared in the box only at $t = L_x/\beta_\infty \sim 5600\omega_p^{-1}$. The coherent magnetisation, i.e. associated to the coherent background component B_0 , decreases in time due to heating of the plasma and the consequent increase of plasma enthalpy. As expected, the turbulent magnetisation is clearly higher where the turbulence is sustained ($4200 < x[c/\omega_p] < 4800$) and it reaches a stationary regime and a roughly constant value, on average, elsewhere.

A simulation using the same parameters but with open-ended conditions at the left boundary, hence without forming a shock and containing a drifting periodic turbulence only, have also been run (sub-case D1).

Figure 6.4 shows the $x - t$ diagram for the positron species of sub-cases (A1), top panel, and (B1), bottom panel. The transition between the teal and sand zones marks the shock position, in correspondence of which there is a density jump. In

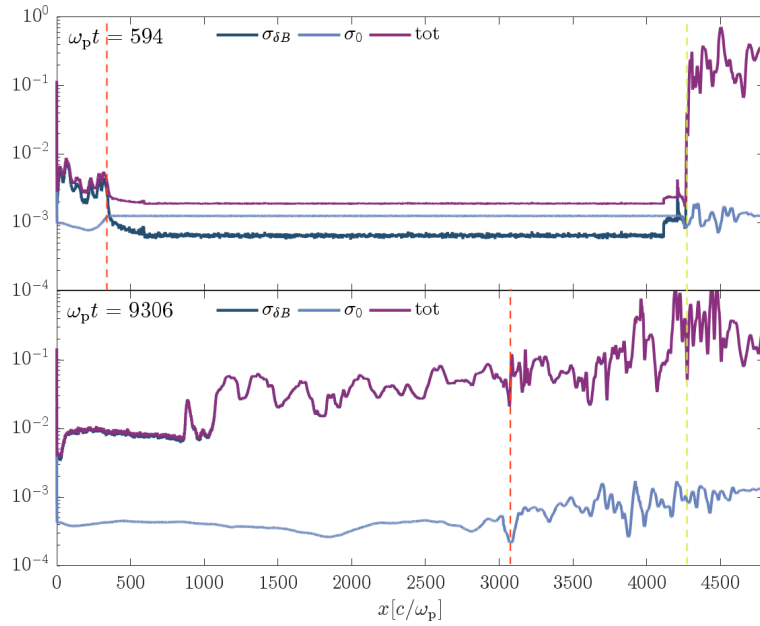


FIGURE 6.2: Longitudinal profiles of the (transversely averaged) coherent (σ_0) and turbulent ($\sigma_{\delta B}$) magnetisations at two different times for simulation run A1). In orange the position of the shock and in lime the position of the boundary of decaying turbulence. The value of σ_0 varies, in particular slightly decreases, in time/distance as a consequence of plasma heating.

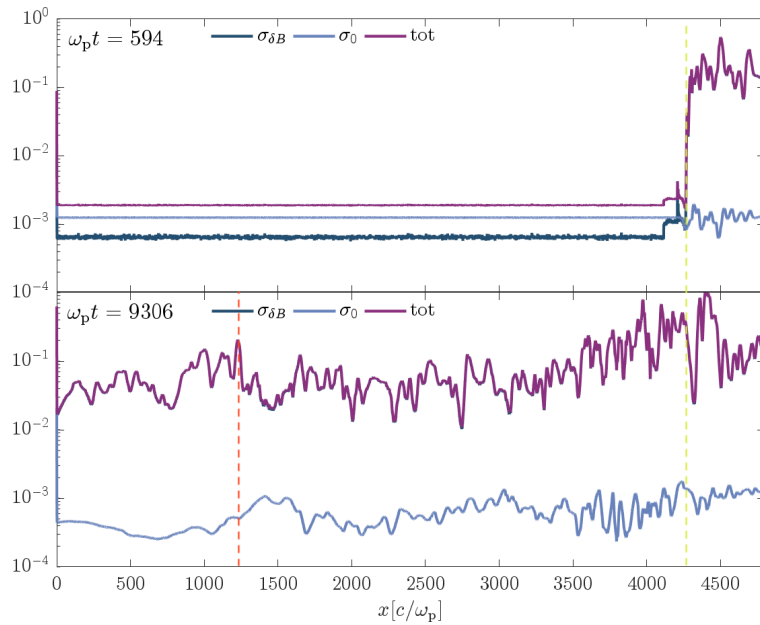


FIGURE 6.3: Same as Fig. 6.2 for simulation run B1).

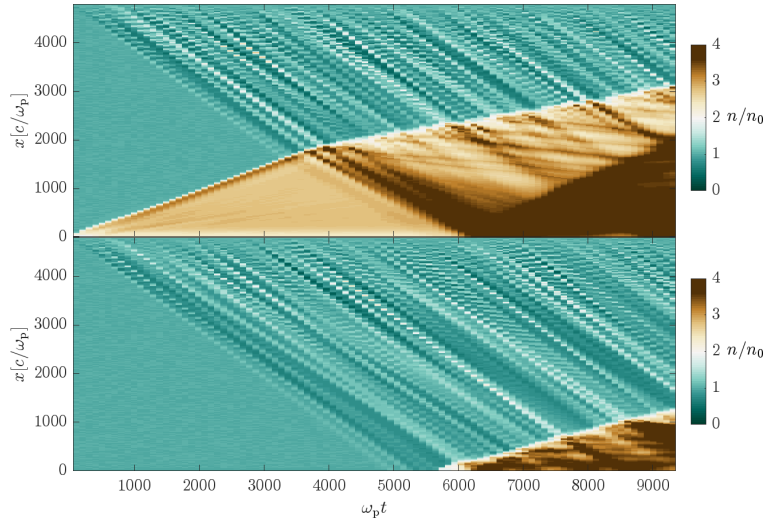


FIGURE 6.4: $x - t$ evolution of the transversely averaged positron density in configurations A1), top, and B1), bottom. The compression ratio in the downstream reference frame is $R_{|d} \sim 3 - 4$ and delimits the region of shock propagation. Upstream, the turbulent drifting fluctuations are visible. See the text for a complete description.

configuration A1), from time origin, one can see turbulent fluctuations propagate to the left; the shock then originates from a non-turbulent plasma and there are indeed no fluctuations either upstream or downstream until it encounters the turbulent inflowing plasma at $t \sim 3600\omega_p^{-1}$, at which time its speed decreases from $\beta_{sh|d} \sim 0.48$ to $\beta_{sh|d} \sim 0.25$. Afterwards, in the downstream of the shock, magnetosonic waves appear. In particular, fast waves visible as strong and wide modulations propagating at $v_F \sim -\max(c_s, v_A) \sim -c_s \sim -0.6c$ (sound velocity of a plasma with adiabatic index = 4/3) and slow waves, visible as weak perturbations propagating nearly horizontally at $v_S \sim -\min(c_s, v_A) \sim -v_A \sim -0.1c$. Interestingly a secondary weak shock ($v'_{sh} \sim 0.6c \sim c_s$), visible as a denser, darker region in the bottom right of the top figure, appears when the turbulence injected through the initially non turbulent shock has hit the reflective wall and propagates back toward positive x -directions faster than the “original” shock. All the above features, with the exception that the shock originates from the turbulent plasma and the downstream is thus turbulent everywhere without the presence of a secondary weak shock, are present also in the configuration B1).

In terms of apparent densities, as shown in Fig. 6.4, as the simulation frame coincides with the downstream frame, the compression ratio reads

$$R_{|d} \equiv n_d/n_{u|d} = \gamma_{u|sh}\beta_{u|sh}/(\gamma_{sh|d}\beta_{sh|d}\gamma_{u|d}), \quad (6.3)$$

with $\beta_{u|sh} = (\beta_{u|d} - \beta_{sh|d})/(1 - \beta_{u|d}\beta_{sh|d})$.

As the energy density of the turbulence is comparable to the energy density of the flow, the interaction with the turbulent flow slows down the shock to $\beta_{sh|d} \sim 0.25$ (0.3) for case A1) (B1). At $t \sim 8300\omega_p^{-1}$, we thus measure $\beta_{u|sh} \simeq -0.92$, for both, which translate in $R_{|d} \sim 4$. The expected compression ratio, as discussed in Sec. 2.1.2, is $R \sim 2 - 3$ assuming an adiabatic index of the plasma, $\hat{\Gamma}_d = 4/3$ (3D geometry) or $\hat{\Gamma}_d = 3/2$ (2D), respectively. The small difference with the theoretical value might be due to the mixed geometry of the simulation (2D in space and 3D in velocity) and to the fact that due to the presence of turbulence in the downstream

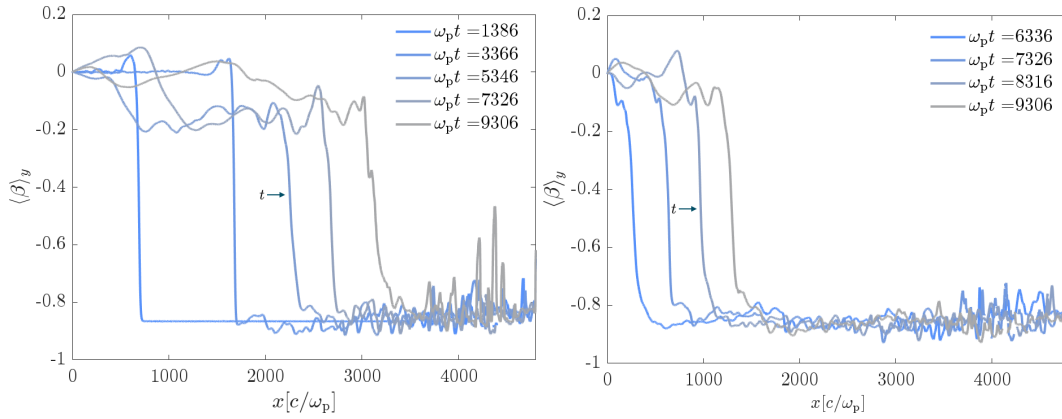


FIGURE 6.5: Plasma velocity averaged over the transverse y - direction for simulation run A1), on the left, and B1) on the right at different time steps. The simulation frame does not correspond anymore with the instantaneous downstream frame of the shock once turbulence affects the downstream.

of the plasma the downstream frame is not everywhere at rest (i.e. the simulation frame does not exactly coincide with the downstream frame, see Fig. 6.5).

Particle tracking

To probe the acceleration process, we follow a large number of test particles injected in energy intervals, from (initial) $\gamma_0 = 10$ to $\gamma_0 = 10^4$, at different times and locations with respect to the shock front in order to study different histories of interaction with the upstream turbulence and the shock. We first build histograms for each energy range counting the number of Fermi cycle performed by the particles. In particular, we extract the shock velocity from the $x - t$ diagram during the time interval where we inject and follow test particles to assign an analytical form to the shock front trajectory. The latter is then compared with the position of tracked particles as directly extracted from simulations to count the number of shock-crossings performed by each particle. Note that the related histograms, shown in Fig. 6.6 for case A1) and in Fig. 6.7 for case B1), are not cumulative, i.e. particles that cross the shock n -times are not counted among those crossing the shock $(n - 1)$ -times. A single Fermi cycle corresponds to two shock-crossings, from upstream to downstream (first shock crossing) and back upstream from downstream (second shock crossing). An even n number of shock crossings hence corresponds to completed Fermi cycles, while odd n shock crossings correspond to $n - 1$ Fermi cycles and a half, with the particle lying in the downstream. The occupation of the bins hence shifts towards lower values as the energy of the particles increases: larger energies correspond to larger gyration radius, correspondingly particles are unable to cross the shock more than a few times. For reference, given that $\delta\bar{B} \equiv \delta B / (m_e \omega_p c / e) \sim 10B_0 \sim 4$, $r_g = \gamma / \delta\bar{B} \sim 750 - 2500c / \omega_p$, in normalised units, for $3000 < \gamma < 10000$. In terms of gyrotime the expectations for the acceleration timescales are given by $t_{\text{acc}} \sim t_{\text{scatt}}$ [33], t_{scatt} the scattering timescale given by

$$t_{\text{scatt}} \sim \begin{cases} \frac{3r_g}{c} & \text{if } r_g \lesssim \ell_c \\ \frac{r_g}{c} \left(\frac{r_g}{\ell_c} \right)^2 & \text{if } r_g > \ell_c \end{cases} \quad (6.4)$$

which hence increases as the energy of the particle increases.

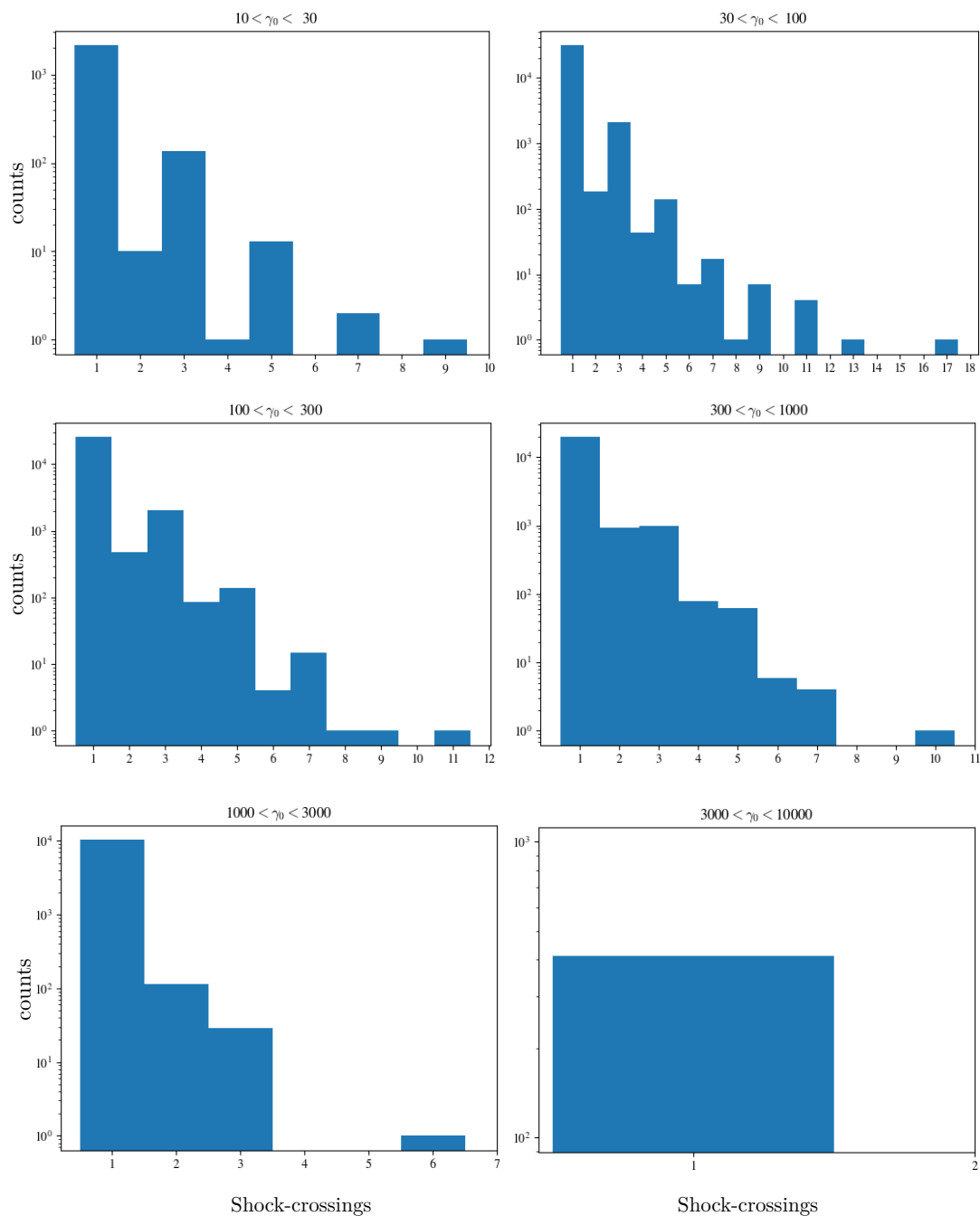


FIGURE 6.6: Histograms of the number of shock-crossings in simulation case A1) for different (initial) energy intervals of the tracked particles. An even number of shock crossings correspond to completed Fermi cycles around the shock front, while an odd number of shock crossings correspond to particles ending up in the downstream. The last two bins are affected by the finite time of the simulation.

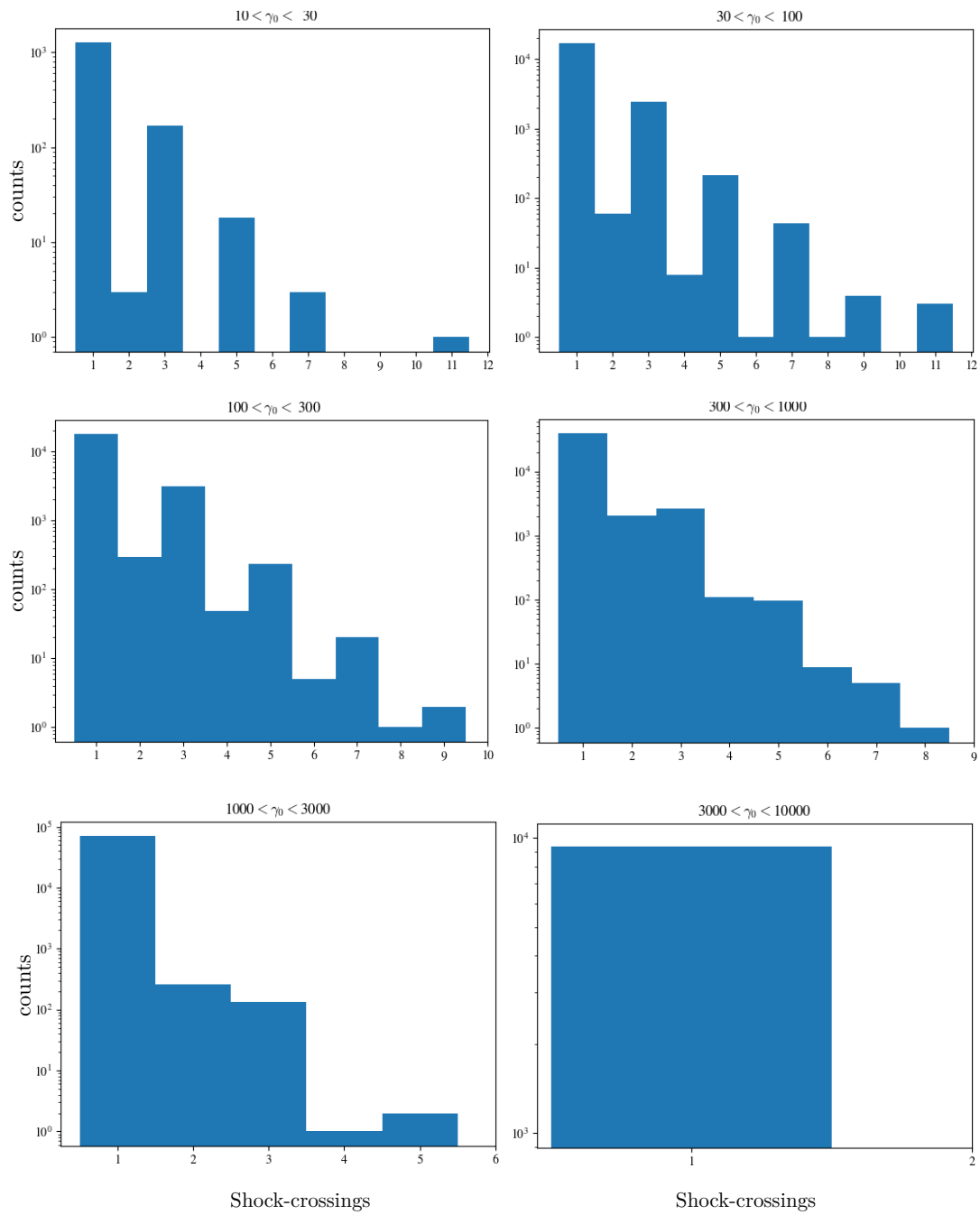


FIGURE 6.7: Same as Fig. 6.6 for run B1).

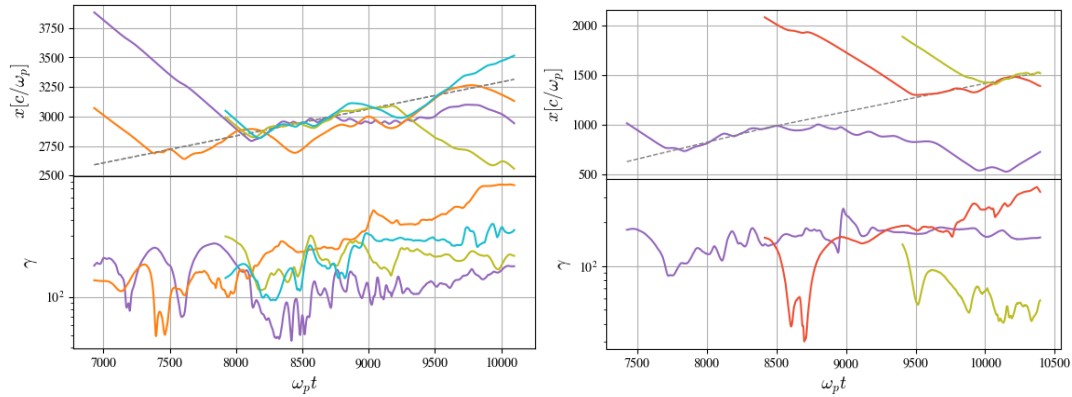


FIGURE 6.8: Trajectories and Lorentz factor evolution for a few representative test particles of run A1) on the left and B1) on the right selected among those in the energy bins of injection $100 < \gamma_0 < 300$. The dashed grey line represents the shock-front trajectory.

In addition, since the test particles are not really injected as new particles but only selected with a given probability from the plasma populating the box, the non-thermal tail needs to be developed for the highest energy particles to be selected. As a consequence, the highest-energy bin is almost entirely made up by particles injected at the latest time $t \sim 9400\omega_p^{-1}$ which have had no time yet to cross the shock more than once and to return upstream before the end of the simulation.

From the histograms we can infer the return probability as the ratio between the number of particles experiencing at least one Fermi cycle and the number of particles crossing the shock only once and remaining in the downstream. This gives $\langle P_{\text{ret}} \rangle \sim 9\%$ for run A1) and $\langle P_{\text{ret}} \rangle \sim 15\%$ for run B1). The mean energy gain per cycle, $\Delta\gamma/\gamma_0$ computed with respect to the value γ_0 at the beginning of the cycle, i.e. from upstream (downstream) to downstream (upstream) for odd (even) turns around, is $\sim 60\%$ averaging on all energy bins for run A1) and $\sim 30\%$ averaging on all energy bins for run B1). Yet, if we track the particle energy and position with respect to the shock front, the energy variation results from both the interaction with the shock front and the interaction with the turbulence experienced in the upstream. This can be read off Fig. 6.8 where we plot the trajectories and the energy evolution of a few test particles in the initial energy bin $100 < \gamma_0 < 300$. The plot on the right also contains one particle for each of the three groups injected at different times and positions with respect to the shock front. The Lorentz factor displays characteristic oscillations associated with the gyromotion of the particle around the magnetic field lines in a frame which is moving at large velocity relative to the simulation frame. By comparing the initial and final particle energies, despite the energization at the shock front associated with a completed Fermi cycle, the stochastic interaction with turbulent islands upstream or downstream of the shock can result overall in both a net energy gain (see e.g. cyan and orange particles in the left plot and red particle in the right plot) or a net energy loss (see e.g. purple and olive particles in the left plot and olive particle in the right plot).

Particle energy spectra

In Fig. 6.9, we show the time evolution of the overall particle energy spectrum $\gamma^2 dN/d\gamma$. The spectra are computed over a moving window across the shock front: at each time step where the spectra is evaluated, the shock position x_{sh} is recovered from the density map, then the energy distribution is obtained through averaging

over a window of half-width $\Delta x = 200 c/\omega_p$ centred on x_{sh} . Hence note that, given the minimum separation between the primary and secondary shock of $\sim 1000 c\omega_p$ at nearly the end of the simulation, the secondary wave, formed by the reflection of the turbulent plasma, does not impact our analysis.

From the thermal distribution of injection, the spectra clearly acquire a power-law tail extending at the end of the simulations to $\gamma_{\text{max}} \sim 4 \times 10^3$. Acceleration is expected to slow down above γ such that $r_g \sim \ell_c$ (see Eq. (6.4)), when the motion of particles over the turbulent fluctuations becomes nearly ballistic. This is satisfied, considering a mean field of $B_0 + \delta B \sim B_0 + 10B_0$, for $\gamma_c \sim 900$, in nice agreement with what we observe in Fig. 6.9.

The energy cut-off is not easy to identify and we interpret the shape of the spectra as the result of the acceleration by the combined effect of Fermi processes and turbulence. Indeed, a nonturbulent shock configuration is expected to produce a suprathermal powerlaw spectrum with spectral index

$$s = 1 - \ln(\langle P_{\text{ret}} \rangle) / \ln(1 + \langle \Delta\gamma/\gamma \rangle), \quad (6.5)$$

in the assumption that the shock moves at sub-relativistic speed in the upstream, and that all particles come back to the shock with a same probability $\langle P_{\text{ret}} \rangle$, and gain in a cycle a same relative amount $\langle \Delta\gamma/\gamma \rangle$. In our case, the return probabilities and the mean energy gains estimated in the above section give $s \sim 6$ (8), for case A1) (B1)[15]. The discrepancy with the observed value of $s \sim 3$, in Fig. 6.10, is

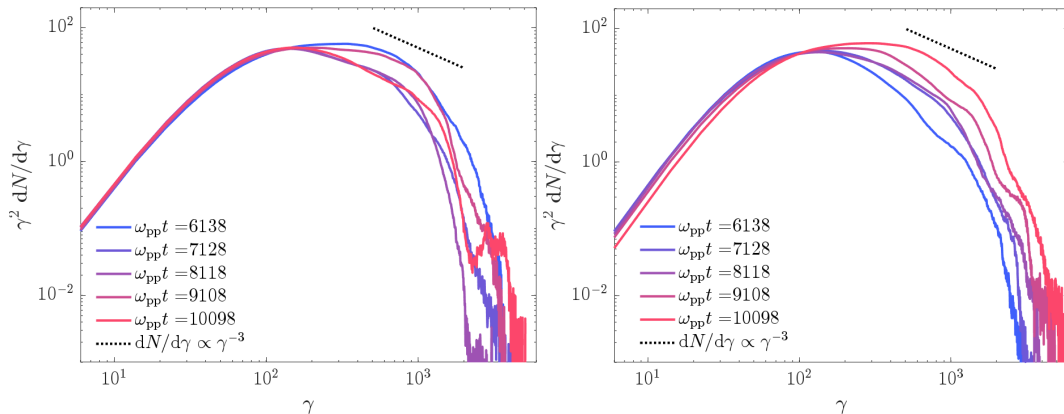


FIGURE 6.9: Time evolution of the particle energy spectrum across the shock front of run A1) on the left and B1) on the right.

probably related to the fact that formula 6.5, valid for a sub-relativistic shock, is employed outside its validity range. Assuming isotropic diffusion both upstream and downstream of the shock, a generalized formula valid in the relativistic regime leads to a slope, in our notations,

$$s = -2 + (3\beta_{\text{sh}|u} - 2\beta_{\text{sh}|u}\beta_{\text{sh}|d}^2 + \beta_{\text{sh}|d}^3)/(\beta_{\text{sh}|u} - \beta_{\text{sh}|d}), \quad (6.6)$$

with $\beta_{\text{sh}|u} = v_{\text{sh}|u}/c$ [80]. As mentioned above, in both cases the shock is slowed down to $\beta_{\text{sh}|d} \sim 0.3$, $\beta_{\text{sh}|u} \sim 0.92$, which gives $s \simeq 2.2$ for the two configurations A1) (B1). Those spectral indices are harder than those we measured, in both setups. This suggests that the hypothesis of isotropic diffusion, or more generally the pitch-angle diffusion underlying the above formula, fails here to reproduce the interaction of particles with a strong turbulence.

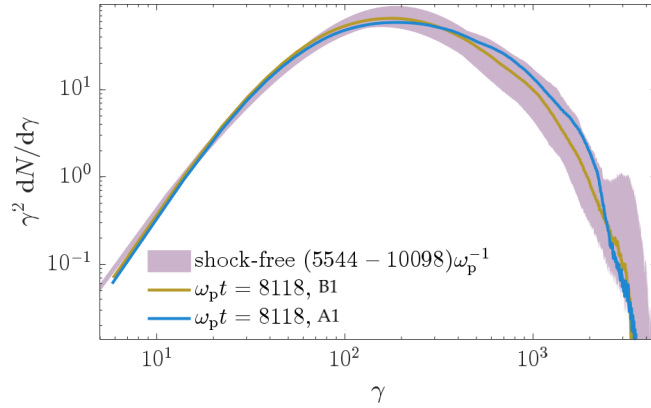


FIGURE 6.10: Particle energy distribution at $t \simeq 8000 \omega_p^{-1}$ in a simulation with ambient magnetisation $\sigma_0 \simeq 0.01$ and $\sigma_{\delta B} \simeq 0.1$. The blue and the orange lines shows the spectra computed across the shock in run A1) and B1) respectively (Fig. 6.9). The pink band represents the range of spectra measured in a same simulation without shock (D1), as extracted in various places and at various times in the interval $6000 - 10000 \omega_p^{-1}$.

Discussion

We conclude that each observed spectrum hardly evolves in time because the non-thermal particle acceleration that we observe in the present case is mostly the result of stochastic acceleration in the mildly-relativistic turbulence. In support of this, we have performed a similar simulation, with in particular the same turbulent fluctuations, i.e. same random number sequence determining the turbulence, albeit without triggering the shock as we left set to periodic the boundary condition on the left hand-side of the domain. We do not observe a substantial difference between the two energy distributions, measured with or without the shock: figure 6.10 shows the spectrum of the shock simulation A1) in blue and B1) in orange at an intermediate integration time, while the shadowed area indicates the range of spectra observed in the simulation without shock (D1) at various times in the interval $6000 - 10000 \omega_p^{-1}$. The similarity of those spectra suggests that the relativistic turbulence alone is able to promote particles into a non-thermal distribution. The increase in magnetisation reduces the acceleration timescale in the turbulence, defined as $t'_{\text{acc}} \sim c\ell_c/v_A^2$ in the proper frame and $t_{\text{acc}} = \gamma_\infty t'_{\text{acc}}$ in the simulation frame, which becomes of the order of $t_{\text{acc}} \sim 10^3 \omega_p^{-1}$, thus shorter than the time it takes for freshly injected particles on the right hand side of the domain to reach and cross the shock. For $\sigma_{\delta B} \sim 0.1$ and $\delta B/B \sim 3 - 5$, stochastic acceleration can produce spectra with slope $s \simeq 3 - 4$ [191, 42, 22], in agreement with what we found. Even though Fermi cycle are possible, and observed by tracking test particles, given the high level of magnetisation of the external fluctuations, acceleration in turbulence takes over Fermi acceleration at the shock front.

6.1.2 Simulation results 2)

As the substantial level of turbulence of the previous set resulted in particle acceleration inside the turbulence taking over Fermi acceleration at the shock, we decreased, for the second set of parameters 2) in Tab. 6.1, the magnetisation down to $\sigma_{\delta B} \sim 2 \times 10^{-2}$ and the strength of turbulent fluctuations down to $\delta B/B_0 \sim 5$, as shown in Fig. 6.11. The reference simulation, B2), has been run in a turbulent-shock

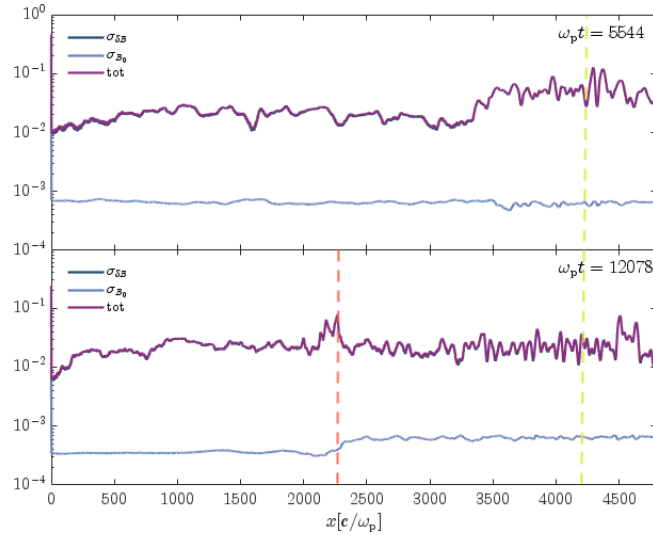


FIGURE 6.11: Transversely averaged spatial profiles of the coherent and turbulent magnetisations at two different times for simulation run B2) as a function of x . In orange the position of the shock and in lime the position of the boundary of decaying turbulence.

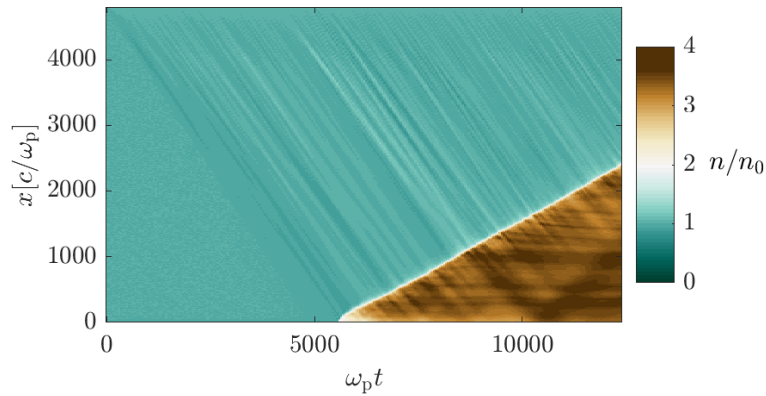


FIGURE 6.12: $x - t$ diagram of the positron density from run B2).

configuration, similar to B1), over 124 000 time steps, corresponding to an integration time $t \simeq 12\,300\omega_p^{-1}$. On top, we conducted an additional simulation with the same box and the shock propagating in the external coherent field only (C2), and a shock-free simulation of drifting periodic turbulence, with identical random number sequence determining the fluctuations covering the whole domain (D2).

At $t \sim 12\,000\omega_p^{-1}$ the shock has reached $x \sim 2\,200c/\omega_p$, traveling toward the right (see the $x - t$ diagram of the positron density in Fig. 6.12). At that time, Fig. 6.13 shows 2D maps of plasma density, mean particle Lorentz factor and magnetic fluctuations, from top to bottom panels.

As previous configurations, turbulence is sustained in a region of extent $L_{\max} = 600c/\omega_p$ near the right hand side boundary. Correspondingly, magnetic fluctuations are more intense in that region (second panel of Fig. 6.13). At the final time, the distance between the shock and the boundary of sustained turbulence is $\simeq 2\,200c/\omega_p$, just below the minimum distance $\gamma_{\infty}\ell_c/v_A$ needed for nonlinear evolution of the turbulence. This guarantees that over the simulation, this constraint was respected. As shown in the bottom panel of Fig. 6.13, the turbulence amplitude reaches a roughly stationary state by the time it reaches the shock; at larger values of x , corresponding to earlier times in the history of the turbulence evolution, stronger variations

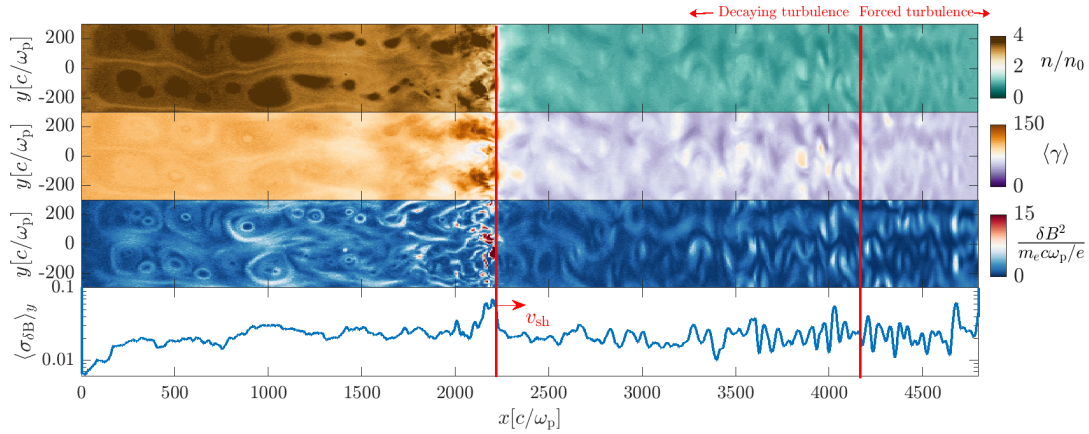


FIGURE 6.13: From top to bottom: 2D maps of plasma electron density, mean Lorentz factor and magnetisation at $t \sim 12000\omega_p^{-1}$ for simulation case B2). The lower bottom panel plots the transversely averaged magnetisation as a function of the x -position.

are observed, as expected. Once the turbulence reaches the shock, the eddies are compressed when crossing the shock front and they continue interacting until the turbulence eventually relaxes further downstream. The general picture observed here resembles that observed in MHD simulations of the interaction of a monochromatic, linear eigenmode of the plasma with a relativistic shock front [52]. There, it was shown that the fast magnetosonic or entropy mode are able to induce the corrugation of the shock front as they income from upstream and they interact with the shock front. An unstable corrugated configuration was also observed in hybrid (PIC+MHD) simulations of non-relativistic shocks with different Alfvénic Mach numbers, as induced by suprathermal particles produced via a pre-heating process akin to shock drift acceleration [165].

Here, in addition to the shock front being corrugated, one can see modulations in the incoming turbulence upstream of the shock, up to length scales $\sim 100c/\omega_p$, which indicate the presence of a precursor of accelerated particles able to dissipate the energy of the turbulent plasma slowing it down before its encounter with the shock. The interaction with the incoming turbulent flow progressively slows down the shock front to $\beta_{\text{sh|d}} \simeq 0.4$ in the simulation (downstream) frame at $t \sim 12000\omega_p^{-1}$. Consequently, the shock moves at $\beta_{\text{sh|u}} \simeq 0.93$ in the upstream frame, corresponding to a shock Lorentz factor $\gamma_{\text{sh|u}} \simeq 2.7$. The upstream medium moves with respect to the downstream at $\beta_{\text{u|d}} = -0.86$ ($\gamma_{\text{u|d}} \sim \gamma_\infty = 2$, see Fig. 6.14) hence the expected compression ratio, as given by Eq. (6.3), is $R_{\text{d}} \sim 3.5$, in good agreement with Fig. 6.12. The level of turbulence attained once the turbulent fluctuations cover the vast majority of the domain ($t \sim 25\ell_c/c \sim 5000\omega_p^{-1}$) is $\langle \sigma_{\text{dB}} \rangle \sim 2 \times 10^{-2}$, implying $\delta B/B_0 \sim 5$. The mean magnetic field, averaged on the transverse direction, is thus roughly $\delta B/(m_e \omega_p c/e) \sim 1.2$, which means that particles with Lorentz factor $\gamma \sim 100 - 300$ have a gyroradius $r_g/(c/\omega_p) \sim 80 - 250$.

Particle tracking

The histograms of the number of shock-crossings by the tracked particles are shown in Fig. 6.15. After shock formation at $t \sim 5600\omega_p^{-1}$, new particles are injected, or, more properly, extracted with a given probability from the existing ones populating the simulation, every $\sim 1000\omega_p^{-1}$ until $t \sim 9500\omega_p^{-1}$ and at different positions with respect to the shock front. Histograms are then built considering all groups divided

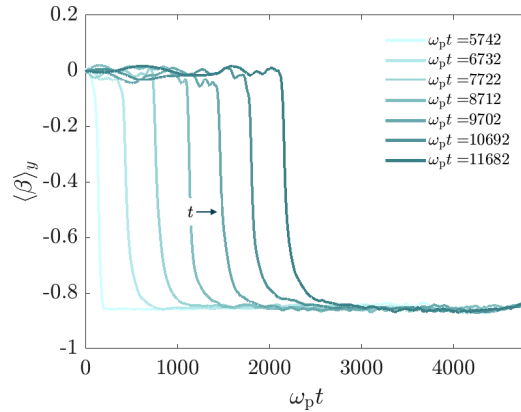


FIGURE 6.14: Plasma velocity averaged over the transverse y - direction for simulation run B2) which shows the evolution of the shock position in time. The simulation frame roughly corresponds to the instantaneous downstream rest-frame of the shock and the upstream medium drifts at $\beta_{u|d} \sim \beta_{\infty} = -0.86$. In between the two medium the shock front is visible propagating at $\beta_{sh|d} \sim 0.4$.

by the energy bin of injection in the simulation. As before, we extract the shock front trajectory from the $x - t$ diagram and we seek for where the difference between the particle and the shock position change sign to keep track of the shock crossings. As a reminder, a completed n - Fermi cycle upstream \rightarrow downstream \rightarrow upstream correspond to even shock crossings.

In contrast to run 1), no particles have been energized to $\gamma > 1000$ and as a consequence, there are no particles found in the energy bins associated with higher energies. We have measured the mean energy gain per cycle $\langle \Delta\gamma/\gamma \rangle$, estimated as the relative variation of the Lorentz factor within a Fermi cycle starting upstream up \rightarrow down \rightarrow up: in the energy bins from $\gamma_0 = 30$ to $\gamma_0 = 300$, we find $\langle \Delta\gamma \rangle/\gamma \simeq 0.4$. This value is slightly lower than the prediction $\langle \Delta\gamma/\gamma \rangle \simeq \beta_{sh|u}$ (recalling $\beta_{sh|u} \simeq 0.93$ here) that pertains to the sub-relativistic regime [15], and lower than the (relative) gain of order unity expected in fully relativistic shocks [4]. We also measure the mean return probability to the shock, as before, defined as the ratio between the number of particles that executed at least a full Fermi cycle starting upstream to the total number of particles. We obtain $\langle P_{ret} \rangle \simeq 0.15$. This value is slightly larger, yet comparable, to the prediction $1 - \beta_{sh|u}$ for a sub-relativistic shock in steady state [15], but lower than the value $\simeq 0.4$ measured in test particle Monte Carlo simulations of relativistic shocks with isotropic scattering [94].

Figure 6.16 shows the trajectories and energy histories of some test particles representative of the population able to undergo multiple shock crossings. The right panel contains at least one particle of each group corresponding to different times of injection. Most of them undergo reflections at grazing angles in the corrugated shock layer, whose mean position is indicated by the dashed line in the upper panel. Those interactions with the shock clearly give rise to energy gain, while particles maintain a constant energy when escaping downstream, see *e.g.* the purple and ochre histories at late times in the right panel. Some other particles execute deep penetrating orbits in the upstream, which are accompanied by large energy gains within one Fermi cycle, *e.g.* the cyan trajectory on the left or the green and ochre trajectory on the right. This might be due to the interaction with a turbulent island encountered upstream, able to reflect the particle back to the downstream.

Finally, note that among all the test particles considered, only a small fraction (\lesssim

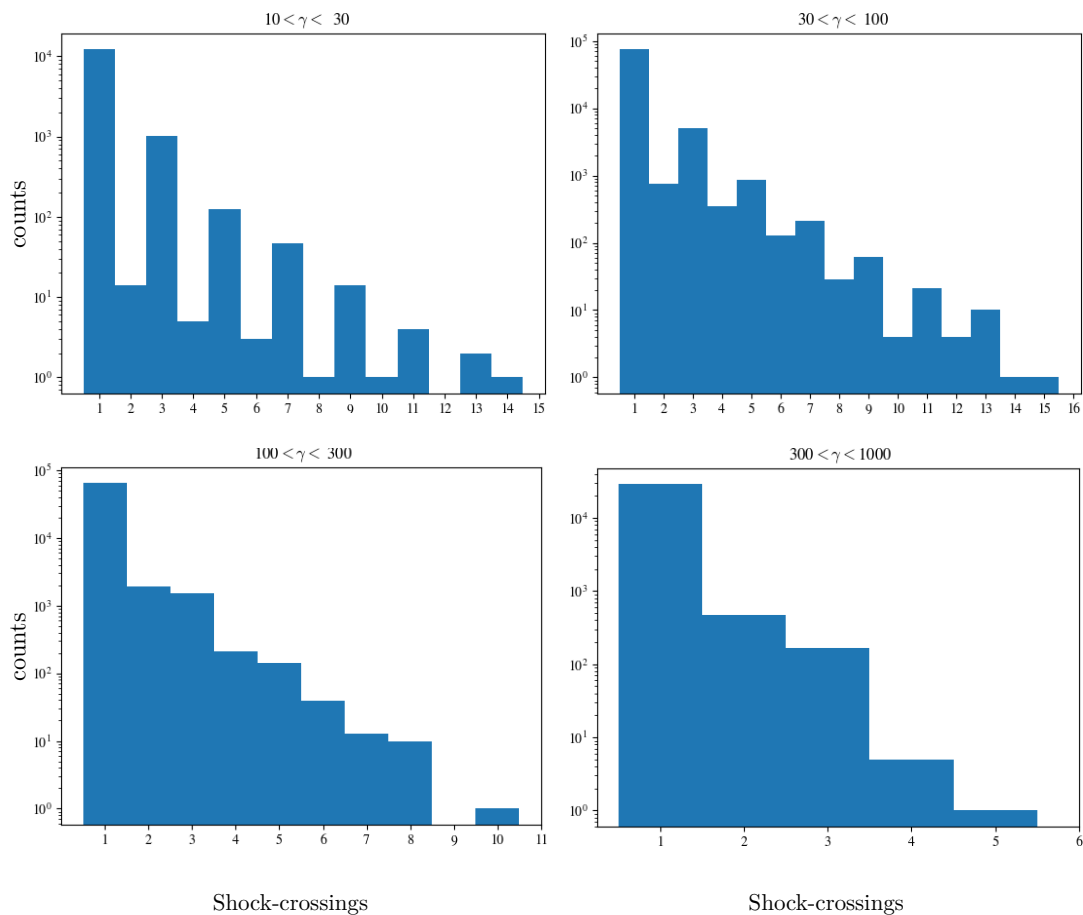


FIGURE 6.15: Histograms of the number of shock-crossings in simulation case B2). Even shock crossings correspond to completed Fermi cycles around the shock front, odd shock crossings correspond to particles in the downstream.

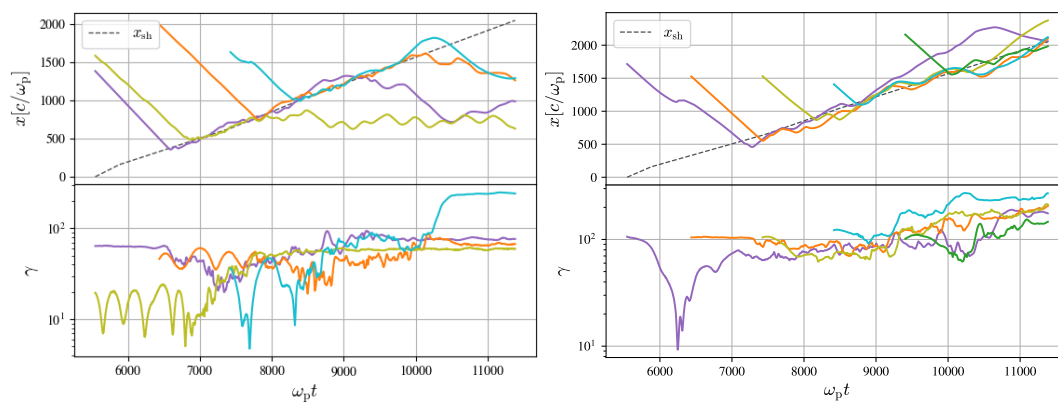


FIGURE 6.16: Trajectories and Lorentz factor evolution for a few representative test particles of run ii) with initial energy of $30 < \gamma_0 < 100$ on the left and $100 < \gamma_0 < 300$ on the right.

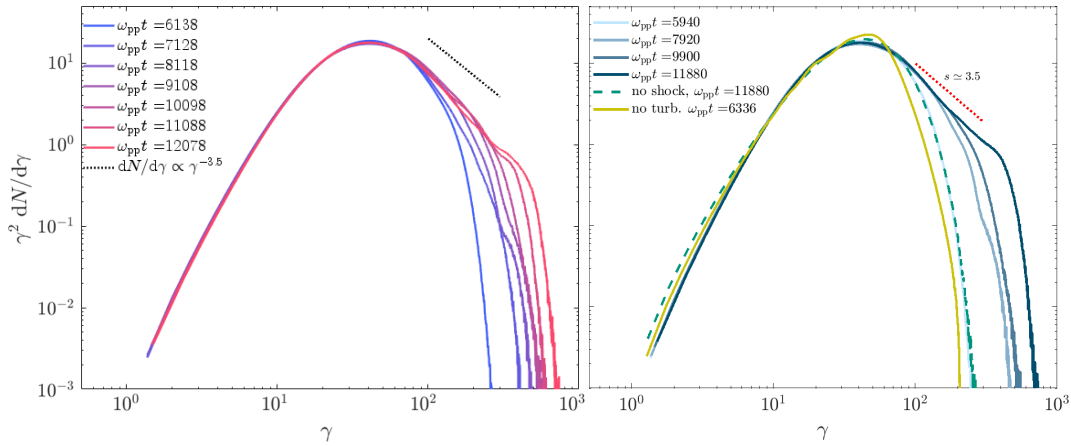


FIGURE 6.17: On the left: time evolution of the particle energy spectrum across the shock front for simulation case B2); the black dotted line indicates the best-fitting powerlaw $dN/d\gamma \propto \gamma^{-s}$, with $s \simeq 3.5$. On the right: time evolution of the particle energy spectrum across the shock front, setup B2)-blue lines, as compared with the spectra extracted from simulations containing either a nonturbulent shock, setup C2)-ochre line, or a drifting turbulence, setup D2)-dashed green line, as explained in the text. The red dotted line indicates the best-fitting powerlaw.

1%) of the selected test particles ($\mathcal{O}(10^5)$) have returned to the shock after bouncing specularly on the reflective wall; those orbits do not significantly alter our results.

Particle energy spectra

The energy spectrum $f(\gamma)$, plotted in the left panel of Fig. 6.17, clearly shows a powerlaw tail up to $\gamma_{\max} \sim 900$ with an energy cutoff at $\gamma_c \sim 400$ at the end of the simulation. The slope of the nonthermal tail is measured to be $s \simeq 3.5$, defining as before s through $dN/d\gamma \propto \gamma^{-s}$. As a reminder, for a sub-relativistic shock, the spectral index can be expressed as $s = 1 - \ln(\langle P_{\text{ret}} \rangle) / \ln(1 + \langle \Delta\gamma/\gamma \rangle)$, in terms of the return probability and mean energy gain evaluated in the previous section. This formula would predict a rather steep spectrum $s \simeq 6.6$, but, again, that is used here outside of its range of validity as our case is typical of strong relativistic shocks for which we have $\beta_{\text{sh|d}} = 0.35$ and $\beta_{\text{sh|u}} = 0.93$ as already cited above. If we apply the generalized relativistic formula 6.6, valid under the assumption of isotropic diffusion both upstream and downstream of the shock, we get $s \simeq 2.5$, harder than what is measured here. Even for this second set of parameters 2), the pitch-angle diffusion approximation used to compute the formula 6.6, fails to represent the particle behavior in the strongly turbulent fluctuations. We recall also that we have measured a return probability and an energy gain which are both slightly lower than those expected for fully relativistic shocks with isotropic scattering; hence, it is not surprising that we observe a steeper spectral index.

Regarding the acceleration timescale, we observe that the cut-off Lorentz factor at which the spectrum turns over from the powerlaw segment increases from $\gamma_c \sim 200$ at $t \simeq 6000 \omega_p^{-1}$ to $\gamma_c \sim 400$ at $t \simeq 12000 \omega_p^{-1}$. In terms of gyrotime, this corresponds to an acceleration timescale $t_{\text{acc}} \sim |\Delta\gamma_c/\gamma_c|^{-1} \Delta t \sim 6000 \omega_p^{-1} \sim 20 - 30 r_g/c$, for particles with a mean Lorentz factor $\in [200 - 400]$ who have a typical Larmor radius of $r_g \sim 200 - 300c/\omega_p$. The expectation here is $t_{\text{acc}} \sim t_{\text{scatt}}$ for the relativistic regime, and, for comparable values of Larmor radius and coherence length, $t_{\text{scatt}} \sim 3r_g/c$ [33], hence the present value of t_{acc} exceeds the theoretical estimate by a factor of

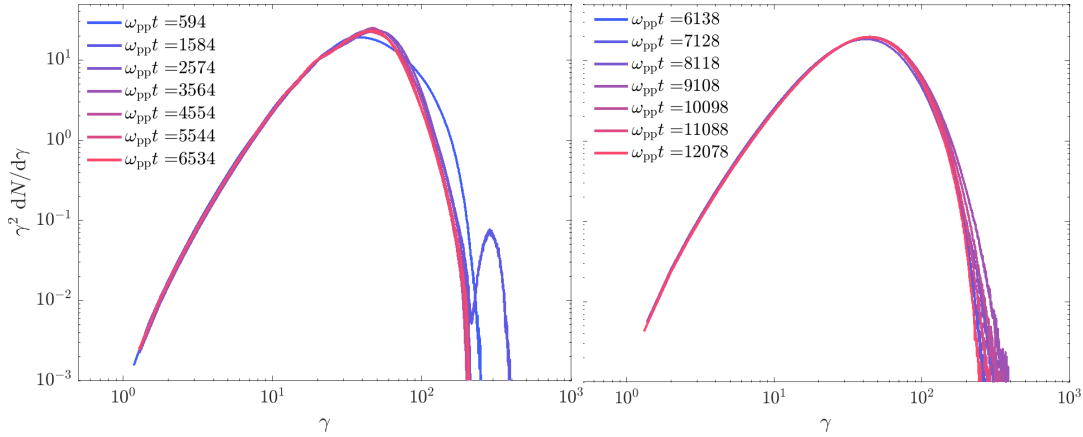


FIGURE 6.18: Time evolution of the particle energy spectrum across the shock front for the additional runs with the same parameters configuration 2) but containing only the shock (left panel, setup C2) or only the turbulence (right panel, run D2).

6 – 10. We note that, as the particle gyration radius becomes of the order of/greater of the coherence length of turbulent structures, its motion becomes ballistic rather than diffusive. Consequently, as the acceleration time scale in this regime as $t_{\text{scatt}} \sim r_g/c (r_g/\ell_c)^2$ (see Eq. (6.4)) we thus expect the evolution of γ_c beyond ~ 300 , at which point $r_g \sim \ell_c$, to slow down.

Comparison and additional runs

To be sure that the thermal tail originates from the joint effect of turbulence and shock, we ran two additional simulations considering at a time only the shock or only the turbulence. The distribution remains thermal in both configurations cited above and no power law forms in either of the two spectra (see Fig. 6.18).

Indeed, for a (non-turbulent) shock propagating in a non-turbulent plasma, the high magnetisation $\sigma \equiv \sigma_0 \simeq 10^{-3}$ of the coherent field is such that the particles are simply advected downstream with the magnetic field lines and the self-generated turbulence is not strong enough to trap a significant fraction of particles at the shock for efficient acceleration. The high level of magnetisation inhibits particle acceleration, preventing Fermi cycles and the development of a non-thermal tail, as expected for a relativistic superluminal magnetized shock [148].

On the other side, in the configuration with turbulence but no shock, acceleration is effective on timescales $t'_{\text{acc}} \sim c\ell_c/v_A^2$ in the proper frame of the turbulence, which translates in $t_{\text{acc}} = \gamma_{\infty} t'_{\text{acc}} \sim 10^4 \omega_p^{-1}$ as measured in the simulation frame. Thus, the magnetic fluctuations are simply not fast enough to accelerate particles within the simulation timescale.

The right panel of figure 6.17 compares the spectra from the simulation containing only the fluctuations in the same conditions of turbulence (dashed green) and from the simulation free of turbulence where the shock forms immediately in the same external field B_0 (solid ochre). We hence conclude that the development of the nonthermal tail observed in our simulation arises through the combined action of scattering off strong turbulent fluctuations, which allow multiple crossings of this relativistic, magnetized shock.

6.2 Discussion

We have performed the first *ab initio* particle-in-cell kinetic simulations of a relativistic shock propagating in a turbulent, magnetized pair plasma. The shock is either initiated by a non-turbulent plasma, and later made to propagate in a turbulent medium, or initiated by directly reflecting a turbulent plasma off a wall, so that that two turbulent plasmas interpenetrate each other at super-Alfvénic speeds. Those simulations allow us to study the interaction between the turbulence and the shock and how that interaction modifies the properties of the relativistic shock wave itself, its dynamics and particle acceleration efficiency. In our main simulation, corresponding to the set of parameters 2) of table Tab. 6.1 and a turbulent shock, the shock Lorentz factor with respect to the unshocked, turbulent plasma is $v_{\text{sh|u}} \simeq 0.93 c$, the background magnetisation level is $\sigma_0 \simeq 10^{-3}$ and the turbulent magnetisation $\sigma_{\delta B} \simeq 0.03$. Our main result is to observe a clear signature of Fermi-type acceleration at the shock front, even though the relativistic magnetized configuration is known to prohibit acceleration in the absence of external turbulence. A non-thermal tail in the particle spectrum develops only once both ingredients, shock and turbulence, are present. Indeed, as one of the two is missing, and as long as the turbulence is not sufficiently magnetised, particles remain thermally distributed: we do not observe evidence for particle acceleration in the magnetized shock simulation without external turbulence, or in the magnetized turbulent simulation but without a shock.

In general, the acceleration properties strongly depend on the characteristic of turbulence and on its natural spatio-temporal intermittency; increasing the average magnetisation of the plasma inhibits the effect of the shock on the acceleration process: at large $\sigma_{\delta B}$ the spectral index due to turbulent acceleration simply becomes harder than that due to the shock and hence dominates the behaviour of the spectra (i.e. first set, 1), of parameters studied).

By following a large number of particles, we have verified that the shock-induced acceleration is related to repeated shock crossings in which particles gain energy through Fermi cycles. Particles, as they gain energy and increase their Larmor radius through multiple shock crossings, can penetrate deeper and deeper in the upstream where they can be randomly reflected by turbulent perturbations present in the shock upstream back into the downstream. The observed spectral index, $s \simeq 3.5$ in configuration B2), is larger than the usual prediction for relativistic shocks, $s \simeq 2.2$, assuming isotropic pitch-angle diffusion. The isotropic assumption of scattering off turbulence in the downstream, as commonly adopted in analytical works [80], is not able to provide a good estimation for both the spectral index and the return probability we observe in our simulations.

Interestingly, the steep spectral index we found, matches the experimental values collected in a large sample of gamma-ray bursts by [29]. Through a synchrotron modeling of the time-resolved spectra observed by the Fermi-BGM instrument, those authors reconstruct an injection powerlaw with index $s \simeq 3.5$, assuming an ambient magnetisation of the order of $0.01 - 0.1$, i.e. close to ours. This coincidence is all the more intriguing as mildly relativistic shocks are naturally expected in such sources from inhomogeneities launched at the base of the jet. Mildly relativistic, magnetized shocks in conditions close to those explored here are similarly expected in blazars. The compilation of parameters obtained from one-zone synchrotron plus inverse Compton models by [34] indicates that magnetisation levels $\sim 0.01 - 0.1$ are the rule, and that the spectral indices range between $s \sim 2.5$ and $s \sim 3.5$. Acceleration in reconnection regions generally leads to steeper spectra unless the magnetisation takes larger values, e.g. $\sigma_0 \gtrsim 1$ [126].

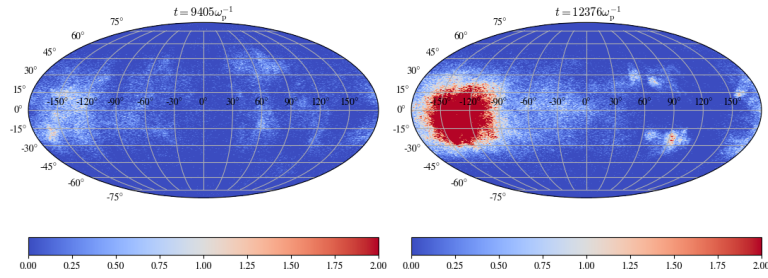


FIGURE 6.19: Sky maps of anisotropy in momentum distribution for suprathermal positrons of $\sqrt{p_x^2 + p_y^2 + p_z^2}/mc = p/mc = 300$ at two different times $t = 9405\omega_p^{-1}$ on the left and $t = 12376\omega_p^{-1}$ on the right, as a function of the longitude $\phi \in [-\pi, \pi]$ and latitude $\in [-\pi/2, \pi/2]$.

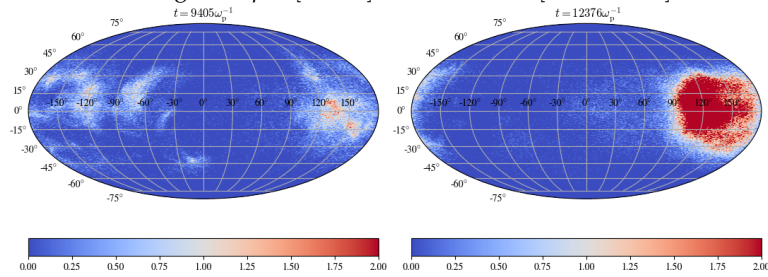


FIGURE 6.20: Same as 6.19 for the electron species.

The distribution of supra-thermal particles in (spherical) momentum space reveals the presence of time-dependent anisotropies. This feature is illustrated in Fig. 6.19 for positrons and in Fig. 6.20 for electrons, which show the angular distributions in terms of longitude, $\phi = \arctan(p_y/p_x) \in [-\pi, \pi]$, and latitude, $\in [-\pi/2, \pi/2]$ defined as $\pi/2 - \theta$, $\theta = \arccos(p_z/\sqrt{p_x^2 + p_y^2 + p_z^2})$, for momentum directions at two different times for our main simulation. Accounting for Lorentz boosting from the simulation (downstream rest) frame to the observer frame, such anisotropy would lead to time variations on (comoving) timescale ℓ_c/c , behaving much in the same way as jet-in-jet models [66]. Such effects could therefore produce small timescale variability, even though most of the dissipation and acceleration would come from the shock itself.

Figures 6.19-6.20 suggests that particles are roughly aligned with the shock front, i.e. y -direction ($\theta = \pi/2$ hence zero latitude, $\phi = \pm\pi/2$), as in the shock drift acceleration process. Supra-thermal particles of $\gamma > 300$ have indeed a gyroradius larger than the coherence length of the turbulence, hence they experience mainly the effect of the external field $B_0 = B_0\hat{z}$, which implies a drift in the y -direction. Thus, they are mostly accelerated by the electric field $E = -q(\beta_x B_0)\hat{y}$ and concentrate around a latitude $\phi \in [\pm 90^\circ, \pm 150^\circ]$ depending on their charge, as visible by comparing Fig. 6.19 with Fig. 6.20. This also is a clue of the fact that particles momentum is not isotropized by pitch-angle scattering on turbulence downstream of the shock. More work is certainly needed to properly characterize the degree of variability, in time of frequency, of the radiated spectra and the diffusion process of the particles downstream.

Generally speaking, our results thus suggest that the interaction of a relativistic shock with external turbulence may play a leading role in dissipation and particle acceleration in a broad range of relativistic sources, up to moderate magnetisations. This significantly extends the realm where shock acceleration can take place in the absence of external turbulence. Interestingly, we observe that particle acceleration

inside the turbulence takes over Fermi acceleration at the shock once the turbulence level increases to values $\sigma_{\delta B} \simeq 0.1$ (sim. parameters (i)), leading to a non-thermal powerlaw spectrum with index $s \simeq 3$. One is tempted to sketch a picture in which shock, or shock plus turbulence, then turbulence, and eventually reconnection control dissipation and acceleration as the magnetisation increases from low to high values.

The physical scenario we have in mind is relevant for various high energy astrophysical systems, from PWNe to AGNs and GRBs, with potentially important consequences on non-thermal signatures in such environments (e.g., synchrotron or inverse Compton). As an example, numerical simulations of collisionless pair plasma reconnection, connected to turbulent regions, have already shown to be able to explain the flares and an acceleration over the synchrotron burn-off limit in the Crab nebula [37]. Any anisotropy the energetic particles inherit from turbulence intermittency directly translates into an anisotropy in their emission, focused in a narrow cone along their ultra-relativistic direction of motion. Therefore, the varying spatio-temporal nature of the magnetic turbulence near the shock should strongly affect the observed radiation and flares could arise in the transiting of particles through the compressed, large, coherent structures at the shock front if the scattering of particles off turbulence behind the shock is not, as generally assumed in literature, isotropic.

The main findings and results of the first *ab initio* particle-in-cell (PIC) numerical simulations of a turbulent relativistic shock propagating in a turbulent, magnetized pair plasma (i.e. case (B2)) are the object of a letter submitted to Physical Review L and currently under review.

Conclusion and perspectives

From a broad perspective, the present thesis aimed at a better understanding of particle acceleration and energy dissipation processes in high-energy astrophysical environments, motivated by puzzling long-standing issues in the domain. The mechanisms of particle acceleration underlying the observed nonthermal emissions from remote astrophysical sources remain widely debated. The acceleration mechanisms likely at play in these sources are presented in Chapter 2. The most commonly invoked scenarios have long relied on Fermi-type acceleration processes at the front of collisionless shock waves. On the one side, the numerical evidence provided by self-consistent PIC simulations that such shock acceleration can indeed occur in relativistic shocks was a major breakthrough of the past decade. On the other, many more questions remain open in the domain: how does the self-generated/amplified turbulence in the precursor evolve in time and which is the mechanism that regulates its saturation; more generally how kinetic simulations can be extrapolated to astrophysical spatiotemporal scales; in magnetised outflows, how energy can be dissipated into particles and acceleration be efficient, as simulations reveal that acceleration gets inhibited once the magnetic energy density exceeds $\sigma \gtrsim 10^{-4}$, a commonplace condition of high-energy astrophysical sources; do alternative or mixed scenarios, e.g. based on magnetic reconnection or turbulence, offer a valid option? A comprehensive understanding of the microphysics behind the acceleration processes that results in observable radiation and in secondary products, as neutrinos, is even more important nowadays in the emerging era of multi-messenger astrophysics. In addition, the physics of particle acceleration and radiation in astrophysical sources, and notably from collisionless shocks, have become extensively studied topics in domains outside high-energy astrophysics, such as laboratory astrophysics and laser-plasma physics.

This thesis has tackled some of the aforementioned aspects. On a theoretical approach and by means of large-scale PIC simulations, we have studied: (1) the physics underlying the precursor of a relativistic weakly magnetised (Weibel mediated) shock, (2) the acceleration of particles in magnetised turbulence and (3) the interaction between a relativistic shock and a magnetized turbulent plasma, as a significant magnetization is expected in a wide class of high-energy astrophysical sources, as encountered in gamma-ray bursts, pulsar wind nebulae or blazars.

In the study presented in Chapter 4, we investigated the acceleration of particles in a collisionless magnetized turbulence, as it offers a promising configuration for generating nonthermal high-energy particles in various astrophysical sites. Previous PIC simulations had already made important findings: a fast, efficient, particle acceleration in the relativistic regime; the formation of powerlaw-like spectra with spectral index in between 2 – 3 depending on the magnetisation level; and an energy dependence of the diffusion coefficient that suggests non-resonant interplay between waves and particles, at odds with the common scaling of resonant wave-particle interactions recovered in the framework of quasi-linear theory. We tested a recent model of non-resonant particle-wave interaction with numerical experiments. The model ascribes the energisation of particles to their interaction with fluctuating

electric fields connected to random velocity fluctuations via the ideal Ohm's law. In the local instantaneous rest frame where the electric field vanishes, the particle spatially diffuses by pitch-angle scattering at hands of the Lorentz force, but its energy gain is related to the inertial force associated with the change in the fluid velocity which determines its local frame: the particle then gains energy as it experiences the compression, the shear and the acceleration of the medium.

In particular, we carried 2D PIC simulations using two different schemes of turbulence forcing, as detailed in the final section of § 3: a 3D PIC forced simulation and a 3D MHD simulation, borrowed from the John Hopkins University database. For each simulation, we compared those three contributions to the variations of particle momenta with the recorded momentum histories of tracked test particles. In particular, we (i) extracted the particle spectra and the properties of the generated turbulence, (ii) we sampled the Pearson correlation coefficients of the observed and predicted trajectories (or chunk of trajectories) to reconstruct the probability distribution functions. Concerning the spectra, we found the formation of powerlaw tails with spectral index consistent with what has already been observed in recent analogous simulations. Concerning test particles, we observed a clear correlation between the model predictions and the numerical experiments, indicating that the non-resonant model can successfully account for the bulk of particle energisation through Fermi-type processes in strongly magnetized turbulence. Moreover, we found that, especially in PIC simulations, the parallel shear dominates in determining the trajectory, and hence likely the late-time particle spectrum. This is the subject of the paper *Non-resonant particle acceleration in strong turbulence: comparison to kinetic and MHD simulations*, to be published in Physical Review D [22].

Perspectives– We did not aim, on purpose, at a direct comparison between PIC and MHD results under the same physical conditions. Our general goal was indeed to test the model using different configurations and simulation frameworks. Retrieving the same results with different forcing methods and turbulent properties allowed us to probe the robustness of the model we tested. However, a difference in contributions between the MHD and the PIC simulations emerged from our results suggesting a dependence of the physics of acceleration on the stirring process and on the nature of the turbulence and/or the velocity regime, as already noted in [187]; those aspects certainly need to be further investigated. In connection with this, it would be useful to extend the non-resonant model and the random walk introduced in the theoretical formalism to extract direct analytical predictions for the particle energy spectrum, and to derive a kinetic equation for the distribution function. This work could also be extended to the sub-relativistic regime and to electron-ion plasmas.

In Chapter 5 we investigated the saturation and the nonlinear evolution of current filaments generated by the current filamentation instability (CFI), that is, the leading mechanism for shock formation in weakly magnetised plasmas where it mediates the conversion of the free energy associated with the anisotropic momentum distribution of particles into intense magnetic fields on skin-depth scales. Such magnetic fields close to near-equipartition are indeed required to explain the electromagnetic counterpart of neutron star mergers, the afterglows of short gamma-ray bursts. Understanding the long-term evolution of this instability is essential to bridge the gap in scales between PIC simulations and the astrophysical phenomenology. The aim of our project has been to examine the saturation mechanism(s) of the CFI in asymmetric relativistic configurations, relevant to the precursor of a collisionless shock wave where a hot, dilute beam of accelerated particles reflected at the shock front propagates against a cold, dense inflowing background plasma. We conducted

this study by means of PIC simulations in the so-called Weibel frame where the instability is (initially) purely magnetic in nature [122]. Practically we (i) set up and conducted the large 2D3V PIC simulations of asymmetric counter-streaming plasma flows in the region of the parameter space dominated by the CFI, (ii) confronted analytical predictions of saturation criteria with PIC simulations, and finally (iii) extended the study to mildly relativistic ion/electron cases. The results of this study allowed us to pinpoint the plasma species controlling saturation and the underlying mechanism, but also to identify the species mainly determining the linear properties (growth rate and wave number) of the instability. The knowledge of the saturation mechanism of the CFI is particularly important since this instability shapes the structure of the shock: the saturation level of the resulting electromagnetic turbulence therefore controls the production of high-energy particles and radiation from powerful explosive transients, as GRB afterglows. This project has led to the article *Saturation of the asymmetric current filamentation instability under conditions relevant to relativistic shock precursors*, published in Physical Review E [21].

Perspectives – Magnetic fields amplified to scales larger than the ion gyroradius have been inferred from the observations of non-thermal X-ray filaments (e.g., [171]), the fast variability of X-ray hot spots in young SNRs (e.g., [164]) and the TeV gamma-ray emission from Tycho’s SNR (e.g., [3]). The typical Alfvénic Mach number $M_A = v_{\text{sh}}/v_A$ of the shocks encountered in those settings can reach values around a few thousands; PIC simulations of quasi-perpendicular high-Mach-number shocks demonstrate that the ion-ion CFI instability mediates the strong amplification of magnetic fields upstream of the shock (e.g., [108]). Hence, it would be of particular importance to apply our study to the saturation mechanism of the magnetic fields to high Mach number electron-ion sub-relativistic shocks (e.g., [116]). Our analysis could be hence applied to PIC kinetic simulations of uniform, counterstreaming electron-ion plasmas in the sub-relativistic, high Mach number regime to identify the relevant mechanism of saturation in this configuration. The result could then be used to estimate the magnetic field attained by the saturated instability in the precursor of the electron-ion shock wave and to compare with available observations.

Chapter 6 contains the main study of this thesis, which investigates the dissipation of magnetic energy into particles through the interaction between a shock wave and turbulence. To do so, we have developed a numerical scheme where the turbulence is set into motion along with the injected plasma while maintaining its excitation in its proper frame. This scheme has been implemented to study two different configurations: one in which the propagating turbulent plasma is let to reflect at one side of the simulation domain to trigger a turbulent shock, and the other where a non-turbulent shock immediately originates in the domain from the reflective boundary and later interacts with an incoming turbulent flow. Our 2D3V simulations, complemented by particle tracking indicate that the external, well-developed turbulence is able to promote Fermi cycles at the front of relativistic superluminal magnetized shock, in which it cannot operate otherwise. The acceleration properties strongly depend on the turbulence characteristics. We explored two different levels of turbulence. We observed that particle acceleration inside the turbulence takes over Fermi acceleration at the shock at high enough levels of magnetization ($\sigma_{\delta B} \sim 10^{-1}$), leading to a nonthermal powerlaw spectrum with soft index $s \simeq 3$ that hardly evolves in time because it mainly originates from stochastic acceleration in the mildly relativistic turbulence. We indeed verified that acceleration was controlled by turbulent fields magnetized by performing an additional simulation with the same conditions of turbulence but without triggering the shock. We

subsequently ran a new set of simulations with a reduced turbulence level. We concluded that the development of the observed nonthermal tail in the particle spectra extracted from simulations arises through the scattering off turbulent magnetic fluctuations, which allow particles to cross repetitively the relativistic shock front, i.e. the acceleration proceeds through the combined effect of turbulence and Fermi cycles at the shock front. Remarkably, the observed spectral index, $s \simeq 3.5$, is consistent with the typical value inferred from fitting a large sample of GRB data to a synchrotron cooling model [29] or to single-zone synchrotron plus inverse Compton models by [34], within a magnetisation range that covers our simulation parameters. By contrast, PIC simulation investigations of acceleration in magnetic reconnection regions generally predict steeper spectra unless the magnetisation is larger than unity [126].

Finally, another noteworthy outcome of our numerical study is to reveal substantial time-dependent anisotropy in the particle momentum distribution function at high energy. These anisotropies vary on comoving timescales $\sim \ell_c/c$, and on Lorentz-boosted timescales from the simulation (downstream) frame to the observer frame. Such effects could therefore produce potentially small timescale variability, while most of the dissipation and acceleration would remain connected to the shock itself.

A crucial consequence of our results is to extend the range of astrophysical conditions under which particle acceleration at relativistic shock fronts remains efficient. The physical scenario we have in mind is potentially applicable to a wider class of astrophysical systems, depending on their Lorentz factor and magnetisation. This is the subject of a paper, *Particle acceleration at magnetized, relativistic turbulent shock fronts*, submitted to Physical Review Letters (under review).

Perspectives – The degree of variability, in time or frequency, of the radiated spectra is certainly of great interest and deserves further scrutiny. The anisotropy the energetic particles inherit from turbulence intermittency translates directly into an anisotropic synchrotron or inverse Compton emission. The maps of the particle momentum distribution extracted from simulations confirm such anisotropies. The natural spatiotemporal intermittency of the magnetic turbulence near the shock could lead to the formation of flares as the particles transit through the compressed large coherent structures at the shock front. It would be hence interesting to derive the spectral energy distribution of photons resulting from synchrotron and inverse Compton radiation to investigate the phenomenology of the emission by direct comparison with observations of blazar jets, or flares in PWNe or GRBs. This would be possible by direct implementation of synchrotron and IC losses in the kinetic code to compute on the fly the photon energy spectra.

Albeit limited by computational costs and issues, a worthwhile (ideal) effort would be to conduct a parameter study in the shock-turbulence setup, varying the Lorentz factor and the magnetisation of the shock which both characterise different astrophysical environments, from sub-relativistic but magnetised systems (as supernova remnants) to unmagnetised ultra-relativistic configurations (as GRBs), going through highly magnetised and highly relativistic objects (as PWNe) and mildly relativistic, magnetised jets. Further numerical developments and optimizations are yet needed in this direction to make the computational cost affordable.

In the sub-relativistic regime, massive star associations have recently gained interest in the context of the gamma-ray emission of the Cygnus superbubble, proposed as PeVatron candidate [2]. The behaviour of a superbubble in terms of particle acceleration critically depends on the magnetic turbulence and its ability to confine particles. The dynamical range of this sources, i.e. the ratio of global length

scale ($L \sim 10\text{pc}$) to particles maximum gyroradius ($r_{g,\text{max}} \lesssim 0.01\text{pc}$), as limited by the shock dimension assuming Bohm diffusion, covers more than three orders of magnitude [170]. That makes the system unattainable to PIC simulations, thus precluding a global fully kinetic description of particle injection, scattering, possible re-acceleration and propagation in the bubbles. However, our module of turbulence could be used to study the interaction of an electron-ion shock with a turbulent medium at the kinetic level to get the spectral shape of the accelerated particles injected by the sources in the bubble. Again, this would be already quite challenging in terms of computational cost given the great disparity in dynamical scales between electrons and ions. Specifically, PIC codes must resolve the electron skin depth, which is orders of magnitude smaller than the scale required to probe ion acceleration, namely, the ion gyroradius, at energies such that the latter equals the system size. The spectrum extracted from kinetic simulations could then be used to shape kinetic particles injected in MHD codes which would then deal with the propagation of particles in the large scale turbulence of the superbubble.

Finally, we wish to emphasize that all of the simulations performed in this work made use of the massively parallelized, fully relativistic particle-in-cell code CALDER code and of the French high-performance computing TGCC facility. Under Grants No. 2019-A0050407666, 2020-A0080411422 and 2021-A0080411422, our project benefited from a total of $\sim 20\text{Mh}$ CPU time to adapt the code to our needs and run the many simulations underpinning our studies. In particular, we added a diagnostic to record the momentum distribution in spherical coordinates, allowing us to explore anisotropy effects in turbulent shock-induced particle acceleration. More importantly, we developed a module of turbulence forcing, either in a periodic box, or in a drifting configuration in the presence of a reflective boundary for shock creation. The module was implemented with a large freedom of choice on the number of excited waves, typical frequency and amplitude, as well as the possibility to create both forced or turbulent configurations.

Appendix A

Test on synthetic turbulence

For completeness, in this Appendix, we compare the non-resonant model to a configuration whereby the turbulence is constructed as a sum of non-interacting linear MHD eigenmodes. As detailed in Section 2.2.1, quasilinear theory predicts that particle energization takes place through two types of interactions: gyroresonant interactions of the form $k_{\parallel} v_{\parallel} - \omega \simeq n c / r_g$ ($n \in \mathbb{Z}^*$) and Landau-synchrotron resonances $k_{\parallel} v_{\parallel} - \omega = 0$. Gyroresonant interactions can take place for all modes, at least in the absence of local anisotropy à la Goldreich-Sridhar [38, 182], while the Landau-synchrotron (transit-time damping) are specific to fast magnetosonic modes. As the transit-time damping interactions are related to magnetic mirroring effects, those are captured by the non-resonant model as the Θ_{\perp} contribution. Yet no gyroresonant interaction is described by the model. Moreover, we expect $\Theta_{\parallel} = 0$ and $\Theta_{\perp} = 0$ for the Alfvén modes, while fast magnetosonic modes lead to $\Theta_{\parallel} = 0$ but $\Theta_{\perp} \neq 0$ [90].

The numerical code used to build the synthetic turbulence and track particles therein is presented in [51]. In brief, particle trajectories are integrated using a Bulirsch-Stoer algorithm. At each timestep, the electromagnetic and velocity fields at the location of particles are constructed as the sum of a background magnetic field and the superposition of the fluctuations carried by a collection of waves with dispersion relation and polarizations of (special relativistic) MHD eigenmodes. The electric field is derived from the total magnetic field and total velocity field through ideal Ohm's law. The wavevectors and amplitudes of the waves are initialized so as to achieve the desired power spectrum of turbulence over a range of scales $[L_{\min}, L_{\max}]$. Particles are injected along random directions in different turbulence realizations with the energy corresponding to the gyroradius of interest. To reconstruct the energy histories using Eq. (2.73), we calculate the spatial and temporal derivatives of the magnetic field and the velocity field, then derive those of the electric field through ideal Ohm's law. In this synthetic turbulence, the derivatives can be expressed analytically in terms of the plane wave expansion.

We conduct two experiments on such synthetic turbulence comprised of 256 modes, with wavelengths extending from $L_{\max} = \ell_c$ down to $L_{\min} = L_{\max}/100$. In experiment (A), we simulate a turbulence of isotropic fast magnetosonic modes with $\delta B/B_0 = 1$, Alfvén velocity $v_A = 0.6 c$, sound velocity $v_s \ll v_A$, which implies a phase velocity for each wave $v_F \simeq v_A$. Isotropic means here that the turbulent magnetic power spectrum does not depend on the direction of the wavenumber; its scaling is assumed to follow Kolmogorov $S_k \propto k^{-5/3}$. We inject particles with a gyroradius outside the range of scales of the turbulence, $r_g = 0.1 L_{\min}$. In that configuration, gyroresonant interactions are suppressed because restricted to high harmonics (large n) so that acceleration is dominated by transit time damping acceleration [161]. We thus expect the theoretical model to provide a fair reconstruction of the trajectories, at least its Θ_{\perp} part. In a second experiment, (B), we simulate an opposite situation, namely a turbulence of Alfvén modes with $v_A = 0.6 c$, $\delta B/B_0 = 1$

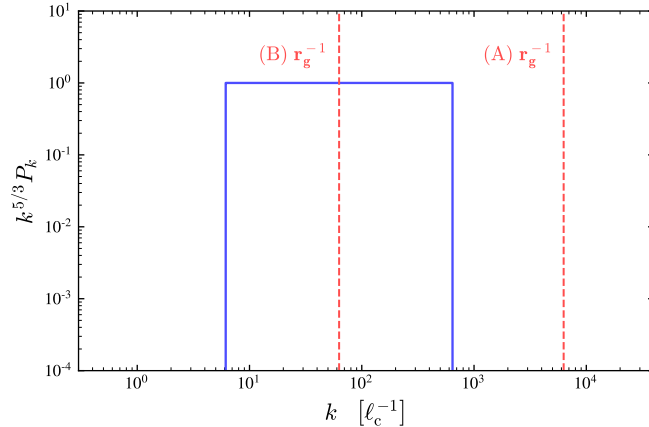


FIGURE A.1: Power spectrum of synthetic turbulence, with locations of the inverse gyroradii indicated by dashed lines for the two experiments (A), corresponding to fast mode turbulence, and (B), for Alfvén modes.

and set the gyroradius of the particles to fall in the range of wavelengths of the turbulence, $r_g = 0.1 L_{\max} = 10 L_{\min}$, which thus permits gyroresonant interactions at the first harmonic $n = 1$. We simulate here simple Alfvén waves, meaning that we neglect any wave damping term and that we assume an isotropic Kolmogorov cascade. Our aim indeed is to bring to light the effect of gyroresonances, or rather, the lack of correlation between observed and reconstructed trajectories in a situation in which most of energy gain is known to result from gyroresonant interactions; we thus deliberately render those resonances sharp. We choose Alfvén waves in order to erase any magnetic mirroring effect. Consequently, we expect the theoretical model to behave poorly in that limit, given that it ignores such gyroresonances, by construction.

Figure A.1 shows the power spectrum (normalized by $k^{5/3}$) of magnetic fluctuations in this synthetic wave turbulence, with the locations of r_g^{-1} indicated as dashed lines for both models: model (A) with r_g below the minimum scale, and model (B) with r_g in the inertial range.

The histogram of the probability density of the Pearson correlation coefficients between the observed and reconstructed trajectories is shown in the left panel of Fig. A.2 for model (A). The concentration of the probability density of r around $+1$ indicates that, as anticipated, the model is highly successful in reproducing the trajectories, most notably so for the magnetic mirror (Θ_{\perp}) contribution. A closer inspection reveals that the non-resonant model, summing over the contributions of all three force terms, provides a better match to the observed energy histories than the contribution of magnetic mirrors alone, as its probability density is more sharply peaked around $+1$. The difference comes from the inertial term $\mathbf{a}_E \cdot \mathbf{b}$, which provides a net contribution, as evidenced by its overall positive degree of correlation. Within the frame of the model that we are testing, this is not altogether surprising, insofar as this inertial term characterizes the influence of accelerations/decelerations of the frame \mathcal{R}_E in which the notion of a magnetic mirror can be properly defined. In that sense, the inertial term should not be left aside when considering the influence of Θ_{\perp} (or Θ_{\parallel} , for similar reasons).

Right panel of figure A.2 shows the corresponding histograms in the case of model (B), which appear relatively structureless and uniformly distributed over the interval $[-1, +1]$. There appears to be a slight bias toward positive values of the

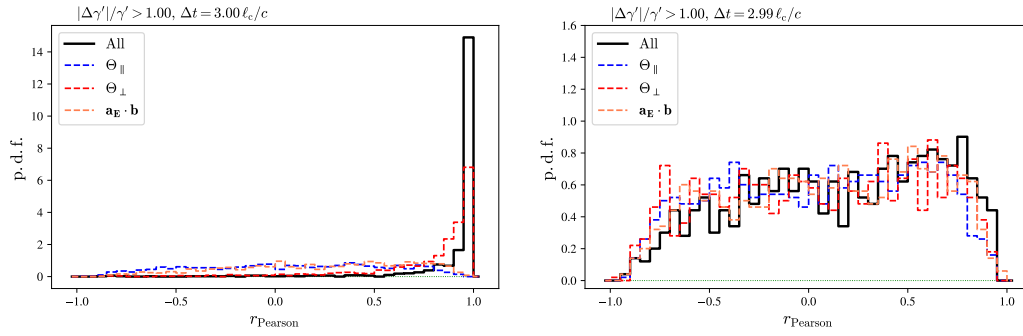


FIGURE A.2: Probability density of correlation coefficients. Left: case (A), in which particle acceleration takes place through interactions with magnetic mirror modes (transit-time damping in fast mode synthetic turbulence). The model fully captures the energy gains, with a strongly dominant contribution of Θ_{\perp} , as expected. Right: case (B), in which particle acceleration now takes place through gyroresonant interactions. In that case, the model is unable to reproduce the energy gains, hence the pdf of correlation coefficients appears devoid of structure, revealing no particular preference for values close to +1.

correlation coefficients, but nothing of the sort discussed previously in Chapter 4 for PIC or MHD simulations. This suggests that most of the energy gains/losses are indeed not captured by the non-resonant model in the present case and that gyroresonant wave-particle interactions do not leave a strong signature in this histogram of correlation coefficients. The positive correlations observed in Chapter 4 can thus be interpreted as genuine evidence in favor of non-resonant acceleration.

Bibliography

- [1] B. P. Abbott, R. Abbott, T. D. Abbott, F. Acernese, K. Ackley, et al. “GW170817: Observation of Gravitational Waves from a Binary Neutron Star Inspiral”. In: *Phys. Rev. Lett.* 119.16, 161101 (Oct. 2017), p. 161101. DOI: [10.1103/PhysRevLett.119.161101](https://doi.org/10.1103/PhysRevLett.119.161101). arXiv: [1710.05832](https://arxiv.org/abs/1710.05832) [gr-qc].
- [2] A. U. Abeysekara, A. Albert, R. Alfaro, C. Alvarez, J. R. Angeles Camacho, et al. “HAWC observations of the acceleration of very-high-energy cosmic rays in the Cygnus Cocoon”. In: *Nature Astronomy* 5 (Mar. 2021), pp. 465–471. DOI: [10.1038/s41550-021-01318-y](https://doi.org/10.1038/s41550-021-01318-y). arXiv: [2103.06820](https://arxiv.org/abs/2103.06820) [astro-ph.HE].
- [3] V. A. Acciari, E. Aliu, T. Arlen, T. Aune, M. Beilicke, et al. “Discovery of TeV Gamma-ray Emission from Tycho’s Supernova Remnant”. In: *Astrophys. J. Lett.* 730.2, L20 (Apr. 2011), p. L20. DOI: [10.1088/2041-8205/730/2/L20](https://doi.org/10.1088/2041-8205/730/2/L20). arXiv: [1102.3871](https://arxiv.org/abs/1102.3871) [astro-ph.HE].
- [4] A. Achterberg, Y. A. Gallant, John G. Kirk, and Axel W. Guthmann. “Particle acceleration by ultrarelativistic shocks: theory and simulations”. In: *Mon. Notices Royal Astron. Soc.* 328.2 (Dec. 2001), pp. 393–408. DOI: [10.1046/j.1365-8711.2001.04851.x](https://doi.org/10.1046/j.1365-8711.2001.04851.x).
- [5] A. Achterberg, J. Wiersma, and C. A. Norman. “The Weibel instability in relativistic plasmas. II. Nonlinear theory and stabilization mechanism”. In: *Astron. Astrophys.* 475 (2007), pp. 19–36. DOI: [10.1051/0004-6361:20065366](https://doi.org/10.1051/0004-6361:20065366).
- [6] N. Ahmad, H. Usui, and Y. Miyake. “Particle in Cell Simulation to Study the Charging and Evolution of Wake Structure of LEO Spacecraft”. In: *Methods and Applications for Modeling and Simulation of Complex Systems*. Ed. by Liang Li, Kyoko Hasegawa, and Satoshi Tanaka. Singapore: Springer Singapore, 2018, pp. 255–268.
- [7] E. Amato. “The Theory Of Pulsar Wind Nebulae: Recent Progress”. In: *High Energy Phenomena in Relativistic Outflows VII*. July 2019, 33, p. 33.
- [8] E. Amato and P. Blasi. “Non-linear particle acceleration at non-relativistic shock waves in the presence of self-generated turbulence”. In: *Mon. Notices Royal Astron. Soc.* 371.3 (Sept. 2006), pp. 1251–1258. DOI: [10.1111/j.1365-2966.2006.10739.x](https://doi.org/10.1111/j.1365-2966.2006.10739.x). arXiv: [astro-ph/0606592](https://arxiv.org/abs/astro-ph/0606592) [astro-ph].
- [9] J. W. Armstrong, B. J. Rickett, and S. R. Spangler. “Electron Density Power Spectrum in the Local Interstellar Medium”. In: *Astrophys. J.* 443 (Apr. 1995), p. 209. DOI: [10.1086/175515](https://doi.org/10.1086/175515).
- [10] K. Asano and M. Hayashida. “Blazar Spectra with Hard-sphere-like Acceleration of Electrons”. In: *Astrophys. J.* 861.1, 31 (July 2018), p. 31. DOI: [10.3847/1538-4357/aac82a](https://doi.org/10.3847/1538-4357/aac82a). arXiv: [1805.09953](https://arxiv.org/abs/1805.09953) [astro-ph.HE].
- [11] K. R. Ballard and A. F. Heavens. “Shock acceleration and steep-spectrum synchrotron sources”. In: *Mon. Notices Royal Astron. Soc.* 259.1 (Nov. 1992), pp. 89–94. DOI: [10.1093/mnras/259.1.89](https://doi.org/10.1093/mnras/259.1.89).

- [12] J. Bednarz and M. Ostrowski. “Energy Spectra of Cosmic Rays Accelerated at Ultrarelativistic Shock Waves”. In: *Phys. Rev. Lett.* 80.18 (May 1998), pp. 3911–3914. DOI: [10.1103/PhysRevLett.80.3911](https://doi.org/10.1103/PhysRevLett.80.3911). arXiv: [astro-ph/9806181](https://arxiv.org/abs/astro-ph/9806181) [astro-ph].
- [13] J. Bednarz and M. Ostrowski. “The acceleration time-scale for first-order Fermi acceleration in relativistic shock waves”. In: *Mon. Notices Royal Astron. Soc.* 283.2 (Nov. 1996), pp. 447–456. DOI: [10.1093/mnras/283.2.447](https://doi.org/10.1093/mnras/283.2.447). arXiv: [astro-ph/9608078](https://arxiv.org/abs/astro-ph/9608078) [astro-ph].
- [14] Mitchell C. Begelman and John G. Kirk. “Shock-Drift Particle Acceleration in Superluminal Shocks: A Model for Hot Spots in Extragalactic Radio Sources”. In: *Astrophys. J.* 353 (Apr. 1990), p. 66. DOI: [10.1086/168590](https://doi.org/10.1086/168590).
- [15] A. R. Bell. “The acceleration of cosmic rays in shock fronts - I.” In: *Mon. Notices Royal Astron. Soc.* 182 (Jan. 1978), pp. 147–156. DOI: [10.1093/mnras/182.2.147](https://doi.org/10.1093/mnras/182.2.147).
- [16] A. R. Bell. “Turbulent amplification of magnetic field and diffusive shock acceleration of cosmic rays”. In: *Mon. Notices Royal Astron. Soc.* 353.2 (Sept. 2004), pp. 550–558. DOI: [10.1111/j.1365-2966.2004.08097.x](https://doi.org/10.1111/j.1365-2966.2004.08097.x). URL: <https://doi.org/10.1111/j.1365-2966.2004.08097.x>.
- [17] C. K. Birdsall and A. B. Langdon. *Plasma Physics via Computer Simulation*. 1991.
- [18] R. Blandford, D. Meier, and A. Readhead. “Relativistic Jets from Active Galactic Nuclei”. In: *Annual Review of Astronomy and Astrophysics* 57 (Aug. 2019), pp. 467–509. DOI: [10.1146/annurev-astro-081817-051948](https://doi.org/10.1146/annurev-astro-081817-051948). arXiv: [1812.06025](https://arxiv.org/abs/1812.06025) [astro-ph.HE].
- [19] A. Bohdan, J. Niemiec, O. Kobzar, and M. Pohl. “Electron Pre-acceleration at Nonrelativistic High-Mach-number Perpendicular Shocks”. In: *Astrophys. J.* 847.1, 71 (Sept. 2017), p. 71. DOI: [10.3847/1538-4357/aa872a](https://doi.org/10.3847/1538-4357/aa872a). arXiv: [1708.05528](https://arxiv.org/abs/1708.05528) [astro-ph.HE].
- [20] J. P. Boris. “Relativistic plasma simulation-optimization of a hybrid code”. In: *Proceeding of Fourth Conference on Numerical Simulations of Plasmas* (1970).
- [21] V. Bresci, L. Gremillet, and M. Lemoine. “Saturation of the asymmetric current filamentation instability under conditions relevant to relativistic shock precursors”. In: *Phys. Rev. E* 105.3, 035202 (Mar. 2022), p. 035202. DOI: [10.1103/PhysRevE.105.035202](https://doi.org/10.1103/PhysRevE.105.035202). arXiv: [2111.04651](https://arxiv.org/abs/2111.04651) [physics.plasm-ph].
- [22] V. Bresci, M. Lemoine, L. Gremillet, L. Comisso, L. Sironi, et al. “Nonresonant particle acceleration in strong turbulence: Comparison to kinetic and MHD simulations”. In: *Phys. Rev. D* 106 (2 2022), p. 023028. DOI: [10.1103/PhysRevD.106.023028](https://doi.org/10.1103/PhysRevD.106.023028). URL: <https://link.aps.org/doi/10.1103/PhysRevD.106.023028>.
- [23] A. Bret, L. Gremillet, and D. Bénisti. “Exact relativistic kinetic theory of the full unstable spectrum of an electron-beam plasma system with Maxwell-Jüttner distribution functions”. In: *Phys. Rev. E* 81 (3 2010), p. 036402. DOI: [10.1103/PhysRevE.81.036402](https://doi.org/10.1103/PhysRevE.81.036402).
- [24] A. Bret, L. Gremillet, D. Bénisti, and E. Lefebvre. “Exact Relativistic Kinetic Theory of an Electron-Beam Plasma System: Hierarchy of the Competing Modes in the System-Parameter Space”. In: *Phys. Rev. Lett.* 100.20, 205008 (May 2008), p. 205008. DOI: [10.1103/PhysRevLett.100.205008](https://doi.org/10.1103/PhysRevLett.100.205008).

- [25] A. Bret, L. Gremillet, and M. E. Dieckman. “Multidimensional electron beam-plasma instabilities in the relativistic regime”. In: *Phys. Plasmas* 17 (2010), p. 120501. DOI: [10.1063/1.3514586](https://doi.org/10.1063/1.3514586).
- [26] A. Bret, A. Stockem, D. Fiuza, C. Ruyer, L. Gremillet, et al. “Collisionless shock formation, spontaneous electromagnetic fluctuations, and streaming instabilities”. In: *Phys. Plasmas* 20 (2013), p. 042102. DOI: [10.1063/1.4798541](https://doi.org/10.1063/1.4798541).
- [27] O. Buneman. “Dissipation of Currents in Ionized Media”. In: *Physical Review* 115.3 (Aug. 1959), pp. 503–517. DOI: [10.1103/PhysRev.115.503](https://doi.org/10.1103/PhysRev.115.503).
- [28] D. Burgess, P. W. Gingell, and L. Matteini. “Multiple Current Sheet Systems in the Outer Heliosphere: Energy Release and Turbulence”. In: 822.1, 38 (May 2016), p. 38. DOI: [10.3847/0004-637X/822/1/38](https://doi.org/10.3847/0004-637X/822/1/38). arXiv: [1603.06778](https://arxiv.org/abs/1603.06778) [physics.space-ph].
- [29] J. M. Burgess, D. Bégué, J. Greiner, D. Giannios, A. Bacelj, et al. “Gamma-ray bursts as cool synchrotron sources”. In: *Nat. Astron.* 4 (Feb. 2020), pp. 174–179. DOI: [10.1038/s41550-019-0911-z](https://doi.org/10.1038/s41550-019-0911-z).
- [30] A. M. Bykov and P. Meszaros. “Electron Acceleration and Efficiency in Non-thermal Gamma-Ray Sources”. In: *Astrophys. J. Lett.* 461 (Apr. 1996), p. L37. DOI: [10.1086/309999](https://doi.org/10.1086/309999). arXiv: [astro-ph/9602016](https://arxiv.org/abs/astro-ph/9602016) [astro-ph].
- [31] D. Caprioli and A. Spitkovsky. “Simulations of ion acceleration at non-relativistic shocks. I. Acceleration efficiency”. In: *Astrophys. J.* 783.2 (2014), p. 91. DOI: [10.1088/0004-637x/783/2/91](https://doi.org/10.1088/0004-637x/783/2/91).
- [32] Damiano Caprioli, Ana-Roxana Pop, and Anatoly Spitkovsky. “Simulations and Theory of Ion Injection at Non-relativistic Collisionless Shocks”. In: 798.2, L28 (Jan. 2015), p. L28. DOI: [10.1088/2041-8205/798/2/L28](https://doi.org/10.1088/2041-8205/798/2/L28). arXiv: [1409.8291](https://arxiv.org/abs/1409.8291) [astro-ph.HE].
- [33] Fabien Casse, Martin Lemoine, and Guy Pelletier. “Transport of cosmic rays in chaotic magnetic fields”. In: 65.2, 023002 (Dec. 2001), p. 023002. DOI: [10.1103/PhysRevD.65.023002](https://doi.org/10.1103/PhysRevD.65.023002). arXiv: [astro-ph/0109223](https://arxiv.org/abs/astro-ph/0109223) [astro-ph].
- [34] A. Celotti and G. Ghisellini. “The power of blazar jets”. In: *Mon. Notices Royal Astron. Soc.* 385.1 (Mar. 2008), pp. 283–300. DOI: [10.1111/j.1365-2966.2007.12758.x](https://doi.org/10.1111/j.1365-2966.2007.12758.x).
- [35] B. Cerutti. “Particle acceleration and radiation in pulsars: New insights from kinetic simulations”. In: *Nuclear and Particle Physics Proceedings* 297-299 (Apr. 2018), pp. 85–90. DOI: [10.1016/j.nuclphysbps.2018.07.013](https://doi.org/10.1016/j.nuclphysbps.2018.07.013).
- [36] B. Cerutti and G. Giacinti. “A global model of particle acceleration at pulsar wind termination shocks”. In: *A&A* 642, A123 (Oct. 2020), A123. DOI: [10.1051/0004-6361/202038883](https://doi.org/10.1051/0004-6361/202038883). arXiv: [2008.07253](https://arxiv.org/abs/2008.07253) [astro-ph.HE].
- [37] B. Cerutti, G. R. Werner, D. A. Uzdensky, and M. C. Begelman. “Simulations of Particle Acceleration beyond the Classical Synchrotron Burnoff Limit in Magnetic Reconnection: An Explanation of the Crab Flares”. In: *Astrophys. J.* 770.2, 147 (June 2013), p. 147. DOI: [10.1088/0004-637X/770/2/147](https://doi.org/10.1088/0004-637X/770/2/147). arXiv: [1302.6247](https://arxiv.org/abs/1302.6247) [astro-ph.HE].
- [38] Benjamin D. G. Chandran. “Scattering of energetic particles by anisotropic magnetohydrodynamic turbulence with a Goldreich-Sridhar power spectrum”. In: *Phys. Rev. Lett.* 85 (2000), pp. 4656–4659. DOI: [10.1103/PhysRevLett.85.4656](https://doi.org/10.1103/PhysRevLett.85.4656). arXiv: [astro-ph/0008498](https://arxiv.org/abs/astro-ph/0008498) [astro-ph].

- [39] A. Chepurnov and A. Lazarian. “Extending the Big Power Law in the Sky with Turbulence Spectra from Wisconsin H α Mapper Data”. In: *Astrophys. J.* 710.1 (Feb. 2010), pp. 853–858. DOI: [10.1088/0004-637X/710/1/853](https://doi.org/10.1088/0004-637X/710/1/853). arXiv: [0905.4413](https://arxiv.org/abs/0905.4413) [astro-ph.GA].
- [40] J. Cho and A. Lazarian. “Compressible magnetohydrodynamic turbulence: mode coupling, scaling relations, anisotropy, viscosity-damped regime and astrophysical implications”. In: *Mon. Notices Royal Astron. Soc.* 345.12 (Oct. 2003), pp. 325–339. DOI: [10.1046/j.1365-8711.2003.06941.x](https://doi.org/10.1046/j.1365-8711.2003.06941.x). arXiv: [astro-ph/0301062](https://arxiv.org/abs/astro-ph/0301062) [astro-ph].
- [41] R. Cochet and A. Marcowith. “Cosmic ray propagation in sub-Alfvénic magnetohydrodynamic turbulence”. In: *A&A* 588, A73 (Apr. 2016), A73. DOI: [10.1051/0004-6361/201527376](https://doi.org/10.1051/0004-6361/201527376). arXiv: [1601.04971](https://arxiv.org/abs/1601.04971) [astro-ph.HE].
- [42] L. Comisso and L. Sironi. “Particle Acceleration in Relativistic Plasma Turbulence”. In: *Phys. Rev. Lett.* 121.25, 255101 (Dec. 2018), p. 255101. DOI: [10.1103/PhysRevLett.121.255101](https://doi.org/10.1103/PhysRevLett.121.255101). arXiv: [1809.01168](https://arxiv.org/abs/1809.01168) [astro-ph.HE].
- [43] L. Comisso and L. Sironi. “The Interplay of Magnetically Dominated Turbulence and Magnetic Reconnection in Producing Nonthermal Particles”. In: *Astrophys. J.* 886.2, 122 (Dec. 2019), p. 122. DOI: [10.3847/1538-4357/ab4c33](https://doi.org/10.3847/1538-4357/ab4c33). arXiv: [1909.01420](https://arxiv.org/abs/1909.01420) [astro-ph.HE].
- [44] L. Comisso, E. Sobacchi, and L. Sironi. “Hard Synchrotron Spectra from Magnetically Dominated Plasma Turbulence”. In: *Astrophys. J. Lett.* 895.2, L40 (June 2020), p. L40. DOI: [10.3847/2041-8213/ab93dc](https://doi.org/10.3847/2041-8213/ab93dc). arXiv: [2004.07315](https://arxiv.org/abs/2004.07315) [astro-ph.HE].
- [45] P. Crumley, D. Caprioli, S. Markoff, and A. Spitkovsky. “Kinetic simulations of mildly relativistic shocks - I. Particle acceleration in high Mach number shocks”. In: *Mon. Notices Royal Astron. Soc.* 485.4 (June 2019), pp. 5105–5119. DOI: [10.1093/mnras/stz232](https://doi.org/10.1093/mnras/stz232). arXiv: [1809.10809](https://arxiv.org/abs/1809.10809) [astro-ph.HE].
- [46] S. Dalena, A. F. Rappazzo, P. Dmitruk, A. Greco, and W. H. Matthaeus. “Test-particle Acceleration in a Hierarchical Three-dimensional Turbulence Model”. In: *Astrophys. J.* 783.2, 143 (Mar. 2014), p. 143. DOI: [10.1088/0004-637X/783/2/143](https://doi.org/10.1088/0004-637X/783/2/143). arXiv: [1402.3745](https://arxiv.org/abs/1402.3745) [astro-ph.SR].
- [47] R. C. Davidson, D. A. Hammer, I. Haber, and C. E. Wagner. “Nonlinear Development of Electromagnetic Instabilities in Anisotropic Plasmas”. In: *Phys. Fluids* 15.2 (1972), pp. 317–333. DOI: [10.1063/1.1693910](https://doi.org/10.1063/1.1693910).
- [48] J. Dawson. “One-Dimensional Plasma Model”. In: *Physics of Fluids* 5.4 (Apr. 1962), pp. 445–459. DOI: [10.1063/1.1706638](https://doi.org/10.1063/1.1706638).
- [49] F. de Hoffmann and E. Teller. “Magneto-Hydrodynamic Shocks”. In: *Physical Review* 80.4 (Nov. 1950), pp. 692–703. DOI: [10.1103/PhysRev.80.692](https://doi.org/10.1103/PhysRev.80.692).
- [50] R. B. Decker and L. Vlahos. “Shock drift acceleration in the presence of waves”. In: 90.A1 (Jan. 1985), pp. 47–56. DOI: [10.1029/JA090iA01p00047](https://doi.org/10.1029/JA090iA01p00047).
- [51] C. Demidem, M. Lemoine, and F. Casse. “Particle acceleration in relativistic turbulence: A theoretical appraisal”. In: *Phys. Rev. D* 102.2, 023003 (July 2020), p. 023003. DOI: [10.1103/PhysRevD.102.023003](https://doi.org/10.1103/PhysRevD.102.023003). arXiv: [1909.12885](https://arxiv.org/abs/1909.12885) [astro-ph.HE].

- [52] C. Demidem, M. Lemoine, and F. Casse. “Relativistic magnetohydrodynamical simulations of the resonant corrugation of a fast shock front”. In: *Mon. Notices Royal Astron. Soc.* 475.2 (Apr. 2018), pp. 2713–2723. DOI: [10.1093/mnras/stx3367](https://doi.org/10.1093/mnras/stx3367). arXiv: [1710.08127](https://arxiv.org/abs/1710.08127) [astro-ph.HE].
- [53] Q. Dong, S. Wang, Q. M. Lu, C. Huang, D. W. Yuan, et al. “Plasmoid Ejection and Secondary Current Sheet Generation from Magnetic Reconnection in Laser-Plasma Interaction”. In: 108.21, 215001 (May 2012), p. 215001. DOI: [10.1103/PhysRevLett.108.215001](https://doi.org/10.1103/PhysRevLett.108.215001). arXiv: [1203.4036](https://arxiv.org/abs/1203.4036) [physics.plasm-ph].
- [54] L. O. Drury. “An introduction to the theory of diffusive shock acceleration of energetic particles in tenuous plasmas”. In: *Rep. Prog. Phys.* 46 (Aug. 1983), pp. 973–1027. DOI: [10.1088/0034-4885/46/8/002](https://doi.org/10.1088/0034-4885/46/8/002).
- [55] D. C. Ellison and G. P. Double. “Nonlinear particle acceleration in relativistic shocks”. In: *Astroparticle Physics* 18.3 (Dec. 2002), pp. 213–228. DOI: [10.1016/S0927-6505\(02\)00142-1](https://doi.org/10.1016/S0927-6505(02)00142-1). arXiv: [astro-ph/0202106](https://arxiv.org/abs/astro-ph/0202106) [astro-ph].
- [56] T. Zh. Esirkepov. “Exact charge conservation scheme for Particle-in-Cell simulation with an arbitrary form-factor”. In: *Computer Physics Communications* 135.2 (Apr. 2001), pp. 144–153. DOI: [10.1016/S0010-4655\(00\)00228-9](https://doi.org/10.1016/S0010-4655(00)00228-9).
- [57] C. Evoli. *The Cosmic-Ray Energy Spectrum*. Oct. 2018. DOI: [10.5281/zenodo.4309926](https://doi.org/10.5281/zenodo.4309926). URL: <https://doi.org/10.5281/zenodo.4309926>.
- [58] G. Eyink, E. Vishniac, C. Lalescu, H. Aluie, K. Kanov, et al. “Flux-freezing breakdown in high-conductivity magnetohydrodynamic turbulence”. In: *Nature (London)* 497.7450 (May 2013), pp. 466–469. DOI: [10.1038/nature12128](https://doi.org/10.1038/nature12128).
- [59] R. Fender. “Jets from X-ray binaries”. In: *Compact stellar X-ray sources*. Vol. 39. 2006, pp. 381–419.
- [60] E. Fermi. “On the Origin of the Cosmic Radiation”. In: *Phys. Rev.* 75 (8 1949), pp. 1169–1174. DOI: [10.1103/PhysRev.75.1169](https://doi.org/10.1103/PhysRev.75.1169). URL: <https://link.aps.org/doi/10.1103/PhysRev.75.1169>.
- [61] G. Fiksel, W. Fox, A. Bhattacharjee, D. H. Barnak, P. Y. Chang, et al. “Magnetic Reconnection between Colliding Magnetized Laser-Produced Plasma Plumes”. In: *Phys. Rev. Lett.* 113.10, 105003 (Sept. 2014), p. 105003. DOI: [10.1103/PhysRevLett.113.105003](https://doi.org/10.1103/PhysRevLett.113.105003).
- [62] F. Fiuza, G. F. Swadling, A. Grassi, H. G. Rinderknecht, D. P. Higginson, et al. “Electron acceleration in laboratory-produced turbulent collisionless shocks”. In: *Nature Physics* 16.9 (June 2020), pp. 916–920. DOI: [10.1038/s41567-020-0919-4](https://doi.org/10.1038/s41567-020-0919-4).
- [63] D. L. Freedman and E. Waxman. “On the Energy of Gamma-Ray Bursts”. In: *Astrophys. J.* 547.2 (Feb. 2001), pp. 922–928. DOI: [10.1086/318386](https://doi.org/10.1086/318386). arXiv: [astro-ph/9912214](https://arxiv.org/abs/astro-ph/9912214) [astro-ph].
- [64] B. D. Fried. “Mechanism for Instability of Transverse Plasma Waves”. In: *Physics of Fluids* 2.3 (May 1959), pp. 337–337. DOI: [10.1063/1.1705933](https://doi.org/10.1063/1.1705933).
- [65] Y. A. Gallant and A. Achterberg. “Ultra-high-energy cosmic ray acceleration by relativistic blast waves”. In: *Mon. Notices Royal Astron. Soc.* 305.1 (May 1999), pp. L6–L10. DOI: [10.1046/j.1365-8711.1999.02566.x](https://doi.org/10.1046/j.1365-8711.1999.02566.x).
- [66] D. Giannios, D. A. Uzdensky, and M. C. Begelman. “Fast TeV variability in blazars: jets in a jet”. In: *Mon. Notices Royal Astron. Soc.* 395.1 (May 2009), pp. L29–L33. DOI: [10.1111/j.1745-3933.2009.00635.x](https://doi.org/10.1111/j.1745-3933.2009.00635.x).

- [67] B. Godfrey. "Numerical Cherenkov instabilities in electromagnetic particle codes". In: *Journal of Computational Physics* 15 (Aug. 1974), pp. 504–521. DOI: [10.1016/0021-9991\(74\)90076-X](https://doi.org/10.1016/0021-9991(74)90076-X).
- [68] B. B. Godfrey and J. L. Vay. "Suppressing the numerical Cherenkov instability in FDTD PIC codes". In: *Journal of Computational Physics* 267 (June 2014), pp. 1–6. DOI: [10.1016/j.jcp.2014.02.022](https://doi.org/10.1016/j.jcp.2014.02.022). arXiv: [1401.0838](https://arxiv.org/abs/1401.0838) [physics.plasm-ph].
- [69] P. Goldreich and S. Sridhar. "Toward a Theory of Interstellar Turbulence. II. Strong Alfvénic Turbulence". In: *Astrophys. J.* 438 (Jan. 1995), p. 763. DOI: [10.1086/175121](https://doi.org/10.1086/175121).
- [70] A.D. Greenwood, K.L. Cartwright, E.A. Baca, and J.W. Luginsland. "On the use of FDTD to simulate systems with charged particles". In: *IEEE Antennas and Propagation Society International Symposium (IEEE Cat. No.02CH37313)*. Vol. 3. 2002, pp. 268–271. DOI: [10.1109/APS.2002.1018207](https://doi.org/10.1109/APS.2002.1018207).
- [71] A.D. Greenwood, K.L. Cartwright, J.W. Luginsland, and Ernest A. Baca. "On the elimination of numerical Cherenkov radiation in PIC simulations". In: *Journal of Computational Physics* 201.2 (2004), pp. 665–684. ISSN: 0021-9991. DOI: <https://doi.org/10.1016/j.jcp.2004.06.021>. URL: <https://www.sciencedirect.com/science/article/pii/S0021999104002608>.
- [72] J. J. Hester. "The Crab Nebula : an astrophysical chimera." In: *Annual Review of Astronomy and Astrophysics* 46 (Sept. 2008), pp. 127–155. DOI: [10.1146/annurev.astro.45.051806.110608](https://doi.org/10.1146/annurev.astro.45.051806.110608).
- [73] T. Hovatta and E. Lindfors. "Relativistic Jets of Blazars". In: *New Astronomy Reviews* 87, 101541 (Dec. 2019), p. 101541. DOI: [10.1016/j.newar.2020.101541](https://doi.org/10.1016/j.newar.2020.101541). arXiv: [2003.06322](https://arxiv.org/abs/2003.06322) [astro-ph.HE].
- [74] G. G. Howes, K. G. Klein, and J. M. TenBarge. "The Quasilinear Premise for the Modeling of Plasma Turbulence". In: *arXiv e-prints*, arXiv:1404.2913 (Apr. 2014), arXiv:1404.2913. arXiv: [1404.2913](https://arxiv.org/abs/1404.2913) [astro-ph.SR].
- [75] P. S. Iroshnikov. "Turbulence of a Conducting Fluid in a Strong Magnetic Field". In: *Astron. Zh.* 40 (Jan. 1963), p. 742.
- [76] Godfrey B. B. and Vay J.-L. "Numerical stability of relativistic beam multidimensional PIC simulations employing the Esirkepov algorithm". In: *Journal of Computational Physics* 248 (2013), pp. 33–46. ISSN: 0021-9991. DOI: <https://doi.org/10.1016/j.jcp.2013.04.006>. URL: <https://www.sciencedirect.com/science/article/pii/S0021999113002556>.
- [77] F. C. Jones and D. C. Ellison. "The plasma physics of shock acceleration". In: *Space Sci. Rev.* 58.1 (May 1991), 259–346. DOI: [10.1007/BF01206003](https://doi.org/10.1007/BF01206003).
- [78] H. H. Kaang, C. M. Ryu, and P. H. Yoon. "Nonlinear saturation of relativistic Weibel instability driven by thermal anisotropy". In: *Phys. Plasmas* 16.8, 082103 (Aug. 2009), p. 082103. DOI: [10.1063/1.3172941](https://doi.org/10.1063/1.3172941).
- [79] T. N. Kato. "Saturation mechanism of the Weibel instability in weakly magnetized plasmas". In: *Phys. Plasmas* 12 (2005), p. 080705. DOI: [10.1063/1.2017942](https://doi.org/10.1063/1.2017942).
- [80] U. Keshet and E. Waxman. "Energy Spectrum of Particles Accelerated in Relativistic Collisionless Shocks". In: *Phys. Rev. Lett.* 94 (11 2005), p. 111102. DOI: [10.1103/PhysRevLett.94.111102](https://doi.org/10.1103/PhysRevLett.94.111102). URL: <https://link.aps.org/doi/10.1103/PhysRevLett.94.111102>.

- [81] J. G. Kirk, A. W. Guthmann, Y. A. Gallant, and A. Achterberg. “Particle Acceleration at Ultrarelativistic Shocks: An Eigenfunction Method”. In: *Astrophys. J.* 542.1 (Oct. 2000), pp. 235–242. DOI: [10.1086/309533](https://doi.org/10.1086/309533). arXiv: [astro-ph/0005222](https://arxiv.org/abs/astro-ph/0005222) [astro-ph].
- [82] J. G. Kirk, Y. Lyubarsky, and J. Petri. “The Theory of Pulsar Winds and Nebulae”. In: *Astrophysics and Space Science Library*. Ed. by Werner Becker. Vol. 357. Astrophysics and Space Science Library. Jan. 2009, p. 421. DOI: [10.1007/978-3-540-76965-1_16](https://doi.org/10.1007/978-3-540-76965-1_16). arXiv: [astro-ph/0703116](https://arxiv.org/abs/astro-ph/0703116) [astro-ph].
- [83] R. H. Kraichnan. “Inertial-Range Spectrum of Hydromagnetic Turbulence”. In: *Physics of Fluids* 8.7 (July 1965), pp. 1385–1387. DOI: [10.1063/1.1761412](https://doi.org/10.1063/1.1761412).
- [84] M. Kärkkäinen, E. Gjonaj, T. Lau, and T. Weiland. “Low-dispersion wake field calculation tools”. In: *Proc. International Computational Accelerator Physics Conference* (Jan. 2006).
- [85] A. Lazar, E. Nakar, and T. Piran. “Gamma-Ray Burst Light Curves in the Relativistic Turbulence and Relativistic Subject Models”. In: *Astrophys. J. Lett.* 695.1 (Apr. 2009), pp. L10–L14. DOI: [10.1088/0004-637X/695/1/L10](https://doi.org/10.1088/0004-637X/695/1/L10). arXiv: [0901.1133](https://arxiv.org/abs/0901.1133) [astro-ph.HE].
- [86] M. A. Lee, V. D. Shapiro, and R. Z. Sagdeev. “Pickup ion energization by shock surfing”. In: 101.A3 (Mar. 1996), pp. 4777–4790. DOI: [10.1029/95JA03570](https://doi.org/10.1029/95JA03570).
- [87] E. Lefebvre, N. Cochet, S. Fritzler, V. Malka, M.-M. Aléonard, et al. “Electron and photon production from relativistic laser plasma interactions”. In: *Nucl. Fusion* 43 (July 2003), pp. 629–633. DOI: [10.1088/0029-5515/43/7/317](https://doi.org/10.1088/0029-5515/43/7/317).
- [88] R. Lehe, A. Lifschitz, C. Thaury, V. Malka, and X. Davoine. “Numerical growth of emittance in simulations of laser-wakefield acceleration”. In: *Physical Review Accelerators and Beams* 16.2, 021301 (Feb. 2013), p. 021301. DOI: [10.1103/PhysRevSTAB.16.021301](https://doi.org/10.1103/PhysRevSTAB.16.021301).
- [89] M. Lemoine. “Generalized Fermi acceleration”. In: *Phys. Rev. D* 99.8, 083006 (Apr. 2019), p. 083006. DOI: [10.1103/PhysRevD.99.083006](https://doi.org/10.1103/PhysRevD.99.083006). arXiv: [1903.05917](https://arxiv.org/abs/1903.05917) [astro-ph.HE].
- [90] M. Lemoine. “Particle acceleration in strong MHD turbulence”. In: *Phys. Rev. D* 104.6, 063020 (Sept. 2021), p. 063020. DOI: [10.1103/PhysRevD.104.063020](https://doi.org/10.1103/PhysRevD.104.063020). arXiv: [2104.08199](https://arxiv.org/abs/2104.08199) [astro-ph.HE].
- [91] M. Lemoine, L. Gremillet, G. Pelletier, and A. Vanthieghem. “The physics of Weibel-mediated relativistic collisionless shocks”. In: *Phys. Rev. Lett.* 123 (3 2019), p. 035101. DOI: [10.1103/PhysRevLett.123.035101](https://doi.org/10.1103/PhysRevLett.123.035101). arXiv: [1907.07595](https://arxiv.org/abs/1907.07595). URL: <https://link.aps.org/doi/10.1103/PhysRevLett.123.035101>.
- [92] M. Lemoine and G. Pelletier. “Dispersion and thermal effects on electromagnetic instabilities in the precursor of relativistic shocks”. In: *Mon. Not. Roy. Astron. Soc.* 417 (2011), pp. 1148–1161. DOI: [10.1111/j.1365-2966.2011.19331.x](https://doi.org/10.1111/j.1365-2966.2011.19331.x).
- [93] M. Lemoine and G. Pelletier. “On electromagnetic instabilities at ultra-relativistic shock waves”. In: *Mon. Not. Roy. Astron. Soc.* 402 (Feb. 2010), pp. 321–334. DOI: [10.1111/j.1365-2966.2009.15869.x](https://doi.org/10.1111/j.1365-2966.2009.15869.x).
- [94] M. Lemoine and G. Pelletier. “Particle Transport in Tangled Magnetic Fields and Fermi Acceleration at Relativistic Shocks”. In: *Astrophys. J. Lett.* 589.2 (June 2003), pp. L73–L76. DOI: [10.1086/376353](https://doi.org/10.1086/376353). arXiv: [astro-ph/0304058](https://arxiv.org/abs/astro-ph/0304058) [astro-ph].

- [95] M. Lemoine, G. Pelletier, and B. Revenu. "On the Efficiency of Fermi Acceleration at Relativistic Shocks". In: *Astrophys. J. Lett.* 645.2 (July 2006), pp. L129–L132. DOI: [10.1086/506322](https://doi.org/10.1086/506322). arXiv: [astro-ph/0606005](https://arxiv.org/abs/astro-ph/0606005) [astro-ph].
- [96] M. Lemoine, O. Ramos, and L. Gremillet. "Corrugation of Relativistic Magnetized Shock Waves". In: *Astrophys. J.* 827.1, 44 (Aug. 2016), p. 44. DOI: [10.3847/0004-637X/827/1/44](https://doi.org/10.3847/0004-637X/827/1/44). arXiv: [1607.00768](https://arxiv.org/abs/1607.00768) [astro-ph.HE].
- [97] M. Lemoine and B. Revenu. "Relativistic Fermi acceleration with shock compressed turbulence". In: *Monthly Notices of the Royal Astronomical Society* 366.2 (Feb. 2006), pp. 635–644. ISSN: 0035-8711. DOI: [10.1111/j.1365-2966.2005.09912.x](https://doi.org/10.1111/j.1365-2966.2005.09912.x). eprint: <https://academic.oup.com/mnras/article-pdf/366/2/635/4050858/366-2-635.pdf>. URL: <https://doi.org/10.1111/j.1365-2966.2005.09912.x>.
- [98] Martin Lemoine. "A corrugated termination shock in pulsar wind nebulae?" In: *Journal of Plasma Physics* 82.4, 635820401 (Aug. 2016), p. 635820401. DOI: [10.1017/S0022377816000659](https://doi.org/10.1017/S0022377816000659). arXiv: [1607.01543](https://arxiv.org/abs/1607.01543) [astro-ph.HE].
- [99] Yi Li, Eric Perlman, Minping Wan, Yunke Yang, Charles Meneveau, et al. "A public turbulence database cluster and applications to study Lagrangian evolution of velocity increments in turbulence". In: *J. Turbul.* 9, N31 (Jan. 2008), N31. DOI: [10.1080/14685240802376389](https://doi.org/10.1080/14685240802376389). arXiv: [0804.1703](https://arxiv.org/abs/0804.1703) [physics.flu-dyn].
- [100] Arianna Ligorini, Jacek Niemiec, Oleh Kobzar, Masanori Iwamoto, Artem Bohdan, et al. "Mildly relativistic magnetized shocks in electron-ion plasmas - I. Electromagnetic shock structure". In: *Mon. Notices Royal Astron. Soc.* 501.4 (Mar. 2021), pp. 4837–4849. DOI: [10.1093/mnras/staa3901](https://doi.org/10.1093/mnras/staa3901).
- [101] Arianna Ligorini, Jacek Niemiec, Oleh Kobzar, Masanori Iwamoto, Artem Bohdan, et al. "Mildly relativistic magnetized shocks in electron-ion plasmas - II. Particle acceleration and heating". In: *Mon. Notices Royal Astron. Soc.* 502.4 (Apr. 2021), pp. 5065–5074. DOI: [10.1093/mnras/stab220](https://doi.org/10.1093/mnras/stab220).
- [102] J. W. Lynn, E. Quataert, B. D. G. Chandran, and I. J. Parrish. "The Efficiency of Second-order Fermi Acceleration by Weakly Compressible Magnetohydrodynamic Turbulence". In: *Astrophys. J.* 777.2, 128 (Nov. 2013), p. 128. DOI: [10.1088/0004-637X/777/2/128](https://doi.org/10.1088/0004-637X/777/2/128). arXiv: [1307.0021](https://arxiv.org/abs/1307.0021) [astro-ph.SR].
- [103] Y. Lyubarsky and D. Eichler. "Are Gamma-Ray Burst Shocks Mediated by the Weibel Instability?" In: *Astrophys. J.* 647 (Aug. 2006), pp. 1250–1254. DOI: [10.1086/505523](https://doi.org/10.1086/505523).
- [104] M. A. Malkov and L. O'C. Drury. "Nonlinear theory of diffusive acceleration of particles by shock waves". In: *Reports on Progress in Physics* 64.4 (Apr. 2001), pp. 429–481. DOI: [10.1088/0034-4885/64/4/201](https://doi.org/10.1088/0034-4885/64/4/201).
- [105] A. Marcowith, G. Ferrand, M. Grech, Z. Meliani, I. Plotnikov, et al. "Multi-scale simulations of particle acceleration in astrophysical systems". In: *Living Reviews in Computational Astrophysics* 6.1, 1 (Mar. 2020), p. 1. DOI: [10.1007/s41115-020-0007-6](https://doi.org/10.1007/s41115-020-0007-6). arXiv: [2002.09411](https://arxiv.org/abs/2002.09411) [astro-ph.HE].
- [106] J. Maron and P. Goldreich. "Simulations of Incompressible Magnetohydrodynamic Turbulence". In: *Astrophys. J.* 554.2 (June 2001), pp. 1175–1196. DOI: [10.1086/321413](https://doi.org/10.1086/321413). arXiv: [astro-ph/0012491](https://arxiv.org/abs/astro-ph/0012491) [astro-ph].
- [107] S. F. Martins, R. A. Fonseca, L. O. Silva, and W. B. Mori. "Ion Dynamics and Acceleration in Relativistic Shocks". In: *Astrophys. J. Lett.* 695 (Apr. 2009), pp. L189–L193. DOI: [10.1088/0004-637X/695/2/L189](https://doi.org/10.1088/0004-637X/695/2/L189).

- [108] Y. Matsumoto, T. Amano, T. N. Kato, and M. Hoshino. “Stochastic electron acceleration during spontaneous turbulent reconnection in a strong shock wave”. In: *Science* 347.6225 (Feb. 2015), pp. 974–978. DOI: [10.1126/science.1260168](https://doi.org/10.1126/science.1260168).
- [109] M. V. Medvedev and A. Loeb. “Generation of Magnetic Fields in the Relativistic Shock of Gamma-Ray Burst Sources”. In: *Astrophys. J.* 526 (Dec. 1999), pp. 697–706. DOI: [10.1086/308038](https://doi.org/10.1086/308038).
- [110] M. Meyer, D. Horns, and H. S. Zechlin. “The Crab Nebula as a standard candle in very high-energy astrophysics”. In: *A&A* 523, A2 (Nov. 2010), A2. DOI: [10.1051/0004-6361/201014108](https://doi.org/10.1051/0004-6361/201014108). arXiv: [1008.4524](https://arxiv.org/abs/1008.4524) [astro-ph.HE].
- [111] G. Michalek, M. Ostrowski, and R. Schlickeiser. “Cosmic-Ray Momentum Diffusion in Magnetosonic versus Alfvénic Turbulent Field”. In: *Solar Physics* 184.2 (Feb. 1999), pp. 339–352. DOI: [10.1023/A:1005028205111](https://doi.org/10.1023/A:1005028205111).
- [112] Yosuke Mizuno, Martin Pohl, Jacek Niemiec, Bing Zhang, Ken-Ichi Nishikawa, et al. “Magnetic-field Amplification by Turbulence in a Relativistic Shock Propagating Through an Inhomogeneous Medium”. In: 726.2, 62 (Jan. 2011), p. 62. DOI: [10.1088/0004-637X/726/2/62](https://doi.org/10.1088/0004-637X/726/2/62). arXiv: [1011.2171](https://arxiv.org/abs/1011.2171) [astro-ph.HE].
- [113] S. S. Moiseev and R. Z. Sagdeev. “Collisionless shock waves in a plasma in a weak magnetic field”. In: *J. Nucl. Energy* 5.1 (1963), p. 43.
- [114] E. Nakar. “Short-hard gamma-ray bursts”. In: *Physics Reports* 442.1-6 (Apr. 2007), pp. 166–236. DOI: [10.1016/j.physrep.2007.02.005](https://doi.org/10.1016/j.physrep.2007.02.005). arXiv: [astro-ph/0701748](https://arxiv.org/abs/astro-ph/0701748) [astro-ph].
- [115] N. Naseri, S. G. Bochkarev, P. Ruan, V. Yu. Bychenkov, V. Khudik, et al. “Growth and propagation of self-generated magnetic dipole vortices in collisionless shocks produced by interpenetrating plasmas”. In: *Phys. Plasmas* 25.1 (2018), p. 012118. DOI: [10.1063/1.5008278](https://doi.org/10.1063/1.5008278).
- [116] J. Niemiec, M. Pohl, A. Bret, and V. Wieland. “Nonrelativistic Parallel Shocks in Unmagnetized and Weakly Magnetized Plasmas”. In: *Astrophys. J.* 759.1, 73 (Nov. 2012), p. 73. DOI: [10.1088/0004-637X/759/1/73](https://doi.org/10.1088/0004-637X/759/1/73). arXiv: [1209.3938](https://arxiv.org/abs/1209.3938) [astro-ph.HE].
- [117] P. M. Nilson, L. Willingale, M. C. Kaluza, C. Kamperidis, S. Minardi, et al. “Bidirectional jet formation during driven magnetic reconnection in two-beam laser-plasma interactions”. In: *Physics of Plasmas* 15.9, 092701 (Sept. 2008), p. 092701. DOI: [10.1063/1.2966115](https://doi.org/10.1063/1.2966115).
- [118] P. M. Nilson, L. Willingale, M. C. Kaluza, C. Kamperidis, S. Minardi, et al. “Magnetic Reconnection and Plasma Dynamics in Two-Beam Laser-Solid Interactions”. In: *Phys. Rev. Lett.* 97.25, 255001 (Dec. 2006), p. 255001. DOI: [10.1103/PhysRevLett.97.255001](https://doi.org/10.1103/PhysRevLett.97.255001).
- [119] M. Ostrowski. “Cosmic-Ray Acceleration at Relativistic Shock Waves in the Presence of Oblique Magnetic Fields with Finite-Amplitude Perturbations”. In: *Mon. Notices Royal Astron. Soc.* 264 (Sept. 1993), p. 248. DOI: [10.1093/mnras/264.1.248](https://doi.org/10.1093/mnras/264.1.248).
- [120] S. O’Sullivan, B. Reville, and A. M. Taylor. “Stochastic particle acceleration in the lobes of giant radio galaxies”. In: *Mon. Notices Royal Astron. Soc.* 400.1 (Nov. 2009), pp. 248–257. DOI: [10.1111/j.1365-2966.2009.15442.x](https://doi.org/10.1111/j.1365-2966.2009.15442.x). arXiv: [0903.1259](https://arxiv.org/abs/0903.1259) [astro-ph.HE].

- [121] T. N. Parashar, M. Cuesta, and W. H. Matthaeus. “Reynolds Number and Intermittency in the Expanding Solar Wind: Predictions Based on iVoyager/i Observations”. In: *The Astrophysical Journal* 884.2 (2019), p. L57. DOI: [10.3847/2041-8213/ab4a82](https://doi.org/10.3847/2041-8213/ab4a82). URL: <https://doi.org/10.3847/2041-8213/ab4a82>.
- [122] G. Pelletier, L. Gremillet, A. Vanthieghem, and M. Lemoine. “Physics of relativistic collisionless shocks: The scattering center frame”. In: *Phys. Rev. E* 100 (1 2019), p. 013205. DOI: [10.1103/PhysRevE.100.013205](https://doi.org/10.1103/PhysRevE.100.013205). arXiv: [1907.07750](https://arxiv.org/abs/1907.07750). URL: <https://link.aps.org/doi/10.1103/PhysRevE.100.013205>.
- [123] G. Pelletier, M. Lemoine, and A. Marcowith. “On Fermi acceleration and magnetohydrodynamic instabilities at ultra-relativistic magnetized shock waves”. In: *Mon. Notices Royal Astron. Soc.* 393.2 (Feb. 2009), pp. 587–597. ISSN: 0035-8711. DOI: [10.1111/j.1365-2966.2008.14219.x](https://doi.org/10.1111/j.1365-2966.2008.14219.x). eprint: <https://academic.oup.com/mnras/article-pdf/393/2/587/3044616/mnras0393-0587.pdf>. URL: <https://doi.org/10.1111/j.1365-2966.2008.14219.x>.
- [124] J. R. Peterson, S. Glenzer, and F. Fiuza. “Magnetic Field Amplification by a Nonlinear Electron Streaming Instability”. In: *Phys. Rev. Lett.* 126 (21 2021), p. 215101. DOI: [10.1103/PhysRevLett.126.215101](https://doi.org/10.1103/PhysRevLett.126.215101).
- [125] J.e Pétri and Y. Lyubarsky. “Magnetic reconnection at the termination shock in a striped pulsar wind”. In: *40 Years of Pulsars: Millisecond Pulsars, Magnetars and More*. Ed. by C. Bassa, Z. Wang, A. Cumming, and V. M. Kaspi. Vol. 983. American Institute of Physics Conference Series. Feb. 2008, pp. 207–209. DOI: [10.1063/1.2900142](https://doi.org/10.1063/1.2900142).
- [126] M. Petropoulou, L. Sironi, A. Spitkovsky, and D. Giannios. “Relativistic Magnetic Reconnection in Electron-Positron-Proton Plasmas: Implications for Jets of Active Galactic Nuclei”. In: *Astrophys. J.* 880.1, 37 (July 2019), p. 37. DOI: [10.3847/1538-4357/ab287a](https://doi.org/10.3847/1538-4357/ab287a).
- [127] T. Piran. “Gamma-ray bursts and the fireball model”. In: *Physics Report* 314.6 (June 1999), pp. 575–667. DOI: [10.1016/S0370-1573\(98\)00127-6](https://doi.org/10.1016/S0370-1573(98)00127-6). arXiv: [astro-ph/9810256](https://arxiv.org/abs/astro-ph/9810256) [astro-ph].
- [128] I. Plotnikov, A. Grassi, and M. Grech. “Perpendicular relativistic shocks in magnetized pair plasma”. In: *Mon. Notices Royal Astron. Soc.* 477.4 (July 2018), pp. 5238–5260. DOI: [10.1093/mnras/sty979](https://doi.org/10.1093/mnras/sty979). arXiv: [1712.02883](https://arxiv.org/abs/1712.02883) [astro-ph.HE].
- [129] I. Plotnikov, G. Pelletier, and M. Lemoine. “Particle transport and heating in the microturbulent precursor of relativistic shocks”. In: *Mon. Notices Royal Astron. Soc.* 430.2 (Apr. 2013), pp. 1280–1293. DOI: [10.1093/mnras/sts696](https://doi.org/10.1093/mnras/sts696). arXiv: [1206.6634](https://arxiv.org/abs/1206.6634) [astro-ph.HE].
- [130] A. Pukhov. “Three-dimensional electromagnetic relativistic particle-in-cell code VLPL (Virtual Laser Plasma Lab)”. In: *Journal of Plasma Physics* 61.3 (1999), 425–433. DOI: [10.1017/S0022377899007515](https://doi.org/10.1017/S0022377899007515).
- [131] A. E. Raymond, C. F. Dong, A. McKelvey, C. Zulick, N. Alexander, et al. “Relativistic-electron-driven magnetic reconnection in the laboratory”. In: *Phys. Rev. E* 98.4, 043207 (Oct. 2018), p. 043207. DOI: [10.1103/PhysRevE.98.043207](https://doi.org/10.1103/PhysRevE.98.043207).
- [132] M. J. Rees. “Appearance of Relativistically Expanding Radio Sources”. In: *Nature* 211.5048 (July 1966), pp. 468–470. DOI: [10.1038/211468a0](https://doi.org/10.1038/211468a0).
- [133] Gustavo E. Romero, M. Boettcher, S. Markoff, and F. Tavecchio. “Relativistic Jets in Active Galactic Nuclei and Microquasars”. In: *Space Science Review* 207.1-4 (July 2017), pp. 5–61. DOI: [10.1007/s11214-016-0328-2](https://doi.org/10.1007/s11214-016-0328-2). arXiv: [1611.09507](https://arxiv.org/abs/1611.09507) [astro-ph.HE].

- [134] M. J. Rosenberg, C. K. Li, W. Fox, I. Igumenshchev, F. H. Séguin, et al. “A laboratory study of asymmetric magnetic reconnection in strongly driven plasmas”. In: *Nature Communications* 6, 6190 (Feb. 2015), p. 6190. DOI: [10.1038/ncomms7190](https://doi.org/10.1038/ncomms7190).
- [135] C. Ruyer, L. Gremillet, and G. Bonnaud. “Weibel-mediated collisionless shocks in laser-irradiated dense plasmas: Prevailing role of the electrons in generating the field fluctuations”. In: *Phys. Plasmas* 22.8 (2015), p. 082107. DOI: [10.1063/1.4928096](https://doi.org/10.1063/1.4928096).
- [136] C. Ruyer, L. Gremillet, G. Bonnaud, and C. Riconda. “Analytical Predictions of Field and Plasma Dynamics during Nonlinear Weibel-Mediated Flow Collisions”. In: *Phys. Rev. Lett.* 117 (6 2016), p. 065001. DOI: [10.1103/PhysRevLett.117.065001](https://doi.org/10.1103/PhysRevLett.117.065001). URL: <https://link.aps.org/doi/10.1103/PhysRevLett.117.065001>.
- [137] C. Ruyer, L. Gremillet, A. Debayle, and G. Bonnaud. “Nonlinear dynamics of the ion Weibel-filamentation instability: An analytical model for the evolution of the plasma and spectral properties”. In: *Phys. Plasmas* 22.3 (2015), p. 032102. DOI: [10.1063/1.4913651](https://doi.org/10.1063/1.4913651).
- [138] R. Z. Sagdeev. “Cooperative Phenomena and Shock Waves in Collisionless Plasmas”. In: *Reviews of Plasma Physics* 4 (Jan. 1966), p. 23.
- [139] A. A. Schekochihin, S. C. Cowley, W. Dorland, G. W. Hammett, G. G. Howes, et al. “Astrophysical Gyrokinetics: Kinetic and Fluid Turbulent Cascades in Magnetized Weakly Collisional Plasmas”. In: *Astrophysical Journal Supplement Series* 182.1 (May 2009), pp. 310–377. DOI: [10.1088/0067-0049/182/1/310](https://doi.org/10.1088/0067-0049/182/1/310). arXiv: [0704.0044](https://arxiv.org/abs/0704.0044) [astro-ph].
- [140] R. Schlickeiser. *Cosmic Ray Astrophysics*. 2002.
- [141] A. Shalchi and R. Schlickeiser. “Cosmic ray transport in anisotropic magnetohydrodynamic turbulence. III. Mixed magnetosonic and Alfvénic turbulence”. In: *A&A* 420 (June 2004), pp. 799–808. DOI: [10.1051/0004-6361:20034304](https://doi.org/10.1051/0004-6361:20034304).
- [142] N. Shukla, K. Schoeffler, J. Vieira, R. Fonseca, E. Boella, et al. *Slowdown of interpenetration of two counterpropagating plasma slab due to collective effects*. 2021. arXiv: [2109.00023](https://arxiv.org/abs/2109.00023) [physics.plasm-ph].
- [143] O. Silva L. “Physical Problems (Microphysics) in Relativistic Plasma Flows”. In: *AIP Conference Proceedings* 856 (2006), p. 109. DOI: [10.1063/1.2356387](https://doi.org/10.1063/1.2356387).
- [144] L. Sironi, U. Keshet, and M. Lemoine. “Relativistic Shocks: Particle Acceleration and Magnetization”. In: *Space Science Reviews volume* 191.1-4 (Oct. 2015), pp. 519–544. DOI: [10.1007/s11214-015-0181-8](https://doi.org/10.1007/s11214-015-0181-8). arXiv: [1506.02034](https://arxiv.org/abs/1506.02034) [astro-ph.HE].
- [145] L. Sironi, M. Petropoulou, and D. Giannios. “Relativistic jets shine through shocks or magnetic reconnection?” In: *Mon. Notices Royal Astron. Soc.* 450.1 (June 2015), pp. 183–191. DOI: [10.1093/mnras/stv641](https://doi.org/10.1093/mnras/stv641). arXiv: [1502.01021](https://arxiv.org/abs/1502.01021) [astro-ph.HE].
- [146] L. Sironi and A. Spitkovsky. “Acceleration of Particles at the Termination Shock of a Relativistic Striped Wind”. In: *Astrophys. J.* 741.1, 39 (Nov. 2011), p. 39. DOI: [10.1088/0004-637X/741/1/39](https://doi.org/10.1088/0004-637X/741/1/39). arXiv: [1107.0977](https://arxiv.org/abs/1107.0977) [astro-ph.HE].

- [147] L. Sironi and A. Spitkovsky. “Particle Acceleration in Relativistic Magnetized Collisionless Electron-Ion Shocks”. In: *Astrophys. J.* 726.2, 75 (Jan. 2011), p. 75. DOI: [10.1088/0004-637X/726/2/75](https://doi.org/10.1088/0004-637X/726/2/75). arXiv: [1009.0024](https://arxiv.org/abs/1009.0024) [astro-ph.HE].
- [148] L. Sironi and A. Spitkovsky. “Particle Acceleration in Relativistic Magnetized Collisionless Pair Shocks: Dependence of Shock Acceleration on Magnetic Obliquity”. In: *Astrophys. J.* 698.2 (June 2009), pp. 1523–1549. DOI: [10.1088/0004-637X/698/2/1523](https://doi.org/10.1088/0004-637X/698/2/1523). arXiv: [0901.2578](https://arxiv.org/abs/0901.2578) [astro-ph.HE].
- [149] L. Sironi, A. Spitkovsky, and J. Arons. “The Maximum Energy of Accelerated Particles in Relativistic Collisionless Shocks”. In: *Astrophys. J.* 771, 54 (2013), p. 54. DOI: [10.1088/0004-637X/771/1/54](https://doi.org/10.1088/0004-637X/771/1/54).
- [150] W. B. Sparks, J. A. Biretta, and F. Macchetto. “The Jet of M87 at Tenth-Arcsecond Resolution: Optical, Ultraviolet, and Radio Observations”. In: *Astrophys. J.* 473 (Dec. 1996), p. 254. DOI: [10.1086/178141](https://doi.org/10.1086/178141).
- [151] A. Spitkovsky. “On the Structure of Relativistic Collisionless Shocks in Electron-Ion Plasmas”. In: *Astrophys. J. Lett.* 673, L39 (Jan. 2008), p. L39. DOI: [10.1086/527374](https://doi.org/10.1086/527374).
- [152] A. Spitkovsky. “Particle Acceleration in Relativistic Collisionless Shocks: Fermi Process at Last?” In: *Astrophys. J. Lett.* 682, L5 (2008), p. L5. DOI: [10.1086/590248](https://doi.org/10.1086/590248).
- [153] Ł. Stawarz and V. Petrosian. “On the Momentum Diffusion of Radiating Ultrarelativistic Electrons in a Turbulent Magnetic Field”. In: *Astrophys. J.* 681.2 (July 2008), pp. 1725–1744. DOI: [10.1086/588813](https://doi.org/10.1086/588813). arXiv: [0803.0989](https://arxiv.org/abs/0803.0989) [astro-ph].
- [154] A. Stockem, F. Fiuza, A. Bret, R. A. Fonseca, and L. O. Silva. “Exploring the nature of collisionless shocks under laboratory conditions”. In: *Sci. Rep.* 4, 3934 (Feb. 2014), p. 3934. DOI: [10.1038/srep03934](https://doi.org/10.1038/srep03934).
- [155] E. Tademaru. “Plasma Instabilities of Streaming Cosmic Rays”. In: *Astrophys. J.* 158 (Dec. 1969), p. 959. DOI: [10.1086/150255](https://doi.org/10.1086/150255).
- [156] M. Takamoto and A. Lazarian. “Compressible Relativistic Magnetohydrodynamic Turbulence in Magnetically Dominated Plasmas and Implications for a Strong-coupling Regime”. In: *Astrophys. J. Lett.* 831.2, L11 (Nov. 2016), p. L11. DOI: [10.3847/2041-8205/831/2/L11](https://doi.org/10.3847/2041-8205/831/2/L11). arXiv: [1610.01373](https://arxiv.org/abs/1610.01373) [astro-ph.HE].
- [157] M. Takamoto and A. Lazarian. “Strong coupling of Alfvén and fast modes in compressible relativistic magnetohydrodynamic turbulence in magnetically dominated plasmas”. In: *Mon. Notices Royal Astron. Soc.* 472.4 (Dec. 2017), pp. 4542–4550. DOI: [10.1093/mnras/stx2292](https://doi.org/10.1093/mnras/stx2292). arXiv: [1709.00785](https://arxiv.org/abs/1709.00785) [astro-ph.HE].
- [158] Matsumoto Y. Takamoto M. and Kato T. N. “Magnetic Field Saturation of the Ion Weibel Instability in Interpenetrating Relativistic Plasmas”. In: *The Astrophysical Journal* 860.1 (2018), p. L1. DOI: [10.3847/2041-8213/aac6d6](https://doi.org/10.3847/2041-8213/aac6d6). URL: <https://doi.org/10.3847/2041-8213/aac6d6>.
- [159] J. M. TenBarge, G. G. Howes, W. Dorland, and G. W. Hammett. “An oscillating Langevin antenna for driving plasma turbulence simulations”. In: *Computer Physics Communications* 185.2 (Feb. 2014), pp. 578–589. DOI: [10.1016/j.cpc.2013.10.022](https://doi.org/10.1016/j.cpc.2013.10.022). arXiv: [1305.2212](https://arxiv.org/abs/1305.2212) [physics.plasm-ph].

- [160] J. M. TenBarge, B. Ripperda, A. Chernoglazov, A. Bhattacharjee, J. F. Mählmann, et al. “Weak Alfvénic turbulence in relativistic plasmas. Part 1. Dynamical equations and basic dynamics of interacting resonant triads”. In: *Journal of Plasma Physics* 87.6 (Dec. 2021), p. 905870614. DOI: [10.1017/S002237782100115X](https://doi.org/10.1017/S002237782100115X). arXiv: [2105.01146](https://arxiv.org/abs/2105.01146) [astro-ph.HE].
- [161] Yuto Teraki and Katsuaki Asano. “Particle energy diffusion in linear magnetohydrodynamic waves”. In: *Astrophys. J.* 877.2, 71 (2019), p. 71. DOI: [10.3847/1538-4357/ab1b13](https://doi.org/10.3847/1538-4357/ab1b13). arXiv: [1904.08579](https://arxiv.org/abs/1904.08579) [astro-ph.HE].
- [162] C. Thompson and O. Blaes. “Magnetohydrodynamics in the extreme relativistic limit”. In: *Phys. Rev. D* 57.6 (Mar. 1998), pp. 3219–3234. DOI: [10.1103/PhysRevD.57.3219](https://doi.org/10.1103/PhysRevD.57.3219).
- [163] Domenico Trotta, Francesco Valentini, David Burgess, and Sergio Servidio. “Phase space transport in the interaction between shocks and plasma turbulence”. In: *Proceedings of the National Academy of Science* 118.21, 2026764118 (May 2021), p. 2026764118. DOI: [10.1073/pnas.2026764118](https://doi.org/10.1073/pnas.2026764118).
- [164] Y. Uchiyama, F. A. Aharonian, T. Tanaka, T. Takahashi, and Y. Maeda. “Extremely fast acceleration of cosmic rays in a supernova remnant”. In: *Nature* 449.7162 (Oct. 2007), pp. 576–578. DOI: [10.1038/nature06210](https://doi.org/10.1038/nature06210).
- [165] A. J van Marle, F. Casse, and A. Marcowith. “On magnetic field amplification and particle acceleration near non-relativistic astrophysical shocks: particles in MHD cells simulations”. In: *Mon. Notices Royal Astron. Soc.* 473.3 (Jan. 2018), pp. 3394–3409. DOI: [10.1093/mnras/stx2509](https://doi.org/10.1093/mnras/stx2509). arXiv: [1709.08482](https://arxiv.org/abs/1709.08482) [astro-ph.HE].
- [166] A. Vanthieghem. “Theoretical and numerical studies of relativistic collisionless shock waves”. Theses. Sorbonne Université, Sept. 2019. URL: <https://tel.archives-ouvertes.fr/tel-03010503>.
- [167] A. Vanthieghem, M. Lemoine, and L. Gremillet. “Stability analysis of a periodic system of relativistic current filaments”. In: *Phys. Plasmas* 25.7, 072115 (July 2018), p. 072115. DOI: [10.1063/1.5033562](https://doi.org/10.1063/1.5033562).
- [168] Arno Vanthieghem, Martin Lemoine, Ilya Plotnikov, Anna Grassi, Mickael Grech, et al. “Physics and Phenomenology of Weakly Magnetized, Relativistic Astrophysical Shock Waves”. In: *Galaxies* 8.2 (Apr. 2020), p. 33. DOI: [10.3390/galaxies8020033](https://doi.org/10.3390/galaxies8020033). arXiv: [2002.01141](https://arxiv.org/abs/2002.01141) [astro-ph.HE].
- [169] J.-L. Vay, Geddes C.G.R., Cormier-Michel E., and D.P. Grote. “Numerical methods for instability mitigation in the modeling of laser wakefield accelerators in a Lorentz-boosted frame”. In: *Journal of Computational Physics* 230.15 (2011), pp. 5908–5929. ISSN: 0021-9991. DOI: <https://doi.org/10.1016/j.jcp.2011.04.003>. URL: <https://www.sciencedirect.com/science/article/pii/S0021999111002270>.
- [170] Thibault Vieu, Brian Reville, and Felix Aharonian. “Can superbubbles accelerate ultra-high energy protons?” In: *arXiv e-prints*, arXiv:2207.01432 (July 2022), arXiv:2207.01432. arXiv: [2207.01432](https://arxiv.org/abs/2207.01432) [astro-ph.HE].
- [171] J. Vink. “Supernova remnants: the X-ray perspective”. In: *The Astronomy and Astrophysics Review* 20, 49 (Dec. 2012), p. 49. DOI: [10.1007/s00159-011-0049-1](https://doi.org/10.1007/s00159-011-0049-1). arXiv: [1112.0576](https://arxiv.org/abs/1112.0576) [astro-ph.HE].
- [172] A. Vladimirov, D. C. Ellison, and A. Bykov. “Nonlinear Diffusive Shock Acceleration with Magnetic Field Amplification”. In: *Astrophys. J.* 652.2 (Dec. 2006), pp. 1246–1258. DOI: [10.1086/508154](https://doi.org/10.1086/508154). arXiv: [astro-ph/0606433](https://arxiv.org/abs/astro-ph/0606433) [astro-ph].

- [173] Eli Waxman. “Gamma-Ray–Burst Afterglow: Supporting the Cosmological Fireball Model, Constraining Parameters, and Making Predictions”. In: *Astrophys. J. Lett.* 485.1 (Aug. 1997), pp. L5–L8. DOI: [10.1086/310809](https://doi.org/10.1086/310809). arXiv: [astro-ph/9704116](https://arxiv.org/abs/astro-ph/9704116) [astro-ph].
- [174] G. M. Webb. “Relativistic Transport Theory for Cosmic Rays”. In: *Astrophys. J.* 296 (Sept. 1985), p. 319. DOI: [10.1086/163451](https://doi.org/10.1086/163451).
- [175] G. M. Webb. “The Diffusion Approximation and Transport Theory for Cosmic Rays in Relativistic Flows”. In: *Astrophys. J.* 340 (May 1989), p. 1112. DOI: [10.1086/167462](https://doi.org/10.1086/167462).
- [176] E. S. Weibel. “Spontaneously Growing Transverse Waves in a Plasma Due to an Anisotropic Velocity Distribution”. In: *Phys. Rev. Lett.* 2 (3 1959), pp. 83–84. DOI: [10.1103/PhysRevLett.2.83](https://doi.org/10.1103/PhysRevLett.2.83). URL: <https://link.aps.org/doi/10.1103/PhysRevLett.2.83>.
- [177] J. Wiersma and A. Achterberg. “Magnetic field generation in relativistic shocks. An early end of the exponential Weibel instability in electron-proton plasmas”. In: *A&A* 428 (Dec. 2004), pp. 365–371. DOI: [10.1051/0004-6361:20041882](https://doi.org/10.1051/0004-6361:20041882).
- [178] K. Wong, V. Zhdankin, D. A. Uzdensky, G. R. Werner, and M. C. Begelman. “First-principles Demonstration of Diffusive-advective Particle Acceleration in Kinetic Simulations of Relativistic Plasma Turbulence”. In: *Astrophys. J. Lett.* 893.1, L7 (Apr. 2020), p. L7. DOI: [10.3847/2041-8213/ab8122](https://doi.org/10.3847/2041-8213/ab8122). arXiv: [1901.03439](https://arxiv.org/abs/1901.03439) [astro-ph.HE].
- [179] S. E. Woosley and J. S. Bloom. “The Supernova Gamma-Ray Burst Connection”. In: *Annual Review of Astronomy and Astrophysics* 44.1 (Sept. 2006), pp. 507–556. DOI: [10.1146/annurev.astro.43.072103.150558](https://doi.org/10.1146/annurev.astro.43.072103.150558). arXiv: [astro-ph/0609142](https://arxiv.org/abs/astro-ph/0609142) [astro-ph].
- [180] S. Xu, N. Klingler, O. Kargaltsev, and B. Zhang. “On the Broadband Synchrotron Spectra of Pulsar Wind Nebulae”. In: *Astrophys. J.* 872.1, 10 (Feb. 2019), p. 10. DOI: [10.3847/1538-4357/aafb2e](https://doi.org/10.3847/1538-4357/aafb2e). arXiv: [1812.10827](https://arxiv.org/abs/1812.10827) [astro-ph.HE].
- [181] S. Xu and H. Yan. “Cosmic-Ray Parallel and Perpendicular Transport in Turbulent Magnetic Fields”. In: *Astrophys. J.* 779.2, 140 (Dec. 2013), p. 140. DOI: [10.1088/0004-637X/779/2/140](https://doi.org/10.1088/0004-637X/779/2/140). arXiv: [1307.1346](https://arxiv.org/abs/1307.1346) [astro-ph.HE].
- [182] H. Yan and A. Lazarian. “Scattering of Cosmic Rays by Magnetohydrodynamic Interstellar Turbulence”. In: *Phys. Rev. Lett.* 89.28, 281102 (Dec. 2002), p. 281102. DOI: [10.1103/PhysRevLett.89.281102](https://doi.org/10.1103/PhysRevLett.89.281102). arXiv: [astro-ph/0205285](https://arxiv.org/abs/astro-ph/0205285) [astro-ph].
- [183] T. Y. Brian Yang, Jonathan Arons, and A. Bruce Langdon. “Evolution of the Weibel instability in relativistically hot electron-positron plasmas”. In: *Phys. Plasmas* 1.9 (Sept. 1994), pp. 3059–3077. DOI: [10.1063/1.870498](https://doi.org/10.1063/1.870498).
- [184] K. Yee. “Numerical solution of initial boundary value problems involving maxwell’s equations in isotropic media”. In: *IEEE Transactions on Antennas and Propagation* 14.3 (1966), pp. 302–307. DOI: [10.1109/TAP.1966.1138693](https://doi.org/10.1109/TAP.1966.1138693).
- [185] G. P. Zank, Ye Zhou, W. H. Matthaeus, and W. K. M. Rice. “The interaction of turbulence with shock waves: A basic model”. In: *Physics of Fluids* 14.11 (Nov. 2002), pp. 3766–3774. DOI: [10.1063/1.1507772](https://doi.org/10.1063/1.1507772).
- [186] B. Zhang. *The Physics of Gamma-Ray Bursts*. 2018. DOI: [10.1017/9781139226530](https://doi.org/10.1017/9781139226530).

- [187] V. Zhdankin. “Particle Energization in Relativistic Plasma Turbulence: Solenoidal versus Compressive Driving”. In: *Astrophys. J.* 922.2, 172 (Dec. 2021), p. 172. DOI: [10.3847/1538-4357/ac222e](https://doi.org/10.3847/1538-4357/ac222e). arXiv: [2106.00743](https://arxiv.org/abs/2106.00743) [[astro-ph.HE](#)].
- [188] V. Zhdankin, D. A. Uzdensky, G. R. Werner, and M. C. Begelman. “Electron and Ion Energization in Relativistic Plasma Turbulence”. In: *Phys. Rev. Lett.* 122.5, 055101 (Feb. 2019), p. 055101. DOI: [10.1103/PhysRevLett.122.055101](https://doi.org/10.1103/PhysRevLett.122.055101). arXiv: [1809.01966](https://arxiv.org/abs/1809.01966) [[astro-ph.HE](#)].
- [189] V. Zhdankin, D. A. Uzdensky, G. R. Werner, and M. C. Begelman. “Numerical investigation of kinetic turbulence in relativistic pair plasmas - I. Turbulence statistics”. In: *Mon. Notices Royal Astron. Soc.* 474.2 (Feb. 2018), pp. 2514–2535. DOI: [10.1093/mnras/stx2883](https://doi.org/10.1093/mnras/stx2883). arXiv: [1709.04963](https://arxiv.org/abs/1709.04963) [[astro-ph.HE](#)].
- [190] V. Zhdankin, D. A. Uzdensky, G. R. Werner, and M. C. Begelman. “System-size Convergence of Nonthermal Particle Acceleration in Relativistic Plasma Turbulence”. In: *Astrophys. J. Lett.* 867.1, L18 (Nov. 2018), p. L18. DOI: [10.3847/2041-8213/aae88c](https://doi.org/10.3847/2041-8213/aae88c). arXiv: [1805.08754](https://arxiv.org/abs/1805.08754) [[astro-ph.HE](#)].
- [191] V. Zhdankin, G. R. Werner, D. A. Uzdensky, and M. C. Begelman. “Kinetic Turbulence in Relativistic Plasma: From Thermal Bath to Nonthermal Continuum”. In: *Phys. Rev. Lett.* 118.5, 055103 (Feb. 2017), p. 055103. DOI: [10.1103/PhysRevLett.118.055103](https://doi.org/10.1103/PhysRevLett.118.055103). arXiv: [1609.04851](https://arxiv.org/abs/1609.04851) [[physics.plasm-ph](#)].
- [192] J. Zhong, Y. Li, X. Wang, J. Wang, Q. Dong, et al. “Modelling loop-top X-ray source and reconnection outflows in solar flares with intense lasers”. In: *Nature Physics* 6.12 (Dec. 2010), pp. 984–987. DOI: [10.1038/nphys1790](https://doi.org/10.1038/nphys1790).
- [193] J. Zrake and W. E. East. “Freely Decaying Turbulence in Force-free Electrodynamics”. In: *Astrophys. J.* 817.2, 89 (Feb. 2016), p. 89. DOI: [10.3847/0004-637X/817/2/89](https://doi.org/10.3847/0004-637X/817/2/89). arXiv: [1509.00461](https://arxiv.org/abs/1509.00461) [[astro-ph.HE](#)].
- [194] J. Zrake and A. MacFadyen. “Numerical Simulations of Driven Supersonic Relativistic MHD Turbulence”. In: *Gamma Ray Bursts 2010*. Ed. by J. E. McEnery, J. L. Racusin, and N. Gehrels. Vol. 1358. American Institute of Physics Conference Series. Aug. 2011, pp. 102–105. DOI: [10.1063/1.3621748](https://doi.org/10.1063/1.3621748). arXiv: [1109.6294](https://arxiv.org/abs/1109.6294) [[astro-ph.HE](#)].